Network Histories as Entanglement Probes in Spacetimes

Cecilia Giavoni

München 2024

Network Histories as Entanglement Probes in Spacetimes

Cecilia Giavoni

Dissertation
an der Fakultät für Physik
der Ludwig–Maximilians–Universität
München

vorgelegt von
Cecilia Giavoni
aus Verona

München, den 4. November 2024

Erstgutachter: Prof. Dr. Stefan Hofmann

Zweitgutachter: PD Dr. Michael Haack

Tag der mündlichen Prüfung: 19. Dezember 2024

Ai miei nonni,

and to you, who find yourself diving into this thesis

Contents

List of Figures

Zusammenfassung

In dieser Dissertation entwickeln wir einen neuartigen Ansatz zur Untersuchung natürlicher Phänomene in (gekrümmten) Raumzeiten und bieten eine Alternative zu herkömmlichen $(1+3)$-dimensionalen Feldtheorien, wann immer diese unzureichend sind. Inspiriert von der Einfachheit nieder-dimensionaler Theorien, insbesondere $(1+1)$-dimensionaler, die oft komplexe Phänomene stark vereinfachen und teils exakte Lösungen liefern, konstruieren wir theoretische Strukturen, Netzwerke und deren Weltflächen, an die (Quanten-)Felder gebunden sind. Jede Kante des Netzwerks trägt eine einfache, räumlich eindimensionale Feldtheorie, während die Knoten die Ausbreitung der Felder steuern. Da Netzwerke in die $(1+3)$-dimensionale (gekrümmte) Raumzeit eingebettet sind, können Felder durch verschiedene Regionen der Raumzeit entlang eindimensionaler Pfade propagieren.

Die zentrale Idee besteht darin, Felder auf Netzwerkweltflächen als Instrumente zur Untersuchung $(1+3)$-dimensionaler Phänomene vorzuschlagen, anstatt Felder, die im voll-dimensionalen Hintergrund eingebettet sind.

Um unseren Ansatz zu prüfen, untersuchten wir die Verschränkungseigenschaften von Vakuumfluktuationen auf Netzwerken in der Minkowski-Raumzeit. Bemerkenswerterweise zeigt die Verschränkungsentropie, obwohl die Felder eindimensional lokalisiert sind, die gleiche Flächen-Skalierung wie Felder in der $(1+3)$-dimensionalen Raumzeit. Insbesondere, lösen unter bestimmten Bedingungen die Felder die grobe Struktur des Netzwerks nicht auf und verhalten sich wie in einer voll-dimensionalen Raumzeit. Zusätzlich untersuchten wir die Abhängigkeit bezüglich der Form des Subsystems von der Verschränkungsentropie in der $(1+3)$-dimensionalen Minkowski-Raumzeit, was die Gültigkeit unseres Ansatzes bestätigte und ein erstes neues Ergebnis lieferte.

So haben sich Netzwerke als starke theoretische Strukturen erwiesen, um voll-dimensionale Phänomene mit nieder-dimensionalen Instrumente zu erforschen.

Abstract

In this thesis we develop and propose a novel approach for investigating natural phenomena in (curved) spacetimes, offering an alternative to conventional $(1+3)$-dimensional field theory methods, whenever these may prove insufficient. Inspired by the simplicity of lower-dimensional theories – particularly $(1+1)$-dimensional ones, which offer significant simplifications in describing complex phenomena and, in some cases, provide exact solutions – we construct theoretical devices, networks and their histories, to which (quantum) fields are confined. Specifically, each edge of the network is equipped with a simple, spatial one-dimensional field theory with the nodes ruling fields propagation throughout the network. Since networks are embedded within the $(1+3)$-dimensional (curved) spacetime and extend throughout it, fields on networks can propagate through different regions of the embedding spacetime, albeit confined to one-dimensional paths.

The key idea is to propose fields confined to network histories as probes for $(1+3)$-dimensional phenomena, instead of fields embedded in the full-dimensional background.

To test the validity of our proposal, we explored the entanglement properties of vacuum fluctuations confined to network histories embedded in Minkowski spacetime. Remarkably, even though the fields are spatially localized along the one-dimensional edges of the network, the entanglement entropy exhibits the same area scaling characteristic of fields in the full $(1+3)$-dimensional embedding spacetime. In particular, under specific conditions, fields populating the network do not resolve its coarse-grained structure, effectively experiencing the full background. As an additional test, we examined the shape dependence of the entanglement entropy for fields in $(1+3)$-dimensional Minkowski spacetime, with fields confined to network histories. This analysis not only reinforced the validity of our approach but also yielded its first novel result.

Through these investigations, networks have proven to be potent arenas in which full-dimensional phenomena can be investigated through the lens of lower-dimensional probes.

Chapter 1

Introduction

Quantum field theory has proven to be one of the most accurate and experimentally verifiable frameworks available for physicists to explore the fundamental aspects of nature. However, several field-theoretic phenomena remain inaccessible. Despite the theory providing us with well-established principles and equations ruling them, their solutions are often unknown. For instance, exact solutions to the equations of motion for (quantum) fields often turn out to be unavailable in curved spacetimes [1]; most known solutions in fact rely either on approximations or require a high degree of symmetry. Even in the well-known case of a static (Schwarzschild) black hole, a general field propagator remains inaccessible and, as a consequence, even a simple phenomenon like light propagation is not fully comprehended. This challenge, however, is not exclusive to curved spacetimes. The Navier-Stokes equations, which describe the dynamics of fluid-flow fields such as that of water, exemplify how, when a system becomes too complex, we are left without general solutions.

Conversely, focusing on lower spatial dimensions often reduces the complexity of the system remarkably. In particular, considering only a single spatial dimension usually enables for a complete understanding of the system and, in many cases, provides exact solvability, even for interacting theories or in curved backgrounds, where it also drastically simplifies the spacetime, allowing for conformally flat metrics [2–4].

However, by reducing the dimensions of the spacetime itself, such methods are limited to analyze a simplified – often different – version of the initial phenomenon within a lower-dimensional framework. For example, exact solutions for photon propagation in curved spacetimes are presented in [5]; however, they are limited to the case of a photon propagating in a $(1 + 2)$-dimensional curved background. While models involving spacetimes of reduced dimensions can offer valuable insights and may reveal previously unknown solutions, they do not fully capture the complexity or provide a complete description of the original full-dimensional phenomena.

This highlights the need for a new, alternative description that, while relying on the simplicity of lower-dimensional theories, still aims to grasp and convey properties of full-dimensional natural phenomena.

In this work, we take on this challenge by proposing an approach that strikes this balance, offering a new way to investigate the most complex processes in nature. Rather than simplifying the background by reducing its dimensions, we keep the full four-dimensional spacetime as the natural arena for phenomena. What we simplify, instead, are the probes we use – classical or quantum fields – by confining them spatially to one-dimensional supports, which are then embedded into the higher-dimensional ambient space. Therefore, although relying on the simplicity of $(1 + 1)$-dimensional field theories, our focus still lies on processes occurring in the full embedding spacetime.

Yet, a fair question naturally arises: *Can a lower-dimensional theory, such as a* $(1+1)$*-dimensional field theory, accurately describe and provide insights into higher-dimensional natural phenomena?*

Suppose we perform a simple experiment in which light is confined to propagate through a single optical fiber (a one-dimensional spatial support) placed in our lab, i.e. a system of clocks and rulers approximated as a $(1 + 3)$-dimensional, flat spacetime. This single optical fiber can certainly be used to study light propagation in one spatial dimension and similar lower-dimensional experiments. However, no matter how we turn or bend the fiber, it cannot capture phenomena such as the relation between the incident and transmitted angles of light at an interface, as governed by Snell's law of refraction. In our lab, light within the optical fiber carries no information about the angle at which the fiber is positioned within the surrounding space.

Nevertheless, the use of $(1 + 1)$-dimensional theories seems far too powerful not to pursue their implementation. It is exactly from this challenge that our new approach is forged. How do we reconcile working with spatially one-dimensional field theories while probing an higher-dimensional ambient space and the phenomena occurring therein?

If light confined to an optical fiber – or, more generally, fields spatially confined to any one-dimensional support – cannot convey information about the surrounding spacetime, then our idea is to connect multiple one-dimensional supports together, forming a structure that extends into three spatial dimensions within the ambient space (Fig. 1.1). The emerging physical structure is composed of one-dimensional supports of finite size (idealized as edges), e.g. optical fibers, electrical cables, water pipes, or any form of communication channels, connected at their endpoints into junctions (idealized as point-like vertices) to form a network-like structure of finite size. Light, water or any field initially confined to the edges of the structure remain spatially confined to one-dimensional channels, but can now propagate and extend throughout the entire network. This allows the degrees of freedom to travel, still along one-dimensional paths, through different regions of the embedding spacetime.

The choice of background can vary depending on the particular system of interest. It may be as simple as our lab on Earth, resembling a flat spacetime, or alternatively, we could place our physical network in the exterior of a compact star, or even across the horizon of a black hole.

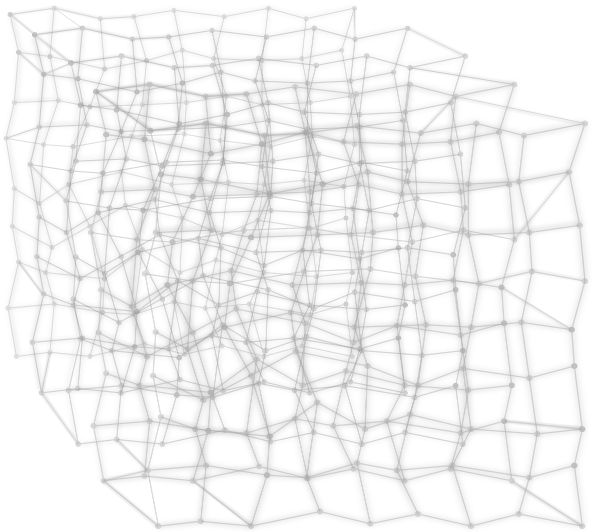

Figure 1.1: Visualization of a quantum field (depicted in gray shades) spatially confined to a physical structure, idealized as a network, which extends into three spatial dimensions within the ambient space.

By considering this new, bizarre physical object, idealized as a network, or graph, and equipped with fields, we can now refine our initial question: *Can such a network, relying on a collection of* $(1+1)$*-dimensional field theories, describe phenomena occurring in the full* $(1+3)$*-dimensional embedding spacetime?*

Throughout this work, we aim to answer this question. If the answer is affirmative, we will demonstrate that networks, or graphs, equipped with fields and embedded in arbitrary spacetimes can serve as powerful diagnostic tools. By relying on the simplicity of $(1+1)$-dimensional field theories, they could achieve objectives that conventional $(1+3)$-dimensional field theory methods have yet to reach.

We dedicate Chapter 2 to the geometric construction of such networks and their embedding in arbitrary, curved spacetimes. Once a network, or any of its elements, is embedded in a background, its dynamics and evolution with respect to a (time) parameter, referred to as its worldsheet or history, becomes central to our analysis. In Section 2.1, we begin by exploring the simple case of a graph consisting of a single edge, constructing its history and embedding it in arbitrary spacetimes. Then, in Section 2.2, we introduce a general $(1+1)$-dimensional field theory on this history and lay the groundwork for a general description of fields spatially confined to single-edge graphs embedded in arbitrary, curved spacetimes.

After fully constructing and investigating the single-edge case, in Chapter 3 we move on to consider a collection of such finite-sized single-edge graphs and explore how to connect them to forge a network and its history, as detailed in Section 3.1. In Section 3.2, a field theory is then defined on the network's history, through intermediate steps of increasing complexity, considering elementary building blocks of the network. By embedding the resulting network in an arbitrary, curved spacetime, we establish a general prescription which rules, at each vertex, the (one-dimensional) spatial propagation of arbitrary fields throughout the network.

With the developments in these first two chapters, we constructed innovative, theoretical devices, ready to be implemented in arbitrary curved spacetimes, allowing us to address higher-dimensional physical phenomena through lower-dimensional theories confined to the network's histories. In the final chapter of this thesis, we put these diagnostic tools to the test, probing their validity and tackling the central question of our investigation.

To this end, we need an initial *pilot* phenomenon. Specifically, we seek a phenomenon that has been thoroughly studied within $(1+3)$-dimensional field theories, thereby serving as a robust test. Simultaneously, we aim for this phenomenon to pave the way for our exploration of quantum fields in black hole backgrounds – particularly across horizons – investigating black hole thermodynamics, entanglement, and, more broadly, information processing at causal boundaries.

Since Bekenstein's groundbreaking proposal of black hole entropy's dependence on the horizon's area [6], numerous efforts have attempted to uncover the physical nature of black hole entropy and its proportionality to the area of the horizon [7,8]. However, the puzzle of black hole entropy remains unsolved.

Among the various attempts, the explanations that most naturally account for why the entropy of black holes is proportional to the area are those that understand the entropy in terms of quantum field correlations between the exterior and interior of the black hole. Notably, seminal works [9,10] demonstrate a direct proportionality between the entanglement entropy of quantum field degrees of freedom outside the black hole and its horizon area. This suggests that black hole entropy is fundamentally quantum in nature, arising specifically from quantum correlations across the horizon. However, in these approaches, black holes are typically modeled as flat $(1+3)$-dimensional spacetime regions intersected with the interior of an artificial sphere, made inaccessible to an external observer. The need of this simplification roots from the lack of a $(1+3)$-dimensional propagator for quantum fields in black hole spacetimes, rendering direct entropy computations and comparisons with Bekenstein's proposal impractical.

This is where our alternative approach becomes crucial. By placing a network across the black hole horizon within a full $(1+3)$-dimensional Schwarzschild background, we could directly study quantum correlations across the causal boundary on the network, potentially revealing an area scaling that, through direct comparison with Bekenstein's proposal, could deliver a verdict on the nature of black hole entropy.

To initiate our program, we first test our model by naturally identifying, as a pilot phenomenon, the area scaling of entanglement entropy for vacuum fluctuations in Minkowski spacetime, as investigated in [9,10]. Instead of embedding a quantum field in its ground state in the $(1+3)$-dimensional Minkowski spacetime, we embed a network equipped with a ground-state quantum field on its edges. By tracing out a spherical region, we can investigate whether the resulting entanglement entropy for the field on the network follows the same area scaling of, for example, [10]. A visualization of the setup within our approach is shown in Fig. 1.2. The computation of the entanglement entropy is detailed in Chapter 4. We begin by examining entanglement entropy for subgraphs of the network shown in Fig. 1.2, progressively considering, in Sec. 4.2, the same elementary building blocks presented in Chapter 3 as they increase in complexity. Sec. 4.3 culminates in the full computation of the entanglement entropy for quantum fields confined to the entire network.

If quantum fields on network histories, serving as an alternative to quantum fields in

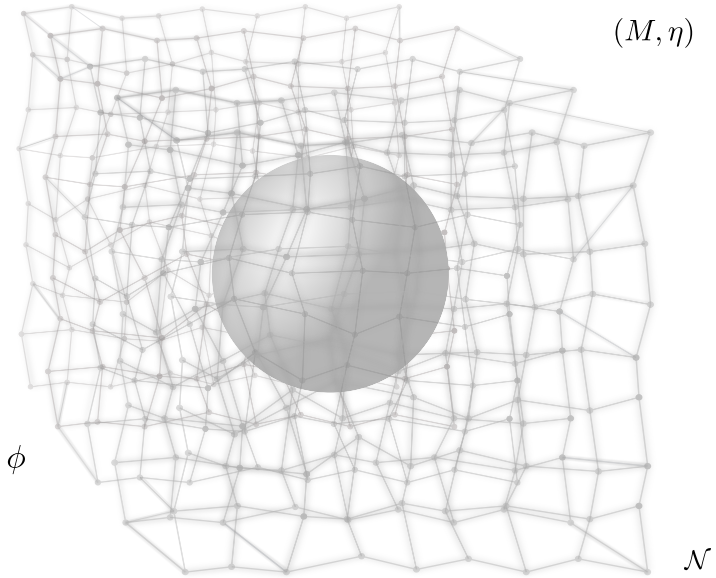

Figure 1.2: Three-dimensional visualization of a quantum field ϕ (depicted in gray shades along the edges) spatially confined to an arbitrary network $\mathcal{N}$ embedded in Minkowski spacetime (M, η). An arbitrary sphere divides the network setup into an interior and an exterior sector. If the interior of the sphere is inaccessible, an external observer loses information about the internal quantum field degrees of freedom. Due to quantum field correlations across the sphere's surface, the exterior and interior sectors of the network may be entangled, with the entanglement entropy quantifying the degree of entanglement.

the full $(1+3)$-dimensional spacetime, capture the same entanglement properties by also exhibiting an area-dependent entropy, this would reveal that the properties of quantum fields in full spacetime emerge from fields confined to lower-dimensional supports. Consequently, the alternative method of fields on network histories could stand as a powerful and robust approach to probe higher-dimensional spacetimes and the phenomena therein, while relying solely on simple lower-dimensional theories. Throughout this work, we use the metric signature $\mathrm{diag}(-,+,+,+)$ and units such that $c = G = \hbar = 1$.

Chapter 2

Physics on Single-Edge Graphs in Arbitrary Spacetimes

Physical networks can be idealized mathematically as graphs. Graphs are meant, in this work, as ordered triples $\mathcal{G} = (\mathcal{V}, \mathcal{E}, \iota)$, where $\mathcal{V}$ is a set of *vertices*, or nodes, $\mathcal{E}$ is a set of *edges* and ι is an incident function $\iota : \mathcal{E} \to \mathcal{V} \times \mathcal{V}$ mapping every edge e in $\mathcal{E}$ to an unordered pair of vertices in $\mathcal{V}$.

Loop structures arise when the two vertices are not distinct, with the map ι associating an edge to the same vertex. When a node is joined by only one edge, it is called the *endpoint* of that edge. Under these definitions, a single edge is itself a graph with two endpoints. Note that ι always maps an edge to two vertices, such that in our investigation we do not consider infinitely long edges – i.e. edges with an open end – in agreement with what we would expect when modeling physical infrastructures.

Before considering more complex idealized structures made up of several nodes and edges, we may want to focus on the simple case of a single edge. This configuration is an idealization of many physical setups, like one-dimensional optical fibers, electrical wires, free space laser links, or one-dimensional potential wells in which particles are trapped. It might also model a simple one-dimensional communication channel.

To implement graphs as models for such devices, additional mathematical concepts must be incorporated into the graph definitions provided above. In fact, in our theory, the edge of the graph acts as a support for degrees of freedom, in the same way a physical optical fiber provides the medium which light is confined to and propagates on. The endpoints of the edge, on the contrary, idealize the physical boundaries (or junctions for nodes) as appropriate boundary conditions.

Therefore, in our work, edges -and thus graphs- are not considered as fundamental structures, but rather as mathematical devices on which physics occurs, as is the case of physical networks. Consequently, in the same way physical networks undergo phenomena and are used as physical devices to perform experiments in the natural world, our theoretical devices also serve as arenas for experiments for physics happening on them. They are mathematical structures to which physics is confined to and which are thus embedded in a higher dimensional background. Only in this way, graphs can be used to probe the full dimensional spacetime and full dimensional natural phenomena happening in it.

In the following, based on our work [11], we will incorporate all the mathematical properties necessary to model physical networks, leading to the constructions of our theoretical devices, which we will simply refer to as *networks*, network histories, or graphs interchangeably.

2.1 The History of a Single-Edge Graph

As previously mentioned, networks or graphs are not considered as fundamental structures. Fields, or degrees of freedom, defined on the fully dimensional manifold are confined to these devices. This means that even a simple single edge is embedded in a background spacetime.

If the single edge were a fundamental structure, the entire spacetime would simply consist of a compact $(1+1)$-dimensional manifold and the edge would no longer be a theoretical device that we can place and use to perform measurements in the spacetime we live in. To this aim, the edge needs to be embedded in an higher dimensional manifold [11].

Consider a globally hyperbolic spacetime (M, g) and, for some parameter τ, its foliation in three-dimensional spacelike hypersurfaces Σ_τ. Then, consider an edge e in $\mathcal{E}$ that we aim to embed in (M, g). The finite *history*, or worldsheet, of the single edge e in (M, g) is a two-dimensional compact and connected Lorentzian submanifold (H_e, h_e) of M, where h_e is the induced metric on H_e obtained from g through the pullback to H_e. The fact that it is a Lorentzian submanifold ensures that causality is incorporated on the edge.

Let U be an open subset of the parameter plane $\mathbb{R}^2$ such that horizontal and vertical lines intersect U either in intervals or not at all. The history of the edge e is given by a smooth two-parameter map $P : U \to H_e$, such that $(\tau, \sigma) \mapsto P(\tau, \sigma)$, which is composed of two families of one-parameter curves: The τ-parameter curve $\sigma = \sigma_0$ of P is $\tau \to P(\tau, \sigma_0)$, and the σ-parameter curve $\tau = \tau_0$ of P is $\sigma \to P(\tau_0, \sigma)$. In this way, the edge is a

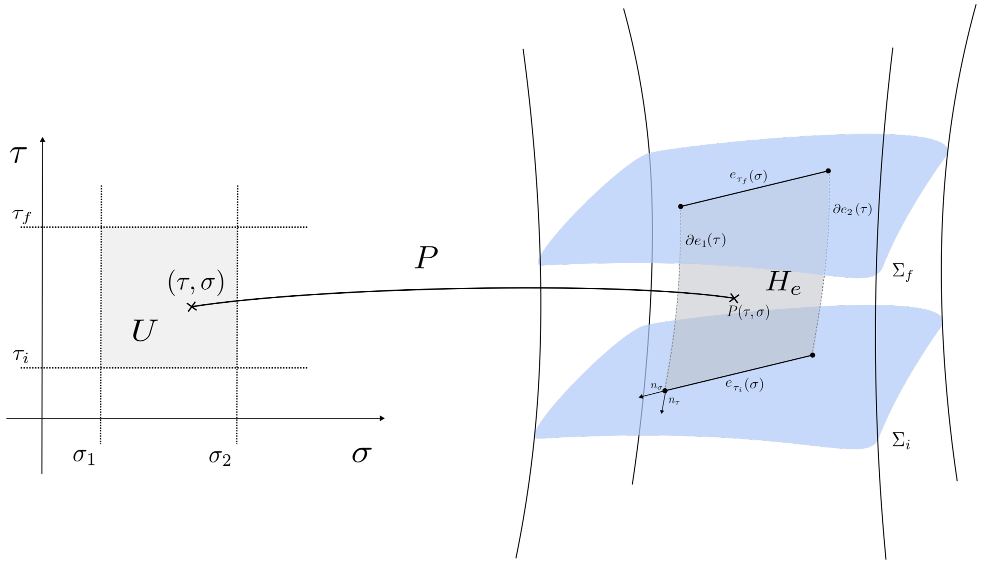

Figure 2.1: Finite history (H_e, h_e) of a single edge e embedded in a globally hyperbolic spacetime (M, g). If τ is a time parameter and σ a spatial one, then the history H_e can be visualized as the worldsheet of the edge e. Note that each Σ_τ is a three-dimensional spacelike hypersurface.

homeomorphic image of the σ-parameter curve and the endpoints of e are identified with the endpoints of the image $P(\tau_0, \sigma)$. Therefore, we can think of the embedding of an edge e on $H_e \subset M$ as a representation of this edge on H_e. Note that τ and σ are intended as general parameters, not yet defining any specific coordinate system. In particular, τ should not be confused with the proper time of a given observer, unless explicitly stated otherwise.

The above mathematical construction is illustrated in Fig. 2.1. As an instructive example, let τ be the time parameter through which we describe the time evolution of our system. A given initial time τ_i determines an interval for σ in U. Through the two-parameter map P, at the time τ_i the edge is parametrized by the σ-parameter curve $P(\tau_i, \sigma)$ with σ in the specified interval. Hence, at each time τ, each point on $e \subset H_e$ is expressed in terms of the parameter σ. On the other hand, by fixing a value of $\sigma = \sigma_0$ and hence a specific point on e, the τ-parameter curve evolves the considered point of the edge in time. The worldline of the point is then parametrized through τ as $P(\tau, \sigma_0)$. If we consider, for each time τ, the entire interval of values for σ, and consequently the whole image of the σ-parameter curve, we obtain, for all times, the time evolution of the whole edge and hence its two-dimensional worldsheet, or *history* H_e.

Note that we allow the edge to be in principle deformable such that it can lengthen, shorten, or bend during the τ-evolution. This might be crucial especially when we consider curved spacetimes where, for example, different points of the edge can move at different velocities.

In the following, let us assume τ is indeed a time parameter and σ a spatial one. The finite history (H_e, h_e) is constituted by a boundary ∂H_e. In particular, as depicted in Fig. 2.1, ∂H_e consists of four boundary terms, two spatial and two temporal. At each history parameter $\tau \in U$, the spatial boundaries of the history are the endpoints of the image of σ-parameter curve, and hence the endpoints of the edge. As an optical fiber is finitely extended in space, so we want the edge to be of finite size. The entire spatial boundaries of H_e are then given by the worldlines of the edge endpoints, i.e. $P(\tau, \sigma_i)$ where $i \in \{1, 2\}$ denotes the two endpoints of the edge. The two $P(\tau, \sigma_i)$ curves are depicted as vertical dashed lines in Fig. 2.1. On the other hand, for each history parameter $\sigma \in U$, the temporal boundaries of the edge history are the endpoints of the image of the τ-parameter curve. The entire temporal boundaries of H_e are then given by $P(\tau_A, \sigma)$, where $A \in \{i, f\}$ labels the initial and final time $\tau_i \in U$, $\tau_f \in U$ respectively. Hence, the edge at initial time and the same edge at a final time are the temporal boundaries of the history. The existence of temporal boundaries ensures the accurate modeling of physical experiments on graphs as devices. In fact, in an experiment, we are interested in specific initial conditions and their evolution till the time a measurement is performed at a later time, when the signal is absorbed. In other words, we consider the history of the edge in the lifespan of the experiment or phenomenon of interest. The boundaries ∂H_e of the finite history can then be mathematically expressed in the following way. Let $\tau_i, \tau_f, \sigma_1, \sigma_2 \in U$ be history parameters. Let ∂e_1 be a τ-parameter curve, i.e. $\partial e_1 : [\tau_\mathrm{i}, \tau_\mathrm{f}] \to H_e$, $\tau \mapsto \partial e_1(\tau) := P(\tau, \sigma_1)$. If σ_1 is such that, for each given $\tau = \tau_0$, $P(\tau, \sigma_1)$ is the first endpoint of the image $P(\tau_0, \sigma)$, then $\partial e_1(\tau)$ is the worldline of that edge endpoint and consequently the spatial boundary of H_e. Accordingly, the same definition holds for the worldline of the second edge endpoint $\partial e_2(\tau)$. Thus, we can define the two spatial boundaries of H_e as the following two τ-parameter curves

$$\begin{aligned} \partial H_e|_{\partial e_1} &:= \partial e_1(\tau) \\ \partial H_e|_{\partial e_2} &:= \partial e_2(\tau) \qquad \forall \tau \in U\,. \end{aligned} \tag{2.1}$$

Furthermore, let e_{τ_i} be a σ-parameter curve $e_{\tau_i} : [\sigma_1, \sigma_2] \to H_e$, such that $\sigma \mapsto e_{\tau_i}(\sigma) :=$

$P(\tau_i, \sigma)$. If τ_i is such that, for each given $\sigma = \sigma_0$, $P(\tau_i, \sigma)$ is the initial endpoint of the image $P(\tau, \sigma_0)$, then $e_{\tau_i}(\sigma)$ is the initial temporal boundary of H_e. Accordingly, similar definitions hold for $e_{\tau_f}(\sigma)$. In other words, the two temporal boundaries are nothing else than the two homeomorphic images of the σ-parameter curves, that is, the edge in H_e at the initial time τ_i and final time τ_f. Thus, we can define the two temporal boundaries of H_e as the following two σ-parameter curves

$$\begin{aligned} \partial H_e|_{e_{\tau_i}} &:= e_{\tau_i}(\sigma) \\ \partial H_e|_{e_{\tau_f}} &:= e_{\tau_f}(\sigma) \qquad \forall \sigma \in U\,. \end{aligned} \tag{2.2}$$

For illustrative purposes, the two spatial boundaries $\partial e_1(\tau)$ and $\partial e_2(\tau)$ and the two temporal boundaries $e_{\tau_i}(\sigma)$ and $e_{\tau_f}(\sigma)$ are depicted in Fig. 2.1.

In conclusion, it is important to emphasize that although the edge is homeomorphic to points in H_e through the two-parameter map P, the edge itself is an object embedded in M, that is, the collection of points $e_\tau := \{e_\tau(\sigma) \,\big|\, \tau = \mathit{const.}\,, \sigma \in \{\sigma_1, \sigma_2\}\}$ in H_e satisfies a geodesic equation and evolves in spacetime. As we will see, this fact will be crucial when studying boundary conditions and observers on the edge.

The Induced Metric on the History H_e

The metric h_e is the metric on the history H_e which is induced by embedding the edge in the background spacetime (M, g). In particular, it is obtained through the pullback from g on M to H_e. In components,

$$h_{e\,ab} = g_{\mu\nu}\, \partial_a x^\mu\, \partial_b x^\nu\,, \tag{2.3}$$

where $x^\mu = x^\mu(\xi^a)$ with $\mu, \nu \in \{0,1,2,3\}$ are coordinates on M. In fact, if ξ^a are coordinates on H_e with $a, b \in \{0, 1\}$, the embedding of the edge in the manifold M is expressed through $x^\mu(\xi^a)$ on M.

Consider a globally hyperbolic spacetime (M, g) and its foliation in spacelike hypersurfaces Σ_τ for a time parameter τ, which implies a $1+3$ splitting of the metric. For any given pair of initial and final hypersurfaces Σ_i, Σ_f we can find the induced metric on the edge history h_e.

A single edge embedded in the Minkowski spacetime

As a first application, let us embed the single edge in a (1 + 3)-dimensional *Minkowski* spacetime. Hence, let us consider as the embedding background the flat spacetime (M, η) where η is the Minkowski metric tensor. In order to embed the edge, let us find the coordinates ξ^a such that we can write $x^\mu(\xi^a)$ accordingly. Given that the edge is spatially one-dimensional, we can write $\xi^a = (\xi^0, \xi^1)$. Since we performed an ADM foliation, we can choose ξ^0 to be the same time coordinate as the one on the Minkowski background. We aim now to write $x^\mu(\xi^a)$. Given a coordinate chart (U, φ) with $U \subset M$, we can write $x^\mu = (T, x, y, z)$ for each point in the neighborhood U of an arbitrary point in Minkowski spacetime (M, η). In terms of these Cartesian coordinates, the two endpoints of the edge can be expressed as the two vectors $\vec{x}_1 = (x_1, y_1, z_1)$ and $\vec{x}_2 = (x_2, y_2, z_2)$ respectively. In this way, an arbitrarily displaced edge in Minkowski can be spatially parametrized as

$$\vec{x} = (x_1, y_1, z_1) + \xi^1 \left((x_2, y_2, z_2) - (x_1, y_1, z_1)\right) , \tag{2.4}$$

with $\xi^1 \in [0, 1]$. Note that we have assumed the edge to be rigid, non-deformable, and straight. Therefore, we can write

$$\begin{aligned} x^0(\xi^0, \xi^1) &= \xi^0 = T \\ x(\xi^0, \xi^1) &= x_1 + \xi^1(x_2 - x_1) \\ y(\xi^0, \xi^1) &= y_1 + \xi^1(y_2 - y_1) \\ z(\xi^0, \xi^1) &= z_1 + \xi^1(z_2 - z_1) \,. \end{aligned} \tag{2.5}$$

Recalling Eq. (2.3), we obtain $h_{e\,ab} = \eta_{\mu\nu}\, \partial_a x^\mu\, \partial_b x^\nu$ and hence

$$\begin{aligned} h_{e\,00} &= -1 \\ h_{e\,01} &= 0 = h_{e\,10} \\ h_{e\,11} &= \eta_{\mu\nu}\, \partial_1 x^\mu\, \partial_1 x^\nu = \partial_1 x\, \partial_1 x + \partial_1 y\, \partial_1 y + \partial_1 z\, \partial_1 z \,, \end{aligned} \tag{2.6}$$

which finally leads to

$$\begin{aligned} h_{e\,00} &= -1 \\ h_{e\,01} &= h_{e\,10} = 0 \\ h_{e\,11} &= (x_2 - x_1)^2 + (y_2 - y_1)^2 + (z_2 - z_1)^2 \,. \end{aligned} \tag{2.7}$$

By identifying the edge length L_e as $L_e = \sqrt{(x_2 - x_1)^2 + (y_2 - y_1)^2 + (z_2 - z_1)^2}$, the line element for the induced metric h_e reads

$$ds^2_{h_e} = -dT^2 + L_e^2\, d\xi^{1\,2}\,. \tag{2.8}$$

Since L_e is constant, the metric components are constant, and thus we have a globally flat metric tensor on the edge, regardless of which point on the edge we consider. If we re-scale the spatial coordinate ξ^1 by introducing $\tilde{\xi}$ as $\tilde{\xi} = L_e \xi^1$ with a coordinates transformation $(T, \xi) \to (T, \tilde{\xi})$, the metric tensor transforms as $\tilde{h}_{e\,uv} = h_{e\,ab}\, \partial_u \xi^a\, \partial_v \xi^b$ and we can rewrite the line element in the new coordinates as

$$ds^2_{\tilde{h}_e} = -dT^2 + d\tilde{\xi}^{\,2}\,, \tag{2.9}$$

which is the $(1+1)$-dimensional Minkowski metric in the coordinates $(T, \tilde{\xi})$. Notice that this line element holds for every point on the edge, such that it is a globally Minkowski-like metric on the edge.

This metric describes an observer always at rest with respect to the coordinates $(T, \tilde{\xi})$, as can be shown as follows: The observer speed is the time-like vector $u^a = \frac{d}{d\tau}(T, \tilde{\xi}) = \frac{dT}{d\tau}\left(1, \frac{d\tilde{\xi}}{dT}\right)$. In order to calculate the motion of the observer following a geodesic $\xi^a(\tau)$ with proper time T, we set $\frac{dT}{d\tau} = 1$. Hence, $u^a = \left(1, \frac{d\tilde{\xi}}{dT}\right)$, which has to satisfy $\tilde{h}_{e\,ab} u^a u^b = -1 + u^{1\,2} \overset{!}{=} -1$, and hence $u^1 = \frac{d\tilde{\xi}}{dT} = 0$. Alternatively, this could be directly derived from the line element. In fact, since $-d\tau^2 = ds^2$, in order for $d\tau = dT$ to be true, $d\tilde{\xi}$ has to vanish. Therefore, the observer follows a worldline with a fixed spatial coordinate $\tilde{\xi}$, i.e. is at rest on the edge. More generally, all coordinate systems for which h_e reduces to the two-dimensional Minkowski metric, or more generally, to $h_{e\,00} = -1$ and $h_{e\,01} = 0$, describe observers at rest on the edge, with $u^a = (1, 0)$.

On the other hand, if we allow a dynamics for the single edge, that is, the edge can move around in (M, g) with a given velocity or acceleration, or even can stretch and shrink (i.e. $L_e = L_e(T)$), the coordinates of the edge endpoints would have a time dependence: $\vec{x}_{1,2} = \vec{x}_{1,2}(T)$. In this case, the induced metric on H_e would include additional terms in $h_{e\,00}$ as well as new terms $h_{e\,01} = h_{e\,10}$, and analogously for $\tilde{h}_e$. These types of metrics do not necessarily describe an observer at rest on the edge; in fact, the observer following a geodesic with proper time T might now not necessarily be at rest and choosing T as proper time might not imply $u^1 = \frac{d\tilde{\xi}}{d\tau} = 0$ for the observer velocity. Therefore, for an edge moving in the background, the same coordinates $(T, \tilde{\xi})$ might not describe an observer at rest, comoving with the edge. However, as long as the edge velocity is constant, a Minkowski-like induced metric can be anyway obtained through a further coordinate transformation to a local comoving observer, at the cost of a re-parametrization of time.

In conclusion, regardless of how the edge is displaced and oriented in the embedding Minkowski background, as long as the edge does not undergo an acceleration, the induced metric h_e on H_e can be always expressed as a simple $(1+1)$-dimensional Minkowski-like metric.

A single edge embedded in curved spacetimes

As already mentioned, one of the main aims of confining (quantum) fields on networks is to obtain a significant simplification of the calculations, since we reduce the three spatial coordinates to just one spatial parameter. The field theory is simplified to two dimensions, which hopefully facilitates the analysis of field propagation on the graph and the computation of related observables. In the Minkowski background, the use of networks as supports for degrees of freedom confined on them tackles complications on the field theory side, since the induced metric on the edge history reduces anyway to a simple two dimensional Minkowski metric.

However, an additional difficulty arises when embedding a single-edge graph in a curved, possibly dynamical, spacetime. In arbitrary curved backgrounds, the locality of the metric tensor – which makes it change at different spacetime points – is such that even the solution to the equation of motion for a simple free scalar field may not be known, and the propagator in the full-dimensional background might not be found. In the curved and/or dynamical case, the reduction of spatial dimensions provided by graphs could not only address potential complications that may arise from a field theory perspective, but also drastically simplify the metric on the edge history in contrast to the full-dimensional, curved one.

On the other hand, if we have shown that in a flat Minkowski background, the induced metric h_e on the edge history is always globally flat on the edge, this does not necessarily hold in curved spacetimes. In fact, the curvature of the embedding manifold prevents an observer to be globally inertial on the edge history (if the edge extension is larger than the size of a normal neighborhood of the spacetime); the induced metric will inevitably be different at each different point on the edge history. Consequently, even in the mentioned case of free scalar fields propagating on the edge, the equations of motion may exhibit non-trivial terms due to the metric, and in some cases, even in two dimensions a solution may not be found.

However, the potential of networks resides precisely in their dimensionality. In fact, it has been demonstrated [12] in the context of Lorentzian geometry that the following theorem holds:

Theorem 1. *Every two-dimensional Lorentzian manifold* (H, h) *is* <u>*conformally flat*</u>*, that is there are local parametrizations* ϕ*, such that for the induced metric* h *one has*

$$\phi^* h = \Omega^2 \eta = \Omega^2 \begin{pmatrix} -1 & 0 \\ 0 & 1 \end{pmatrix} , \tag{2.10}$$

where Ω *is a smooth function, referred to as conformal factor.*

Since the edge history (H_e, h_e) is by definition a two-dimensional Lorentzian submanifold, we obtain that, no matter how curved or dynamical the embedding spacetime (M, g) is, we can always find a local parametrization such that the induced metric on the edge history can be written in conformally flat form. Therefore, for a single edge embedded in an arbitrary curved, dynamical spacetime, we can always write

$$h_e = \Omega^2 \eta \,. \tag{2.11}$$

As we will see, the two-dimensionality of the edge history is the key ingredient for modeling physics with fields on networks, since the metric on each network's edge can be brought in this simple conformally flat form. Although the conformal factor might still be a complicated function of the coordinates, in some cases it anyway simplifies the computations significantly. For free massless scalar fields, for example, the action functional even assumes the same form as the action functional for the same fields in the two-dimensional Minkowski spacetime, no matter how Ω looks. In this case, free massless scalar fields propagating on a single edge would not be able to probe the curved embedding spacetime.

In the following, we consider as an example the spacetime of an eternal black hole as the embedding background (M, g) and hence we consider the case where the edge is placed in the exterior of a *Schwarzschild* black hole. The four-dimensional Schwarzschild metric g_s is expressed in isotropic coordinates $x^\mu = (T, x, y, z)$ as

$$ds^2 = -\frac{(1 - \frac{2M}{4R})^2}{(1 + \frac{2M}{4R})^2} dT^2 + \left(1 + \frac{2M}{4R}\right)^4 \left(dx^2 + dy^2 + dz^2\right) , \tag{2.12}$$

where $R = \sqrt{x^2 + y^2 + z^2}$. This metric describes exclusively the black hole exterior, i.e.

$R > \frac{M}{2}$.

Similarly to the flat spacetime case, we are interested in placing the edge – which models a physical edge such as an optical fiber or an electric wire – near a black hole, to study possible effects of gravity on fields propagating on the edge. Therefore, we need to embed the edge into the four-dimensional background (M, g_s). A rigid edge outside the black hole horizon can be spatially parameterized, analogously to the flat case, as

$$\vec{x} = (x_1, y_1, z_1) + \xi^1 \left((x_2, y_2, z_2) - (x_1, y_1, z_1)\right) \,, \tag{2.13}$$

with $\xi^1 \in [0, 1]$. Again, $\vec{x}_1$ and $\vec{x}_2$ are the spatial coordinates of the two edge endpoints. Note that, in this example, we let the endpoints spatial coordinates be constant, hence we assume the edge to be at rest in the four-dimensional Schwarzschild spacetime. If the edge were assumed to be free falling towards the black hole, we would have to introduce the dynamics of the edge by writing $\vec{x}_1 = \vec{x}_1(T)$ and $\vec{x}_2 = \vec{x}_2(T)$. Furthermore, it is worth noting that the assumption of a rigid edge is actually a simplification of the system since, when embedded in a curved spacetime, the edge points follow distinct geodesics and acquire different velocities, which may result in the edge no longer being rigid. For a proper parametrization of an arbitrary curved edge, we need to consider the edge displacement and orientation in the embedding spacetime case to case. Here, we consider the case of a rigid straight edge only as an instructive example.

In terms of the coordinates $\xi^a = (T, \xi^1)$ on the edge history, the coordinates of the isotropic Schwarzschild observer $x^\mu = x^\mu(\xi^a)$ lead to the induced metric $h_{e\,ab} = g_{\mu\nu}\,\partial_a x^\mu\,\partial_b x^\nu$, with $g_{\mu\nu}$ the four-dimensional Schwarzschild metric in isotropic coordinates. We obtain

$$\begin{aligned}
h_{e\,00} &= -\frac{(1-\frac{2M}{4R})^2}{(1+\frac{2M}{4R})^2} \\
h_{e\,01} &= 0 = h_{e\,10} \\
h_{e\,11} &= g_{\mu\nu}\,\partial_1 x^\mu\,\partial_1 x^\nu = \left(1+\frac{2M}{4R}\right)^4 \left[(x_2-x_1)^2 + (y_2-y_1)^2 + (z_2-z_1)^2\right] \,.
\end{aligned} \tag{2.14}$$

Hence, the line element for a rigid edge embedded in the exterior of a Schwarzschild black hole reads, in the coordinates $\xi^a = (T, \xi^1)$,

$$ds^2_{h_e} = -\frac{(1-\frac{2M}{4R})^2}{(1+\frac{2M}{4R})^2} dT^2 + \left(1+\frac{2M}{4R}\right)^4 L_e^2\, d\xi^{1\,2} \,. \tag{2.15}$$

Notice that the radius $R = \sqrt{x^2 + y^2 + z^2}$ is now evaluated at points $(x(\xi^1), y(\xi^1), z(\xi^1))$ on the edge.

Analogously to the Minkowski case, we can rescale the spatial coordinate by introducing a new coordinate system $\tilde{\xi}^a = (T, \tilde{\xi})$ such that $d\tilde{\xi} = \left(1 + \frac{2M}{4R}\right)^2 L_e d\xi^1$. In terms of these coordinates the line element related to the induced metric on the edge history in a black hole background reads

$$ds^2_{\tilde{h}_e} = -\frac{(1 - \frac{2M}{4R})^2}{(1 + \frac{2M}{4R})^2} dT^2 + d\tilde{\xi}^2 \,. \tag{2.16}$$

It is important to notice that although the metric $\tilde{h}_e$ is defined on the two-dimensional edge history, the observer measures events on the edge with time T of an observer sitting far away from the horizon at $R \gg M/2$.

In contrast to the flat spacetime case, we now observe that the temporal components of the metric are no longer constant but instead vary with the position $\tilde{\xi}$ along the edge, as determined by $R = R(\tilde{\xi})$. Hence, the proper time of a local observer at rest on the edge would flow differently depending on where the observer sits and a globally Minkowski-like two-dimensional metric is not available.

Furthermore, we can perform one final coordinate transformation which, according to Theorem 1, brings the line element in a conformally flat form. To this aim we introduce a new spatial coordinate ξ' such that

$$d\xi' = \frac{(1 + \frac{2M}{4R})}{(1 - \frac{2M}{4R})} d\tilde{\xi} \,. \tag{2.17}$$

Then, in the new coordinates (T, ξ'), the line element of the induced metric on the edge history reads

$$ds^2_{h'_e} = \frac{(1 - \frac{2M}{4R})^2}{(1 + \frac{2M}{4R})^2} \left(-dT^2 + d\xi'^2\right) \,, \tag{2.18}$$

where $\Omega(R) = \frac{(1-\frac{2M}{4R})}{(1+\frac{2M}{4R})}$ is the conformal factor. Since $R = R(\xi')$, the conformal factor is a function of the spatial coordinate ξ' and will vary at each different point of the edge. Note that, more generally, if the embedding spacetime would not be static as the Schwarzschild one, but dynamical, the conformal factor would in general depend also on the time coordinate, i.e. $\Omega = \Omega(x^0, x^1)$.

The line element Eq. 2.18 is related to an observer which measures time with the same time coordinate T as the four-dimensional Schwarzschild observer and space with the local spatial coordinate ξ' on the edge. In particular, the observer is moving on the edge with a velocity $u^1(R) = \frac{d\xi'}{dT} = \sqrt{1 - \frac{1}{\Omega^2(R)}}$. Therefore, the observer's velocity is a vector field that changes at each edge point, showing that the observer is not an inertial observer as in Minkowski, but is accelerating along the edge. Furthermore, note that the induced metric on the edge does not explicitly depend on the edge orientation.

2.2 Fields on a Single-Edge History

As already announced, the core idea of our method is to spatially constrain degrees of freedom, so that they are confined and propagate on one-dimensional supports, that serve as models for physical cables, optical fibers, or one-dimensional traps. Experimentally, there are various methods to confine fields propagating through full space onto one-dimensional supports, using mechanisms such as Snell's law for total internal reflection, optical lattices, or magnetic fields. However, complete confinement is physically impossible to achieve, and both classical and (especially) quantum fields leak beyond the one-dimensional support. While most of the field remains on the support, describing fields confined to histories with $(1+1)$-dimensional field theories is, in fact, an approximation. Moreover, in our theoretical framework we do not explicitly include the confinement mechanism; instead, for simplicity, we begin by assuming an intrinsic $(1+1)$-dimensional field theory.

In the previous section, we modeled each one-dimensional support by a single-edge graph e, and after defining a single-edge history H_e, its boundaries, and the induced metric h_e on it, we identified points of the edge with points on the two-dimensional compact Lorentzian history (H_e, h_e).

The next ingredient needed to model experiments on theoretical devices such as graphs, e.g. modeling light confined to an optical fiber, is to establish the mathematical framework that allows degrees of freedom to propagate on them. In particular, as degrees of freedom, we want to confine classical – and eventually quantum – fields to single edges.

The idea of studying quantum fields on graphs has been developed in the last two decades and finds its roots in quantum graph theory, a field of studies in which metric graphs are equipped with differential operators, like for example Hamiltonians [13]. On a quantum graph, differential operators act along the edges with appropriate conditions as junction conditions at the vertices. Over the years, metric graphs have been the arena to analyze partial differential equations with junction conditions, spectral theory of linear operators, quantum chaos and scattering of waves on vertices, for instance, [14–18]. With the increasing attention acquired by the Laplacian operator, even the quantum theory of fields was introduced on graphs [19], and a thorough discussion of quantum fields on star graphs has been given in [20, 21].

However, the main difference between our method and the quantum graph theory literature is that in our case the graph itself is not a fundamental structure but, as we have seen, it is a theoretical device embedded in a background and hence with an induced metric on it. In fact, in the network histories approach, fields are *confined* to the graph and consequently can probe the embedding background.

In this subsection, we want to consider a single-edge graph embedded in an arbitrary spacetime and introduce a field theory on it. For a geometrical introduction of the field theory on a single edge we refer the reader to [11]. In the following, a simpler but less geometric and rigorous approach is favoured. Furthermore, in this section we refer exclusively to classical fields, while for a construction of the field theory which is already suitable for a possible quantization program on networks, we again refer to [11].

Firstly, for the sake of simplicity, we consider the case of a real scalar field ϕ. Consider a single edge e and its history (H_e, h_e), embedded in a arbitrary globally hyperbolic background (M, g). We define the action functional $\mathcal{A}_e[\phi]$ for the field ϕ confined to the history H_e, by

$$\mathcal{A}_e[\phi] := \int_{H_e} \mathcal{L}_e(x, \phi, \mathrm{d}\phi)\ \mathrm{dvol}_{h_e}\ , \tag{2.19}$$

where, for some abstract coordinate system $x = \{\xi^a\} = (T, \xi)$, $\mathcal{L}_e(T, \xi, \phi, \mathrm{d}\phi)$ denotes the Lagrangian of the theory and dvol_{h_e} the volume element with h_e the two-dimensional metric tensor induced on the history of the edge e.

In order to find the field evolution along the edge, we make use of the variational principle: given two field configurations at initial and final time T_i and T_f respectively, we look for the stationary point of the action functional, for arbitrary and independent field variations $\delta\phi$,

$$\delta\mathcal{A}_e = \int_{H_e} \left(\frac{\partial\mathcal{L}_e}{\partial\phi}\delta\phi + \frac{\partial\mathcal{L}_e}{\partial\partial_a\phi}\partial_a\delta\phi \right) \sqrt{-h_e}\, dTd\xi \overset{!}{=} 0, \tag{2.20}$$

where $a = 0, 1$ and in our notation we define $\sqrt{-h_e} := \sqrt{-\det h_e}$. By using the identity for the divergence and including $\sqrt{-h_e}$ in it, we can rewrite Eq. (2.20) as

$$\delta\mathcal{A}_e = \int_{H_e} \frac{\partial\mathcal{L}_e}{\partial\phi}\delta\phi\sqrt{-h_e}\, dTd\xi + \int_{H_e} \left[\partial_a\left(\sqrt{-h_e}\frac{\partial\mathcal{L}_e}{\partial\partial_a\phi}\delta\phi \right) - \partial_a\left(\sqrt{-h_e}\frac{\partial\mathcal{L}_e}{\partial\partial_a\phi} \right)\delta\phi \right] dTd\xi \overset{!}{=} 0. \tag{2.21}$$

By applying the divergence theorem, the above equation yields

$$\delta\mathcal{A}_e = \int_{H_e}\left(\frac{\partial\mathcal{L}_e}{\partial\phi}\sqrt{-h_e} - \partial_a\left(\sqrt{-h_e}\frac{\partial\mathcal{L}_e}{\partial\partial_a\phi}\right)\right)\delta\phi dT d\xi + \int_{\partial H_e}\frac{\partial\mathcal{L}_e}{\partial\partial_a\phi}\delta\phi\, n_a\sqrt{-h_e^\partial}\, dq \overset{!}{=} 0, \tag{2.22}$$

where h_e^∂ indicates the determinant of the induced metric at the boundary, q are coordinates on it and n is the vector field normal to the considered boundary.

The two terms of Eq. (2.22) have different supports for the field ϕ except at the boundaries of the edge history ∂H_e. This implies that in the interior of H_e the first term must vanish independently in order for the total variation of the action functional to be zero. This leads to the Euler-Lagrange equation,

$$\frac{\partial\mathcal{L}_e}{\partial\phi} - \frac{1}{\sqrt{-h_e}}\partial_a\left(\sqrt{-h_e}\frac{\partial\mathcal{L}_e}{\partial\partial_a\phi}\right) = 0\,, \tag{2.23}$$

i.e. the equation of motion for the field along the edge. At the boundaries ∂H_e both terms of Eq. (2.22) contribute and their sum has to vanish,

$$\int_{\partial H_e}\left(\frac{\partial\mathcal{L}_e}{\partial\phi}\sqrt{-h_e^\partial} - \partial_a\left(\sqrt{-h_e^\partial}\frac{\partial\mathcal{L}_e}{\partial\partial_a\phi}\right)\right)\delta\phi dq + \int_{\partial H_e}\frac{\partial\mathcal{L}_e}{\partial\partial_a\phi}\delta\phi\, n_a\sqrt{-h_e^\partial} dq \overset{!}{=} 0\,. \tag{2.24}$$

Both boundary terms in Eq. (2.24) are actually consisting of four different terms each for one of the four boundaries of ∂H_e. Mathematically,

$$\begin{aligned}
&\int_{\partial H_e}\left(\frac{\partial\mathcal{L}_e}{\partial\phi}\sqrt{-h_e^\partial} - \partial_a\left(\sqrt{-h_e^\partial}\frac{\partial\mathcal{L}_e}{\partial\partial_a\phi}\right)\right)\delta\phi dq = \\
&\quad = \int_{\partial H_e|_{\partial e_1}}\left(\frac{\partial\mathcal{L}_e}{\partial\phi}\sqrt{-h_e^\partial} - \partial_a\left(\sqrt{-h_e^\partial}\frac{\partial\mathcal{L}_e}{\partial\partial_a\phi}\right)\right)\delta\phi dT + \\
&\quad + \int_{\partial H_e|_{\partial e_2}}\left(\frac{\partial\mathcal{L}_e}{\partial\phi}\sqrt{-h_e^\partial} - \partial_a\left(\sqrt{-h_e^\partial}\frac{\partial\mathcal{L}_e}{\partial\partial_a\phi}\right)\right)\delta\phi dT + \\
&\quad + \int_{\partial H_e|_{e_{\tau_i}}}\left(\frac{\partial\mathcal{L}_e}{\partial\phi}\sqrt{-h_e^\partial} - \partial_a\left(\sqrt{-h_e^\partial}\frac{\partial\mathcal{L}_e}{\partial\partial_a\phi}\right)\right)\delta\phi d\xi + \\
&\quad + \int_{\partial H_e|_{e_{\tau_f}}}\left(\frac{\partial\mathcal{L}_e}{\partial\phi}\sqrt{-h_e^\partial} - \partial_a\left(\sqrt{-h_e^\partial}\frac{\partial\mathcal{L}_e}{\partial\partial_a\phi}\right)\right)\delta\phi d\xi\,,
\end{aligned} \tag{2.25}$$

and, for the second term,

$$\begin{aligned}
&\int_{\partial H_e} \frac{\partial \mathcal{L}_e}{\partial \partial_a \phi} \delta\phi \, n_a \sqrt{-h_e^\partial} dq = \\
&= \int_{\partial H_e|_{\partial e_1}} \frac{\partial \mathcal{L}_e}{\partial \partial_a \phi} n_{\sigma\, a} \sqrt{-h_e^\partial} \delta\phi dT + \int_{\partial H_e|_{\partial e_2}} \frac{\partial \mathcal{L}_e}{\partial \partial_a \phi} n_{\sigma\, a} \sqrt{-h_e^\partial} \delta\phi dT + \\
&+ \int_{\partial H_e|_{e_{\tau_i}}} \frac{\partial \mathcal{L}_e}{\partial \partial_a \phi} n_{\tau\, a} \sqrt{-h_e^\partial} \delta\phi d\xi + \int_{\partial H_e|_{e_{\tau_f}}} \frac{\partial \mathcal{L}_e}{\partial \partial_a \phi} n_{\tau\, a} \sqrt{-h_e^\partial} \delta\phi d\xi \,. \qquad (2.26)
\end{aligned}$$

For temporal boundaries, $n_\tau \perp \partial H_e|_{e_{\tau_i}}$ is chosen to be a vector field normal to the initial edge e_{τ_i} and pointing to the past. On the other hand, for spatial boundaries $n_\sigma \perp \partial H_e|_{\partial e_j}$, with $j \in \{1, 2\}$ is the vector field normal to the worldline of the edge endpoint ∂e_j and chosen to be oriented away from the edge. Both types of normal vector fields are depicted in Fig. 2.2, through two exemplary vectors at the first edge endpoint $\partial e_1(\tau_i) = (\tau_i, \sigma_1)$. Note that whenever we explicitly refer to the history or its structure, we use the general parameter τ and σ instead of T, ξ, for consistency with the figures and the general construction of Sec. 2.1.

The last two terms of Eq. (2.25) and Eq. (2.26), relative to the temporal boundaries of ∂H_e, do vanish according to the variational principle; in fact, at the initial and final time the field configuration is known and the field variations $\delta\phi$ are constrained to be zero, i.e. $\delta\phi = \delta\phi(T_i, \xi) = \delta\phi(T_f, \xi) = 0$, for all values of ξ. These terms actually reflect the choice of initial - and final - conditions for the field configuration.

Concerning Eq. (2.25), the two remaining terms on $\partial H_e|_{\partial e_1}$ and $\partial H_e|_{\partial e_2}$ are also vanishing, since by continuity we can set the term $\frac{\partial \mathcal{L}_e}{\partial \phi} \sqrt{-h_e^\partial} - \partial_a \left(\sqrt{-h_e^\partial} \frac{\partial \mathcal{L}_e}{\partial \partial_a \phi} \right)$ to zero at the spatial boundaries as well. Consequently, this implies that the first term of Eq. (2.24) is zero. Therefore, for the total variation of the action functional to vanish, we obtain

$$\int_{\partial H_e} \frac{\partial \mathcal{L}_e}{\partial \partial_a \phi} \delta\phi \, n_a \sqrt{-h_e^\partial} dq \overset{!}{=} 0 \,, \qquad (2.27)$$

or, according to Eq. (2.26)

$$\begin{aligned}
&\int_{\partial H_e} \frac{\partial \mathcal{L}_e}{\partial \partial_a \phi} \delta\phi \, n_a \sqrt{-h_e^\partial} dq = \\
&= \int_{\partial H_e|_{\partial e_1}} \frac{\partial \mathcal{L}_e}{\partial \partial_a \phi} n_{\sigma\, a} \sqrt{-h_e^\partial} \delta\phi dT + \int_{\partial H_e|_{\partial e_2}} \frac{\partial \mathcal{L}_e}{\partial \partial_a \phi} n_{\sigma\, a} \sqrt{-h_e^\partial} \delta\phi dT \overset{!}{=} 0 \,. \qquad (2.28)
\end{aligned}$$

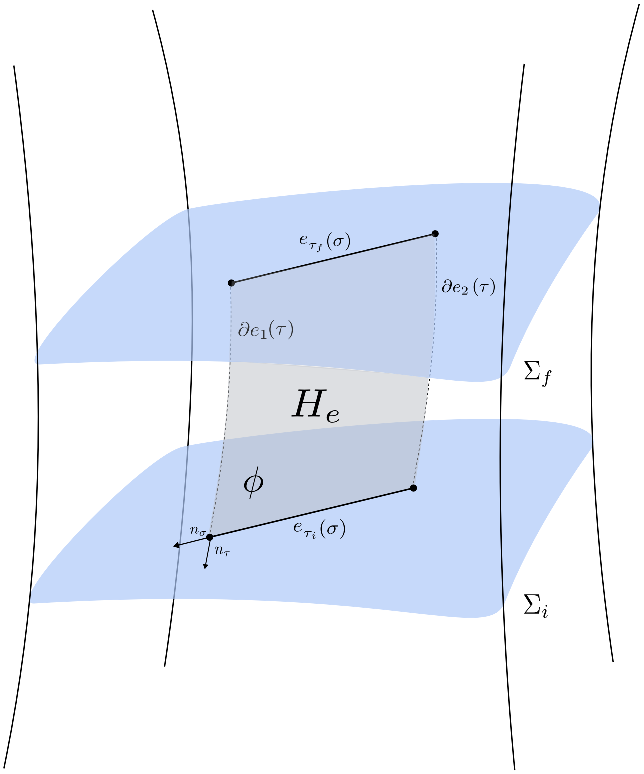

Figure 2.2: Temporal and spatial boundaries of the finite history (H_e, h_e) of a single edge e. If τ is a time parameter and σ a spatial one, then the history H_e can be visualized as the worldsheet of the edge e. In the figure, the two normal vectors fields $n_\tau(\tau_i, \sigma)$ and $n_\sigma(\tau, \sigma_1)$ are shown representatively at the spacetime point $\partial e_1(\tau_i) = (\tau_i, \sigma_1)$, the first endpoint of the edge.

These remaining two terms lead to actual boundary conditions for the field on the edge. Since they have non-overlapping supports, the action variation can only vanish if each of the two integrals vanishes individually. As the fields variations $\delta\phi = \delta\phi(T, \xi)$ are arbitrary functions, the two integrals vanish if and only if the respective integrand is zero, that is

$$\frac{\partial \mathcal{L}_e}{\partial \partial_a \phi} n_{\sigma\, a} \sqrt{-h_e^\partial}\,\Big|_{\partial H_e|_{\partial e_j}} \overset{!}{=} 0 \qquad \textit{with}\ \ j \in \{1, 2\} \tag{2.29}$$

for each time T, at the two endpoints of the edge ∂e_1 and ∂e_2, respectively.

Therefore, the variational principle implemented in Eq. (2.20) yields the following conditions, for arbitrary, non-vanishing, field variations $\delta\phi$

$$\frac{\partial \mathcal{L}_e}{\partial \phi} - \frac{1}{\sqrt{-h_e}}\partial_a \left(\sqrt{-h_e}\frac{\partial \mathcal{L}_e}{\partial \partial_a \phi} \right) = 0 \qquad \wedge \qquad \frac{\partial \mathcal{L}_e}{\partial \partial_a \phi} n_{\sigma\, a} \sqrt{-h_e^{\partial}} \Bigg|_{\partial H_e|_{\partial e_j}} = 0 \quad \mathit{with} \;\; j \in \{1, 2\} \tag{2.30}$$

which are the equation of motion for the field ϕ along the edge and the boundary conditions at its two endpoints, respectively.

To see how the conditions Eq. (2.29) turn into boundary conditions for the field, let us consider, as an example, the Lagrangian density $\mathcal{L}_e$ of a free real scalar field of mass μ, spatially confined to the edge e

$$\mathcal{L}_e = \frac{1}{2} \left(h_e^{ab}\, \partial_a \phi\, \partial_b \phi - \mu^2 \phi^2 \right) . \tag{2.31}$$

The metric h_e is the induced metric on the edge history and therefore $a, b \in \{0, 1\}$. Note that, although in this work we will focus on free scalar fields, the same construction holds for interacting fields or for other spin values.

By introducing the Lagrangian density Eq. (2.31) in Eq. (2.30), we obtain

$$\left(\Box_{h_e} + \mu^2 \right) \phi = 0 \tag{2.32}$$

as equation of motion for the field ϕ on the edge and, for the boundary conditions,

$$h_e^{ab} \partial_a \phi\, n_{\sigma\, b} \sqrt{-h_e^{\partial}} \Bigg|_{\partial H_e|_{\partial e_j}} \overset{!}{=} 0 \qquad \mathit{with} \;\; j \in \{1, 2\} . \tag{2.33}$$

The vector field n_σ, normal to the worldline of each edge endpoint, can be computed by considering the two-velocity $u^a_{\partial e_j}$ of the two endpoints ∂e_1 and ∂e_2. In fact, n_σ is defined to be orthogonal to the tangent two-vector $u^a_{\partial e_j}$ of each worldline. We also require n_σ to be normalized to unity. For an arbitrary observer on the edge, the two-velocity of the endpoint ∂e_j is a timelike future-directed vector expressed, in the coordinates on the edge, as

$$u^a_{\partial e_j} = \frac{d\xi^a}{d\tau} = \frac{d}{d\tau}(T, \xi) = \frac{dT}{\partial \tau} \frac{d}{dT} (T, \xi) = \frac{dT}{d\tau} \left(1, \frac{d\xi}{dT} \right) . \tag{2.34}$$

As a matter of fact, unless the observer is a comoving observer on the edge, the spatial velocities of the edge endpoints are a priori not vanishing. Since the normal vector field is orthogonal to $u^a_{\partial e_j}$ and consequently a spacelike unit vector, it has to satisfy the following relations:

$$\begin{aligned} h_{e\,ab} u^a_{\partial e_j} n^b_\sigma &= 0 \\ h_{e\,ab} n^a_\sigma n^b_\sigma &= 1\,. \end{aligned} \tag{2.35}$$

By inserting the induced metric h_e on the edge history, we can use the above equations to find the components of the normal vector field at the spatial boundaries.

2.2.1 Single-Edge Graphs Embedded in Minkowski Spacetime

In the following, we will examine the conditions given by Eq. (2.35) for an edge embedded in a four-dimensional Minkowski background. For the purposes of this analysis, we will assume that the edge does not shrink or stretch over time; in particular, we assume that it is in free fall. If the edge is embedded in the Minkowski spacetime (M, η), we have shown in Subsec. 2.1 that, no matter how the edge is displaced, the induced metric reduces to the two-dimensional Minkowski metric tensor $h_{e\,ab} = \begin{pmatrix} -1 & 0 \\ 0 & 1 \end{pmatrix}$. Accordingly, the induced metric h^∂_e of the spatial boundaries reads $h^\partial_e = -1$ and hence its determinant is $\det h^\partial_e = -1$. Let $\xi^a = (T, \xi)$ be the coordinates such that h_e is the two-dimensional Minkowski metric. The line element is then $ds^2_{h_e} = -dT^2 + d\xi^2$ and the observer is at rest on the edge. If we insert $h_{e\,ab}$ in the conditions Eq. (2.35), we find

$$\begin{aligned} -u^0_{\partial e_j} n^0_\sigma + u^1_{\partial e_j} n^1_\sigma &= 0 \\ -n^0_\sigma n^0_\sigma + n^1_\sigma n^1_\sigma &= 1\,. \end{aligned} \tag{2.36}$$

The two two-velocities of the endpoints of the edge are given, for the observer at rest on the edge, as $u^a_{\partial e_j} = (1, 0)$, for both endpoints ∂e_j with $j \in \{1, 2\}$. In fact, we have used the fact that the endpoint coordinates are constant $\frac{d\xi_{\partial e_j}}{dT} = 0$ and hence $d\tau = dT$. According to Eq. (2.36), the normal vector field n^a_σ is then given by

$$n^a_\sigma = (0, \pm 1)\,, \tag{2.37}$$

which is constant along each spatial boundary of H_e. Hence, for an edge embedded in the Minkowski spacetime, Eq. (2.33) simplifies to

$$\partial_\xi \phi \overset{!}{=} 0\,, \tag{2.38}$$

at the two endpoints ∂e_1, ∂e_2 of the edge, for all times T.

Physically, this condition ensures that there is no leakage of degrees of freedom out of the edge while they propagate and approach the endpoints. As an illustrative physical example, light confined to an optical fiber (idealized as the edge) with two mirrors at its extremities is totally reflected back to the fiber and when approaching the endpoints the optical signal is kept on the fiber and cannot leave to other materials or air. In this example, the two mirrors are the physical boundaries which ensure Eq. (2.38) for the electromagnetic field. The above condition Eq. (2.38) is a Neumann boundary condition for the field at the spatial boundaries. Alternatively, we could have assumed the arbitrary field variations $\delta\phi(T,\xi)$ to be vanishing for all times on the spatial boundaries in Eq. (2.26). Consequently, the value of the field would have been set to constant at the spatial boundaries, resulting in Dirichlet boundary conditions for the field, i.e. $\phi(T,\xi) = const.$ at the two edge endpoints. Thus, the stationarity condition for the action functional of a field confined to a single edge embedded in the Minkowski background ensures that, regardless of the boundary conditions, the degrees of freedom are confined to the edge and cannot leave it.

2.2.2 Single-Edge Graphs Embedded in Curved Spacetimes

We have seen in Subsec. 2.1 that for a single edge embedded in a curved, possibly dynamical spacetime, the induced metric h_e on the edge history H_e can always be brought into the conformally flat form $h_e = \Omega^2\eta$, where η is the two-dimensional Minkowski metric.

In these coordinates, the calculations for the boundary conditions simplify significantly. Let $\xi^a = (T,\xi)$ be the – conformal – coordinates in which, for an arbitrary choice of the embedding spacetime, the induced metric takes the conformally flat form with line element $ds^2_{h_e} = -\Omega^2(T,\xi)dT^2 + \Omega^2(T,\xi)d\xi^2$. More explicitly, $h_{e\,ab} = \Omega^2(T,\xi)\begin{pmatrix} -1 & 0 \\ 0 & 1 \end{pmatrix}$. The conditions in Eq. (2.33) become, for the single edge in conformally flat form,

$$h_e^{ab}\partial_a\phi\, n_{\sigma\, b}\sqrt{-h_e^{\partial}}\,\Big|_{\partial H_e|_{\partial e_j}} = \frac{1}{\Omega^2(T,\xi)}(-\partial_T\phi\, n_{\sigma\, 0} + \partial_\xi\phi\, n_{\sigma\, 1})\sqrt{-h_e^{\partial}}\Big|_{\partial H_e|_{\partial e_j}} \overset{!}{=} 0\,. \qquad (2.39)$$

In order to find the normal vector field n_σ^a, we need to compute the endpoints two-velocities $u^a_{\partial e_j}$, for both $j \in \{1,2\}$. The observer's velocity, and consequently the edge endpoints worldlines, depends on the conformal factor $\Omega(T,\xi)$. In fact, from the line element $ds^2_{h_e} = -\Omega^2(T,\xi)dT^2 + \Omega^2(T,\xi)d\xi^2$, the observer velocity reads

$$u^1(T,\xi) = \sqrt{1 - \frac{1}{\Omega^2(T,\xi)}}\,, \tag{2.40}$$

and depends generally on both the time and space coordinates. Thus, the observer on the edge in conformally flat form is, in general, not at rest with the edge.

The two-velocities $u^a_{\partial e_j}$ of the edge endpoints have to satisfy, together with the normal vector field to the spatial boundaries n^a_σ, the conditions given by Eq. (2.35). However, for an observer moving on the edge, we cannot a priori assume $\frac{d\xi}{d\tau} = 0$. As a result, the temporal component of the normal vector field is not necessary vanishing. Therefore, for an edge embedded in an arbitrary spacetime and in conformal coordinates, the boundary conditions for a free scalar field is given by Eq. (2.39); in particular, in the general case the boundary condition is not only a Neumann condition on the field spatial derivative but also on the time derivative of the field at the spatial boundary.

The conditions in Eq. (2.35), read, for h_e in conformally flat form,

$$\begin{aligned} -\Omega^2(T,\xi)u^0_{\partial e_j}n^0_\sigma + \Omega^2(T,\xi)u^1_{\partial e_j}n^1_\sigma &= 0 \\ -\Omega^2(T,\xi)n^0_\sigma n^0_\sigma + \Omega^2(T,\xi)n^1_\sigma n^1_\sigma &= 1\,. \end{aligned} \tag{2.41}$$

Solving for n^1_σ, we obtain $n^1_\sigma = \pm\sqrt{\frac{1}{\Omega^2(T,\xi)} + n^{0\,2}_\sigma}$, and hence $n^0_\sigma = \pm\frac{d\xi}{dT}\frac{1}{\Omega(T,\xi)}\sqrt{\frac{1}{1-\left(\frac{d\xi}{dT}\right)^2}}$, where we have used that $\frac{u^1_{\partial e_j}}{u^0_{\partial e_j}} = \frac{d\xi_j}{dT}$. Finally, at the edge endpoints ∂e_j with $j \in \{1,2\}$ we can write

$$n^0_\sigma = \pm\frac{d\xi_j}{dT}\frac{1}{\Omega(T,\xi_j)}\sqrt{\frac{1}{1-\left(\frac{d\xi_j}{dT}\right)^2}} \qquad n^1_\sigma = \pm\frac{1}{\Omega(T,\xi_j)}\sqrt{1+\left(\frac{d\xi_j}{dT}\right)^2\frac{1}{1-\left(\frac{d\xi_j}{dT}\right)^2}}\,, \tag{2.42}$$

and

$$n_{\sigma\,0} = \mp\frac{d\xi_j}{dT}\Omega(T,\xi_j)\sqrt{\frac{1}{1-\left(\frac{d\xi_j}{dT}\right)^2}} \qquad n_{\sigma\,1} = \pm\Omega(T,\xi_j)\sqrt{1+\left(\frac{d\xi_j}{dT}\right)^2\frac{1}{1-\left(\frac{d\xi_j}{dT}\right)^2}}\,. \tag{2.43}$$

Note that, as a consistency check, when we consider the embedding background to be the four-dimensional Minkowski spacetime, we have $\Omega(T,\xi)=1$ and $\frac{d\xi}{dT}=0$. Then, the above equations yield $n^a_\sigma = n_{\sigma\, a} = (0,\pm 1)$, in agreement with normal vector field obtained in the previous subsection.

Therefore, the general form for the boundary conditions for a free scalar field confined to a single edge embedded in an arbitrary curved, dynamical spacetime, is given by

$$\left[\pm\partial_T\phi\left(\frac{d\xi}{dT}\sqrt{\frac{1}{1-\left(\frac{d\xi}{dT}\right)^2}}\right)\pm\partial_\xi\phi\left(\sqrt{1+\left(\frac{d\xi}{dT}\right)^2\frac{1}{1-\left(\frac{d\xi}{dT}\right)^2}}\right)\right]\Bigg|_{\partial H_e|_{\partial e_j}} \overset{!}{=} 0\,. \tag{2.44}$$

Again, in the case of an edge embedded in the Minkowski spacetime, Eq. (2.44) reduces to $\partial_\xi\phi \overset{!}{=} 0$ at the spatial boundaries, in agreement with the result of the previous section.

As noted above, if the observer is not comoving with the edge endpoints, the boundary conditions obtained from the variation of the action will generalize the Neumann conditions to include an additional term involving the time derivative of the field, at the spatial boundaries $\partial H_e|_{\partial e_1}$ and $\partial H_e|_{\partial e_2}$ of H_e. Alternatively, Dirichlet boundary conditions could have been imposed by assuming the field variations $\delta\phi(T,\xi)$ to be vanishing for all times at the spatial boundaries, i.e. $\phi = const.$ at $\partial H_e|_{\partial e_j}$.

In this section we constructed the field theory on a single-edge graph, embedded in an arbitrary background. The propagation of the field along the edge is known and determined by the equation of motion while the behavior of the field at the edge endpoints is controlled by the above boundary conditions. Whether Dirichlet or Neumann, the degrees of freedom confined on the edge cannot leak out to the embedding spacetime.

Chapter 3

Physics on Network Histories in Arbitrary Spacetimes

As already introduced, the main leitmotiv of our investigation is to be able to describe and study four-dimensional natural phenomena, with lower dimensional theories. In fact, a (spatially) lower dimensional theory might simplify significantly computations, creating the opportunity to solve equations which are not yet solved in full dimensions. However, the question which naturally arises is whether and how a lower dimensional theory, e.g. a $(1+1)$-dimensional field theory, can be employed to gain insights and describe a four-dimensional phenomenon. As a matter of fact, light propagating in a single fiber can for sure be used to study light propagation in one dimension and related $(1+1)$-dimensional experiments, however it will never be able to provide a description of, for example, Snell's law of refraction of light at an interface. Nevertheless, the employment of lower dimensional theories seems too powerful not to pursue an innovative method that, on the one hand, do not give up on the use of lower dimensions, but still aims to describe full-dimensional physics.

The core idea to achieve this objective is the following. Instead of one single-edge graph, consider a collection $\mathcal{C}$ of N single-edge graphs, as the one depicted in Fig. 3.1. We know that this is a triple $\mathcal{C} = (\mathcal{E}, \mathcal{V}, \iota)$ of a set $\mathcal{E}$ of N edges, equipped through ι with two vertices each, the endpoints. According to the previous section, this collection can be embedded in an arbitrary background (M, g), by embedding each single-edge graph in a four-dimensional background and defining a field theory on it. Although each theory would have support extending spatially in only one direction, we would have multiple copies of the $(1+1)$-dimensional theory covering an extended region of the embedding spacetime.

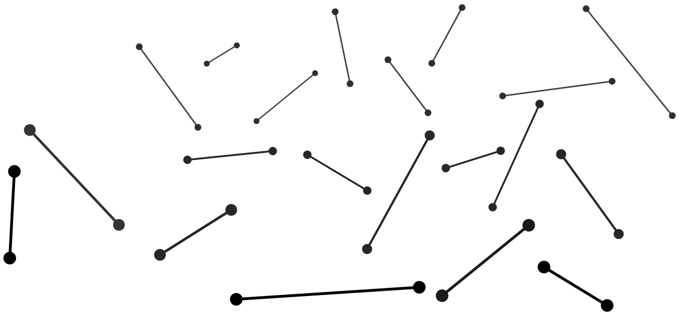

Figure 3.1: Collection $\mathcal{C}$ of N single edges, each equipped with endpoints. The graphs are all disconnected.

Nevertheless, each field theory would be independent, and degrees of freedom could not leak out of each edge.

However, if we modified the mapping of edges in $\mathcal{E}$ to the vertices in $\mathcal{V}$ such that the single-edge graphs in $\mathcal{C}$ were connected into a network $\mathcal{N}$, we would obtain a structure of finite extent in the embedding spacetime on which the field could propagate, as shown in Fig. 3.2. Thus, although just along one-dimensional paths, the field on the network could effectively propagate in different directions and regions of the embedding spacetime. Therefore, the key idea of our method would be to keep the field theory spatially one-dimensional by confining the field to single edges, but at the same time to increase the number of possible paths and directions the field can travel, by constructing an arbitrarily

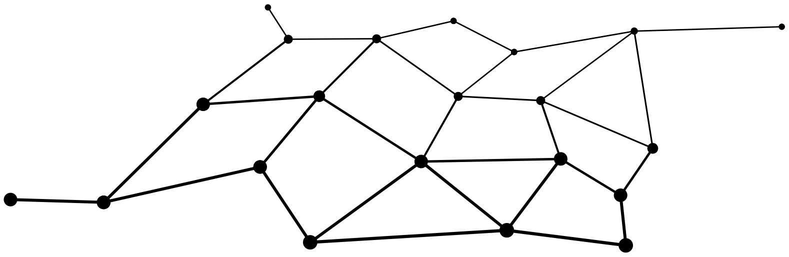

Figure 3.2: Example of a network, i.e. a collection of N single-edge graphs connected together through vertices.

extended network in spacetime. Hence, within this new framework, the four-dimensional natural phenomenon is not described by a spatially three-dimensional theory, but by a spatially one-dimensional field theory on a three-dimensional structure.

Therefore, the first main objective of our work is to validate this idea by answering the question as to whether a field theory spatially confined to a network can describe phenomena occurring in the full embedding spacetime. Reformulated in terms of our framework, we can rephrase it as

> *Can field theories confined to network histories describe phenomena occurring in the full embedding spacetime?*

If we have a positive answer to this question, we can employ our theoretical devices to investigate the most challenging phenomena occurring in backgrounds of our choice.

3.1 The History of an Arbitrary Network

Let us see how such a spatially three-dimensional network, extended in the embedding spacetime, can be constructed mathematically. Consider a four-dimensional globally hyperbolic spacetime (M, g) and, for a given time parameter τ, its foliation in spacelike three-dimensional hypersurfaces Σ_τ, for each τ. Consider the collection of single-edge graphs $\mathcal{C}$ of Fig. 3.1. For each edge e_i we apply the mathematical structure of Sec. 2.1, i.e. we define its history as the two-dimensional compact and connected Lorentzian submanifold (H_{e_i}, h_{e_i}) of M and we introduce the smooth two-parameter map P to identify the edge points with points of the two-dimensional history H_{e_i}. In this way, each edge is represented on each hypersurface Σ_τ and embedded in M. For illustrative purposes, we show in Fig. 3.3 the embedding of the collection of single-edge graphs. As we will see, the definitions given in Sec. 2.1 for single-edge histories will set the basis for constructing the definition of network histories.

Each edge of the embedded collection is supplied with a $(1+1)$-dimensional field theory. As long as the single edges are disconnected from each other, each field is confined to one edge solely – as the boundary conditions studied in Sec. 2.2 prescribe – and we simply obtain a collection of copies of the $(1+1)$-dimensional field theory on a single-edge history that we analyzed above. In fact, if we vary the action functional as in Eq. (2.20) on each edge, we obtain boundary terms at the edge endpoints, the two integrals on $\partial H_e|_{\partial e_j}$ in Eq. (2.26). However, since the endpoints of each edge are disconnected from all other

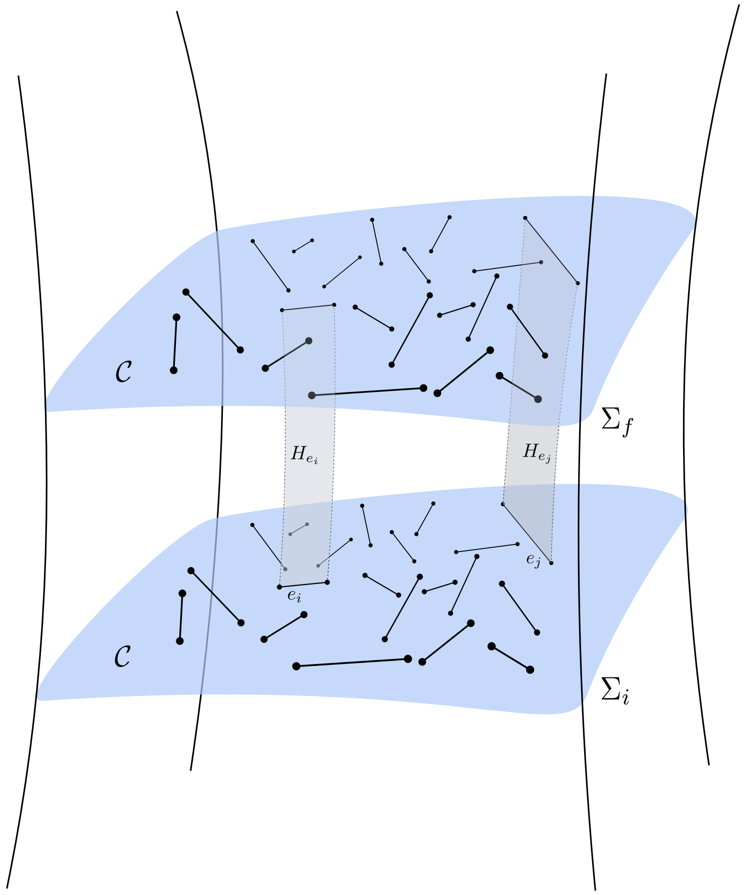

Figure 3.3: Embedded collection $\mathcal{C}$ of single-edge graphs in a globally hyperbolic spacetime (M, g). For each edge e, we define a history (H_e, h_e) as in Sec. 2.2. Each history is disconnected from the others. If τ is a time parameter, each edge history is visualized as the worldsheet of the specific edge considered. On each edge, a $(1+1)$-dimensional field theory is defined as in the previous section.

endpoints, no boundary terms in $\mathcal{C}$ have common support and therefore the integrals in Eq. (2.26) must again vanish individually, leading to the boundary conditions Eq. (2.29) for each edge. Consequently, each field is spatially confined to its respective edge.

Suppose we now allow the embedded edges in Fig. 3.3 to be connected, that is, we let each edge of $\mathcal{C}$ have at least one endpoint in common with another edge. In terms of two smooth maps P_i and P_j, this means that we identify two endpoints of two edges e_i, e_j with the same spacetime point, the joining vertex v, i.e. $v = P_i(\tau, \sigma_k) = P_j(\tau, \sigma_l)$ with $k, l \in \{1, 2\}$ for all times τ. In this way, we obtain an arbitrary network $\mathcal{N} = (\mathcal{V}, \mathcal{E}, \iota)$, like the one in Fig. 3.2, embedded in (M, g). We depict this resulting embedded network in Fig. 3.4. Each edge history H_{e_i} now shares a common spatial boundary with the history

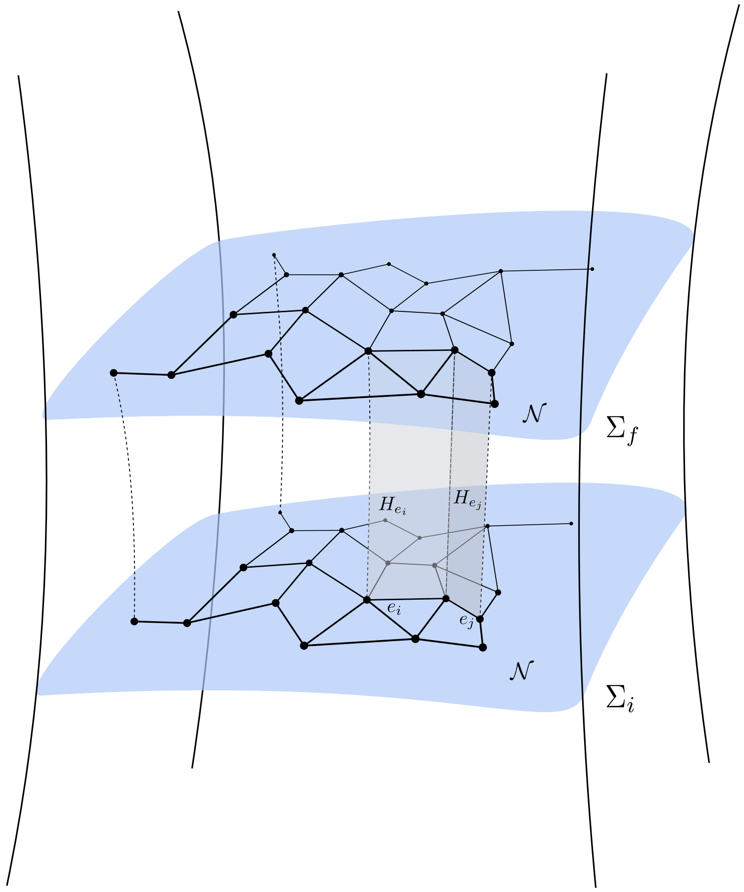

Figure 3.4: Arbitrary network $\mathcal{N}$ embedded in a globally hyperbolic spacetime (M, g). If τ is a time parameter, the history of the network can be visualized as the network worldsheet. For the sake of clarity, only a part of the network history $H_{\mathcal{N}}$ is shown in the picture. On the history of each edge of the network, a (1+1)-dimensional field theory is defined as in the previous section. At each node, junction conditions control field propagation throughout the network.

of the adjacent edge H_{e_j}, as exemplified for two adjacent edges in Fig. 3.4. Without losing generality, we refer to this common spatial boundary as the worldline $v(\tau)$ of the joining vertex v.

The *network history* $H_{\mathcal{N}}$ is then defined as the two-dimensional compact and connected, piecewise smooth Lorentzian submanifold $(H_{\mathcal{N}}, h)$ of M, given by the union of the histories H_{e_i} of all the N edges constituting the network, i.e. $H_{\mathcal{N}} = \cup_{i=1}^{N} H_{e_i}$. The metric tensor h is the induced metric on the whole network history and, on each edge history H_{e_i}, it reduces to the induced metric h_{e_i}. On each vertex worldline, Israel junction conditions are imposed for h. It is worth noting that the vertices worldlines are boundaries for the edge histories H_{e_i} but not for the whole network history $H_{\mathcal{N}}$, which is smooth at each node worldline. On the other hand, the worldlines of free endpoints, i.e. endpoints which are not connected to further edges, are spatial boundaries for the edge history H_{e_i} as well as for the network history $H_{\mathcal{N}}$.

In fact, the network history boundaries $\partial H_{\mathcal{N}}$ are defined in the following way. The two temporal boundaries $\partial H_{\mathcal{N}}|_{\tau_i}$ and $\partial H_{\mathcal{N}}|_{\tau_f}$ are the union of the initial and final temporal boundaries of each edge history respectively: $\partial H_{\mathcal{N}}|_{\tau_i} = \cup_{k=1}^{N} \partial H_{e_k}|_{e_{\tau_i}}$ and $\partial H_{\mathcal{N}}|_{\tau_f} = \cup_{k=1}^{N} \partial H_{e_k}|_{e_{\tau_f}}$. Thus, the two temporal boundaries of the network history are nothing other than the network at the initial time τ_i and at the final time τ_f.

The spatial boundaries $\partial H_{\mathcal{N}}|_{\partial e}$ of the network history are defined as the worldlines of the free endpoints or, in other words, as the union of the one spatial boundary of each edge history H_{e_i} that is not a node worldline, i.e. it is not a common spatial boundary of two adjacent edge histories. Mathematically, $\partial H_{\mathcal{N}}|_{\partial e} = \cup_s \partial H_{e_s}|_{\partial e}$, where by ∂e we refer here to the free endpoint of the edge and with s we label the edges with a free endpoint. In Fig. 3.4, the vertical curves representing the worldlines of the free endpoints are examples of spatial boundaries of the network history. Note that if the network is such that each edge endpoint is shared by at least two edges, i.e. there are no free endpoints, then $H_{\mathcal{N}}$ admits no spatial boundaries. Physically, this simply means that potential degrees of freedom on the network are free to propagate on it along paths that have no endpoints.

The fact that the edges are now connected to form a network is the core feature of the method of network histories. In fact, the presence of nodes instead of endpoints turns boundaries into junctions. At each vertex, the degrees of freedom can propagate further to other edges, spreading and reaching different regions of the network. While the edges of the network serve as support for the field propagation, the nodes of the network play a fundamental role by controlling the propagation throughout the network via the junction conditions. Depending on the choice of junction conditions, at each node fields can transmit or reflect back to the edge, so that the dynamics on the network is strongly determined by its nodes.

3.2 Fields on Network Histories

So far we have constructed a mathematical structure on which fields or arbitrary degrees of freedom can propagate through nodes and edges. Now we want to focus on the degrees of freedom themselves and investigate how to define their dynamics over the whole network history. Similarly to the previous section, we will focus on field theories and, for simplicity, on real scalar fields. As already mentioned, the same construction holds for different spin values or interacting theories. To equip networks with fields confined to them we base our construction on the analysis developed for the single-edge graph.

Consider the network of Fig. 3.4. A *subgraph* of this network is another graph/network formed from a subset of the vertices and edges of $\mathcal{N}$. Instead of directly constructing a field theory extended over the whole network, it is instructive to start locally by investigating the field theory on elementary subgraphs of $\mathcal{N}$. In fact, by knowing how the theory is constructed in the presence of a node connecting two or more edges, the knowledge of the field theory on the whole network follows naturally.

After the single-edge graph, the second simplest subgraph is the one that contains at least one node. In particular, the simplest configuration containing a node is a subgraph given by two edges connected by a vertex.

3.2.1 Two Edges Connected by a Vertex

In this subsection we then focus on a subgraph $\mathcal{G}_2 = (\mathcal{V}, \mathcal{E}, \iota)$ of $\mathcal{N}$, for which $\mathcal{E} = \{e_i, e_j\}$ and $\mathcal{V} = \{\partial e_{1i}, \partial e_{2j}, v\}$, with v the node connecting the two arbitrary edges e_i and e_j of the network, as highlighted in Fig. 3.5. Notice that, even if the two edges are actually connected to other elements of the network, the subgraph $\mathcal{G}_2$ is considered as disconnected from the rest in this initial analysis. Once we know how a field evolves across a node connecting two or more edges, we will be able to study $\mathcal{G}_2$ with all the real connections it has in the network.

Consider the histories of the two edges H_{e_i} and H_{e_j} between an initial and final hypersurface Σ_i and Σ_f. Let $x_i = \{\xi_i^a\} = (T, \xi_i)$ be a coordinate system on (H_{e_i}, h_{e_i}) and define for a field ϕ_i on H_{e_i} an action functional as in Eq. (2.19). Similarly, we consider a coordinate system $x_j = \{\xi_j^a\} = (T, \xi_j)$ on (H_{e_j}, h_{e_j}), and an action functional for a field ϕ_j on H_{e_j}. Note that in principle, due to our foliation, we can always choose the time T to be the same parameter on both histories.

If we were interested in studying the propagation of a single field ϕ along the subgraph $\mathcal{G}_2$, we could define the field locally at one edge of $\mathcal{G}_2$ and set its initial conditions. By studying the field evolution in time and imposing continuity, we would obtain the propagated field at the second edge of $\mathcal{G}_2$. In this case, ϕ_i and ϕ_j would not be independent from each other, but would satisfy specific initial conditions. In the following, however, we consider the more general case of two independent fields ϕ_i, ϕ_j which, by continuity at the

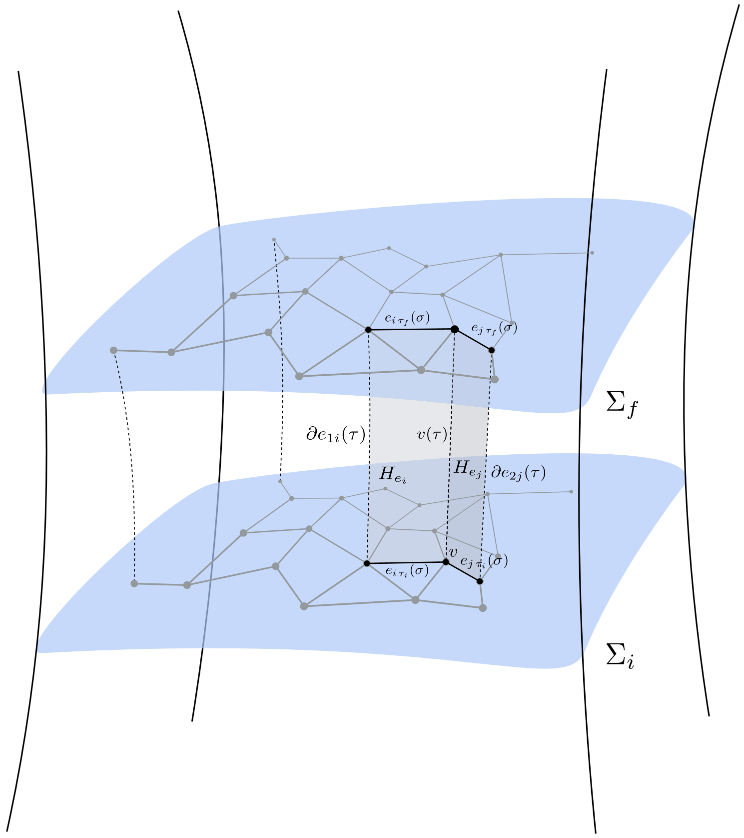

Figure 3.5: Two-dimensional finite history $(H_{\mathcal{G}_2}, h_{\mathcal{G}_2})$ of a two-edge subgraph configuration $\mathcal{G}_2$, embedded in a globally hyperbolic spacetime (M, g). If τ is a time parameter and σ a spatial one, then the history $H_{\mathcal{G}_2} = H_{e_i} \cup H_{e_j}$ can be visualized as the worldsheet of the two connected edges e_i and e_j. Note that each Σ_τ is a three-dimensional spacelike hypersurface.

node, form a continuum field configuration on the subgraph.

Although two of the spatial boundaries of the edges histories are identified in the vertex worldline, we need to specify how this condition translates for the field theory on $\mathcal{G}_2$. Consider for a moment the two edges to be disjoint from each other. The total action for the two disconnected edges would be the sum of the two single edge actions, $\mathcal{A}_{e_ie_j} = \mathcal{A}_{e_i} + \mathcal{A}_{e_j}$. If we consider the field theory defined as in Sec. 2.2 on each edge history, then $\mathcal{A}_{e_i}$ and $\mathcal{A}_{e_j}$ are defined also on the boundaries of H_{e_i} and H_{e_j}. Thus, the fields ϕ_i and ϕ_j have the endpoints of e_i and e_j in their domains. Consequently, if we now connect the two edges by identifying two endpoints in the same spacetime point, i.e. the vertex, the worldline of the vertex belongs to both fields supports. Since now $\mathcal{A}_{e_i}$ and $\mathcal{A}_{e_j}$ have an overlapping domain, a sum over the two action functionals would yield two terms at the vertex worldline. If we require the two fields to coincide at the vertex worldline, i.e. $\phi_i = \phi_j$ at $v(T)$ for all T, we obtain two times the same action functional at $v(T)$. However, in our work we are interested in analysing a single field ϕ populating the subgraph and, more generally, the network. In this perspective, we would like the two independent fields ϕ_i and ϕ_j to form a continuum field configuration on the subgraph.

To avoid the double term at the vertex worldline, we can proceed in two ways: either we consider the fields domains as open subsets, that is, they do not include the spatial boundaries of the histories and we consider the vertex as a defect, as for example in [21]; or we assume that the vertex worldline belongs either to one or the other field domain. Without loss of generality, we assume the following intervals as the spatial domains for the fields $\phi_i = \phi_i(T, \xi_i)$ and $\phi_j = \phi_j(T, \xi_j)$ respectively,

$$\begin{aligned} &\xi_i \in [\partial e_{1i}, \partial e_{2i}) \\ &\xi_j \in [\partial e_{1j}, \partial e_{2j}] \,. \end{aligned} \tag{3.1}$$

Recall that, in our current analysis, ∂e_{2i} and ∂e_{1j} are identified in the vertex v, so that in the following we write $H_{e_i} \setminus \partial H_{e_i}|_{\partial e_{2i}}$ or $H_{e_i} \setminus v(\tau)$ interchangeably for the domain of ϕ_i.

The total action $\mathcal{A}_{\mathcal{G}_2}$ for the fields on the subgraph $\mathcal{G}_2$ is thus given by

$$\begin{aligned} \mathcal{A}_{\mathcal{G}_2}[\phi_i, \phi_j, \lambda] &= \mathcal{A}_{e_i}[\phi_i] + \mathcal{A}_{e_j}[\phi_j] + \mathcal{J}[\phi_i, \phi_j, \lambda] = \\ &= \int_{H_{e_i} \setminus v(\tau)} \mathcal{L}_{e_i}(x_i, \phi_i, \mathrm{d}\phi_i) \mathrm{dvol}_{h_{e_i}} + \int_{H_{e_j}} \mathcal{L}_{e_j}(x_j, \phi_j, \mathrm{d}\phi_j) \mathrm{dvol}_{h_{e_j}} + \\ &+ \lim_{\epsilon \to 0} \left[\int_{H_{e_i} \setminus v(\tau)} \mathcal{X}_{v-\epsilon} \lambda \phi_i \, \mathrm{dvol}_{h_{e_i}} - \int_{H_{e_j}} \mathcal{X}_v \lambda \phi_j \, \mathrm{dvol}_{h_{e_j}} \right] , \end{aligned} \tag{3.2}$$

where, for all times, $\mathcal{X}_v$ and $\mathcal{X}_{v-\epsilon}$ project the fields at the vertex v and at a distance ϵ away from it respectively. Note that whenever we explicitly refer to histories or their structures, or when the coordinate system is not specified in the integral measure, we use the general parameters τ and σ instead of T and ξ, for consistency with the figures and the general construction of Sec. 3.1. The term $\mathcal{J}[\phi_i, \phi_j, \lambda]$ represents the constraint, imposed by the continuous Lagrange multiplier field λ, that the two fields have the same value at the common boundary of the two histories, giving rise to a piecewise continuous field configuration on $\mathcal{G}_2$. In fact, if we vary the action functional with respect to λ we obtain, from the variational principle, $\lim_{\epsilon \to 0} \phi_i|_{v-\epsilon} = \phi_j|_v$ at the vertex v for all times. Specifically, the definitions in Eq. (3.1) for the fields domains imply that the vertex is not included in the spatial support of ϕ_i, thus requiring a limit procedure to approach ∂e_{2i}. With the limit $\epsilon \to 0$ and the notation "$v - \epsilon$", we mean to approach the vertex v by an infinitesimal distance ϵ, from the edge e_i. This condition is fundamental in the general case when we want to analyze a field configuration defined on the whole network, which must therefore be continuous at each node.

To find the equation of motion for the total field configuration on $H_{\mathcal{G}_2} = H_{e_i} \cup H_{e_j}$ we apply the variational principle for the total action between the two field configurations ϕ_i and ϕ_j on the two edges, at initial and final time T_i and T_f respectively,

$$\begin{aligned}\delta\mathcal{A}_{\mathcal{G}_2} &= \delta\mathcal{A}_{e_i} + \delta\mathcal{A}_{e_j} + \delta\mathcal{J} = \\ &= \int_{H_{e_i}\setminus v(\tau)} \left(\frac{\partial \mathcal{L}_{e_i}}{\partial \phi_i}\delta\phi_i + \frac{\partial \mathcal{L}_{e_i}}{\partial\partial_a \phi_i}\partial_a\delta\phi_i \right) \mathrm{dvol}_{h_{e_i}} + \\ &+ \int_{H_{e_j}} \left(\frac{\partial \mathcal{L}_{e_j}}{\partial \phi_j}\delta\phi_j + \frac{\partial \mathcal{L}_{e_j}}{\partial\partial_a \phi_j}\partial_a\delta\phi_j \right) \mathrm{dvol}_{h_{e_j}} + \delta\mathcal{J} \overset{!}{=} 0\,. \end{aligned} \tag{3.3}$$

Let us first focus on the variation $\delta\mathcal{J}$ of the junction term $\mathcal{J}[\phi_i, \phi_j, \lambda]$. Since $\mathcal{J}$ depends on the fields ϕ_i, ϕ_j and on the Lagrange multiplier field λ, we can write,

$$\begin{aligned}\delta\mathcal{J} = &\int_{H_{e_i}\setminus v(T)} \frac{\delta\mathcal{J}}{\delta\phi_i(x_i)}\delta\phi_i(x_i)\, d^2x_i + \int_{H_{e_j}} \frac{\delta\mathcal{J}}{\delta\phi_j(x_j)}\delta\phi_j(x_j)\, d^2x_j + \\ + &\int_{H_{e_i}\setminus v(T)} \frac{\delta\mathcal{J}}{\delta\lambda(x_i)}\delta\lambda(x_i)\, d^2x_i + \int_{H_{e_j}} \frac{\delta\mathcal{J}}{\delta\lambda(x_j)}\delta\lambda(x_j)\, d^2x_j\,, \end{aligned} \tag{3.4}$$

for some coordinates $x_i = \{\xi_i^a\}$, $x_j = \{\xi_j^a\}$ on H_{e_i} and H_{e_j} respectively. Throughout this thesis, whenever we use the notation d^2x_i, we also implicitly account for the determinant of the induced metric. The Lagrange multiplier field λ is independent of the scalar fields ϕ_i and ϕ_j, i.e. $\delta\lambda$ does not produce a variation in $\mathcal{A}_{e_i}[\phi_i]$ and $\mathcal{A}_{e_j}[\phi_j]$ and for Eq. (3.3) to be satisfied, the variations of $\mathcal{J}$ with respect to λ have to be independently zero. This leads to

$$\int_{H_{e_i}\setminus v(T)} \frac{\delta\mathcal{J}}{\delta\lambda(x_i)}\delta\lambda(x_i)\, d^2x_i + \int_{H_{e_j}} \frac{\delta\mathcal{J}}{\delta\lambda(x_j)}\delta\lambda(x_j)\, d^2x_j \overset{!}{=} 0\,. \tag{3.5}$$

Explicitly, for arbitrary variations $\delta\lambda$,

$$\lim_{\epsilon\to 0}\left[\int_{H_{e_i}\setminus v(\tau)} \mathcal{X}_{v-\epsilon}\phi_i\, \mathrm{dvol}_{h_{e_i}} - \int_{H_{e_j}} \mathcal{X}_v \phi_j\, \mathrm{dvol}_{h_{e_j}} \right] \overset{!}{=} 0\,, \tag{3.6}$$

which gives the (piecewise) continuity condition for ϕ_i and ϕ_j mentioned above,

$$\lim_{\epsilon \to 0} \phi_i|_{v-\epsilon} \overset{!}{=} \phi_j|_v \tag{3.7}$$

for all times, where $\phi_j|_v$ and $\phi_i|_{v-\epsilon}$ are the fields at the vertex v and at a distance ϵ from it respectively. Note that, since the fields are required to agree on the vertex worldline, they are not independent anymore and the variations $\delta\phi_i$ of ϕ_i vary ϕ_j as well.

Let us now consider the variations of $\mathcal{J}$ with respect to the fields ϕ_i and ϕ_j. We can write them explicitly as

$$\begin{aligned}\int_{H_{e_i} \setminus v(T)} \frac{\delta \mathcal{J}}{\delta \phi_i(x_i)} \delta\phi_i(x_i)\, d^2x_i &= \int_{H_{e_i} \setminus v(T)} \lim_{\epsilon \to 0} \int_{H_{e_i} \setminus v(\tau)} \mathcal{X}_{v-\epsilon} \lambda \frac{\delta \phi_i}{\delta \phi_i(x_i)} \mathrm{dvol}_{h_{e_i}}\, \delta\phi_i(x_i) d^2x_i = \\ &= \lim_{\epsilon \to 0} \int_{H_{e_i} \setminus v(\tau)} \mathcal{X}_{v-\epsilon} \lambda\, \delta\phi_i \mathrm{dvol}_{h_{e_i}}\,,\end{aligned} \tag{3.8}$$

and, similarly,

$$\begin{aligned}\int_{H_{e_j}} \frac{\delta \mathcal{J}}{\delta \phi_j(x_j)} \delta\phi_j(x_j)\, d^2x_j &= -\int_{H_{e_j}} \int_{H_{e_j}} \mathcal{X}_v \lambda\, \frac{\delta \phi_j}{\delta \phi_j(x_j)} \mathrm{dvol}_{h_{e_j}}\, \delta\phi_j(x_j) d^2x_j = \\ &= -\int_{H_{e_j}} \mathcal{X}_v \lambda\, \delta\phi_j\, \mathrm{dvol}_{h_{e_j}}\,.\end{aligned} \tag{3.9}$$

Therefore, we can rewrite the total variation of the action functional $\delta\mathcal{A}_{\mathcal{G}_2}$ as

$$\begin{aligned}&\delta\mathcal{A}_{\mathcal{G}_2} = \delta\mathcal{A}_{e_i} + \delta\mathcal{A}_{e_j} + \delta\mathcal{J} = \\ &= \int_{H_{e_i} \setminus v(\tau)} \left(\frac{\partial \mathcal{L}_{e_i}}{\partial \phi_i} \delta\phi_i + \frac{\partial \mathcal{L}_{e_i}}{\partial \partial_a \phi_i} \partial_a \delta\phi_i \right) \mathrm{dvol}_{h_{e_i}} + \\ &+ \int_{H_{e_j}} \left(\frac{\partial \mathcal{L}_{e_j}}{\partial \phi_j} \delta\phi_j + \frac{\partial \mathcal{L}_{e_j}}{\partial \partial_a \phi_j} \partial_a \delta\phi_j \right) \mathrm{dvol}_{h_{e_j}} + \\ &+ \lim_{\epsilon \to 0} \int_{H_{e_i} \setminus v(\tau)} \mathcal{X}_{v-\epsilon} \lambda\, \delta\phi_i\, \mathrm{dvol}_{h_{e_i}} - \int_{H_{e_j}} \mathcal{X}_v \lambda\, \delta\phi_j\, \mathrm{dvol}_{h_{e_j}} \overset{!}{=} 0\,,\end{aligned} \tag{3.10}$$

In Sec. 2.2, we have seen that each term δA_{e_λ}, with $\lambda \in \{i, j\}$, yields two terms: one integral with support on the history H_{e_λ} and one with support only on its boundaries ∂H_{e_λ}, as in Eq. (2.22). This implies that the first two integrals in Eq. (3.10) yield two terms each. Mathematically, using the same notation as in the previous section and with the two normal vector fields n^i_σ and n^j_σ related to each edge respectively and not necessarily the same,

$$\begin{aligned}
&\delta\mathcal{A}_{e_i} + \delta\mathcal{A}_{e_j} = \\
&\int_{H_{e_i}\setminus v(T)} \left(\frac{\partial \mathcal{L}_{e_i}}{\partial \phi_i} \sqrt{-h_{e_i}} - \partial_a \left(\sqrt{-h_{e_i}} \frac{\partial \mathcal{L}_{e_i}}{\partial \partial_a \phi_i} \right) \right) \delta\phi_i dT d\xi_i + \int_{\partial H_{e_i}} \frac{\partial \mathcal{L}_{e_i}}{\partial \partial_a \phi_i} \delta\phi_i \, n^i_a \sqrt{-h^{\partial}_{e_i}} dq \, + \\
&+ \int_{H_{e_j}} \left(\frac{\partial \mathcal{L}_{e_j}}{\partial \phi_j} \sqrt{-h_{e_j}} - \partial_a \left(\sqrt{-h_{e_j}} \frac{\partial \mathcal{L}_{e_j}}{\partial \partial_a \phi_j} \right) \right) \delta\phi_j dT d\xi_j + \int_{\partial H_{e_j}} \frac{\partial \mathcal{L}_{e_j}}{\partial \partial_a \phi_j} \delta\phi_j \, n^j_a \sqrt{-h^{\partial}_{e_j}} dq.
\end{aligned} \tag{3.11}$$

By looking at Fig. 3.5, we notice that the two histories only share a boundary, i.e. the bulks of the two histories H_{e_i} and H_{e_j} have an empty intersection. Therefore, in order for the variation of the total action in Eq. (3.3) to vanish, the integrals on H_{e_i} and H_{e_j} in Eq. (3.11) must vanish individually. According to Sec. 2.2, this leads to Euler-Lagrange equations on both histories H_{e_λ}. Recall that by continuity, we can require the term $\left(\frac{\partial \mathcal{L}_{e_\lambda}}{\partial \phi_\lambda} \sqrt{-h_{e_\lambda}} - \partial_a \left(\sqrt{-h_{e_\lambda}} \frac{\partial \mathcal{L}_{e_\lambda}}{\partial \partial_a \phi_\lambda} \right) \right)$ to be zero at the spatial boundaries as well, in particular at the vertex worldline or at a distance ϵ from it. The field propagation on each edge is thus determined. However, any propagation through the node to the other edge is dictated by the junction conditions. Thus, let us study which conditions follow Eq. (3.11) at the common boundary.

Consider Fig. 3.6. As previously mentioned, we consider only the two edges e_i and e_j, ignoring the other edges that join them at the node. Each edge history entails four boundaries, two spatial and two temporal. Accordingly, each integral on ∂H_{e_λ} in Eq. (3.11) consists of four integrals on the four boundaries of each H_{e_λ} as in Eq. (2.25) and Eq. (2.26). As already analyzed in Sec. 2.2, the field variations $\delta\phi$ are vanishing on the temporal boundaries as they reflect the choice of initial and final conditions for the field configuration; $\delta\phi(T_i, \xi_\lambda) = 0$ and $\delta\phi(T_f, \xi_\lambda) = 0$ for all values of ξ_λ, with $\lambda \in \{i, j\}$. This implies that the integrals on temporal boundaries are vanishing. Therefore, we can write

$$\begin{aligned}
&\int_{\partial H_{e_i}} \frac{\partial \mathcal{L}_{e_i}}{\partial \partial_a \phi} \delta\phi_i \, n^i_a \sqrt{-h^{\partial}_{e_i}} dq + \int_{\partial H_{e_j}} \frac{\partial \mathcal{L}_{e_j}}{\partial \partial_a \phi_j} \delta\phi_j \, n^j_a \sqrt{-h^{\partial}_{e_j}} dq = \\
&= \int_{\partial H_{e_i}\big|_{\partial e_{1i}}} \frac{\partial \mathcal{L}_{e_i}}{\partial \partial_a \phi_i} n^i_{\sigma\, a} \sqrt{-h^{\partial}_{e_i}} \delta\phi_i \, dT + \lim_{\epsilon \to 0} \int_{\partial H_{e_i}\big|_{\partial e_{2i-\epsilon}}} \frac{\partial \mathcal{L}_{e_i}}{\partial \partial_a \phi_i} n^i_{\sigma\, a} \sqrt{-h^{\partial}_{e_i}} \delta\phi_i \, dT + \\
&+ \int_{\partial H_{e_j}\big|_{\partial e_{1j}}} \frac{\partial \mathcal{L}_{e_j}}{\partial \partial_a \phi_j} n^j_{\sigma\, a} \sqrt{-h^{\partial}_{e_j}} \delta\phi_j \, dT + \int_{\partial H_{e_j}\big|_{\partial e_{2j}}} \frac{\partial \mathcal{L}_{e_j}}{\partial \partial_a \phi_j} n^j_{\sigma\, a} \sqrt{-h^{\partial}_{e_j}} \delta\phi_j \, dT \, .
\end{aligned} \tag{3.12}$$

This allows us to rewrite the condition of Eq. (3.10) as

$$\begin{aligned}
&\int_{\partial H_{e_i}\big|_{\partial e_{1i}}} \frac{\partial \mathcal{L}_{e_i}}{\partial\partial_a\phi_i} n^i_{\sigma\,a}\sqrt{-h^\partial_{e_i}}\,\delta\phi_i\,dT + \lim_{\epsilon\to 0}\int_{\partial H_{e_i}\big|_{\partial e_{2i-\epsilon}}} \frac{\partial \mathcal{L}_{e_i}}{\partial\partial_a\phi_i} n^i_{\sigma\,a}\sqrt{-h^\partial_{e_i}}\,\delta\phi_i\,dT+\\
&+\int_{\partial H_{e_j}\big|_{\partial e_{1j}}} \frac{\partial \mathcal{L}_{e_j}}{\partial\partial_a\phi_j} n^j_{\sigma\,a}\sqrt{-h^\partial_{e_j}}\,\delta\phi_j\,dT + \int_{\partial H_{e_j}\big|_{\partial e_{2j}}} \frac{\partial \mathcal{L}_{e_j}}{\partial\partial_a\phi_j} n^j_{\sigma\,a}\sqrt{-h^\partial_{e_j}}\,\delta\phi_j\,dT+\\
&+\lim_{\epsilon\to 0}\int_{H_{e_i}\setminus v(\tau)} \mathcal{X}_{v-\epsilon}\,\lambda\;\delta\phi_i\,\mathrm{dvol}_{h_{e_i}} - \int_{H_{e_j}} \mathcal{X}_v\lambda\;\delta\phi_j\,\mathrm{dvol}_{h_{e_j}} \overset{!}{=} 0\,. \qquad (3.13)
\end{aligned}$$

Let us analyse the first four integrals. The first two are over the spatial boundaries of H_{e_i}, which are nothing more than the worldlines of the two endpoints ∂e_{1i} and ∂e_{2i} of the edge e_i. The spatial boundaries of H_{e_i} are shown as dashed lines in Fig. 3.6. Recall that the worldline of ∂e_{2i} is not contained in the domain of ϕ_i and hence the limit procedure is required. The last two integrals are instead on the spatial boundaries of H_{e_j}, which, in analogy to the previous case, are the two worldlines of the endpoints of the second edge e_j. They are shown as dotted lines in the figure. As mentioned above, in this first analysis we consider the endpoint ∂e_{1i} of the edge e_i as well as the endpoint ∂e_{2j} of e_j as disconnected from other edges, i.e. they are both free endpoints and not nodes. On the other hand, the endpoint ∂e_{2i} of the edge e_i and the endpoint ∂e_{1j} of the edge e_j are connected by a vertex v, that is, the two boundaries $\partial e_{2i}(\tau)$ and $\partial e_{1j}(\tau)$ are actually identified for all τ in the worldline of the vertex, $v(\tau)$. Under the current assumption that we only focus on the two edges e_i and e_j, the node is considered to connect only these two edges, contrary to the real case of the network in Fig. 3.5.

According to the considered configuration, in order for the sum of Eq. (3.13) to be vanishing, the integral on $\partial H_{e_i}|_{\partial e_{1i}}$ and the one over $\partial H_{e_j}\big|_{\partial e_{2j}}$ – the worldlines of the first endpoint ∂e_{1i} of e_i and of the second endpoint ∂e_{2j} of e_j respectively – have to vanish independently, since they have non-overlapping supports. Since the field variations $\delta\phi_\lambda = \delta\phi_\lambda(T,\xi_\lambda)$, with $\lambda \in \{i,j\}$, are arbitrary functions, the two integrals vanish if and only if their respective integrands are zero, that is

$$\frac{\partial \mathcal{L}_{e_\lambda}}{\partial\partial_a\phi_\lambda} n^\lambda_{\sigma\,a}\sqrt{-h^\partial_{e_\lambda}}\,\Bigg|_{\partial H_e|_{\partial e_{k\,\lambda}}} \overset{!}{=} 0 \qquad \textit{with}\ \ \lambda\in\{i,j\}\ \wedge\ k\in\{1,2\}\,, \qquad (3.14)$$

for each time T, at the two endpoints ∂e_{1i} and ∂e_{2j}, respectively. Alternatively, the conditions for the integrals to vanish are also satisfied if we assume that the field variations are identically zero at ∂e_{1i} and ∂e_{2j} for all T, i.e. $\delta\phi_\lambda|_{\partial H_e|_{\partial e_{k\,\lambda}}} = \delta\phi_\lambda(T)|_{\partial H_e|_{\partial e_{k\,\lambda}}} = 0$, which

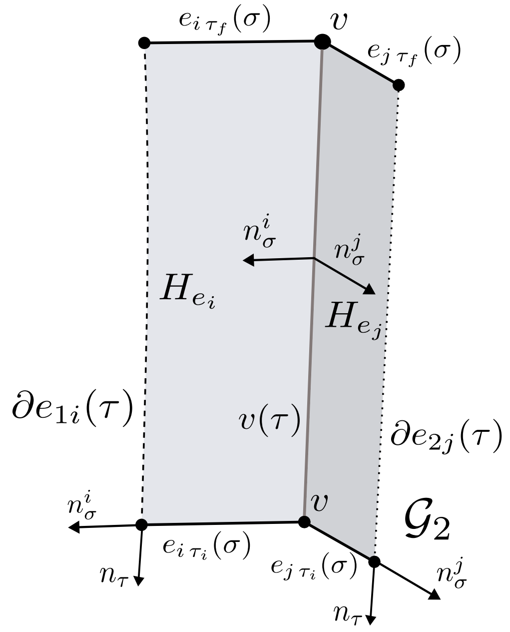

Figure 3.6: Details of the two-dimensional finite history $(H_{\mathcal{G}_2} = H_{e_i} \cup H_{e_j}, h_{e_i \cup e_j})$ of a two-edge subgraph configuration $\mathcal{G}_2$, embedded in a globally hyperbolic spacetime (M, g). The common spatial boundary of the two histories H_{e_i} and H_{e_i} is the worldline $v(\tau)$ of the vertex. The spatial boundaries of $H_{\mathcal{G}_2}$ are the two free endpoint worldlines $\partial e_{1i}(\tau)$ and $\partial e_{2j}(\tau)$, depicted with dashed and dotted lines respectively. The two-edge configuration $\mathcal{G}_2$ at initial and final time defines the two temporal boundaries of $H_{\mathcal{G}_2}$. Two, generally different, normal vector fields n^i_σ and n^j_σ point out of each edge e_i and e_j; the normal vector field n_τ is instead the same on both edges of $\mathcal{G}_2$.

implies that the field is constant at the considered boundary.

The first of these two conditions, Eq. (3.14), corresponds to Neumann boundary conditions at the endpoints of the edges. In fact, as already analysed in Sec. 2.2 for a real scalar field on a single edge, such a condition implies for the field

$$h^{ab}_{e_\lambda} \partial_a \phi_\lambda \, n^\lambda_{\sigma\, b} \sqrt{-h^\partial_{e_\lambda}}\, \Big|_{\partial H_e|_{\partial e_{k\,\lambda}}} \overset{!}{=} 0 \qquad with\ \ \lambda \in \{i, j\} \ \wedge\ k \in \{1, 2\}\,, \tag{3.15}$$

for all times T, which can be seen as a Neumann boundary condition generalized to arbitrary spacetimes. By setting the field derivatives along the normal vector fields to vanish at the free endpoints, the variational principle ensures that there can be no leakage of degrees of freedom from the two-edge configuration and that the field is confined to it. The second condition, $\phi = const.$ at $\partial e_{1i}(\tau)$ and $\partial e_{2j}(\tau)$, is a Dirichlet boundary conditions for the field. Whether Dirichlet or Neumann, the boundary conditions derived with the variational principle prevent the field or degrees of freedom from escaping the two edges into the ambient space. Therefore, we have found that two integrals of Eq. (3.12) constrain the field to the two-edge configuration. We still need a condition at the node that will regulate the propagation through it.

Since the two integrals over the free endpoint worldlines must vanish individually, we can rewrite Eq. (3.13) as

$$\begin{aligned}\lim_{\epsilon\to 0}\int_{v(T)-\epsilon}\frac{\partial\mathcal{L}_{e_i}}{\partial\partial_a\phi_i}n^i_{\sigma\,a}\sqrt{-h^{\partial}_{e_i}}\delta\phi_i\,dT+\int_{v(T)}\frac{\partial\mathcal{L}_{e_j}}{\partial\partial_a\phi_j}n^j_{\sigma\,a}\sqrt{-h^{\partial}_{e_j}}\delta\phi_j\,dT+\\ +\lim_{\epsilon\to 0}\int_{H_{e_i}\setminus v(\tau)}\mathcal{X}_{v-\epsilon}\,\lambda\;\delta\phi_i\,\mathrm{dvol}_{h_{e_i}}-\int_{H_{e_j}}\mathcal{X}_v\lambda\;\delta\phi_j\,\mathrm{dvol}_{h_{e_j}}\overset{!}{=}0\,.\end{aligned}\tag{3.16}$$

Note that the integrals related to the two boundaries $\partial H_{e_i}\big|_{\partial e_{2i}}$ and $\partial H_{e_j}\big|_{\partial e_{1j}}$, that we identified together as $v(T)$, share the same support as the λ integrals. As a consequence, they do not necessarily have to vanish individually. If this would be the case, we would obtain exactly the same Neumann conditions as in Eq. (3.14) for each edge – or Dirichlet for vanishing field variations $\delta\phi = 0$ – and the degrees of freedom would not be allowed to leave each edge. The two edges would in fact act as effectively disconnected.

However, since they share a common support with another term, if one of the two integrals does not vanish, then the other integral must cancel it out to zero. In fact, we can write

$$\lim_{\epsilon\to 0}\left[\int_{v(T)-\epsilon}\frac{\partial\mathcal{L}_{e_i}}{\partial\partial_a\phi_i}n^i_{\sigma\,a}\sqrt{-h^{\partial}_{e_i}}\delta\phi_i\,dT+\int_{H_{e_i}\setminus v(\tau)}\mathcal{X}_{v-\epsilon}\,\lambda\;\delta\phi_i\,\mathrm{dvol}_{h_{e_i}}\right]\overset{!}{=}0\tag{3.17}$$

and

$$\int_{v(T)}\frac{\partial\mathcal{L}_{e_j}}{\partial\partial_a\phi_j}n^j_{\sigma\,a}\sqrt{-h^{\partial}_{e_j}}\delta\phi_j\,dT-\int_{H_{e_j}}\mathcal{X}_v\lambda\;\delta\phi_j\,\mathrm{dvol}_{h_{e_j}}\overset{!}{=}0\,,\tag{3.18}$$

for Eq. (3.16) to be satisfied.

Since the field variations $\delta\phi_i$ and $\delta\phi_j$ are arbitrary functions, the above conditions are satisfied if and only if

$$\lim_{\epsilon\to 0}\left.\frac{\partial\mathcal{L}_{e_i}}{\partial\partial_a\phi_i}n^i_{\sigma\,a}\sqrt{-h^{\partial}_{e_i}}\right|_{v(T)-\epsilon}\overset{!}{=}-\lim_{\epsilon\to 0}\lambda\,\Big|_{v(T)-\epsilon}\tag{3.19}$$

and

$$\left.\frac{\partial\mathcal{L}_{e_j}}{\partial\partial_a\phi_j}n^j_{\sigma\,a}\sqrt{-h^{\partial}_{e_j}}\right|_{v(T)}\overset{!}{=}\lambda\,\Big|_{v(T)}\,.\tag{3.20}$$

Due to continuity of the Lagrange multiplier field λ at the vertex, if we now perform the limit we obtain $\lim_{\epsilon\to 0} \lambda\,|_{v(T)-\epsilon} = \lambda|_{v(T)}$. Therefore,

$$\lim_{\epsilon\to 0} \frac{\partial \mathcal{L}_{e_i}}{\partial\partial_a\phi_i} n^i_{\sigma\,a}\sqrt{-h^\partial_{e_i}}\bigg|_{v(T)-\epsilon} \overset{!}{=} -\lim_{\epsilon\to 0}\lambda\,\Big|_{v(T)-\epsilon} = -\lambda\,\Big|_{v(T)} \overset{!}{=} -\frac{\partial \mathcal{L}_{e_j}}{\partial\partial_a\phi_j} n^j_{\sigma\,a}\sqrt{-h^\partial_{e_j}}\bigg|_{v(T)}\,, \tag{3.21}$$

or, equivalently,

$$\lim_{\epsilon\to 0} \frac{\partial \mathcal{L}_{e_i}}{\partial\partial_a\phi_i} n^i_{\sigma\,a}\sqrt{-h^\partial_{e_i}}\bigg|_{v(T)-\epsilon} + \frac{\partial \mathcal{L}_{e_j}}{\partial\partial_a\phi_j} n^j_{\sigma\,a}\sqrt{-h^\partial_{e_j}}\bigg|_{v(T)} \overset{!}{=} 0\,, \tag{3.22}$$

for all times T. Note that at the vertex, the two normal vectors are parallel but pointing on opposite directions, that is, they both point into their relative edge. This equation is fundamental. It determines the behavior of the field at the node of the graph configuration. Let us see what this condition implies for the case of a free massive real scalar field ϕ, as an instructive example. Consider the Lagrangian density $\mathcal{L}_{e_\lambda} = \frac{1}{2}\left(h^{ab}_{e_\lambda}\partial_a\phi_\lambda\,\partial_b\phi_\lambda - \mu^2\phi_\lambda^2\right)$ with $\lambda \in \{i,j\}$. Then, Eq. (3.22) reads

$$\lim_{\epsilon\to 0} h^{ab}_{e_i}\partial_a\phi_i\, n^i_{\sigma\,b}\sqrt{-h^\partial_{e_i}}\,\Big|_{v(T)-\epsilon} + h^{ab}_{e_j}\partial_a\phi_j\, n^j_{\sigma\,b}\sqrt{-h^\partial_{e_j}}\,\Big|_{v(T)} \overset{!}{=} 0\,, \tag{3.23}$$

or,

$$\lim_{\epsilon\to 0} h^{ab}_{e_i}\partial_a\phi_i\, n^i_{\sigma\,b}\sqrt{-h^\partial_{e_i}}\,\Big|_{v(T)-\epsilon} \overset{!}{=} -\, h^{ab}_{e_j}\partial_a\phi_j\, n^j_{\sigma\,b}\sqrt{-h^\partial_{e_j}}\,\Big|_{v(T)}\,. \tag{3.24}$$

Thus, the condition Eq. (3.22) translates in a condition on the field derivatives, which we refer to as *junction condition.* Recalling Eq. (2.22) in Sec. 2.2, we can notice that each side of this equation is the outcome of the divergence theorem. In fact, each side quantifies the flux $\partial\phi_\lambda$ from the edge e_λ, along the normal vector field n^λ_σ at the node. By setting the two fluxes towards the vertex to be equal, it is ensured that the node does not act as a sink or a source and the total flux at the vertex is conserved.

It is important to note that if the spacetime in which the edge configuration is embedded is the Minkowski spacetime, that is, the globally hyperbolic spacetime of Fig. 3.5 is (M,η), then the above junction condition reduces to

$$\lim_{\epsilon\to 0} \partial_{\xi_i}\phi_i\Big|_{v(T)-\epsilon} \overset{!}{=} \partial_{\xi_j}\phi_j\Big|_{v(T)}\,. \tag{3.25}$$

In this specific case, the variation of the field ϕ_i is fully transferred in a variation of ϕ_j, such that in terms of propagation, whatever enters the node from one edge, is totally

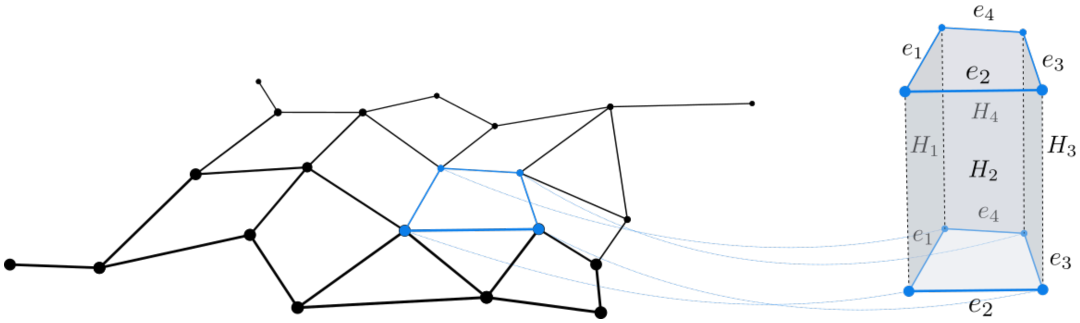

Figure 3.7: Subgraph of the network consisting of four edges connected to form a loop configuration. On the right is shown the history of the loop, i.e., the four-edge configuration considered as disjoint from any other edge of the network.

transmitted to the other. This reflects the fact that, in the Minkowski spacetime, the vertex is not a special point since physically there is no reason for the field to be reflected or only partially transmitted. Mathematically, Eq. (3.25) sets piecewise continuity for the fields derivatives. In addition with the continuity condition of Eq. (3.7), the vertex between two edges embedded in the Minkowski spacetime can be eliminated in favor of a longer single edge. In fact, the conditions at the node guarantee that two fields match into a single field on the resulting long edge, which is continuous and with continuous derivative. Therefore, if the ambient space is the Minkowski spacetime, any node connecting only two edges can be eliminated; connecting two field theories at a vertex is equivalent to considering a single field theory on a (longer) single edge as in Sec. 2.2.

The fact that a node connecting two edges is not relevant when embedded in the Minkowski spacetime can be further explored by analyzing the interesting case of a subgraph of Fig. 3.4 that consists of a closed circuit, or a *loop*.

In Fig. 3.7, an example of a subgraph is shown, consisting of four edges combined to form a loop. If we extract these four edges from the network and idealize them as disjoint from any other edges, we find that each vertex in the subgraph connects only two edges. According to the previous result, if the embedding background is the Minkowski spacetime, or any spacetime where Eq. (3.25) holds, then all four vertices can be removed from the subgraph, resulting in a longer single edge with periodic boundary conditions. Therefore, whenever we study a graph consisting of a loop, we can equivalently consider a single field theory on a single edge. Thus, a $(1+1)$-dimensional field theory is sufficient to describe fields on single edges, two edges connected at a vertex, and loop graphs. In the following section, we will study the first example of a subgraph containing a node that cannot be removed, where a $(1+1)$-dimensional field theory alone is insufficient for its description. It is precisely in this case that network histories, as a new and pioneering approach, become essential.

3.2.2 Three-Edge Star Graph

In the previous section, we analyzed fundamental graph configurations, such as two edges connected at a node or forming a loop configuration. However, we have seen that when embedded in particular ambient spaces, they are equivalent to a single edge configuration, and a $(1+1)$-dimensional field theory is sufficient for their description. Therefore, we now aim to find the minimal subgraph for which a simple $(1+1)$-dimensional field theory ceases to be sufficient, regardless of the embedding spacetime in which the network configuration is placed.

Consider again the arbitrary network $\mathcal{N}$ constructed in the previous section and embedded in an arbitrary globally hyperbolic spacetime (M, g). Besides the two-edge or the loop configurations, the minimal structure we can consider is the subgraph $\mathcal{G}_3$ of $\mathcal{N}$ formed by three edges connected at a vertex v, i.e. a star graph with three legs, as highlighted in Fig. 3.8. Mathematically, $\mathcal{G}_3 = (\mathcal{V}, \mathcal{E}, \iota)$ is a subgraph for which $\mathcal{E} = \{e_i, e_j, e_z\}$ and $\mathcal{V} = \{\partial e_{1i}, \partial e_{2j}, \partial e_{1_z}, v\}$.

Just as we did for $\mathcal{G}_2$ in the previous section, we treat $\mathcal{G}_3$ as disconnected from the rest of the network for the following analysis. We want to construct a continuous field configuration on the subgraph. To this aim, consider the three histories (H_{e_i}, h_{e_i}), (H_{e_j}, h_{e_j}) and (H_{e_z}, h_{e_z}) of the three edges. Each history, as for single-edge histories, is a two-dimensional compact Lorentzian submanifold of M with induced metric h_{e_λ}, $\lambda \in \{i, j, z\}$. As explained in the previous section, the total history of $\mathcal{G}_3$ is given by the union of the three histories, $\mathcal{G}_3 = H_{e_i} \cup H_{e_j} \cup H_{e_z}$, while the spatial boundaries $\partial e_{2i}(\tau)$, $\partial e_{1j}(\tau)$ and $\partial e_{2z}(\tau)$, for some time parameter τ, are all identified in the same spacetime curve $v(\tau)$, the worldline of the vertex.

Following the procedure of Sec. 3.2.1, we define a $(1+1)$-dimensional scalar field theory on each edge history. Thus, we obtain three field configurations ϕ_i, ϕ_j, and ϕ_z on H_{e_i}, H_{e_j}, and H_{e_z}, respectively. As already explained, we want the vertex worldline $v(\tau)$ to belong only to one of the field domains. Therefore, given some coordinates $x_\lambda = \{\xi^a_\lambda\} = (T, \xi_\lambda)$ on each history H_{e_λ}, the spatial coordinate ξ_λ for the fields ranges within the following

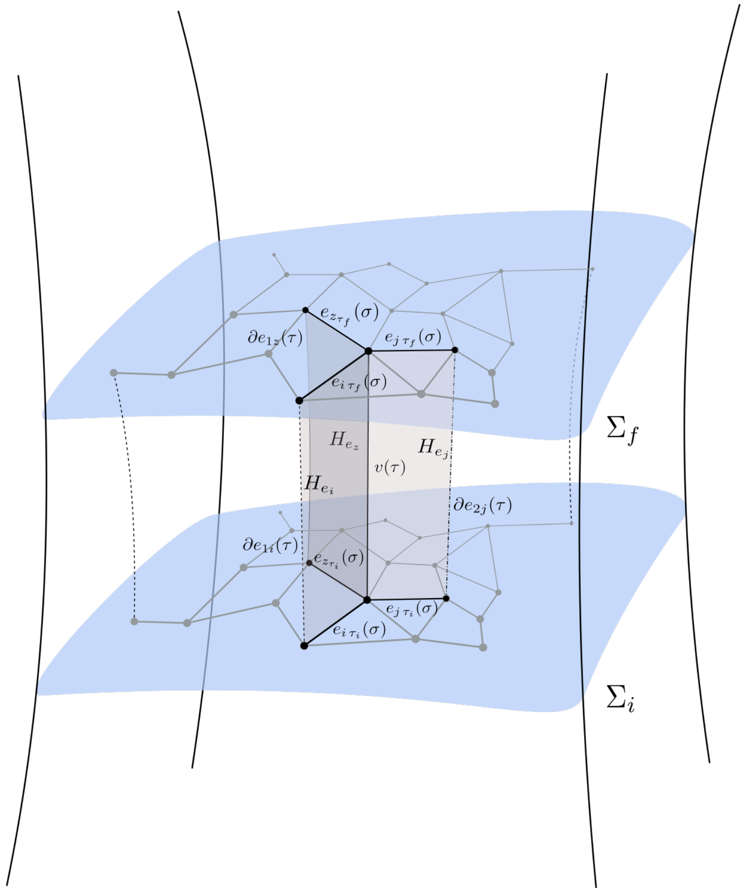

Figure 3.8: Two-dimensional finite history $(H_{\mathcal{G}_3}, h_{\mathcal{G}_3})$ of a subgraph $\mathcal{G}_3$ of the network, consisting of three edges connected by a vertex, embedded in a globally hyperbolic spacetime (M, g). If τ is a time parameter and σ a spatial one, then the history $H_{\mathcal{G}_3} = H_{e_i} \cup H_{e_j} \cup H_{e_z}$ can be visualized as the worldsheet spanned by the three connected edges e_i, e_j, and e_z.

intervals:

$$\begin{aligned} \xi_i &\in [\partial e_{1i}, \partial e_{2i}) \\ \xi_j &\in [\partial e_{1j}, \partial e_{2j}] \\ \xi_z &\in [\partial e_{1z}, \partial e_{2z}) \,. \end{aligned} \tag{3.26}$$

Without loss of generality, we have chosen the vertex worldline to lie solely in the domain of ϕ_j. As a consequence, we will refer to the domain of the fields ϕ_i and ϕ_z as $H_{e_i} \setminus v(\tau)$ and $H_{e_z} \setminus v(\tau)$, for some time parameter τ.

As in Sec. 3.2.1, we define an action functional $\mathcal{A}_{e_\lambda}[\phi_\lambda]$ for each field ϕ_λ and consider the total action functional $\mathcal{A}_{\mathcal{G}_3}$ defined on the entire history of the subgraph as,

$$\begin{aligned}\mathcal{A}_{\mathcal{G}_3}[\phi_i, \phi_j, \phi_z, \lambda^{ij}, \lambda^{jz}] &= \mathcal{A}_{e_i}[\phi_i] + \mathcal{A}_{e_j}[\phi_j] + \mathcal{A}_{e_z}[\phi_z] + \mathcal{J}[\phi_i, \phi_j, \phi_z, \lambda^{ij}, \lambda^{jz}] = \\ &= \int_{H_{e_i}\setminus v(\tau)} \mathcal{L}_{e_i}(x_i, \phi_i, \mathrm{d}\phi_i)\mathrm{dvol}_{h_{e_i}} + \int_{H_{e_j}} \mathcal{L}_{e_j}(x_j, \phi_j, \mathrm{d}\phi_j)\mathrm{dvol}_{h_{e_j}} + \\ &+ \int_{H_{e_z}\setminus v(\tau)} \mathcal{L}_{e_z}(x_z, \phi_z, \mathrm{d}\phi_z)\mathrm{dvol}_{h_{e_z}} + \lim_{\epsilon\to 0} \int_{H_{e_i}\setminus v(\tau)} \mathcal{X}^{i\to v}_{v-\epsilon} \lambda^{ij} \phi_i \,\mathrm{dvol}_{h_{e_i}} + \\ &- \int_{H_{e_j}} \mathcal{X}_v \lambda^{ij} \phi_j \,\mathrm{dvol}_{h_{e_j}} + \lim_{\epsilon\to 0} \int_{H_{e_z}\setminus v(\tau)} \mathcal{X}^{z\to v}_{v-\epsilon} \lambda^{jz} \phi_z \,\mathrm{dvol}_{h_{e_z}} + \\ &- \int_{H_{e_j}} \mathcal{X}_v \lambda^{jz} \phi_j \,\mathrm{dvol}_{h_{e_j}} \,. \end{aligned} \tag{3.27}$$

The functional $\mathcal{J}[\phi_i, \phi_j, \phi_z, \lambda^{ij}, \lambda^{jz}]$ sets the continuity conditions for the fields at the vertex, in fact as we will show, if we vary the action functional with respect to the two Lagrange multiplier fields λ^{ij} and λ^{jz}, defined on H_{e_i}, H_{e_j} and H_{e_j}, H_{e_z} respectively, we obtain $\lim_{\epsilon\to 0} \phi_i\big|^{i\to v}_{v(\tau)-\epsilon} \overset{!}{=} \phi_j\big|_{v(\tau)}$ and $\lim_{\epsilon\to 0} \phi_z\big|^{z\to v}_{v(\tau)-\epsilon} \overset{!}{=} \phi_j\big|_{v(\tau)}$ such that, $\lim_{\epsilon\to 0} \phi_i\big|^{i\to v}_{v(\tau)-\epsilon} = \phi_j\big|_{v(\tau)} = \lim_{\epsilon\to 0} \phi_z\big|^{z\to v}_{v(\tau)-\epsilon}$ and the field configuration is continuous at the vertex, for all times τ. Note that when using the notation $\lambda \to v$ for superscripts, it indicates that the limit is taken along the edge e_λ towards the vertex v. Furthermore, the Lagrange field λ^{ij} is assumed to be continuous across the vertex on $H_{e_i} \cup H_{e_j}$, and similarly, λ^{jz} is assumed to be continuous across the vertex on $H_{e_j} \cup H_{e_z}$.

As in the previous section, to derive the equation of motion for the field configuration on $\mathcal{G}_3$, we apply the variational principle and require that the first-order variations of the action functional $\mathcal{A}_{\mathcal{G}_3}$ vanish, given the field configurations at the initial and final times τ_i and τ_f,

$$\delta\mathcal{A}_{\mathcal{G}_3} = \delta\mathcal{A}_{e_i}[\phi_i] + \delta\mathcal{A}_{e_j}[\phi_j] + \delta\mathcal{A}_{e_z}[\phi_z] + \delta\mathcal{J}[\phi_i, \phi_j, \phi_z, \lambda^{ij}, \lambda^{jz}] \overset{!}{=} 0\,. \tag{3.28}$$

First, let us focus on variations of the action functional due to arbitrary variations of the Lagrange multiplier fields $\delta\lambda$. Given that the Lagrange multiplier fields λ^{ij} and λ^{jz} are independent of the fields ϕ_i, ϕ_j, and ϕ_z, any variation in λ^{ij} or λ^{jz} does not cause variations in ϕ_i, ϕ_j, or ϕ_z. As a result, the only functional affected by these variations is $\mathcal{J}[\phi_i, \phi_j, \phi_z, \lambda^{ij}, \lambda^{jz}]$. Therefore, for $\delta\mathcal{A}_{\mathcal{G}_3} \overset{!}{=} 0$ to be satisfied, the variations of $\mathcal{J}$ with respect to $\delta\lambda$ must vanish independently. Mathematically,

$$\begin{aligned}\delta_\lambda \mathcal{J} = \int_{H_{e_i}\setminus v(T)} \frac{\delta \mathcal{J}}{\delta\lambda^{ij}(x_i)}\delta\lambda^{ij}(x_i)\, d^2x_i + \int_{H_{e_j}} \frac{\delta \mathcal{J}}{\delta\lambda^{ij}(x_j)}\delta\lambda^{ij}(x_j)\, d^2x_j + \\ + \int_{H_{e_j}} \frac{\delta \mathcal{J}}{\delta\lambda^{jz}(x_j)}\delta\lambda^{jz}(x_j)\, d^2x_j + \int_{H_{e_z}\setminus v(T)} \frac{\delta \mathcal{J}}{\delta\lambda^{jz}(x_z)}\delta\lambda^{jz}(x_z)\, d^2x_z \overset{!}{=} 0\,, \qquad (3.29)\end{aligned}$$

where $\delta_\lambda \mathcal{J}$ refers to the variations of $\mathcal{J}$ induced by λ^{ij} and λ^{jz}.

Furthermore, λ^{ij} and λ^{jz} are also independent of each other. Since variations with respect to one of the two fields do not imply a change in the other, for Eq. (3.29) to vanish, the terms involving each field must independently sum to zero. This leads to

$$\lim_{\epsilon\to 0}\int_{H_{e_i}\setminus v(\tau)} \mathcal{X}^{i\to v}_{v-\epsilon}\phi_i\,\delta\lambda^{ij}\,\mathrm{dvol}_{h_{e_i}} - \int_{H_{e_j}} \mathcal{X}_v\phi_j\,\delta\lambda^{ij}\,\mathrm{dvol}_{h_{e_j}} \overset{!}{=} 0 \qquad (3.30)$$

for variations induced by $\delta\lambda^{ij}$ and

$$\lim_{\epsilon\to 0}\int_{H_{e_z}\setminus v(\tau)} \mathcal{X}^{z\to v}_{v-\epsilon}\phi_z\,\delta\lambda^{jz}\,\mathrm{dvol}_{h_{e_z}} - \int_{H_{e_j}} \mathcal{X}_v\phi_j\,\delta\lambda^{jz}\,\mathrm{dvol}_{h_{e_j}} \overset{!}{=} 0 \qquad (3.31)$$

for the ones induced by $\delta\lambda^{jz}$. Since these two equations have to hold for arbitrary variations $\delta\lambda^{ij}$ and $\delta\lambda^{jz}$, we can write, at the vertex worldline $v(T)$,

$$\begin{aligned}\lim_{\epsilon\to 0}\phi_i\Big|^{i\to v}_{v(T)-\epsilon} - \phi_j\Big|_{v(T)} \overset{!}{=} 0 \\ \lim_{\epsilon\to 0}\phi_z\Big|^{z\to v}_{v(T)-\epsilon} - \phi_j\Big|_{v(T)} \overset{!}{=} 0 \qquad (3.32)\end{aligned}$$

which can be rewritten as

$$\lim_{\epsilon\to 0}\phi_i\Big|^{i\to v}_{v(T)-\epsilon} \overset{!}{=} \phi_j\Big|_{v(T)} \overset{!}{=} \lim_{\epsilon\to 0}\phi_z\Big|^{z\to v}_{v(T)-\epsilon} \qquad (3.33)$$

which states continuity of the total field configuration at the vertex for all times. For a visualization of the above condition, we refer to the following Fig. 3.9 A.

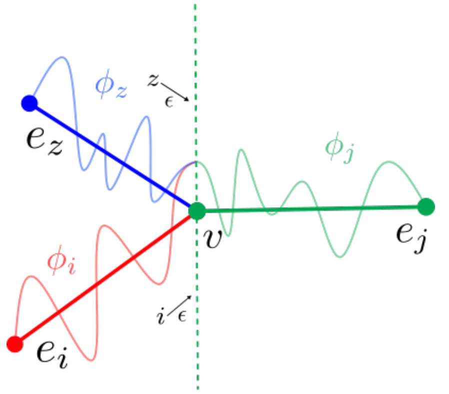

Figure 3.9: *A*. Visualization of the continuity condition across the vertex for the total field configuration on $\mathcal{G}_3$, given by the agreement of the three field configurations ϕ_i, ϕ_j and ϕ_z at the vertex worldline. At a given time, each field's spatial domain is highlighted with the same color as for the corresponding field. Note that the vertex only belongs to the domain of ϕ_j. *B*. As an example, Dirichlet boundary conditions $\phi_\lambda = 0$ for $\lambda \in \{i, j, z\}$ are assumed at the free endpoints of the subgraph, for all times. At the vertex worldline, together with the continuity condition, boundary conditions on the fields derivatives are applied, resulting in the Kirchhoff-Neumann conditions.

The variations of $\mathcal{A}_{\mathcal{G}_3}$ induced by $\delta\phi_i$, $\delta\phi_j$ and $\delta\phi_z$ yield, analogously to Eq. (3.10),

$$\begin{aligned}\delta\mathcal{A}_{\mathcal{G}_3} &= \delta\mathcal{A}_{e_i} + \delta\mathcal{A}_{e_j} + \delta\mathcal{A}_{e_z} + \delta\mathcal{J} = \int_{H_{e_i}\setminus v(\tau)} \left(\frac{\partial\mathcal{L}_{e_i}}{\partial\phi_i}\delta\phi_i + \frac{\partial\mathcal{L}_{e_i}}{\partial\partial_a\phi_i}\partial_a\delta\phi_i\right)\mathrm{dvol}_{h_{e_i}} + \\ &+ \int_{H_{e_j}} \left(\frac{\partial\mathcal{L}_{e_j}}{\partial\phi_j}\delta\phi_j + \frac{\partial\mathcal{L}_{e_j}}{\partial\partial_a\phi_j}\partial_a\delta\phi_j\right)\mathrm{dvol}_{h_{e_j}} + \int_{H_{e_z}\setminus v(\tau)} \left(\frac{\partial\mathcal{L}_{e_z}}{\partial\phi_z}\delta\phi_z + \frac{\partial\mathcal{L}_{e_z}}{\partial\partial_a\phi_z}\partial_a\delta\phi_z\right)\mathrm{dvol}_{h_{e_z}} + \\ &+ \lim_{\epsilon\to 0}\int_{H_{e_i}\setminus v(\tau)} \mathcal{X}^{i\to v}_{v-\epsilon}\lambda^{ij}\,\delta\phi_i \mathrm{dvol}_{h_{e_i}} - \int_{H_{e_j}} \mathcal{X}_v\lambda^{ij}\,\delta\phi_j\,\mathrm{dvol}_{h_{e_j}} + \\ &+ \lim_{\epsilon\to 0}\int_{H_{e_z}\setminus v(\tau)} \mathcal{X}^{z\to v}_{v-\epsilon}\lambda^{jz}\,\delta\phi_z\,\mathrm{dvol}_{h_{e_z}} - \int_{H_{e_j}} \mathcal{X}_v\lambda^{jz}\,\delta\phi_j\,\mathrm{dvol}_{h_{e_j}} \overset{!}{=} 0\,, \end{aligned} \tag{3.34}$$

where the last four terms are derived by varying $\mathcal{J}$ with respect to the fields ϕ_i, ϕ_j and ϕ_z, i.e. by computing

$$\begin{aligned}\delta\mathcal{J} = &\int_{H_{e_i}\setminus v(T)} \frac{\delta\mathcal{J}}{\delta\phi_i(x_i)}\delta\phi_i(x_i)d^2x_i + \int_{H_{e_j}} \frac{\delta\mathcal{J}}{\delta\phi_j(x_j)}\delta\phi_j(x_j)\,d^2x_j + \\ &+ \int_{H_{e_z}\setminus v(T)} \frac{\delta\mathcal{J}}{\delta\phi_z(x_z)}\delta\phi_z(x_z)d^2x_z\,. \end{aligned} \tag{3.35}$$

The first three integrals of Eq. (3.34) yield once again the same terms as those analyzed in the previous section, in Eq. (3.11). In fact, if we use the divergence theorem, for each integral we obtain two terms, one integral over the entire field domain and one boundary term. Explicitly, in terms of the coordinates $x_\lambda = \{\xi^a_\lambda\} = (T, \xi_\lambda)$,

$$\begin{aligned}
\delta\mathcal{A}_{\mathcal{G}_3} &= \delta\mathcal{A}_{e_i} + \delta\mathcal{A}_{e_j} + \delta\mathcal{A}_{e_z} + \delta\mathcal{J} = \\
&= \int_{H_{e_i}\setminus v(T)} \left(\frac{\partial \mathcal{L}_{e_i}}{\partial \phi_i}\sqrt{-h_{e_i}} - \partial_a \left(\sqrt{-h_{e_i}}\frac{\partial \mathcal{L}_{e_i}}{\partial\partial_a\phi_i} \right) \right) \delta\phi_i dT d\xi_i + \\
&+ \int_{\partial H_{e_i}} \frac{\partial \mathcal{L}_{e_i}}{\partial\partial_a\phi_i}\delta\phi_i\, n^i_a \sqrt{-h^\partial_{e_i}} dq + \\
&+ \int_{H_{e_j}} \left(\frac{\partial \mathcal{L}_{e_j}}{\partial \phi_j}\sqrt{-h_{e_j}} - \partial_a \left(\sqrt{-h_{e_j}}\frac{\partial \mathcal{L}_{e_j}}{\partial\partial_a\phi_j} \right) \right) \delta\phi_j dT d\xi_j + \\
&+ \int_{\partial H_{e_j}} \frac{\partial \mathcal{L}_{e_j}}{\partial\partial_a\phi_j}\delta\phi_j\, n^j_a \sqrt{-h^\partial_{e_j}} dq + \\
&+ \int_{H_{e_z}\setminus v(T)} \left(\frac{\partial \mathcal{L}_{e_z}}{\partial \phi_z}\sqrt{-h_{e_z}} - \partial_a \left(\sqrt{-h_{e_z}}\frac{\partial \mathcal{L}_{e_z}}{\partial\partial_a\phi_z} \right) \right) \delta\phi_z dT d\xi_z + \\
&+ \int_{\partial H_{e_z}} \frac{\partial \mathcal{L}_{e_z}}{\partial\partial_a\phi_z}\delta\phi_z\, n^z_a \sqrt{-h^\partial_{e_z}} dq + \\
&+ \lim_{\epsilon\to 0} \int_{H_{e_i}\setminus v(\tau)} \mathcal{X}^{i\to v}_{v-\epsilon} \lambda^{ij}\, \delta\phi_i\, \mathrm{dvol}_{h_{e_i}} - \int_{H_{e_j}} \mathcal{X}_v \lambda^{ij}\, \delta\phi_j\, \mathrm{dvol}_{h_{e_j}} + \\
&+ \lim_{\epsilon\to 0} \int_{H_{e_z}\setminus v(\tau)} \mathcal{X}^{z\to v}_{v-\epsilon} \lambda^{jz}\, \delta\phi_z\, \mathrm{dvol}_{h_{e_z}} - \int_{H_{e_j}} \mathcal{X}_v \lambda^{jz}\, \delta\phi_j\, \mathrm{dvol}_{h_{e_j}} \overset{!}{=} 0\,.
\end{aligned} \tag{3.36}$$

First, we can observe that the integrals induced by variations of $\mathcal{J}$ are also boundary terms. Therefore, for the total variation of the action functional to be zero, each integral supported on the bulk of the corresponding history must independently vanish, as they all have disjoint support. Since we assume the field variations to be arbitrary on the bulk of each history, we obtain that for all $\lambda \in \{i, j, z\}$, $\frac{\partial \mathcal{L}_{e_\lambda}}{\partial\phi_\lambda}\sqrt{-h_{e_\lambda}} - \partial_a \left(\sqrt{-h_{e_\lambda}} \frac{\partial\mathcal{L}_{e_\lambda}}{\partial\partial_a\phi_\lambda} \right) \overset{!}{=} 0$. This leads to the equations of motion for the fields ϕ_i, ϕ_j, and ϕ_z on their respective histories.

As shown explicitly for Eq. (2.25), the same integrals must also be performed over the temporal and spatial boundaries of each history, in particular at the vertex worldline or on curves at a distance ϵ from it. However, by continuity, we can set $\frac{\partial \mathcal{L}_{e_\lambda}}{\partial\phi_\lambda}\sqrt{-h_{e_\lambda}} - \partial_a \left(\sqrt{-h_{e_\lambda}} \frac{\partial\mathcal{L}_{e_\lambda}}{\partial\partial_a\phi_\lambda} \right)$ to vanish at spatial boundaries as well. On temporal boundaries, all integrals vanish. By implementing these results into Eq. (3.36), we can rewrite the same condition as follows

$$
\begin{aligned}
&\int_{\partial H_{e_i}} \frac{\partial \mathcal{L}_{e_i}}{\partial \partial_a \phi_i} \delta\phi_i \, n^i_a \sqrt{-h^\partial_{e_i}} dq + \\
&+ \int_{\partial H_{e_j}} \frac{\partial \mathcal{L}_{e_j}}{\partial \partial_a \phi_j} \delta\phi_j \, n^j_a \sqrt{-h^\partial_{e_j}} dq + \int_{\partial H_{e_z}} \frac{\partial \mathcal{L}_{e_z}}{\partial \partial_a \phi_z} \delta\phi_z \, n^z_a \sqrt{-h^\partial_{e_z}} dq + \\
&+ \lim_{\epsilon \to 0} \int_{H_{e_i} \setminus v(\tau)} \mathcal{X}^{i \to v}_{v-\epsilon} \lambda^{ij} \, \delta\phi_i \mathrm{dvol}_{h_{e_i}} - \int_{H_{e_j}} \mathcal{X}_v \lambda^{ij} \, \delta\phi_j \, \mathrm{dvol}_{h_{e_j}} + \\
&+ \lim_{\epsilon \to 0} \int_{H_{e_z} \setminus v(\tau)} \mathcal{X}^{z \to v}_{v-\epsilon} \lambda^{jz} \, \delta\phi_z \, \mathrm{dvol}_{h_{e_z}} - \int_{H_{e_j}} \mathcal{X}_v \lambda^{jz} \, \delta\phi_j \, \mathrm{dvol}_{h_{e_j}} \overset{!}{=} 0 \, .
\end{aligned}
\tag{3.37}
$$

The first three integrals are on the boundaries of each history and therefore contain four terms each, two on spatial boundaries and two on temporal ones. To facilitate the analysis of each term, we refer to Fig. 3.10, for a clearer visualization of the mathematical expressions.

The integrals on the temporal boundaries are all vanishing. This is because, according to the variational principle, the field variations are zero at the temporal boundaries; that is, for $\lambda \in \{i, j, z\}$, $\phi_\lambda(T_i, \xi_\lambda) = const.$ and $\phi_\lambda(T_f, \xi_\lambda) = const.$ for all values of ξ_λ, reflecting the choice of initial and final conditions for the field configurations.

Therefore, the integrals on the boundaries of each history ∂H_{e_λ} reduce to

$$
\begin{aligned}
&\int_{\partial H_{e_i}} \frac{\partial \mathcal{L}_{e_i}}{\partial \partial_a \phi_i} \delta\phi_i \, n^i_a \sqrt{-h^\partial_{e_i}} dq \; + \int_{\partial H_{e_j}} \frac{\partial \mathcal{L}_{e_j}}{\partial \partial_a \phi_j} \delta\phi_j \, n^j_a \sqrt{-h^\partial_{e_j}} dq + \\
&+ \int_{\partial H_{e_z}} \frac{\partial \mathcal{L}_{e_z}}{\partial \partial_a \phi_z} \delta\phi_z \, n^z_a \sqrt{-h^\partial_{e_z}} dq = \\
&= \int_{\partial H_{e_i}\big|_{\partial e_{1i}}} \frac{\partial \mathcal{L}_{e_i}}{\partial \partial_a \phi_i} n^i_{\sigma\, a} \sqrt{-h^\partial_{e_i}} \delta\phi_i \, dT + \lim_{\epsilon \to 0} \int_{\partial H_{e_i}\big|_{\partial e_{2i-\epsilon}}} \frac{\partial \mathcal{L}_{e_i}}{\partial \partial_a \phi_i} n^i_{\sigma\, a} \sqrt{-h^\partial_{e_i}} \delta\phi_i \, dT + \\
&+ \int_{\partial H_{e_j}\big|_{\partial e_{1j}}} \frac{\partial \mathcal{L}_{e_j}}{\partial \partial_a \phi_j} n^j_{\sigma\, a} \sqrt{-h^\partial_{e_j}} \delta\phi_j \, dT + \int_{\partial H_{e_j}\big|_{\partial e_{2j}}} \frac{\partial \mathcal{L}_{e_j}}{\partial \partial_a \phi_j} n^j_{\sigma\, a} \sqrt{-h^\partial_{e_j}} \delta\phi_j \, dT \\
&+ \int_{\partial H_{e_z}|_{\partial e_{1z}}} \frac{\partial \mathcal{L}_{e_z}}{\partial \partial_a \phi_z} n^z_{\sigma\, a} \sqrt{-h^\partial_{e_z}} \delta\phi_z \, dT + \lim_{\epsilon \to 0} \int_{\partial H_{e_z}|_{\partial e_{2z-\epsilon}}} \frac{\partial \mathcal{L}_{e_z}}{\partial \partial_a \phi_z} n^z_{\sigma\, a} \sqrt{-h^\partial_{e_z}} \delta\phi_z \, dT \, .
\end{aligned}
\tag{3.38}
$$

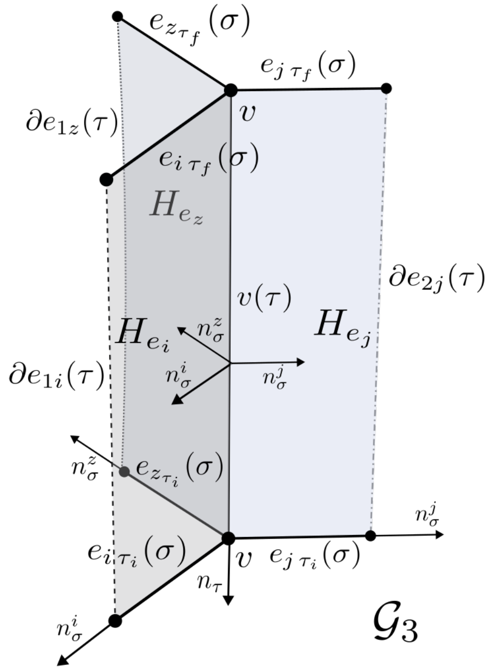

Figure 3.10: Details of the two-dimensional finite history $(H_{\mathcal{G}_3}, h_{\mathcal{G}_3})$ of a three-edge subgraph configuration $\mathcal{G}_3$, embedded in a globally hyperbolic spacetime (M, g). The common spatial boundary of the three histories H_{e_i}, H_{e_i} and H_{e_z} is the worldline $v(\tau)$ of the vertex. The spatial boundaries of $H_{\mathcal{G}_3}$ are the three free endpoints worldlines $\partial e_{1i}(\tau)$, $\partial e_{2j}(\tau)$ and $\partial e_{1z}(\tau)$, depicted with dashed, dashed-dotted and dotted lines respectively. The three-edge star graph configuration $\mathcal{G}_3$ at initial and final time defines the two temporal boundaries of $H_{\mathcal{G}_3}$. Three, generally different, normal vector fields n^i_σ, n^j_σ and n^z_σ point out of each edge e_i, e_j and e_z; the normal vector field n_τ is instead the same on all edges of $\mathcal{G}_3$.

Thus, we can rewrite Eq. (3.37) as

$$\begin{aligned}
&\int_{\partial H_{e_i}|_{\partial e_{1i}}} \frac{\partial \mathcal{L}_{e_i}}{\partial \partial_a \phi_i} n^i_{\sigma\,a} \sqrt{-h^\partial_{e_i}}\delta\phi_i\, dT + \lim_{\epsilon\to 0}\int_{\partial H_{e_i}|_{\partial e_{2i}-\epsilon}} \frac{\partial \mathcal{L}_{e_i}}{\partial \partial_a \phi_i} n^i_{\sigma\,a} \sqrt{-h^\partial_{e_i}}\delta\phi_i\, dT + \\
&+ \int_{\partial H_{e_j}|_{\partial e_{1j}}} \frac{\partial \mathcal{L}_{e_j}}{\partial \partial_a \phi_j} n^j_{\sigma\,a} \sqrt{-h^\partial_{e_j}}\delta\phi_j\, dT + \int_{\partial H_{e_j}|_{\partial e_{2j}}} \frac{\partial \mathcal{L}_{e_j}}{\partial \partial_a \phi_j} n^j_{\sigma\,a} \sqrt{-h^\partial_{e_j}}\delta\phi_j\, dT + \\
&+ \int_{\partial H_{e_z}|_{\partial e_{1z}}} \frac{\partial \mathcal{L}_{e_z}}{\partial \partial_a \phi_z} n^z_{\sigma\,a} \sqrt{-h^\partial_{e_z}}\delta\phi_z\, dT + \lim_{\epsilon\to 0}\int_{\partial H_{e_z}|_{\partial e_{2z}-\epsilon}} \frac{\partial \mathcal{L}_{e_z}}{\partial \partial_a \phi_z} n^z_{\sigma\,a} \sqrt{-h^\partial_{e_z}}\delta\phi_z\, dT + \\
&+ \lim_{\epsilon\to 0}\int_{H_{e_i}\setminus v(\tau)} \mathcal{X}^{i\to v}_{v-\epsilon}\lambda^{ij}\,\delta\phi_i \mathrm{dvol}_{h_{e_i}} - \int_{H_{e_j}} \mathcal{X}_v \lambda^{ij}\,\delta\phi_j\,\mathrm{dvol}_{h_{e_j}} + \\
&+ \lim_{\epsilon\to 0}\int_{H_{e_z}\setminus v(\tau)} \mathcal{X}^{z\to v}_{v-\epsilon}\lambda^{jz}\,\delta\phi_z\,\mathrm{dvol}_{h_{e_z}} - \int_{H_{e_j}} \mathcal{X}_v \lambda^{jz}\,\delta\phi_j\,\mathrm{dvol}_{h_{e_j}} \overset{!}{=} 0\,.
\end{aligned} \tag{3.39}$$

Therefore, for the variations of the action functional $\mathcal{A}_{\mathcal{G}_3}$ to be vanishing, the variational principle requires that the above integrals must sum to zero. As we can see from the picture in Fig. 3.10, the three free endpoints worldines $\partial e_{1i}(\tau)$, $\partial e_{2j}(\tau)$ and $\partial e_{1z}(\tau)$, for some time parameter τ, are distinct and do not intersect with each other or with the vertex worldline. Consequently, the three integrals performed along these specific worldlines do not share any common support with other integrals in the sum and thus, for the sum to be zero, they must vanish individually. This yields

$$\begin{aligned}
&\int_{\partial H_{e_i}\big|_{\partial e_{1i}}} \frac{\partial \mathcal{L}_{e_i}}{\partial \partial_a \phi_i} n^i_{\sigma\, a} \sqrt{-h^{\partial}_{e_i}}\, \delta\phi_i \, dT \overset{!}{=} 0 \\
&\int_{\partial H_{e_j}\big|_{\partial e_{2j}}} \frac{\partial \mathcal{L}_{e_j}}{\partial \partial_a \phi_j} n^j_{\sigma\, a} \sqrt{-h^{\partial}_{e_j}}\, \delta\phi_j \, dT \overset{!}{=} 0 \\
&\int_{\partial H_{e_z}|_{\partial e_{1z}}} \frac{\partial \mathcal{L}_{e_z}}{\partial \partial_a \phi_z} n^z_{\sigma\, a} \sqrt{-h^{\partial}_{e_z}}\, \delta\phi_z \, dT \overset{!}{=} 0 \,,
\end{aligned} \tag{3.40}$$

which, according to Sec. 2.2, depending on the choice of the fields variations, lead to generalized Dirichlet or Neumann conditions at the free endpoints of the subgraph, for each time T. In fact, if the fields variations are arbitrary and non-vanishing, then we obtain

$$\begin{aligned}
&\frac{\partial \mathcal{L}_{e_i}}{\partial \partial_a \phi_i} n^i_{\sigma\, a} \sqrt{-h^{\partial}_{e_i}} \overset{!}{=} 0 \\
&\frac{\partial \mathcal{L}_{e_j}}{\partial \partial_a \phi_j} n^j_{\sigma\, a} \sqrt{-h^{\partial}_{e_j}} \overset{!}{=} 0 \\
&\frac{\partial \mathcal{L}_{e_z}}{\partial \partial_a \phi_z} n^z_{\sigma\, a} \sqrt{-h^{\partial}_{e_z}} \overset{!}{=} 0 \,,
\end{aligned} \tag{3.41}$$

at the free endpoints, for all times T. If we consider free real scalar massive fields on each edge, we can write $\mathcal{L}_{e_\lambda} = \frac{1}{2}\left(h^{ab}_{e_\lambda}\partial_a\phi_\lambda\, \partial_b\phi_\lambda - \mu^2\phi_\lambda^2\right)$ for each $\lambda \in \{i, j, z\}$. The above conditions then reduce to

$$\begin{aligned}
&h^{ab}_{e_i}\partial_a\phi_i \, n^i_{\sigma\, a}\sqrt{-h^{\partial}_{e_i}} \overset{!}{=} 0 \\
&h^{ab}_{e_j}\partial_a\phi_j \, n^j_{\sigma\, a}\sqrt{-h^{\partial}_{e_j}} \overset{!}{=} 0 \\
&h^{ab}_{e_z}\partial_a\phi_z \, n^z_{\sigma\, a}\sqrt{-h^{\partial}_{e_z}} \overset{!}{=} 0 \,,
\end{aligned} \tag{3.42}$$

for all T, which are a generalized version of the Neumann boundary conditions to arbitrary spacetimes. As already explained in previous sections, these conditions, along with the Dirichlet ones, ensure that there is no leakage of degrees of freedom out of the subgraph $\mathcal{G}_3$, i.e. particles or fields are confined to $\mathcal{G}_3$ and cannot propagate or leak into the surrounding ambient space. As an example, Dirichlet boundary conditions are chosen at the free endpoints of $\mathcal{G}_3$ in Fig. 3.9, B.

We still need a condition for the fields at the node. The remaining integrals of Eq. (3.39) have to sum to zero, otherwise the overall variation of the action functional is not vanishing. This implies,

$$\begin{aligned}
&\lim_{\epsilon\to 0}\int_{\partial H_{e_i}|_{\partial e_{2i}-\epsilon}} \frac{\partial \mathcal{L}_{e_i}}{\partial\partial_a\phi_i} n^{i}_{\sigma\,a}\sqrt{-h^{\partial}_{e_i}}\delta\phi_i\,dT + \int_{\partial H_{e_j}|_{\partial e_{1j}}} \frac{\partial \mathcal{L}_{e_j}}{\partial\partial_a\phi_j} n^{j}_{\sigma\,a}\sqrt{-h^{\partial}_{e_j}}\delta\phi_j\,dT + \\
&+\lim_{\epsilon\to 0}\int_{\partial H_{e_z}|_{\partial e_{2z}-\epsilon}} \frac{\partial \mathcal{L}_{e_z}}{\partial\partial_a\phi_z} n^{z}_{\sigma\,a}\sqrt{-h^{\partial}_{e_z}}\delta\phi_z\,dT + \\
&+\lim_{\epsilon\to 0}\int_{H_{e_i}\setminus v(\tau)} \mathcal{X}^{i\to v}_{v-\epsilon}\lambda^{ij}\,\delta\phi_i \mathrm{dvol}_{h_{e_i}} - \int_{H_{e_j}} \mathcal{X}_v\lambda^{ij}\,\delta\phi_j\,\mathrm{dvol}_{h_{e_j}} + \\
&+\lim_{\epsilon\to 0}\int_{H_{e_z}\setminus v(\tau)} \mathcal{X}^{z\to v}_{v-\epsilon}\lambda^{jz}\,\delta\phi_z\,\mathrm{dvol}_{h_{e_z}} - \int_{H_{e_j}} \mathcal{X}_v\lambda^{jz}\,\delta\phi_j\,\mathrm{dvol}_{h_{e_j}} \overset{!}{=} 0\,. \qquad (3.43)
\end{aligned}$$

Recall that the worldline of the endpoints ∂e_{2i}, ∂e_{1j} and ∂e_{2z} are all identified together in the vertex worldline $v(\tau)$, where τ is a time parameter. This implies that the first and third integrals are performed at a distance ϵ away from the vertex along the edge e_i and e_z, respectively, in the same way as the fourth and sixth integrals. The fact that they share a common support allows us to write,

$$\begin{aligned}
\lim_{\epsilon\to 0}\int_{v(T)-\epsilon} \frac{\partial \mathcal{L}_{e_i}}{\partial\partial_a\phi_i} n^{i}_{\sigma\,a}\sqrt{-h^{\partial}_{e_i}}\delta\phi_i\,dT &\overset{!}{=} -\lim_{\epsilon\to 0}\int_{H_{e_i}\setminus v(\tau)} \mathcal{X}^{i\to v}_{v-\epsilon}\lambda^{ij}\,\delta\phi_i \mathrm{dvol}_{h_{e_i}}\,, \\
\int_{v(T)} \frac{\partial \mathcal{L}_{e_j}}{\partial\partial_a\phi_j} n^{j}_{\sigma\,a}\sqrt{-h^{\partial}_{e_j}}\delta\phi_j\,dT &\overset{!}{=} \int_{H_{e_j}} \mathcal{X}_v\lambda^{ij}\,\delta\phi_j\,\mathrm{dvol}_{h_{e_j}} + \int_{H_{e_j}} \mathcal{X}_v\lambda^{jz}\,\delta\phi_j\,\mathrm{dvol}_{h_{e_j}}\,, \\
\lim_{\epsilon\to 0}\int_{v(T)-\epsilon} \frac{\partial \mathcal{L}_{e_z}}{\partial\partial_a\phi_z} n^{z}_{\sigma\,a}\sqrt{-h^{\partial}_{e_z}}\delta\phi_z\,dT &\overset{!}{=} -\lim_{\epsilon\to 0}\int_{H_{e_z}\setminus v(\tau)} \mathcal{X}^{z\to v}_{v-\epsilon}\lambda^{jz}\,\delta\phi_z\,\mathrm{dvol}_{h_{e_z}}\,, \qquad (3.44)
\end{aligned}$$

as the only way for Eq. (3.43) to be satisfied is that the time integrals performed at the same spatial point cancel each other to zero.

If the field variations $\delta\phi_i$, $\delta\phi_j$ and $\delta\phi_z$ are vanishing for all times τ at the vertex worldline or at a distance ϵ from it along the edges e_i and e_z, then the above conditions are satisfied and we obtain constant field configurations at the vertex for all times, i.e.

$\lim_{\epsilon\to 0}\,\phi_i\big|^{i\to v}_{v(\tau)-\epsilon} = \textit{const.}$, $\phi_j\big|_{v(\tau)} = \textit{const.}$ and $\lim_{\epsilon\to 0}\,\phi_z\big|^{z\to v}_{v(\tau)-\epsilon} = \textit{const.}$. Which, by setting the constant to be the same for all fields, agree with the continuity condition Eq. (3.33). These conditions represent Dirichlet boundary conditions at the vertex of the subgraph. Note that imposing these conditions at the node effectively results in a configuration equivalent to three disconnected edges. Any propagation from the edges towards the node leads to total reflection. Although continuous at the node, the total field configuration on $\mathcal{G}_3$ behaves as three independent field configurations that exist separately from one another.

Conversely, if we assume $\delta\phi_i$, $\delta\phi_j$ and $\delta\phi_z$ to be arbitrary and independent, then we obtain the following conditions respectively:

$$\begin{aligned}
\lim_{\epsilon\to 0}\,\frac{\partial\mathcal{L}_{e_i}}{\partial\partial_a\phi_i} n^i_{\sigma\,a}\sqrt{-h^{\partial}_{e_i}}\,\Bigg|^{i\to v}_{v(T)-\epsilon} &\overset{!}{=} -\lim_{\epsilon\to 0}\,\lambda^{ij}\,\Big|^{i\to v}_{v(T)-\epsilon}\,,\\
\frac{\partial\mathcal{L}_{e_j}}{\partial\partial_a\phi_j} n^j_{\sigma\,a}\sqrt{-h^{\partial}_{e_j}}\,\Bigg|_{v(T)} &\overset{!}{=} \lambda^{ij}\,\Big|_{v(T)} + \lambda^{jz}\,\Big|_{v(T)}\,,\\
\lim_{\epsilon\to 0}\,\frac{\partial\mathcal{L}_{e_z}}{\partial\partial_a\phi_z} n^z_{\sigma\,a}\sqrt{-h^{\partial}_{e_z}}\,\Bigg|^{z\to v}_{v(T)-\epsilon} &\overset{!}{=} -\lim_{\epsilon\to 0}\,\lambda^{jz}\,\Big|^{z\to v}_{v(T)-\epsilon}\,.
\end{aligned}\tag{3.45}$$

By continuity of the Lagrange fields λ^{ij} and λ^{jz} through the node along the edges e_i, e_j and e_j, e_z respectively, i.e. $\lim_{\epsilon\to 0}\,\lambda^{ij}\big|^{i\to v}_{v(T)-\epsilon} = \lambda^{ij}\big|_{v(T)}$ and $\lim_{\epsilon\to 0}\,\lambda^{jz}\big|^{z\to v}_{v(T)-\epsilon} = \lambda^{jz}\big|_{v(T)}$, we can write,

$$\begin{aligned}
\lim_{\epsilon\to 0}\,\frac{\partial\mathcal{L}_{e_i}}{\partial\partial_a\phi_i} n^i_{\sigma\,a}\sqrt{-h^{\partial}_{e_i}}\,\Bigg|^{i\to v}_{v(T)-\epsilon} &\overset{!}{=} -\lim_{\epsilon\to 0}\,\lambda^{ij}\,\Big|^{i\to v}_{v(T)-\epsilon} = -\,\lambda^{ij}\,\Big|_{v(T)}\,,\\
\lim_{\epsilon\to 0}\,\frac{\partial\mathcal{L}_{e_z}}{\partial\partial_a\phi_z} n^z_{\sigma\,a}\sqrt{-h^{\partial}_{e_z}}\,\Bigg|^{z\to v}_{v(T)-\epsilon} &\overset{!}{=} -\lim_{\epsilon\to 0}\,\lambda^{jz}\,\Big|^{z\to v}_{v(T)-\epsilon} = -\,\lambda^{jz}\,\Big|_{v(T)}\,,
\end{aligned}\tag{3.46}$$

which finally brings to

$$\lim_{\epsilon\to 0}\,\frac{\partial\mathcal{L}_{e_i}}{\partial\partial_a\phi_i} n^i_{\sigma\,a}\sqrt{-h^{\partial}_{e_i}}\,\Bigg|^{i\to v}_{v(T)-\epsilon} + \frac{\partial\mathcal{L}_{e_j}}{\partial\partial_a\phi_j} n^j_{\sigma\,a}\sqrt{-h^{\partial}_{e_j}}\,\Bigg|_{v(T)} + \lim_{\epsilon\to 0}\,\frac{\partial\mathcal{L}_{e_z}}{\partial\partial_a\phi_z} n^z_{\sigma\,a}\sqrt{-h^{\partial}_{e_z}}\,\Bigg|^{z\to v}_{v(T)-\epsilon} \overset{!}{=} 0\,,\tag{3.47}$$

at the worldline of the node of $\mathcal{G}_3$. When considered together with the continuity condition Eq. (3.33), the two pair of equations are a generalized version of the known *Kirchhoff-Neumann* boundary conditions to arbitrary spacetimes. For free real scalar fields on each edge of $\mathcal{G}_3$, we can rewrite the Kirchhoff-Neumann conditions as

$$\begin{cases} \lim\limits_{\epsilon\to 0} \phi_i \Big|_{v(T)-\epsilon}^{i\to v} \overset{!}{=} \phi_j \Big|_{v(T)} \overset{!}{=} \lim\limits_{\epsilon\to 0} \phi_z \Big|_{v(T)-\epsilon}^{z\to v} , \\ \lim\limits_{\epsilon\to 0} h^{ab}_{e_i}\, \partial_a\phi_i\, n^i_{\sigma\, b}\sqrt{-h^\partial_{e_i}} \Big|_{v(T)-\epsilon}^{i\to v} + h^{ab}_{e_j}\, \partial_a\phi_j\, n^j_{\sigma\, b}\sqrt{-h^\partial_{e_j}} \Big|_{v(T)} + \\ + \lim\limits_{\epsilon\to 0} h^{ab}_{e_z}\, \partial_a\phi_z\, n^z_{\sigma\, b}\sqrt{-h^\partial_{e_z}} \Big|_{v(T)-\epsilon}^{z\to v} \overset{!}{=} 0 \, . \end{cases} \tag{3.48}$$

Each term summed in the second condition originally arises from the divergence theorem and quantifies the flux $\partial\phi_\lambda$ along the normal n^λ_σ of each edge e_λ, evaluated at or near the node. The fact that these terms are summed to zero implies that the fluxes are conserved through the node and the vertex does not act as a source or sink for the total field configuration on $\mathcal{G}_3$. In particular, Eq. (3.45) offers room for physical interpretation. Specifically, we note that the Lagrange fields are acting as auxiliary sources to impose junction conditions at the vertex. In fact, if for instance the Lagrangian density $\mathcal{L}_{e_j}$ would contain a source term $J\phi_j$ at the vertex, for example through a point-like source $J(T,\xi_j)$ vanishing for $\xi_j \neq v$, the third term of Eq. (3.36) would also contribute to Eq. (3.45) with a term $\int_{H_{e_j}} J\, \delta\phi_j\, \mathrm{dvol}_{h_{e_j}}$. Mathematically, Eq. (3.45) would read

$$\begin{aligned} \lim_{\epsilon\to 0} \frac{\partial\mathcal{L}_{e_i}}{\partial\partial_a\phi_i} n^i_{\sigma\, a}\sqrt{-h^\partial_{e_i}} \Big|_{v(T)-\epsilon}^{i\to v} &\overset{!}{=} -\lim_{\epsilon\to 0} \lambda^{ij} \Big|_{v(T)-\epsilon}^{i\to v} , \\ \frac{\partial\mathcal{L}_{e_j}}{\partial\partial_a\phi_j} n^j_{\sigma\, a}\sqrt{-h^\partial_{e_j}} \Big|_{v(T)} &\overset{!}{=} \lambda^{ij} \Big|_{v(T)} + \lambda^{jz} \Big|_{v(T)} + J \Big|_{v(T)} , \\ \lim_{\epsilon\to 0} \frac{\partial\mathcal{L}_{e_z}}{\partial\partial_a\phi_z} n^z_{\sigma\, a}\sqrt{-h^\partial_{e_z}} \Big|_{v(T)-\epsilon}^{z\to v} &\overset{!}{=} -\lim_{\epsilon\to 0} \lambda^{jz} \Big|_{v(T)-\epsilon}^{z\to v} . \end{aligned} \tag{3.49}$$

This equation suggests that the source J at the vertex and the Lagrange fields λ^{ij} and λ^{jz} contribute in a similar way to the flux balance along the edge e_j. Essentially, the equation indicates that the total flux term for the edge e_j, $\frac{\partial\mathcal{L}_{e_j}}{\partial\partial_a\phi_j} n^j_{\sigma\, a}\sqrt{-h^\partial_{e_j}}$, calculated at the vertex, is influenced not only by the external source J at the vertex but also by two additional contributions: λ^{ij}, λ^{jz}. The continuity of the Lagrange fields shows that these contributions correspond to the fluxes $\frac{\partial\mathcal{L}_{e_i}}{\partial\partial_a\phi_i} n^i_{\sigma\, a}\sqrt{-h^\partial_{e_i}}$ and $\frac{\partial\mathcal{L}_{e_z}}{\partial\partial_a\phi_z} n^z_{\sigma\, a}\sqrt{-h^\partial_{e_z}}$ from the edges e_i and e_z, respectively. Thus, the Lagrange multiplier act as auxiliary sources, which, while not physical sources themselves, represent additional flux contributions arising because the edge e_j is connected to two other edges. In fact, this connection allows the fields ϕ_i and

ϕ_z to influence the flux on e_j by propagating into it.

If the three edges were treated as disconnected, without enforcing the continuity condition specified in Eq. (3.33), the terms λ^{ij} and λ^{jz} would be zero. In that scenario, the flux on e_j would solely originate from the external source J, with the equation $\frac{\partial \mathcal{L}_{e_j}}{\partial \partial_a \phi_j} n^j_{\sigma\, a} \sqrt{-h^{\partial}_{e_j}} = J$ ensuring flux conservation at the vertex. However, because of the continuity condition, the three field theories are linked, and the Lagrange fields account for flux contributions to e_j that are independent of J and arise from field variations in other edges of the subgraph.

When the subgraph $\mathcal{G}_3$ is embedded in the Minkowski spacetime (M, η), the above generalized Kirchhoff-Neumann conditions Eq. (3.48), for free real scalar fields on the subgraph, simplify to

$$\begin{cases} \lim\limits_{\epsilon \to 0} \phi_i \Big|_{v(T)-\epsilon}^{i \to v} \overset{!}{=} \phi_j \Big|_{v(T)} \overset{!}{=} \lim\limits_{\epsilon \to 0} \phi_z \Big|_{v(T)-\epsilon}^{z \to v} , \\ \lim\limits_{\epsilon \to 0} \partial_{\xi_i} \phi_i \Big|_{v(T)-\epsilon}^{i \to v} + \partial_{\xi_j} \phi_j \Big|_{v(T)} + \lim\limits_{\epsilon \to 0} \partial_{\xi_z} \phi_z \Big|_{v(T)-\epsilon}^{z \to v} \overset{!}{=} 0 . \end{cases} \tag{3.50}$$

These are the commonly known Kirchhoff-Neumann conditions. As the above equation shows, it is ensured that the spatial variation of one field at the vertex has to be fully compensated by a variation of the other two fields.

The physical nature of these conditions becomes even clearer when considering complex scalar fields on $\mathcal{G}_3$, since in this case the Kirchhoff-Neumann conditions guarantee that the sum of the Noether currents related to the three fields is zero at the vertex, highly resembling the Kirchhoff's law at a node in electrical circuits, for which *what enters in has to come out*, without the node being a source or sink for the electrical currents. At the same time, the conservation of the corresponding charge is ensured [13, 20].

For convenience, whenever the normal vector field has a vanishing temporal component, the junction conditions Eq. (3.48) at the vertex v of the subgraph can be jointly expressed in the general form

$$A\,\Phi(T, v) + B\,\Phi'(T, v) = 0 , \tag{3.51}$$

where A and B are complex $n \times n$ matrices and Φ together with Φ' are vectors including the field and its derivative for all n edges. Note that if C is any invertible matrix, the pairs $\{A, B\}$ and $\{CA, CB\}$, define equivalent boundary conditions [20]. If we define the fields ϕ_i and ϕ_z at the vertex worldline as $\phi_i \big|_v := \lim_{\epsilon \to 0} \phi_i \big|_{v(T)-\epsilon}^{i \to v}$ and $\phi_z \big|_v := \lim_{\epsilon \to 0} \phi_z \big|_{v(T)-\epsilon}^{z \to v}$ and their spatial derivatives as $\partial_{\xi_\lambda} \phi_\lambda \big|_v := \lim_{\epsilon \to 0} \partial_{\xi_\lambda} \phi_\lambda \big|_{v(T)-\epsilon}^{\lambda \to v}$, where $\lambda = \{i, z\}$, we can write Φ and Φ' explicitly as

$$\Phi(T,v) := \begin{pmatrix} \phi_i\big|_v \\ \phi_j\big|_v \\ \phi_z\big|_v \end{pmatrix}, \quad \Phi'(T,v) := \begin{pmatrix} \partial_{\xi_i}\phi_i\big|_v \\ \partial_{\xi_j}\phi_j\big|_v \\ \partial_{\xi_z}\phi_z\big|_v \end{pmatrix}. \tag{3.52}$$

Accordingly, since the studied subgraph is $\mathcal{G}_3$, consisting of $n = 3$ edges connected in one node, the matrices A and B are both 3×3 matrices.

Although the choice of boundary conditions is arbitrary, it should guarantee that certain symmetries for the field theory are preserved, as already suggested above. In particular, if we are interested in quantum fields or components of wave packets on $\mathcal{G}_3$, the Laplace operator defined on the subgraph has to be self-adjoint everywhere and hence also at the node. This is crucial because, in this case, the Laplace operator eigenfunctions satisfy the completeness relations, enabling the construction of quantum field and conjugate momentum operators on the whole subgraph, which satisfy the equal-time commutation relation.

The fact that the Laplace operator is self-adjoint has also another crucial consequence for the field theory on the subgraph. In fact, in this case the scattering matrix associated to the vertex is ensured to be unitary. Since the scattering matrix encodes the transmission and reflection coefficients for the field across the node, its unitarity implies that the probability current, or Noether current for classical fields, is conserved at the node.

Remarkably, it has been proved that if the $n \times 2n$ composite matrix (A, B) has rank n and $AB^\dagger$ is self-adjoint, then the Laplace operator on $\mathcal{G}_3$ is also self-adjoint [16, 19].

If Eq. (3.51) satisfies the above requirements for the matrices A and B, the Laplace operator is self-adjoint and the scattering matrix unitary on $\mathcal{G}_3$. Therefore, in quantum field theory on a graph, the Kirchhoff-Neumann conditions emerge as the quantum counterpart of Kirchhoff's law.

If we consider $\mathcal{G}_3$ to be embedded in the Minkowski spacetime (M, η), then the matrices A and B are given by

$$A = \begin{pmatrix} 1 & -1 & 0 \\ 0 & 1 & -1 \\ 0 & 0 & 0 \end{pmatrix}, \quad B = \begin{pmatrix} 0 & 0 & 0 \\ 0 & 0 & 0 \\ 1 & 1 & 1 \end{pmatrix}, \tag{3.53}$$

according to Eq. (3.50). With this form of A and B, the 3×6 composite matrix (A, B) has rank 3 and $AB^\dagger$ is self-adjoint. Thus, the Kirchhoff-Neumann conditions for three edges embedded in Minkowski and joined at a vertex – visualized in Fig. 3.9 B –, ensure a unitary scattering matrix and a quantizable field configuration on it.

As reflected in the conditions of Eq. (3.48), a single $(1+1)$-dimensional field theory has proven to be insufficient to fully capture the physics on the subgraph, as the presence of the vertex and two additional edges causes each field theory to be influenced by the fields on other edges. In contrast to two edges connected at a node, the vertex of $\mathcal{G}_3$ is not removable, and we must depart from a simple $(1+1)$-dimensional field theoretical framework in favor of a full network-histories description.

3.2.3 Arbitrary Networks

We are finally ready to set the field theory framework on arbitrary networks by generalizing what we have studied for two edges connected at a node, $\mathcal{G}_2$, a loop, and the minimal graph configuration of a non-removable vertex: three edges connected together into a vertex, $\mathcal{G}_3$.

Consider again the arbitrary network $\mathcal{N} = (\mathcal{V}, \mathcal{E}, \iota)$ embedded in an arbitrary globally hyperbolic spacetime (M, g) that we considered in Fig. 3.4. Recall that $\mathcal{V}$ is the set of vertices and $\mathcal{E}$ the set of edges of the network. Let $V := \sharp\mathcal{V}$ denote the cardinality of $\mathcal{V}$, i.e. the number of vertices of $\mathcal{N}$ and $N := \sharp\mathcal{E}$ the number of its edges. Furthermore, let a be an index that runs over the set of edges $\mathcal{E}$ and b an index that labels each node in $\mathcal{V}$, with $a \in \{1, \ldots, N\}$ and $b \in \{1, \ldots, V\}$. The arbitrary network $\mathcal{N}$ can be thought of as being constructed from V star graphs, each with N_b legs, connected together. Therefore, at each vertex we apply the result of the previous section, generalizing it to star graphs with an arbitrary number of edges. Furthermore, note that we consider networks consisting of at least one minimal star graph, i.e. such that $V \geq 4$ and $N \geq 3$, otherwise the network-histories method is equivalent to a simple $(1+1)$-dimensional field theory on a line. Whenever a vertex v of $\mathcal{V}$ is connected to only two edges, we know that it can be removed and thus discarded (Sec. 3.2.1). Vertices corresponding to free endpoints are included in this construction by considering them as star graphs with only one leg $N_b = 1$. All remaining vertices connect at least three edges. For convenience, the network is reported again in Fig. 3.11, with only non-removable nodes depicted.

As constructed in Sec. 3.1, the network's history $(H_{\mathcal{N}}, h)$ is given by the union of all the histories of each edge of the network, i.e. $H_{\mathcal{N}} = \cup_{a=1}^{N} H_{e_a}$. Recall that the metric tensor h is the induced metric on the network and reduces to each edge's induced metric h_{e_a} on each history H_{e_a}. Accordingly, we can introduce a coordinate system $x_a = \{\xi_a^c\} = (T, \xi_a)$ on each (H_{e_a}, h_{e_a}). We define a $(1+1)$-dimensional field theory for a real scalar field ϕ_a on each edge history H_{e_a} of the network.

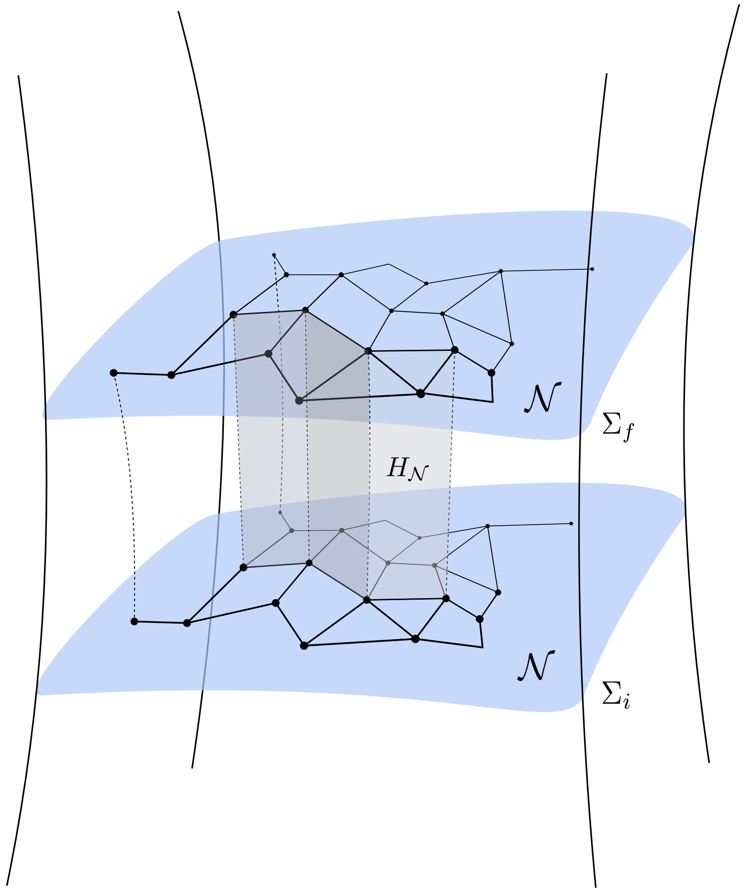

Figure 3.11: Arbitrary network $\mathcal{N}$ embedded in a globally hyperbolic spacetime (M, g). If τ is a time parameter, the history of the network can be visualized as the network worldsheet. For the sake of clarity, only a part of the network history $H_{\mathcal{N}}$ is shown in the picture. On the history of each edge of the network, a $(1+1)$-dimensional field theory is defined as in the previous section. At each node, junction conditions control field propagation throughout the network. Removable nodes have been omitted.

Suppose that for each vertex v_b in the network, there are N_b edges connected to it, that is, it is a star graph with N_b legs. Among these N_b edges, we select an edge e_b such that the field ϕ_b on H_{e_b} includes the vertex within its domain.[1] The fields on the remaining $N_b - 1$ edges do not have the vertex included in their domains. By generalizing the results of Sec. 3.2.2 for three edges, we can express the total action functional $\mathcal{A}_{\mathcal{N}}$ for the total field configuration on $\mathcal{N}$ as the sum of the N action functionals $\mathcal{A}_{e_a}$, each defined on the history H_{e_a} of the corresponding edge in the network, along with junction terms for each

---

[1] Please note that although we label the field ϕ_b with the same index b of the vertex v_b, when labeling the field, b only aims to single out the field ϕ_a with the vertex v_b in its domain, and as such, is a special value of a, running over the N_b edges connected to the node.

vertex v_b of $\mathcal{N}$, setting boundary conditions at v_b for fields on the edges connected to it. Mathematically,

$$\mathcal{A}_{\mathcal{N}}[\phi_1,\phi_2,\dots\phi_N,\lambda\,]=\sum_{a=1}^{N}\mathcal{A}_{e_a}[\phi_a]+\mathcal{J}[\phi_1,\phi_2,\dots\phi_N,\,\lambda]\,, \tag{3.54}$$

where by λ we indicate the $\sum_{b=1}^{V}(N_b-1)$ continuous Lagrange fields λ^{ab}, that connect, for each vertex v_b, N_b edges together. Furthermore, for all $v_b\in\mathcal{V}$,

$$\mathcal{A}_{e_a}[\phi_a]=\begin{cases}\displaystyle\int_{H_{e_a}\setminus v_b(\tau)}\mathcal{L}_{e_a}(x_a,\phi_a,\mathrm{d}\phi_a)\mathrm{dvol}_{h_{e_a}} & if\quad a\neq b\\ \displaystyle\int_{H_{e_b}}\mathcal{L}_{e_b}(x_b,\phi_b,\mathrm{d}\phi_b)\mathrm{dvol}_{h_{e_b}} & if\quad a=b\end{cases}\,. \tag{3.55}$$

The functional $\mathcal{J}$ introduced in Sec. 3.2.2 for three edges, can be generalized for an arbitrary network of N edges as

$$\begin{aligned}&\mathcal{J}[\phi_1,\phi_2,\dots\phi_N,\lambda\,]=\\&=\sum_{b=1}^{V}\left[\sum_{a=1}^{N_b}(1-\delta_{ab})\left(\lim_{\epsilon\to0}\int_{H_{e_a}\setminus v_b(\tau)}\mathcal{X}^{a\to v_b}_{v_b-\epsilon}\lambda^{ab}\phi_a\,\mathrm{dvol}_{h_{e_a}}-\int_{H_{e_b}}\mathcal{X}_{v_b}\lambda^{ab}\phi_b\,\mathrm{dvol}_{h_{e_b}}\right)\right]\,,\end{aligned} \tag{3.56}$$

where, for clarity, we relabeled the N_b edges connected to the node v_b from 1 to N_b. As a consistency check we can notice that by setting $V=4$ and $N=3$, we obtain again the junction functional $\mathcal{J}$ of Eq. (3.27), for the graph consisting of three edges connected in one vertex.

Generalizing the same steps as for the case of three edges, we consider an initial and final field configuration on the network and apply the variational principle to the total action functional $\mathcal{A}_{\mathcal{N}}$, ultimately setting its first variations to zero. Mathematically,

$$\delta\mathcal{A}_{\mathcal{N}}=\sum_{a=1}^{N}\delta\mathcal{A}_{e_a}+\delta\mathcal{J}\overset{!}{=}0\,. \tag{3.57}$$

The variations of $\mathcal{A}_{\mathcal{N}}$ with respect to the Lagrange multiplier fields lead to continuity conditions at each vertex for the fields on edges connected to it. In fact, for each vertex

v_b, we can write

$$\delta_\lambda \mathcal{J}\big|_{v_b} = \sum_{a=1}^{N_b}(1-\delta_{ab})\left(\lim_{\epsilon\to 0}\int_{H_{e_a}\setminus v_b(\tau)} \mathcal{X}^{a\to v_b}_{v_b-\epsilon}\delta\lambda^{ab}\phi_a\,\mathrm{dvol}_{h_{e_a}} - \int_{H_{e_b}}\mathcal{X}_{v_b}\delta\lambda^{ab}\phi_b\,\mathrm{dvol}_{h_{e_b}}\right)\,, \tag{3.58}$$

since the Lagrange fields are independent of the scalar fields ϕ_a, $\forall a$. This leads, for all vertices, to

$$\begin{aligned}&\delta_\lambda \mathcal{J} =\\ &= \sum_{b=1}^{V}\left[\sum_{a=1}^{N_b}(1-\delta_{ab})\left(\lim_{\epsilon\to 0}\int_{H_{e_a}\setminus v_b(\tau)} \mathcal{X}^{a\to v_b}_{v_b-\epsilon}\delta\lambda^{ab}\phi_a\,\mathrm{dvol}_{h_{e_a}} - \int_{H_{e_b}}\mathcal{X}_{v_b}\delta\lambda^{ab}\phi_b\,\mathrm{dvol}_{h_{e_b}}\right)\right] \overset{!}{=} 0\,.\end{aligned} \tag{3.59}$$

Note that for different values of a and b, the λ^{ab} are different Lagrange multiplier fields and are independent of each other. Furthermore, note also that each Lagrange field is evaluated at the corresponding vertex, and hence, even if labeled by the same pair a, b, Lagrange fields corresponding to different vertices are to be considered independent.

This implies that for the above equation to vanish integrals involving the same field λ^{ab} must independently sum to zero. In this way, for each vertex v_b of the network, we obtain $N_b - 1$ equations of the form:

$$\lim_{\epsilon\to 0}\int_{H_{e_a}\setminus v_b(\tau)} \mathcal{X}^{a\to v_b}_{v_b-\epsilon}\delta\lambda^{ab}\phi_a\,\mathrm{dvol}_{h_{e_a}} - \int_{H_{e_b}}\mathcal{X}_{v_b}\delta\lambda^{ab}\phi_b\,\mathrm{dvol}_{h_{e_b}} \overset{!}{=} 0\,. \tag{3.60}$$

Since the Lagrange field variations $\delta\lambda^{ab}$ are arbitrary, we can write for each vertex

$$\sum_{a=1}^{N_b}(1-\delta_{ab})\left[\lim_{\epsilon\to 0}\phi_a\Big|^{a\to v_b}_{v_b(T)-\epsilon} - \phi_b\Big|_{v_b(T)}\right] \overset{!}{=} 0\,, \tag{3.61}$$

which sets that at each vertex worldline, each field configuration ϕ_a equals the value of $\phi_b\big|_{v_b(T)}$, under the limit of an infinitesimal distance ϵ away from the vertex, from each edge e_a respectively. In other words, Eq. (3.61) establishes continuity for the total field configuration on the arbitrary network at each vertex for all times, and we can explicitly write

$$\lim_{\epsilon\to 0}\phi_1\Big|_{v_b(T)-\epsilon}^{1\to v_b} \overset{!}{=} \lim_{\epsilon\to 0}\phi_2\Big|_{v_b(T)-\epsilon}^{2\to v_b} \overset{!}{=} \ldots \overset{!}{=} \phi_b\Big|_{v_b(T)} \overset{!}{=} \ldots \overset{!}{=} \lim_{\epsilon\to 0}\phi_{N_b}\Big|_{v_b(T)-\epsilon}^{N_b\to v_b}, \tag{3.62}$$

at an arbitrary vertex v_b of the network. Recall that in our notation, by writing "$a \to v_b$" we mean that in the limit $\epsilon \to 0$, we approach the vertex v_b from the edge e_a.

Finally, as a general continuity condition for an arbitrary network $\mathcal{N}$ populated by scalar fields and consisting of N edges $\{e_a\}$ and V vertices $\{v_b\}$ with $a \in \{1, \ldots, N\}$ and $b \in \{1, \ldots, V\}$, we can write

$$\begin{cases} \phi_1\big|_{v_1(T)} \overset{!}{=} \lim\limits_{\epsilon\to 0}\phi_2\Big|_{v_1(T)-\epsilon}^{2\to v_1} \overset{!}{=} \lim\limits_{\epsilon\to 0}\phi_3\Big|_{v_1(T)-\epsilon}^{3\to v_1} \overset{!}{=} \ldots \overset{!}{=} \ldots \overset{!}{=} \lim\limits_{\epsilon\to 0}\phi_{N_1}\Big|_{v_1(T)-\epsilon}^{N_1\to v_1} \\ \phi_1\big|_{v_2(T)} \overset{!}{=} \lim\limits_{\epsilon\to 0}\phi_2\Big|_{v_2(T)-\epsilon}^{2\to v_2} \overset{!}{=} \lim\limits_{\epsilon\to 0}\phi_3\Big|_{v_2(T)-\epsilon}^{3\to v_2} \overset{!}{=} \ldots \overset{!}{=} \ldots \overset{!}{=} \lim\limits_{\epsilon\to 0}\phi_{N_2}\Big|_{v_2(T)-\epsilon}^{N_2\to v_2} \\ \quad\vdots \qquad\qquad \vdots \qquad\qquad\qquad \vdots \qquad\qquad\qquad\qquad \vdots \\ \quad\vdots \qquad\qquad \vdots \qquad\qquad\qquad \vdots \qquad\qquad\qquad\qquad \vdots \\ \phi_1\big|_{v_V(T)} \overset{!}{=} \lim\limits_{\epsilon\to 0}\phi_2\Big|_{v_V(T)-\epsilon}^{2\to v_V} \overset{!}{=} \lim\limits_{\epsilon\to 0}\phi_3\Big|_{v_V(T)-\epsilon}^{3\to v_V} \overset{!}{=} \ldots \overset{!}{=} \ldots \overset{!}{=} \lim\limits_{\epsilon\to 0}\phi_{N_V}\Big|_{v_V(T)-\epsilon}^{N_V\to v_V} \end{cases} \tag{3.63}$$

where each vertex v_b connects N_b edges. Specifically, in the above equations, we choose the edge e_b to always denote the edge e_1. By direct comparison with Eq. (3.33), we can observe that the above conditions simplify to the result for the minimal graph when $V = 4$ and $N = 3$. For an illustrative visualization of the above condition, we refer to the following Fig. 3.12.

The analysis of the first variations of the total action functional $\mathcal{A}_{\mathcal{N}}$ with respect to the real scalar fields populating the network follows directly the results for three edges connected together in a vertex studied in Sec. 3.2.2. In fact, consider again the condition imposed by the variational principle. If $\mathcal{E}_v$ is the subset of $\mathcal{E}$ consisting of edges that

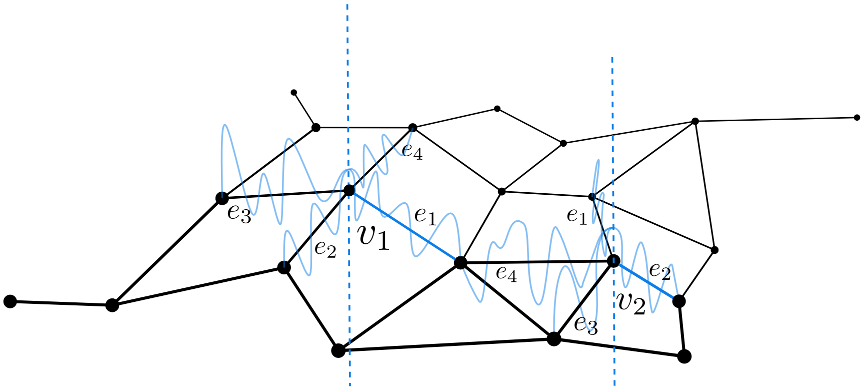

Figure 3.12: Visualization of the continuity conditions across the worldlines of two vertices for the total field configuration on an arbitrary network $\mathcal{N}$. The two edges e_1 and e_2, shown in blue, were specifically chosen to support the fields ϕ_1 and ϕ_2 defined to include the vertices v_1 and v_2 within their respective domains.

support fields containing two vertices of the network within their domains, we can write

$$
\begin{aligned}
\delta\mathcal{A}_{\mathcal{N}} &= \sum_{a=1}^{N}\delta\mathcal{A}_{e_a} + \delta_\phi\mathcal{J} = \\
&= \sum_{e_a\in\mathcal{E}\setminus\mathcal{E}_v}\Bigg[\int_{H_{e_a}\setminus v(T)}\left(\frac{\partial\mathcal{L}_{e_a}}{\partial\phi_a}\sqrt{-h_{e_a}} - \partial_\nu\left(\sqrt{-h_{e_a}}\frac{\partial\mathcal{L}_{e_a}}{\partial\partial_\nu\phi_a}\right)\right)\delta\phi_a dT d\xi_a + \\
&\qquad\qquad + \int_{\partial H_{e_a}}\frac{\partial\mathcal{L}_{e_a}}{\partial\partial_\nu\phi_a}\delta\phi_a\, n^a_\nu\sqrt{-h^\partial_{e_a}}dq\Bigg] + \\
&+ \sum_{e_a\in\mathcal{E}_v}\Bigg[\int_{H_{e_a}}\left(\frac{\partial\mathcal{L}_{e_a}}{\partial\phi_a}\sqrt{-h_{e_a}} - \partial_\nu\left(\sqrt{-h_{e_a}}\frac{\partial\mathcal{L}_{e_a}}{\partial\partial_\nu\phi_a}\right)\right)\delta\phi_a dT d\xi_a + \\
&\qquad\qquad + \int_{\partial H_{e_a}}\frac{\partial\mathcal{L}_{e_a}}{\partial\partial_\nu\phi_a}\delta\phi_a\, n^a_\nu\sqrt{-h^\partial_{e_a}}dq\Bigg] + \\
&+ \sum_{b=1}^{V}\left[\sum_{a=1}^{N_b}(1-\delta_{ab})\left(\lim_{\epsilon\to 0}\int_{H_{e_a}\setminus v_b(\tau)}\mathcal{X}^{a\to v_b}_{v_b-\epsilon}\lambda^{ab}\delta\phi_a\,\mathrm{dvol}_{h_{e_a}} - \int_{H_{e_b}}\mathcal{X}_{v_b}\lambda^{ab}\delta\phi_b\,\mathrm{dvol}_{h_{e_b}}\right)\right] = \\
&\overset{!}{=} 0\,,
\end{aligned}
\tag{3.64}
$$

where $\delta_\phi\mathcal{J}$ denotes the variations of $\mathcal{J}$ induced by variations in the fields and $v(T)$ generally denotes the vertices to which each edge is connected for any time. Recall that each integral of the form $\int_{\partial H_{e_a}}\frac{\partial\mathcal{L}_{e_a}}{\partial\partial_\nu\phi_a}\delta\phi_a\, n^a_\nu\sqrt{-h^\partial_{e_a}}dq$ is performed on the entire boundary ∂H_{e_a} of the edge history: temporal and spatial boundaries. For these integrals, for the sake of generality and clarity in the notation, we do not differentiate whether the spatial boundaries of the edge history are included in the domain of ϕ_a. By referring to Eq. (3.64) and extending the steps outlined in Sec. 3.2.2, we can directly derive the following results:

- **Equations of motion on $\mathcal{N}$:** On each edge history H_{e_a} of the network, following the same arguments as in Sec. 3.2.2, we find that, in the bulk of the history, Eq. (3.64) leads to

$$\int_{H_{e_a}\setminus v(T)} \left(\frac{\partial \mathcal{L}_{e_a}}{\partial \phi_a} \sqrt{-h_{e_a}} - \partial_\nu \left(\sqrt{-h_{e_a}} \frac{\partial \mathcal{L}_{e_a}}{\partial \partial_\nu \phi_a} \right) \right) \delta\phi_a \, dT d\xi_a \overset{!}{=} 0$$

$$\int_{H_{e_b}} \left(\frac{\partial \mathcal{L}_{e_b}}{\partial \phi_b} \sqrt{-h_{e_b}} - \partial_\nu \left(\sqrt{-h_{e_b}} \frac{\partial \mathcal{L}_{e_b}}{\partial \partial_\nu \phi_b} \right) \right) \delta\phi_b \, dT d\xi_b \overset{!}{=} 0 \,, \tag{3.65}$$

  where $H_{e_a} \setminus v(T)$ refers generally to the edge history H_{e_a} excluding, at any time, one or both vertices to which e_a is connected. Since the field variations $\delta\phi_a$ are arbitrary on the bulk of the edge history, we can rewrite the above equations as

$$\frac{\partial \mathcal{L}_{e_a}}{\partial \phi_a} - \frac{1}{\sqrt{-h_{e_a}}} \partial_\nu \left(\sqrt{-h_{e_a}} \frac{\partial \mathcal{L}_{e_a}}{\partial \partial_\nu \phi_a} \right) \overset{!}{=} 0 \,, \tag{3.66}$$

  for all edges e_a of the network. These are the well-known Euler-Lagrange equations for the fields populating the edges and determine their equations of motion. Note that the integrals of Eq. (3.65) must also be performed at the temporal and spatial boundaries of each history H_{e_a}, in particular at the vertex wordline or along curves that are at a distance ϵ from it. However, we can once again set $\frac{\partial \mathcal{L}_{e_a}}{\partial \phi_a} \sqrt{-h_{e_a}} - \partial_\nu \left(\sqrt{-h_{e_a}} \frac{\partial \mathcal{L}_{e_a}}{\partial \partial_\nu \phi_a} \right)$ to vanish there as well, by continuity. On temporal boundaries, all integrals vanish. For a free real massive scalar field with $\mathcal{L}_{e_a} = \frac{1}{2} \left(h^{cd}_{e_a} \partial_c \phi_a \, \partial_d \phi_a - \mu^2 \phi_a^2 \right)$, we find, on each edge of the network,

$$\left(\Box_{h_{e_a}} + \mu^2 \right) \phi_a = 0 \,. \tag{3.67}$$

- **Boundary conditions at free endpoints of $\mathcal{N}$:** At the free endpoints $\partial H_{\mathcal{N}}|_{\partial e} = \cup_s \partial H_{e_s}|_{\partial e}$ of the network, if any, we obtain in agreement with the discussion of Sec. 3.2.2,

$$\int_{\partial H_{e_s}|_{\partial e}} \frac{\partial \mathcal{L}_{e_s}}{\partial \partial_a \phi_s} n^s_{\sigma\, a} \sqrt{-h^\partial_{e_s}} \delta\phi_s \, dT \overset{!}{=} 0 \,, \qquad \forall \, e_s \in \mathcal{N} \tag{3.68}$$

  according to Eq. (3.40). Recall that in our notation, by e_s we refer to an edge containing a free endpoint and ∂e denotes the free endpoint itself. Depending on whether the field variations $\delta\phi_s$ for each e_s are arbitrary or vanishing at ∂e for any time T, we obtain Neumann or Dirichlet boundary conditions respectively. In fact, if the field variations are vanishing, the field is constant at the free endpoint worldlines and Dirichlet boundary conditions are imposed; if the variations are arbitrary and independent of each other we obtain, at the free endpoints

$$\frac{\partial \mathcal{L}_{e_s}}{\partial \partial_a \phi_s} n^{s}_{\sigma\, a} \sqrt{-h^{\partial}_{e_s}} \overset{!}{=} 0 \qquad \forall\, e_s \in \mathcal{N}\,, \tag{3.69}$$

for all time T. If we consider free real massive scalar fields on each edge e_s, we can write $\mathcal{L}_{e_s} = \frac{1}{2}\left(h^{ab}_{e_s} \partial_a \phi_s \, \partial_b \phi_s - \mu^2 \phi_s^2\right)$. The above conditions then reduce to

$$h^{ab}_{e_s} \partial_a \phi_s \, n^{s}_{\sigma\, b} \sqrt{-h^{\partial}_{e_s}} \overset{!}{=} 0 \qquad \forall\, e_s \in \mathcal{N}\,, \tag{3.70}$$

which once again, are a generalized version of the Neumann conditions to arbitrary embedding spacetimes. If the arbitrary network contains any free endpoints, the above conditions – whether Dirichlet or generalized Neumann – ensure that there is no leakage of degrees of freedom out of the network and fields populating $\mathcal{N}$ are entirely confined within it, without diffusing into the surrounding ambient space.

- **Junction conditions at the nodes of $\mathcal{N}$:** Finally, we are left with the junction conditions at the nodes of the network. Indeed, applying the same reasoning as in Sec. 3.2.2, for Eq. (3.64) to be satisfied, the following condition must hold independently at each node v_b of the network:

$$\begin{aligned} &\sum_{a=1}^{N_b - 1} \left(\lim_{\epsilon \to 0} \int_{v_b(T)-\epsilon} \frac{\partial \mathcal{L}_{e_a}}{\partial \partial_\nu \phi_a} n^{a}_{\sigma\, \nu} \sqrt{-h^{\partial}_{e_a}} \delta\phi_a \, dT \right) + \int_{v_b(T)} \frac{\partial \mathcal{L}_{e_b}}{\partial \partial_\nu \phi_b} n^{b}_{\sigma\, \nu} \sqrt{-h^{\partial}_{e_b}} \delta\phi_b \, dT + \\ &+ \sum_{a=1}^{N_b} (1 - \delta_{ab}) \left(\lim_{\epsilon \to 0} \int_{H_{e_a} \setminus v_b(\tau)} \mathcal{X}^{a \to v_b}_{v_b - \epsilon} \lambda^{ab} \delta\phi_a \, \mathrm{dvol}_{h_{e_a}} - \int_{H_{e_b}} \mathcal{X}_{v_b} \lambda^{ab} \delta\phi_b \, \mathrm{dvol}_{h_{e_b}} \right) = \\ &\overset{!}{=} 0\,. \end{aligned} \tag{3.71}$$

This implies, by considering each field ϕ_a separately, that

$$\lim_{\epsilon \to 0} \int_{v_b(T)-\epsilon} \frac{\partial \mathcal{L}_{e_a}}{\partial \partial_\nu \phi_a} n^{a}_{\sigma\, \nu} \sqrt{-h^{\partial}_{e_a}} \delta\phi_a \, dT \overset{!}{=} - \lim_{\epsilon \to 0} \int_{H_{e_a} \setminus v_b(\tau)} \mathcal{X}^{a \to v_b}_{v_b - \epsilon} \lambda^{ab} \delta\phi_a \, \mathrm{dvol}_{h_{e_a}}\,, \tag{3.72}$$

and for the field ϕ_b containing the vertex worldline $v_b(T)$ in its domain,

$$\int_{v_b(T)} \frac{\partial \mathcal{L}_{e_b}}{\partial \partial_\nu \phi_b} n^b_{\sigma\,\nu} \sqrt{-h^\partial_{e_b}} \delta\phi_b \, dT \overset{!}{=} \sum_{a=1}^{N_b} (1-\delta_{ab}) \int_{H_{e_b}} \mathcal{X}_{v_b} \lambda^{ab} \delta\phi_b \, \mathrm{dvol}_{h_{e_b}} \,. \tag{3.73}$$

If we consider the field variations $\delta\phi_a$ and $\delta\phi_b$ to be vanishing at the vertex worldline $v_b(T)$ or at a distance ϵ to it, then the field is constant and we are imposing Dirichlet boundary conditions. As a consequence, if this assumption holds for all vertices, the degrees of freedom cannot propagate across the nodes and the network acts effectively as the collection of N edges considered in Fig. 3.3. However, if for each vertex v_b of the network, we assume the field variations to be arbitrary and independent of each other, we find

$$\lim_{\epsilon\to 0} \frac{\partial \mathcal{L}_{e_a}}{\partial \partial_\nu \phi_a} n^a_{\sigma\,\nu} \sqrt{-h^\partial_{e_a}} \Bigg|_{v_b(T)-\epsilon}^{a\to v_b} \overset{!}{=} -\lim_{\epsilon\to 0} \lambda^{ab} \Bigg|_{v_b(T)-\epsilon}^{a\to v_b} \,, \tag{3.74}$$

for all the fields ϕ_a incident to v_b, for all times T, and

$$\frac{\partial \mathcal{L}_{e_b}}{\partial \partial_\nu \phi_b} n^b_{\sigma\,\nu} \sqrt{-h^\partial_{e_b}} \Bigg|_{v_b(T)} \overset{!}{=} \sum_{a=1}^{N_b} (1-\delta_{ab})\, \lambda^{ab} \Bigg|_{v_b(T)} \,, \tag{3.75}$$

for the only field ϕ_b with the vertex worldline $v_b(T)$ in its domain, for all times T. Recall that in our notation "$a \to v_b$" indicates that in the limit procedure we are approaching the vertex v_b from the edge e_a. Furthermore, note that for free endpoints $N_b = 1$, $e_s = e_b$ and we reduce to the condition of Eq. (3.69). By continuity of the Lagrange multiplier fields across the vertex, i.e.

$$\lim_{\epsilon\to 0} \lambda^{ab} \Bigg|_{v_b(T)-\epsilon}^{a\to v_b} = \lambda^{ab} \Bigg|_{v_b(T)} \,, \tag{3.76}$$

for all a, we can couple the two equations Eq. (3.74) and Eq. (3.75). In fact, Eq. (3.74) can be further expressed as

$$\lim_{\epsilon\to 0} \frac{\partial \mathcal{L}_{e_a}}{\partial \partial_\nu \phi_a} n^a_{\sigma\,\nu} \sqrt{-h^\partial_{e_a}} \Bigg|_{v_b(T)-\epsilon}^{a\to v_b} \overset{!}{=} -\lim_{\epsilon\to 0} \lambda^{ab} \Bigg|_{v_b(T)-\epsilon}^{a\to v_b} = -\lambda^{ab} \Bigg|_{v_b(T)} \,, \tag{3.77}$$

and thus, we can finally write

$$\frac{\partial \mathcal{L}_{e_b}}{\partial \partial_\nu \phi_b} n^b_{\sigma\,\nu} \sqrt{-h^\partial_{e_b}}\,\Big|_{v_b(T)} + \sum_{a=1}^{N_b} (1-\delta_{ab}) \lim_{\epsilon\to 0} \frac{\partial \mathcal{L}_{e_a}}{\partial \partial_\nu \phi_a} n^a_{\sigma\,\nu} \sqrt{-h^\partial_{e_a}}\,\Big|^{a\to v_b}_{v_b(T)-\epsilon} \overset{!}{=} 0\,, \tag{3.78}$$

at each vertex v_b of the network $\mathcal{N}$. Note that this condition is the generalization of Eq. (3.47) to an arbitrary network, originally derived for a graph consisting of three edges connected to a single vertex. Indeed, if we set $V = 4$ and $N = 3$, Eq. (3.78) naturally reduces to Eq. (3.47). At each node of the network, the above Eq. (3.78), together with the continuity condition Eq. (3.62), establishes a generalized version of the Kirchhoff-Neumann conditions to curved spacetimes, for an arbitrary number of edges N_b incident at the vertex. More concisely, the generalized Kirchhoff-Neumann conditions can be rewritten in the following form:

$$\begin{cases} \lim\limits_{\epsilon\to 0} \phi_1 \Big|^{1\to v_b}_{v_b(T)-\epsilon} \overset{!}{=} \lim\limits_{\epsilon\to 0} \phi_2 \Big|^{2\to v_b}_{v_b(T)-\epsilon} \overset{!}{=} \ldots \overset{!}{=} \phi_b \Big|_{v_b(T)} \overset{!}{=} \ldots \overset{!}{=} \lim\limits_{\epsilon\to 0} \phi_{N_b} \Big|^{N_b\to v_b}_{v_b(T)-\epsilon}\,, \\ \frac{\partial \mathcal{L}_{e_b}}{\partial \partial_\nu \phi_b} n^b_{\sigma\,\nu} \sqrt{-h^\partial_{e_b}}\,\Big|_{v_b(T)} + \sum\limits_{a=1}^{N_b} (1-\delta_{ab}) \lim\limits_{\epsilon\to 0} \frac{\partial \mathcal{L}_{e_a}}{\partial \partial_\nu \phi_a} n^a_{\sigma\,\nu} \sqrt{-h^\partial_{e_a}}\,\Big|^{a\to v_b}_{v_b(T)-\epsilon} \overset{!}{=} 0\,. \end{cases} \tag{3.79}$$

For real scalar fields, the Kirchhoff-Neumann conditions read

$$\begin{cases} \lim\limits_{\epsilon\to 0} \phi_1 \Big|^{1\to v_b}_{v_b(T)-\epsilon} \overset{!}{=} \lim\limits_{\epsilon\to 0} \phi_2 \Big|^{2\to v_b}_{v_b(T)-\epsilon} \overset{!}{=} \ldots \overset{!}{=} \phi_b \Big|_{v_b(T)} \overset{!}{=} \ldots \overset{!}{=} \lim\limits_{\epsilon\to 0} \phi_{N_b} \Big|^{N_b\to v_b}_{v_b(T)-\epsilon}\,, \\ h^{\mu\nu}_{e_b} \partial_\mu \phi_b\, n^b_{\sigma\,\nu} \sqrt{-h^\partial_{e_b}}\,\Big|_{v_b(T)} + \lim\limits_{\epsilon\to 0} \sum\limits_{a=1}^{N_b} (1-\delta_{ab})\, h^{\mu\nu}_{e_a} \partial_\mu \phi_a\, n^a_{\sigma\,\nu} \sqrt{-h^\partial_{e_a}}\,\Big|^{a\to v_b}_{v_b(T)-\epsilon} \overset{!}{=} 0\,, \end{cases} \tag{3.80}$$

in analogy with Eq. (3.48). As in Sec. 3.2.2, if we denote $\phi_a|_{v_b(T)} := \lim_{\epsilon\to 0} \phi_a \,|^{a\to v_b}_{v_b(T)-\epsilon}$ and $h^{\mu\nu}_{e_a} \partial_\mu \phi_a\, n^a_{\sigma\,\nu} \sqrt{-h^\partial_{e_a}}\,|_{v_b(T)} := \lim_{\epsilon\to 0} h^{\mu\nu}_{e_a} \partial_\mu \phi_a\, n^a_{\sigma\,\nu} \sqrt{-h^\partial_{e_a}}\,|^{a\to v_b}_{v_b(T)-\epsilon}$, we can rewrite the above conditions as

$$\begin{cases} \phi_1 \Big|_{v_b(T)} \overset{!}{=} \phi_2 \Big|_{v_b(T)} \overset{!}{=} \ldots \overset{!}{=} \phi_b \Big|_{v_b(T)} \overset{!}{=} \ldots \overset{!}{=} \phi_{N_b} \Big|_{v_b(T)}\,, \\ \sum\limits_{a=1}^{N_b} \sqrt{-h^\partial_{e_a}}\, h^{\mu\nu}_{e_a}\, n^a_{\sigma\,\nu}\, \partial_\mu \phi_a \Bigg|_{v_b(T)} \overset{!}{=} 0\,. \end{cases} \tag{3.81}$$

Note that if the arbitrary network $\mathcal{N}$ is embedded in the Minkowski spacetime, the normal vector field n^a_σ has a vanishing temporal component and the above conditions reduce to the common Kirchhoff-Neumann conditions for N_b edges connected to a vertex v_b. Therefore, by enforcing continuity at each vertex for the total field configuration populating the network and applying the variational principle to its action functional, we naturally obtain junction conditions at each node when allowing the field variations to be arbitrary and independent. From the field theory perspective, these conditions differentiate a collection of N edges (Fig. 3.3) to a fully connected network where fields and degrees of freedom can propagate and are partially transmitted at every node. Analogously to the previous section, if the above conditions ensure a self-adjont Laplace operator at the node worldline, then the scattering matrix associated with the vertex is unitary. According to the cluster decomposition principle, the scattering matrix for the entire network can be factorized into the scattering matrices of individual nodes. As a consequence, if the S-matrix of each node is unitary, then the total scattering matrix is also unitary.

In conclusion, in this first chapter, we introduced and defined the concept of a network $\mathcal{N} = (\mathcal{V}, \mathcal{E}, \iota)$ embedded in an arbitrary, possibly curved, spacetime, and we introduced a field theory confined to it. By variational principles, we established a prescription to prevent the degrees of freedom from leaking into the surrounding space and set the conditions that control, at each node, the propagation of fields throughout the network. If these junction conditions ensure a self-adjoint Laplace operator at each node, the fields on the histories can be quantized. This enables the introduction of quantum field and conjugate momentum operators, paving the way for the development of a quantum field theory on networks histories.

With these theoretical tools in hand, we are now equipped to conduct (quantum) field theory experiments, enabling us to explore the structure of curved spacetimes and address unresolved questions in nature where a simple $(1+3)$-dimensional field description falls short.

Chapter 4

Emerging Entanglement on Network Histories

In this chapter we are interested in a first application of networks as devices to investigate natural phenomena. In particular, we need a first analysis to verify our model and its background idea: *Can a network and its history, built upon a collection of* $(1+1)$*-dimensional field theories, really tell something about* $(1+3)$*-dimensional phenomena?* Although initial, simpler answers could be obtained by analyzing phenomena involving classical fields on networks, in this section, we aim to focus on quantum phenomena, which will ultimately play a fundamental role in our exploration of quantum field theory (QFT) in curved backgrounds. Indeed, phenomena such as entanglement and information processing at causal boundaries or trapping surfaces are crucial in deepening our understanding of gravity, the fundamental nature of spacetime, and its interaction with the most advanced quantum theories. If we were able to describe entanglement with networks histories, we would prove that networks can serve to investigate $(1+3)$-dimensional phenomena and, at the same time, develop diagnostic devices to tackle the most recent and unsolved questions on the quantum nature of black holes.

The initial pieces of the black hole information puzzle can be traced back to initial observations that black holes exhibit a tendency to increase their horizon surface area during any transformation [22,23]. More generally, it was proven that the black-hole surface area cannot decrease in any classical process, a principle later formalized as Hawking's area theorem [24]. It was precisely this crucial insight that, in the early 1970s, led physicist Jacob Bekenstein to draw parallels with the second law of thermodynamics, which states that changes in a closed thermodynamic system occur in the direction of increasing entropy.

Bekenstein's intuition suggested that the area of the event horizon could be related to the entropy of the black hole. By proposing the concept of entropy for a black hole as a measure of the information about its interior that is inaccessible to an exterior observer [6], Bekenstein suggested that it should be a monotonically increasing function of the horizon's area. Only a few years later, within the framework of quantum field theory, Stephen Hawking's derivation of black hole radiation [25] confirmed Bekenstein's conjecture by demonstrating that black hole horizons possess a temperature inversely proportional to the black hole's mass, thereby establishing the thermodynamic nature of black holes. The so-called Bekenstein-Hawking entropy for black holes, not only was an increasing function of the area A, as Bekenstein had proposed, but was found to be directly proportional to it, $S_{BH} \sim A$.

One question that naturally arises is the real nature of black hole entropy and why it is proportional to the horizon's area. Providing a full explanation for this proportionality remains one of the profound open questions in the intersection of quantum mechanics, thermodynamics, and gravity. Since Bekenstein's groundbreaking suggestion, various attempts have been made to explain what is the meaning of a black hole entropy and why its proportionality to the horizon area [7,8], with approaches ranging from Euclidean quantum gravity to string theory. Among these, the explanations that most naturally account for why the entropy of black holes is proportional to the area are those that understand the entropy in terms of quantum field correlations between the exterior and interior of the black hole. Notably, the seminal work by Sorkin *et al.* [9] was the first to demonstrate a direct proportionality between the *entanglement entropy* of quantum field theoretic degrees of freedom outside the black hole and its horizon area. Independently, a few years later, Srednicki [10] arrived at the same result using different arguments. This suggests that black hole entropy is fundamentally quantum in nature, arising specifically from quantum correlations across the horizon.

In light of our two-fold objective – demonstrating the potential of the network histories method and simultaneously paving the way for its application to curved spacetimes – we require an initial pilot phenomenon. This phenomenon must serve as a thorough test, fully studied within $(1+3)$ dimensions, while also being crucial for exploring the quantum nature of black holes. By looking closer into approaches like [9,10] we can notice that they typically model black holes as flat $(1+3)$-dimensional spacetime regions, intersected by an artificial surface whose interior is rendered inaccessible to simulate a causal boundary. In fact, performing a direct computation in an actual black hole spacetime would require knowledge of the exact $(1 + 3)$-dimensional propagator for the black hole background – a quantity that remains unknown to this day. As a matter of fact, fully established calculations of entanglement entropy for fields in a curved black hole spacetime are still lacking. Although it does not yet provide a fully comprehensive solution to the black hole entropy puzzle [7], this phenomenon has already been comprehensively analyzed since the works of Sorkin and Srednicki. This would make it an excellent test and reference point for our pioneering approach. At the same time, it lays the foundation for a full black hole analysis by substituting the artificial sphere's surface with a real horizon. It therefore seems natural for us to choose as our pilot phenomenon the proportionality between the entanglement entropy of vacuum fluctuations of a quantum field in Minkowski spacetime and the area of an artificial sphere made inaccessible to an external observer, as illustratively analyzed by Srednicki [10].

Notably, this test phenomenon is particularly well-suited to the network approach, as it naturally links entropy with a geometric quantity – the area of the inaccessible region – allowing us to explore the implications of dimensionality. In fact, unlike fields that extend across the full spacetime, those confined to network histories are restricted to a two-dimensional framework, where the conventional concept of area does not apply in the usual sense. If quantum fields on network histories, as an alternative to fields in the full $(1+3)$-dimensional spacetime, can capture entanglement properties supported in the embedding geometry by exhibiting an *area*-dependent entropy, we would demonstrate that the quantum information properties observed in full spacetime are emergent phenomena of the fields confined to the lower-dimensional network histories and that (quantum) fields on network histories, referred to as *quantum networks*, are a robust new tool for probing higher-dimensional spacetimes and the phenomena within them.

In the following sections, we will therefore delve into the study of entanglement entropy related to quantum fields in Minkowski spacetime, employing networks to capture the phenomenon found by Sorkin and Srednicki. If we successfully describe the area proportionality as emerging on these lower-dimensional devices, we will pave the way towards addressing the more challenging phenomenon of entanglement entropy for quantum fields across a black hole's horizon using quantum networks, providing the long-awaited alternative for directly computing the entanglement entropy in a full black hole scenario and thereby gaining new insights that will contribute to our understanding of the nature of black hole entropy.

4.1 Entropy of Entanglement

One of the most natural measurements of loss of information about a quantum system is the entropy of entanglement, or *entanglement entropy.* In particular, in a bipartite or multipartite system, the entanglement entropy quantifies the extent to which one or more subsystems are entangled with others from which information has been lost. Therefore, the entanglement entropy is always associated with a system in which one or more subsystems have been traced out, preventing the observer from obtaining any information about them. For example, if we consider a quantum field ϕ in a spacetime (M, g) Fig. 4.1, in a given specific state $|\Psi\rangle$, we can choose a region, e.g. a sphere, inaccessible to an external observer, splitting the system into an interior and an exterior sector. If ρ_E is the density matrix reduced to the exterior E of the sphere, $\rho_E = \mathrm{Tr}_I \, |\Psi\rangle \, \langle\Psi|$, then the entanglement entropy

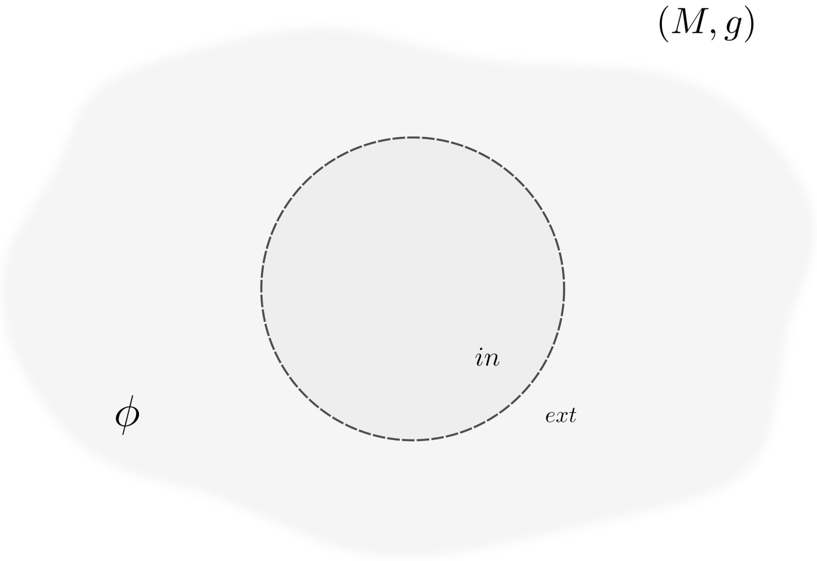

Figure 4.1: Spatial two-dimensional visualization of a quantum field ϕ supported on a spacetime (M, g), in a specific state $|\Psi\rangle$. An arbitrary sphere (represented as a disk in this 2D depiction) divides the setup into an interior and an exterior sector. If the interior of the sphere is inaccessible, an external observer loses information about the internal quantum field degrees of freedom. Due to quantum field correlations across the sphere's surface, the exterior and interior sectors may be entangled, with the entanglement entropy quantifying the degree of entanglement. For this reason, we refer to the sphere as the *entangling* sphere.

is formally expressed as the Von Neumann entropy of ρ_E [26],

$$S_E = -\mathrm{Tr}\left(\rho_E \ln \rho_E\right) . \tag{4.1}$$

Depending on its value, S_E measures the possible entanglement between the two sectors, arising from quantum field correlations across the sphere's surface. Since the surface defines the two sectors that may be entangled with each other, it is referred to as the *entangling surface*, e.g. entangling sphere.

It is natural to draw an analogy between the entangling surface and regions of spacetime to which an observer has no access, such as causal boundaries or, less irrevocably, trapping surfaces. In fact, black hole horizons prevent an observer from obtaining any information about what lies within their radius. Fields and particles on opposite sides of the horizon may be entangled, and the entanglement entropy provides a useful measure of the amount of information about the total system that is lost to an observer outside the black hole. The entanglement entropy seems to provide a natural measure for the black hole entropy, as resulting from quantum field correlations across the horizon.

However, it is a well-known fact that the entanglement entropy Eq. (4.1) for the ground state of a quantum field in adjoining spacetime regions is divergent, due to the high-energy vacuum fluctuations of the field [26, 27] (and references therein). To overcome this issue, physicists and mathematicians have introduced and developed different strategies to deal with this divergence. One of the most natural strategy is to introduce a UV regulator in the theory, which can be a lattice, like in [10], or regulators of different types [26]. However, the entanglement entropy will depend on the choice of the regulator and each different regulator introduced defines a different quantity, such that comparing different calculations might be difficult. Within the various approaches, another strategy is to introduce the concept of relative entropies [28] or mutual information [29, 30], such that the divergences are subtracted resulting in a finite quantity.

Among all the available strategies, we choose to tackle the ultraviolet divergence by introducing a UV cutoff, thereby considering a regularized version of the entanglement entropy. In fact, by performing any physical measurement it is inevitable to introduce a spatial resolution limit of the hardware infrastructure, or for example, a finite physical thickness of the entangling surface. Accordingly, by choosing a finite resolution structure, we impose a minimal separation for the entangling quantum fluctuations, effectively introducing a short-distance cutoff. If the separation of the quantum field correlations across the horizon or the entangling surface is not infinitesimal, but finite, an upper bound for the entanglement entropy is introduced and S_E in Eq. (4.1) is a finite, regularized quantity.

Note that the entanglement entropy, as introduced above, is a quantity designed as an instantaneous measure of entanglement, quantifying the degree of entanglement between subsystems at a specific moment in time for a given quantum state. On its own, entanglement entropy does not capture the evolution of entanglement over time unless time-dependence is explicitly introduced. While such time-dependence can arise naturally in curved spacetimes or be artificially implemented in Minkowski space, in the following sections, we focus on a scenario where the entangling sphere remains stationary. Since the ground state of a free quantum field in Minkowski spacetime is time-independent, we can focus on computing the entanglement entropy at a single, fixed point in time. In the context of our network histories model, this implies that, for this first analysis in Minkowski, we are interested in only one specific spacelike hypersurface of the network's history, partially tracing out the network lying on it.

Therefore, to investigate the proportionality between the entropy and the area with quantum fields confined to network histories, consider an arbitrary, globally hyperbolic spacetime (M, g), which, in this initial investigation, will be the $(1+3)$-dimensional Minkowski spacetime (M, η). Furthermore, consider an arbitrary network $\mathcal{N}$ as defined in the previous chapter, embedded therein. On its history $H_{\mathcal{N}}$, let us focus on a specific moment in time τ, and consider the network on the corresponding hypersurface Σ_τ. For the purpose of studying the $(1+3)$-dimensional phenomenon of entanglement entropy for quantum fields, we construct the network to extend across all three spatial dimensions.

To study entanglement entropy with such a configuration, let us consider again the setup of Fig. 4.1, where instead of a quantum field supported in the full spacetime, we confine it spatially to the embedded network, as depicted in Fig. 4.2. The entangling sphere defines a region of the spacetime inaccessible to an external observer, such that, considering the density matrix $\rho_E^{\mathcal{N}}$ reduced to the network in the exterior E of the sphere, we can measure the degree of entanglement through $S_E^{\mathcal{N}} = -\mathrm{Tr}\left(\rho_E^{\mathcal{N}} \ln \rho_E^{\mathcal{N}}\right)$. Due to the finite resolution structure typical of all experiments, by introducing a short-distance cutoff a as a regulator, we obtain a finite, regularized value for $S_E^{\mathcal{N}}$. The presence of a short-distance cutoff implies that on each edge of the network, the spatial coordinate is discretized. As we will see in details, for the field theory on the network, this means that at each hypersurface Σ_τ, the field on each edge is discretized on a one-dimensional lattice with spacing a.

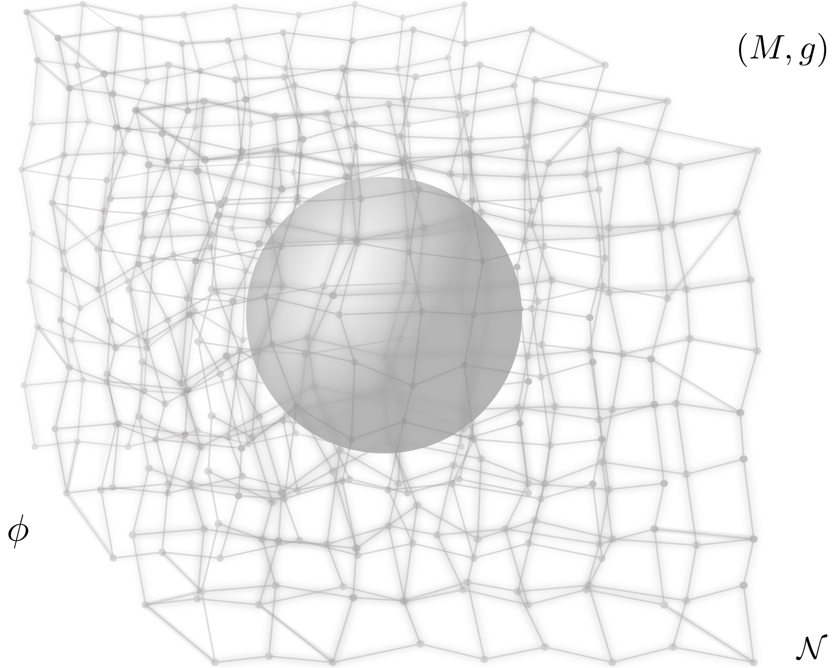

Figure 4.2: Three-dimensional visualization of a quantum field ϕ (depicted in gray shades along the edges) spatially confined to an arbitrary network $\mathcal{N}$ embedded in a spacetime (M, g). The gray fuzzy shading representing the field extends beyond the edges, depicting the experimental limitations in achieving full confinement (Sec. 2.2). An arbitrary sphere divides the network setup into an interior and an exterior sector. If the interior of the sphere is inaccessible, an external observer loses information about the internal quantum field degrees of freedom. Due to quantum field correlations across the sphere's surface, the exterior and interior sectors of the network may be entangled, with the entanglement entropy quantifying the degree of entanglement.

If the regularized entanglement entropy $S_E^{\mathcal{N}}$ shows a proportionality to the sphere's surface area, we demonstrate quantum networks to be able to probe physical phenomena supported in the embedding spacetime, by solely employing fields confined to the networks and their histories. By achieving this goal, we will be ready to implement the configuration depicted in Fig. 4.2 to investigate black hole scenarios. In fact, by placing the network partially across the horizon we can probe its processing of information as an emerging phenomenon on the network.

4.2 Entanglement Entropy on Subgraph Histories in Minkowski

In this initial part of our analysis, we restrict our investigation to Minkowski spacetime (M, η), in order to test our model against established results for quantum fields in flat $(1 + 3)$-dimensional spacetimes, e.g. [9, 10]. To investigate the entanglement entropy for the quantum network configuration of Fig. 4.2, it is instructive to first analyze how entanglement arises on elementary subgraphs of the network partially traced out by the entangling sphere. In fact, as shown in the picture and more clearly in its two-dimensional spatial section in Fig. 4.3, the entangling sphere is pierced and intersected by single edges, which are then connected to other edges to form more complex subgraphs of the network.

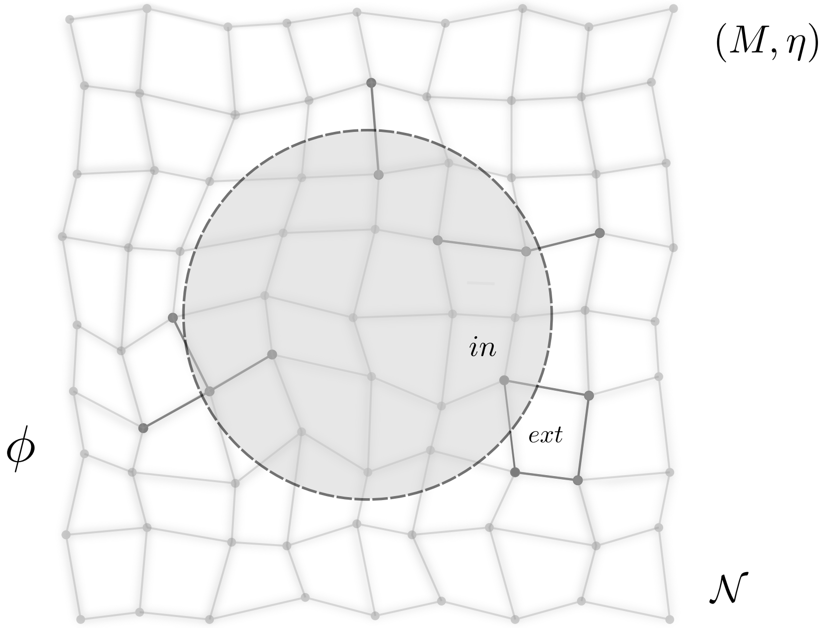

Figure 4.3: Spatial two-dimensional section of Fig. 4.2 for a quantum field ϕ (depicted in gray shades) spatially confined to the arbitrary three-dimensional network $\mathcal{N}$ embedded in Minkowski spacetime (M, η). An entangling sphere (disk in the 2D visualization) divides the network setup into an interior and an exterior sector. Due to quantum field correlations across the sphere's surface (dashed circumference in the 2D section), the exterior and interior sectors of the network may be entangled, with the entanglement entropy quantifying the degree of entanglement. Note that the entangling sphere is pierced by single edges. Highlighted are examples of subgraphs to which these edges belong.

As a result, if we aim to study the entanglement entropy for a quantum field on the entire network, we must first understand, at a local level, quantum field correlations across the entangling sphere along partially traced-out single edges. By gradually expanding the scale of locality, we consider increasingly complex subgraphs until, at a macroscopic level, we can analyze the entanglement of the quantum field across the entire network.

As shown in Fig. 4.3, when we consider the most elementary subgraphs that include a partially traced-out single edge, we once again encounter, in increasing order of complexity, the subgraphs discussed in previous chapters: the single edge itself, two edges connected at a node ($\mathcal{G}_2$), a loop, and a star graph formed by three edges ($\mathcal{G}_3$). Accordingly, in the following sections we will investigate the entanglement entropy for quantum fields spatially confined to all these subgraphs, in order of increasing complexity. Since in Sec. 3.2.3 we noticed that an arbitrary network can be constructed by connecting multiple star graphs, understanding the entanglement entropy for quantum fields spatially confined to star graphs will ultimately allow us to compute the entanglement entropy for quantum fields spatially confined to the entire arbitrary network $\mathcal{N}$.

To start, we consider the simplest possible subgraph: a single edge that pierces the entangling sphere.

4.2.1 Entanglement Entropy on Single-Edge Graphs

Among all the single edges piercing the entangling sphere, consider, without loss of generality, the one highlighted in Fig. 4.4. Even though the edge is actually connected to other elements of the network, in this initial analysis we instructively treat the edge as completely disconnected from the rest. Once we understand how a node connecting two or more edges influences the quantum field correlations across the entangling sphere, and consequently the entanglement entropy, we will be able to study the entanglement entropy for a quantum field spatially supported on the edge, considering all the real connections the edge has in the network.

In Sec. 3.2.1, we learned that when a graph consisting of two single edges connected by a node ($\mathcal{G}_2$) is embedded in Minkowski spacetime, the node can be removed, reducing the quantum field theory on the graph to a $(1+1)$-dimensional theory on a single-edge graph. Consequently, in this initial analysis of entanglement entropy for quantum fields confined to single-edge graphs embedded in Minkowski spacetime, we automatically account for the case of quantum fields spatially confined to two edges connected at a node or to multiple edges forming a loop. Specifically, when considering the arbitrary network $\mathcal{N}$ embedded in

Minkowski spacetime (M, η) and initially treating its subgraphs as disconnected from the rest, the first three subgraphs of $\mathcal{N}$ listed above and shown in Fig. 4.3, are all treated as subgraphs containing no nodes. As a result, their entanglement entropy is fully captured by the same simple $(1+1)$-dimensional theory used for the single-edge case, in contrast to the minimal subgraph that contains a node, as well as more complex subgraphs, where a simple $(1+1)$-dimensional field theory is no longer adequate.

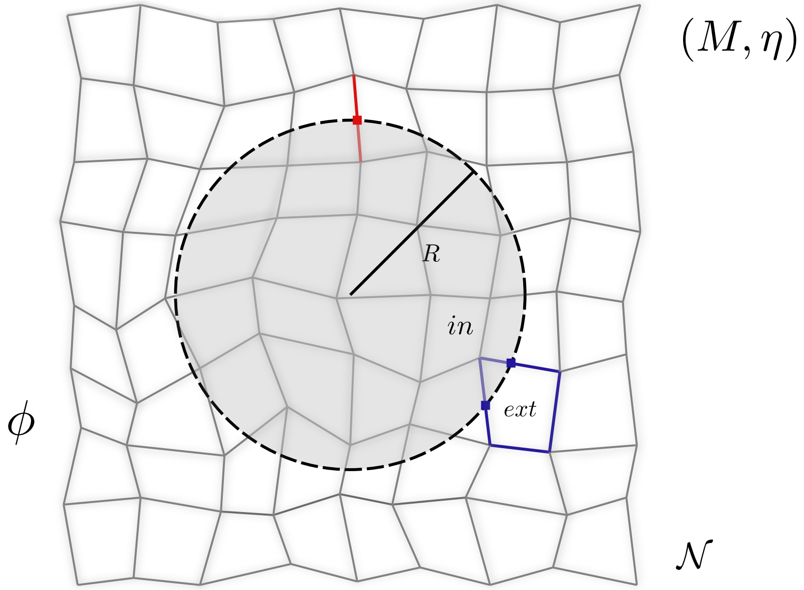

Figure 4.4: Spatial two-dimensional section of Fig. 4.2 for a quantum field ϕ (depicted in gray shades) spatially confined to the arbitrary three-dimensional network $\mathcal{N}$ embedded in Minkowski spacetime (M, η). The entangling sphere of radius R (disk in the 2D visualization) divides the network into an interior and an exterior sector. The depicted red single edge and blue one loop represent essential building blocks of this network. On the single edge highlighted in red, the entangling sphere reduces to an entangling *point*, depicted with a red square. Accordingly, the edge is divided into an interior and an exterior sector. Due to quantum field correlations across the entangling point, the exterior and interior sectors of the edge may be entangled, with the entanglement entropy quantifying the degree of entanglement.

In order to study the entanglement entropy for a quantum field confined to the history of the considered single edge, we introduce a $(1+1)$-dimensional field theory as presented in Sec. 2.2, imposing, at the worldlines of the edge endpoints, either Dirichlet or Neumann boundary conditions. We define the action functional $\mathcal{A}_e[\phi]$ for a scalar field ϕ confined to the edge's history H_e by

$$\mathcal{A}_e[\phi] := \int_{H_e} \mathcal{L}_e(x, \phi, \mathrm{d}\phi)\, \mathrm{dvol}_{h_e}\ , \tag{4.2}$$

where, as in Sec. 2.2, for some abstract coordinate system $x = \{\xi^a\} = (T, \xi),\ \mathcal{L}_e(T, \xi, \phi, \mathrm{d}\phi)$ denotes the Lagrangian of the theory and dvol_{h_e} the volume element, with h_e the $(1+1)$-dimensional metric tensor induced on the history of the edge, which, in our case, corresponds to the two-dimensional Minkowski metric (Sec. 2.1).

To validate our model against established results for the entanglement entropy of free real scalar quantum fields in the ground state in $(1+3)$ dimensions, it is natural to focus, within our network approach, on the Lagrangian density for a free real scalar field of mass μ confined to the two-dimensional edge's history, i.e. $\mathcal{L}_e = \frac{1}{2}\left(\eta^{ab}\partial_a\phi\,\partial_b\phi - \mu^2\phi^2\right)$. From this, we introduce the conjugate field momentum $\pi(T, \xi) = \frac{\partial\mathcal{L}_e}{\partial(\partial_T\phi)}$.

According to Sec. 2.2, by applying the variational principle to the action functional in Eq. (4.2), we derive the equation of motion $-\partial_T^2\phi + \partial_\xi^2\phi + \mu^2\phi = 0$ for the field on the edge history, along with the associated boundary conditions. Since the operator ∂_ξ^2 is self-adjoint on the single edge with Dirichlet or Neumann boundary conditions at its endpoints, we can use its eigenfunctions to construct quantum field and conjugate momentum operators on the single edge history. The quantum field ϕ and the conjugate momentum operator π then satisfy the canonical equal-time commutation relations

$$\begin{aligned} &[\phi(T, \xi), \pi(T, \xi')] = i\delta(\xi - \xi')\,, \\ &[\phi(T, \xi), \phi(T, \xi')] = [\pi(T, \xi), \pi(T, \xi')] = 0\,. \end{aligned} \tag{4.3}$$

As shown in Fig. 4.4, for each time T, an entangling sphere of radius R, traces out part of the field spatial support and, accordingly, the field configuration on the edge divides in two subsystems, one part I lying in the interior of the entangling sphere and one part E in its exterior. On the single edge, the entangling surface between interior and exterior reduces to an entangling *point*, depicted as a square in the figure. To measure a possible entanglement within the two subsystems, due to quantum field correlations along the edge and across the entangling point, we want to compute the entanglement entropy S_E for the quantum field on the single edge as

$$S_E = -\mathrm{Tr}\left(\rho_E \ln \rho_E\right)\ , \tag{4.4}$$

as introduced in Sec. 4.1, with ρ_E being the density matrix ρ reduced to the exterior, $\rho_E = \mathrm{Tr}_I \rho$. Note that, vice versa, we can equivalently compute Eq. (4.4) related to the reduced density matrix to the interior ρ_I, since the entanglement entropy is symmetric under exchange of the two subsystems, i.e. $S_E = S_I = S$.

The entanglement entropy for quantum fields defined on an interval of finite size, equivalent to the single-edge graph within our model, has been extensively analysed in the literature [31–35]. Among the different techniques, to compute Eq. (4.4) for a quantum field in the ground state spatially confined to the single edge, we implement the same approach as in [10], although adapted to a $(1+1)$-dimensional system.

According to [10], we focus on the Schrödinger picture of quantum field theory [36]. Within this picture, the field operator ϕ is time-independent and by considering a basis of the Fock space such that ϕ is diagonal, we can write for an eigenstate $|\phi\rangle$ of ϕ,

$$\phi(\xi)\,|\phi\rangle = \phi(\xi)\,|\phi\rangle \ . \tag{4.5}$$

Note that although the notation is the same, the $\phi(\xi)$ on the left-hand side of the equation represents the field operator acting on the eigenstate $|\phi\rangle$, whereas the $\phi(\xi)$ on the right-hand side is a scalar function – specifically, the classical scalar field ϕ – which is the eigenvalue corresponding to the eigenstate $|\phi\rangle$, by which it is multiplied. The major advantage of choosing the Schrödinger picture is that, similar to quantum mechanics, we can introduce a coordinate representation for an arbitrary, now time-dependent, state $|\Psi\rangle$, in the basis $\{|\phi\rangle\}$, represented by the wave functional $\Psi[\phi] = \langle\phi|\Psi\rangle$. Through a Legendre transformation, we obtain from the Lagrangian density $\mathcal{L}_e$ the associated Hamiltonian density $\mathcal{H}_e(T,\xi,\phi,\pi)$ on the edge history, $\mathcal{H}_e = \frac{1}{2}\left[\pi^2(T,\xi) + (\partial_\xi \phi(T,\xi))^2 + \mu^2\phi^2(T,\xi)\right]$. Within the Schrödinger picture, we can promote it to the Hamiltonian operator

$$H = \int \mathcal{H}_e \, d\xi = \frac{1}{2}\int \left[\pi^2(\xi) + (\partial_\xi \phi(\xi))^2 + \mu^2\phi^2(\xi)\right] \, d\xi \,, \tag{4.6}$$

where, in its functional differential representation, the conjugate momentum field π is expressed as $\pi(\xi) = -i\frac{\delta}{\delta\phi(\xi)}$. Having defined the Hamiltonian operator, we can write a Schrödinger-like equation for the quantum field theory on the single edge history,

$$i\frac{\partial}{\partial T}\,|\Psi\rangle = H\,|\Psi\rangle \ , \tag{4.7}$$

which fully characterizes the time evolution of the quantum field's state and can be expressed, in the functional differential form, as $i\frac{\partial}{\partial T}\Psi[\phi] = H\Psi[\phi]$. The normalized ground state wave functional for a free real scalar field can be found to be [36]

$$\Psi_0[\phi] = \langle\phi|0\rangle = \left(\det\left(\tfrac{\Omega}{\pi}\right)\right)^{1/4} \exp\left(-\tfrac{1}{2}\int d\xi \int d\xi' \phi(\xi)\,\Omega(\xi,\xi')\,\phi(\xi')\right) = \\ = \left(\det\left(\tfrac{\Omega}{\pi}\right)\right)^{1/4} \exp\left(-\tfrac{1}{2}\phi\cdot\Omega\cdot\phi\right)\,, \tag{4.8}$$

where Ω is given as $\Omega(\xi,\xi') = \int \frac{dk}{2\pi}\,\omega_k\, e^{ik(\xi-\xi')}$, with $\omega_k = \sqrt{k^2+\mu^2}$. In order to compute the entanglement entropy Eq. (4.4) for the quantum field spatially confined to the single edge highlighted in Fig. 4.4, we consider the quantum field in the ground state $|0\rangle$ and describe the state through the density operator $\rho = |0\rangle\langle 0|$.

As already mentioned, under the assumption of a classical spacetime, which allows for coincidence limits, the entanglement entropy becomes a divergent quantity in quantum field theory. For the entanglement entropy to be a meaningful concept, there must be a mechanism that prevents these limits. In practice, events are measured over regions rather than at exact points, with experiments approximating these regions as points through error estimation within a given resolution limit. This creates a discrete localization structure, where the smallest distance scale a is determined by the measurement devices. In this way, the experiment's resolution naturally prevents coincidence limits, effectively introducing an extrinsic UV cutoff into the theory. As a result, although dependent on a, the entanglement entropy becomes a regularized, finite quantity.

To reflect this finite resolution structure, the quantum field spatially confined to the edge is discretized on a one-dimensional lattice of N sites, each separated by a fixed spacing $a \in \mathbb{R}^+$ (Fig. 4.5). Each lattice point is labeled by $i \in \{1,...,N\}$, being $\xi_i = ia$ its position along the edge. The edge endpoints are denoted by ξ_0 and ξ_{N+1}. Note that while a implements a short-distance cutoff a^{-1}, the size of the edge $L = (N+1)a$ introduces the infrared cutoff L^{-1}. As discussed before, the entanglement entropy will depend on those cutoffs. Furthermore, as a general prescription, recall that if we discretize ξ as $\xi_i = ia$, then

$$\int d\xi \to a\sum_i$$
$$\frac{\partial f(\xi)}{\partial\xi} \to \frac{f(a(i+1)) - f(ai)}{a}, \qquad \frac{\partial^2 f(\xi)}{\partial\xi^2} \to \frac{f(a(i+1)) - 2f(ai) + f(a(i-1))}{a^2}$$
$$\delta(\xi-\xi') \to \frac{\delta_{ij}}{a}, \quad \pi(\xi) \to \frac{\pi_i}{a}, \quad \phi(\xi) \to \phi_i\,, \tag{4.9}$$

where π_i and ϕ_i are taken to be dimensionless.

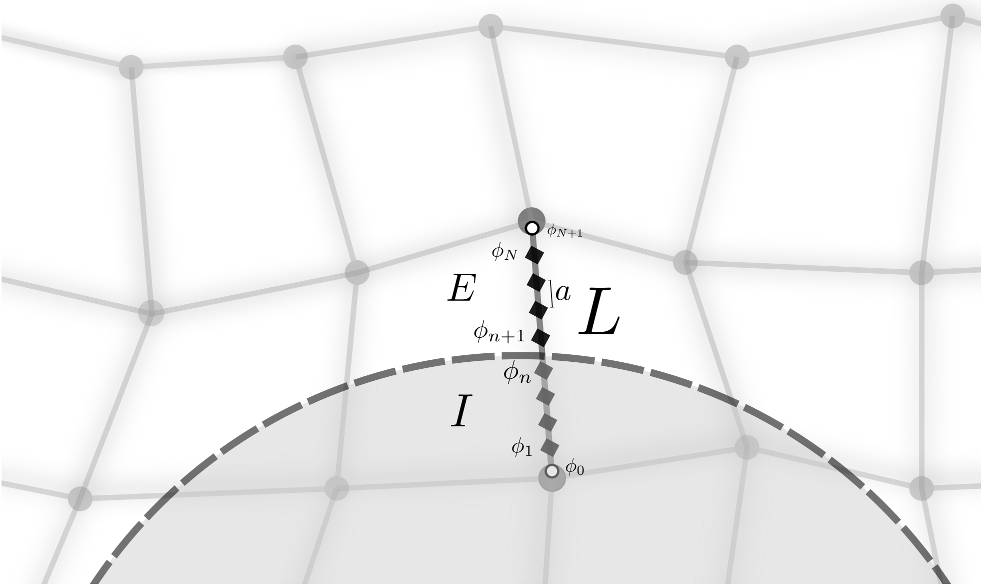

Figure 4.5: Detail of Fig. 4.4. The illustration depicts the finite resolution structure introduced by experimental devices on the quantum field theory spatially confined to the single edge. The quantum field is discretized on a one-dimensional lattice of N sites, with constant spacing a. The length of the edge L is given as $L = (N+1)a$. The entangling sphere separates the edge setup into an interior interval I and an exterior interval E. The label n denotes the last traced-out lattice point. The boundary sites ϕ_0 and ϕ_{N+1} are represented by white circles. Note that, based on the choice of Dirichlet boundary conditions, $\phi_0 = \phi_{N+1} = 0$.

Integrating by parts Eq. (4.6), we can write the discretized Hamiltonian operator as

$$H = \frac{1}{2a} \sum_{i=1}^{N} \left(\pi_i^2 - \phi_i(\phi_{i+1} - 2\phi_i + \phi_{i-1}) + \mu^2 a^2 \phi_i^2 \right) . \tag{4.10}$$

Note that μa is dimensionless and π_i and ϕ_i satisfy $[\phi_j, \frac{\pi_{j'}}{a}] = i\frac{\delta_{jj'}}{a}$. Furthermore, note that by integrating by parts, we obtain boundary terms for H that satisfy the boundary conditions imposed through the variational principle. We start by imposing the Dirichlet boundary conditions $\phi(\xi) = 0$ at the worldlines of the endpoints of the edge. In particular, this specific choice leads the mentioned boundary terms in H to vanish. The discretized version of these conditions imposes $\phi_0 = 0$ and $\phi_{N+1} = 0$, assuming $\xi = 0$ coincides with one of the edge's endpoints. Hence, in a more compact way, we can rewrite the discretized

Hamiltonian operator as

$$H = \frac{1}{2a} \sum_{i=1}^{N} \left(\pi_i^2 + \sum_{j=1}^{N} \phi_i K_{ij} \phi_j \right) , \tag{4.11}$$

where K is a real symmetric $N \times N$ matrix with positive eigenvalues which, with the above introduced Dirichlet boundary conditions, is given by

$$K_{ij} = M^2 \delta_{ij} - \delta_{i,j+1} - \delta_{i+1,j} , \tag{4.12}$$

with $M = \sqrt{2 + \mu^2 a^2}$.

By looking at the form of the Hamiltonian in Eq. (4.11), we can interpret the field on the lattice points ϕ_i as N coupled harmonic oscillators with (next-neighbor) interactions determined by the entries of the matrix K. It is in this specific sense that, for illustrative purposes, we will refer to the lattice points as *oscillators* throughout our investigation.

Within the discretization scheme, the function $\Omega(\xi, \xi')$ in Eq. (4.8), reduces to a matrix $\Omega = \sqrt{K}$, defined such that if there is an orthogonal matrix U with $K = U^T K_D U$, where K_D is diagonal, then $\Omega = U^T \sqrt{K}_D U$. Then, the ground state wave functional of Eq. (4.8) reduces to the wavefunction

$$\Psi_0(\boldsymbol{\phi}) = a^{N/2} \, \pi^{-N/4} \left(\det(\Omega)\right)^{1/4} \exp\left(-\tfrac{1}{2} \boldsymbol{\phi} \cdot (\Omega \boldsymbol{\phi})\right) , \tag{4.13}$$

where $\boldsymbol{\phi} := (\phi_1, \ldots, \phi_i, \ldots, \phi_N)$ and $a^{N/2} \left(\det(\Omega)\right)^{1/4}$ is a dimensionless quantity. The form of the ground state wavefunction highlights the similarity to a system of N coupled harmonic oscillators [10]. As a result, the entanglement entropy for the quantum field spatially confined to the single edge can be calculated in the same way as for a system of N coupled harmonic oscillators. In particular, Ω fully characterizes $\Psi_0(\boldsymbol{\phi})$ and, with it, the density operator $\rho = |0\rangle \langle 0|$, which in coordinate representation reads $\rho(\boldsymbol{\phi}, \boldsymbol{\phi}') = \Psi_0(\boldsymbol{\phi}) \, \Psi_0^*(\boldsymbol{\phi}')$. By computing the reduced density matrix $\rho_E = \mathrm{Tr}_I \rho$, the entanglement entropy is given by $S_E = -\mathrm{Tr}\left(\rho_E \ln \rho_E\right)$. Therefore, it is evident that the matrix Ω plays a crucial role in the computation.

Along the lines of [9, 10], and according to Fig. 4.5, we divide the matrix Ω into four blocks, i.e.

$$\Omega = \begin{pmatrix} \Omega_{\mathrm{II}} & \Omega_{\mathrm{IE}} \\ \Omega_{\mathrm{EI}} & \Omega_{\mathrm{EE}} \end{pmatrix} , \tag{4.14}$$

where Ω_{II} and Ω_{EE} are submatrices that couple oscillators within regions I and E, respectively, while $\Omega_{\mathrm{IE}} = \Omega_{\mathrm{EI}}^{T}$ is the submatrix that couples oscillators inside the entangling sphere to those outside [9].

Let n be the number of oscillators on the edge which are traced out by the entangling sphere, i.e. belonging to I. The reduced density matrix $\rho_{\mathrm{E}}\left(\boldsymbol{\phi}, \boldsymbol{\phi'}\right)$ to the exterior of the entangling sphere is obtained by integrating out the n lattice points in I in $\rho(\boldsymbol{\phi}, \boldsymbol{\phi'})$, that is

$$\rho_{\mathrm{E}}\left(\boldsymbol{\phi}, \boldsymbol{\phi'}\right) = \int \prod_{i=1}^{n} d\phi_i \, \Psi_0(\boldsymbol{\phi}) \, \Psi_0^*(\boldsymbol{\phi'}) \,, \tag{4.15}$$

where $\boldsymbol{\phi}$, $\boldsymbol{\phi'}$ on the left-hand side refer only to lattice points in the exterior of the entangling sphere, i.e. $\boldsymbol{\phi} = (\phi_{n+1} \ldots, \phi_N)$.

By implementing the form in Eq. (4.14) for Ω, we obtain

$$\rho_{\mathrm{E}}\left(\boldsymbol{\phi}, \boldsymbol{\phi'}\right) \sim \exp\left(-\tfrac{1}{2}\left(\boldsymbol{\phi} \cdot (\gamma \boldsymbol{\phi}) + \boldsymbol{\phi'} \cdot (\gamma \boldsymbol{\phi'})\right) + \boldsymbol{\phi'} \cdot (\beta \boldsymbol{\phi})\right), \tag{4.16}$$

where

$$\beta = \frac{1}{2} \Omega_{\mathrm{IE}} \, \Omega_{\mathrm{II}}^{-1} \, \Omega_{\mathrm{IE}}, \quad \gamma = \Omega_{\mathrm{EE}} - \beta \,. \tag{4.17}$$

Note that if there were no coupling between the lattice points inside and outside the entangling sphere, β would be a zero matrix and $\rho_{\mathrm{E}}\left(\boldsymbol{\phi}, \boldsymbol{\phi'}\right)$ would describe a pure state. Therefore, entanglement is encoded in the submatrix Ω_{IE}.

To find the spectrum of the reduced density matrix ρ_E, we need to diagonalize it. This first requires an orthogonal transformation V such that $\boldsymbol{\phi} \mapsto \gamma_D^{1/2}(V\boldsymbol{\phi})$ so that $\gamma =: V^{\mathrm{T}} \gamma_D V$, where γ_D is diagonal, and subsequently another orthogonal transformation W that diagonalizes the matrix $\Lambda := \gamma_D^{-1/2} V \beta V^{\mathrm{T}} \gamma_D^{-1/2}$, i.e. $\Lambda =: W^{\mathrm{T}} \Lambda_D W$ [10]. Let λ_i with $i \in \{n+1, \ldots, N\}$ be the eigenvalues of Λ and note that they are the same as those of the matrix $\gamma^{-1}\beta$. Since Λ is now diagonal, we can write the reduced density matrix $\rho_{\mathrm{E}}\left(\boldsymbol{\phi}, \boldsymbol{\phi'}\right)$ as

$$\rho_{\mathrm{E}}\left(\boldsymbol{\phi}, \boldsymbol{\phi'}\right) \;\sim\; \prod_{\phi_i, \phi'_i \in E} \rho_{\mathrm{E}}\left(\phi_i, \phi'_i\right) , \tag{4.18}$$

where each $\rho_{\mathrm{E}}\left(\phi_i, \phi'_i\right) = e^{-\frac{1}{2}\left(\phi_i^2 + \phi_i'^2\right) + \lambda_i \phi_i \phi'_i}$ is the reduced density matrix of a single lattice point ϕ_i on the interval E of the single edge in the exterior of the entangling sphere. Given that the eigenvalues of each $\rho_{\mathrm{E}}\left(\phi_i, \phi_i'\right)$ are given by $p_{l_i} = (1-\xi_i)\xi_i^{l_i}$, with $l_i \in \mathbb{N}^0$ [10], the spectrum of the reduced density matrix $\rho_{\mathrm{E}}\left(\boldsymbol{\phi}, \boldsymbol{\phi'}\right)$ reads

$$p_{\mathrm{E}\ l_{n+1}\ldots l_N} = \prod_{i=n+1}^{N} (1-\xi_i)\xi_i^{l_i}\,, \tag{4.19}$$

with $\xi_i = \lambda_i \Big/ \left(1+\sqrt{1-\lambda_i^2}\right)$. As a result, the entanglement entropy S_E for free massive vacuum fluctuations on the single-edge graph history, Eq. (4.4), is finally given by

$$S = S_E = \sum_{i=n+1}^{N} \left(-\ln(1-\xi_i) - \frac{\xi_i}{1-\xi_i}\ln \xi_i \right)\,. \tag{4.20}$$

By discretizing the field theory spatially along the edge, the computation of the entanglement entropy reduces to solving the eigenvalue problem for the matrix $\gamma^{-1}\beta$.

As mentioned above, the entanglement entropy in Eq. (4.20) serves as an instantaneous measure of entanglement. Due to the time-independence of the ground state in Minkowski space and our assumption of a stationary entangling surface, the entanglement entropy calculated above is invariant over time. Since in $(1+1)$-dimensional free field theories the matrix K explicitly depends only on $M = \sqrt{2+\mu^2 a^2}$, as shown in Eq. (4.12), we expect the eigenvalues $\{\xi_i\}$ and consequently the entanglement entropy S to depend solely on μa. Once the short-distance cutoff a^{-1} is set by the specific measurement devices, the regularized entanglement entropy is fully determined by the field mass μ. This seems consistent with the continuum case. In fact, in quantum field theory, we know that for spacelike-separated events, the two-point correlation function in one spatial dimension is expressed in terms of the modified Bessel function of the second kind $K_1(\mu\|\sigma\|)$ [37], where $\|\sigma\|$ is the spatial distance between the two locations. Specifically, for large values of $\mu\|\sigma\|$, K_1 assumes the asymptotic form $K_1(\mu\|\sigma\|) \sim \frac{1}{\mu\|\sigma\|}e^{-\mu\|\sigma\|}$. Consequently, spacelike quantum correlations along the edge decay significantly by distances sufficiently larger than the characteristic correlation length $\xi := 1/\mu$. Thus, along the edge, spacelike quantum correlations have a shorter or longer range depending on the quantum field mass μ. This variation results in fewer or more vacuum fluctuations being quantum correlated across the entangling surface. Since the entanglement entropy serves as an instantaneous measure of the amount of quantum field correlations (i.e. of spacelike quantum correlations) within vacuum fluctuations in the interior and exterior of the entangling sphere, a longer or shorter correlation range leads to a higher or lower total entanglement entropy for the system.

Therefore, the quantum field mass μ, or equivalently, the correlation length $\xi = 1/\mu$ totally determines the entanglement entropy. Intuitively, in the following we will refer to the correlation length ξ as the characteristic reference scale for the system. As a is an extrinsic length scale determined by the experimental devices, ξ is the intrinsic length scale of the system.

By comparing the intrinsic length scale of the system with the external length scales – specifically, the short-distance scale a and the long-distance scale L – we identify a window of wavelengths that are operationally allowed for the vacuum fluctuations contributing to the entanglement. In fact, the minimal distance scale a prevents wavelengths shorter than this threshold, thereby providing an ultraviolet cutoff. Furthermore, when the correlation length is much larger than the short-distance scale, i.e. $\xi \gg a$, the long-distance behavior of the correlations gives rise to an effective field behavior of the one-dimensional lattice, which can be effectively described in terms of a (1+1)-dimensional (massive) quantum field theory [33]. However, the finite size of the edge, as part of a finitely extended network, introduces a long-distance scale L. Due to Dirichlet boundary conditions at the edge's endpoints, the intrinsic length scale cannot increase indefinitely but it has to be finite and restricted to $\xi \ll L$. This gives rise to a range $a \ll 1/\mu \ll L$ for the correlation length in which an effective quantum field theory description is possible. For $\xi \leq a$, which reads $\mu a \geq 1$ in terms of the mass μ, the effective field theory interpretation ceases to hold, and the system effectively reduces to a quantum mechanical chain of finitely many, weakly coupled harmonic oscillators.

Numerical Entanglement Entropy

Implementing a numerical computation of the entanglement entropy in Eq. (4.20) results in the plot in Fig. 4.6 for two different choices of μa. Note that since a is fixed by the specific experimental setup, varying μa corresponds to different choices of mass μ. Accordingly, we will often refer to different values of μa as corresponding to different mass values. For numerical details, we refer the reader to the code written for this analysis and published in [38]. Since we are currently only interested in the relative change of the entanglement entropy with respect to the radius of the entangling sphere, rather than its exact value, we rescaled it using its value at the radius $R_{L/2} = 2.5L$ for $\mu a = 10^{-1}$ as a reference, that is, $\bar{S}(R) = S(R)/S(R_{L/2})$. In the configuration depicted in Fig. 4.4, the single edge intersects the surface of the traced-out sphere once. For half the radius of the entangling sphere, there would be no intersections and the entanglement entropy would be zero since no part

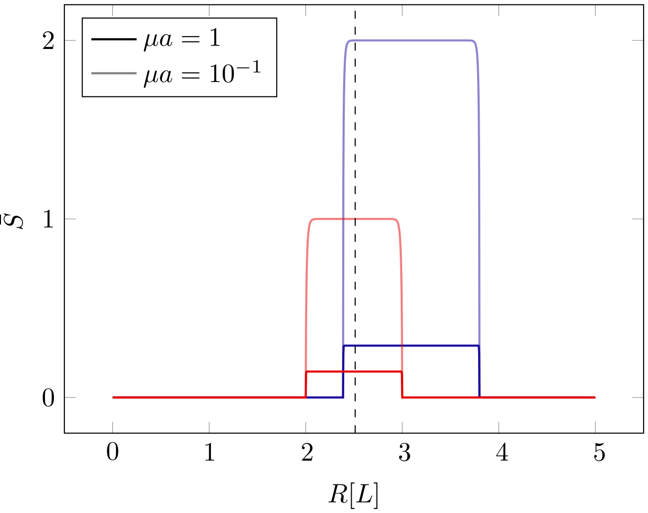

Figure 4.6: Entanglement entropy for vacuum fluctuations confined to elementary subgraphs (histories) of a network $\mathcal{N}$ as shown in Fig. 4.4, in terms of the radius of the entangling sphere. In particular, the entanglement entropy is given for the red edge and the blue loop equipped with a finite resolution structure consisting of $N = 300$ lattice points on each edge, for two different choices of μa. The radius of the entangling sphere is expressed in multiples of the length L of the single edge. The value explicitly chosen in Fig. 4.4, $R = R_{L/2} = 2.5L$ which traces out precisely half of the red edge, is marked by a vertical dashed line.

of the red edge is traced out. Similarly, the entanglement entropy also vanishes for twice the radius, since the entire edge is then traced out. Consequently, the behavior of S shown in Fig. 4.6 emerges.

As can be seen from the plot, in both cases $\mu a = 1$ and $\mu a = 10^{-1}$, the entanglement entropy on the edge does not depend on how many lattice points ϕ_i are traced out; it remains constant with respect to R. Intuitively, this result can be expected in $(1 + 1)$ dimensions, since the cross section of a single edge with the surface of the entangling sphere is a single point. Any communication channel along the edge between vacuum fluctuations residing inside and outside the entangling sphere must pass through this cross section. Since this cross section remains constant as the radius increases – unlike in higher dimensions – there is no increase in the amount of possible quantum field correlations across it as the radius grows. Furthermore, the off-diagonal terms in K in Eq. (4.12), which connect a lattice point ϕ_i with its next neighbor ϕ_{i+1}, are constant and independent of the specific lattice point i, i.e. the coupling between each pair of oscillators does not depend on their position in the lattice. It is important to note that this is not necessarily true for three-dimensional Hamiltonians [10,35]. Since the entries of Ω are fully determined by K through

$\Omega = \sqrt{K}$, they are also constant and independent of any label i. As a consequence, the eigenvalues $\{\lambda_k\}$ carry no information about the oscillators labels, nor do the eigenvalues $\{\xi_k\}$. Thus, the entanglement entropy in Eq. (4.4) does not explicitly depend on the positions of the lattice points, including that of the last traced-out oscillator, labeled by n. Since this label determines the number of traced-out oscillators, the entanglement entropy does not explicitly depend on R.

Moreover, it is crucial to note that the value of the entanglement entropy for a quantum field confined to an embedded single-edge graph is independent of the angle at which the edge intersects the entangling sphere. In fact, in the Minkowski background, the $(1+1)$-dimensional field theory on the edge history carries no information about the extrinsic geometry. This will not necessarily be the case when we study entanglement properties of quantum fields on networks embedded in curved spacetimes.

For values of the mass μ such that $\mu a = 10^{-1}$, we can notice that the value of the entanglement entropy is increased with respect to the larger mass case $\mu a = 1$, as shown in Fig. 4.6. Intuitively, since the characteristic correlation length is $\xi = 1/\mu$, which increases as the mass decreases, it follows that, along the edge, quantum correlations have a longer range for lower masses. Therefore, for the lower mass case $\mu a = 10^{-1}$, the correlations across the entangling sphere encompass more lattice points compared to the case of $\mu a = 1$, introducing new correlations between the interior and exterior of the entangling sphere and thus increasing the overall entanglement.

This also explains the apparent dependence on R of the entanglement entropy close to the edge endpoints, as shown in Fig. 4.6. In fact, we have seen that the entanglement entropy should be independent of R for one-dimensional systems, independently of the mass. However, far-ranging correlations may be sensible to the finite size of the edge, leading to effects such as a dependence on R as in Fig. 4.6, close to the edge's endpoints. In fact, as explained above, for a given non-vanishing mass μ, the correlation length is determined and finite. This implies that a lattice point in E is correlated with lattice points in I that are approximately within a distance ξ from the considered site. However, if the size of I decreases, as the radius of the entangling sphere diminishes and approaches the endpoint of the edge, the distance from the considered lattice point to the edge's endpoint may become smaller than ξ. This implies that there might be fewer oscillators in I that are correlated with the considered site in E, compared to the case where the edge boundary is at a distance greater than ξ from the considered site. The same reasoning applies symmetrically to a given site in I, where the correlation length determines the number of oscillators in E to which it is correlated. Similarly, as R increases and approaches the other endpoint of the edge, there may be fewer oscillators correlated with the considered site in I. Consequently, this results in a decrease in entanglement entropy as R approaches the edge's endpoints. Although this effect is not very pronounced for $\mu a = 10^{-1}$, it certainly has a stronger influence on the entanglement entropy for lower masses.

In particular, if ξ is comparable to the length L of the edge, or even for $\xi \geq L/2$, this finite size effect might influence even the value of the entanglement entropy computed for R crossing the edge at its midpoint, $S(R_{L/2})$. This reflects that, for $\xi \sim L$, the infrared cutoff L^{-1} introduced by the finite size of the edge excludes too many vacuum fluctuations from the computations that would otherwise contribute to the entanglement properties of the ground state. The quantum field theory introduced on the edge's history would fail to fully capture the entanglement properties of ground states of free quantum fields in $(1+1)$ dimensions, leading to an entanglement entropy that strongly depends on the finite size of the system.

However, if l is the length of the interval of the edge residing within the entangling sphere, for characteristic correlation lengths in the range $1/\mu \ll \min(l, L-l)$, finite size effects are significant only near the endpoints of the edge. As a result, we can refine the previously established range of values for the intrinsic length scale – required for an effective quantum field theory description – to the condition: $a \ll 1/\mu \ll \min(l, L-l)$. Correlation lengths within this range enable an accurate description of the entanglement properties of the ground state of the field, independent of the infrared regulator. Note that $1/\mu \ll \min(l, L-l)$ automatically satisfies $1/\mu \ll L$.

Perturbative Entanglement Entropy

An extreme case occurs when ξ approaches the boundary of the effective theory's validity for the field, specifically when $1/\mu \leq a$. In fact, for $\mu \geq a^{-1}$ and beyond, the correlation length diminishes to a point where it is shorter than the lattice spacing and the oscillators act as mostly decoupled, with only a few contributing to the entanglement entropy. This marks a transition into a fully quantum mechanical (QM) regime.

Nonetheless, such large values of the mass enable a perturbative analytical calculation of Eq. (4.20), as showed in [34,35]. The off diagonal terms of K in Eq. (4.12) do not include any mass term such that, for large masses, the diagonal components of K dominate over the non-diagonal entries. Therefore, we can split K into $K = K_D + K_{\text{off}}$ introducing a dominant diagonal component K_D and a sub-leading off-diagonal matrix K_{off}. This allows for a perturbative expansion of $\Omega = \sqrt{K}$ in powers of $1/M$ [34], where we recall that $M = \sqrt{2+\mu^2 a^2}$. Physically, the leading order of the expansion corresponds to the limit where the interaction terms in (4.12) become negligible and the oscillators are effectively decoupled, resulting in a vanishing entanglement entropy. In this $1/M$ expansion, up to the first order $\mathcal{O}(M^{-1})$, Ω becomes

$$\begin{aligned}
\Omega_{II\,ij} &= M\,\delta_{ij} - \frac{\delta_{i+1,j}+\delta_{i,j+1}}{2M} + \mathcal{O}(M^{-3}) \\
\Omega_{EE\,ij} &= M\,\delta_{ij} - \frac{\delta_{i+1,j}+\delta_{i,j+1}}{2M} + \mathcal{O}(M^{-3}) \\
\Omega_{IE\,ij} &= -\frac{\delta_{i,n}\delta_{j,1}}{2M} + \mathcal{O}(M^{-3})
\end{aligned} \tag{4.21}$$

where we recall that Ω_{II} is a $n \times n$ matrix, Ω_{EE} is a $(N-n)\times(N-n)$ matrix and Ω_{IE} is a $n \times (N-n)$ matrix. Up to the order $\mathcal{O}(M^0)$, the matrices Ω_{II} and Ω_{EE} are diagonal and Ω_{IE} is a null matrix as it contains no coupling between the interior and exterior of the entangling sphere. Consequently, the oscillators are not correlated, leading to a vanishing entanglement entropy.

However, at the first order $\mathcal{O}(M^{-1})$ in the inverse mass expansion, next-neighbor couplings are introduced in Ω. In particular, the next-neighbor coupling between the last traced-out lattice point ϕ_n in I and ϕ_{n+1} in E is introduced in Ω_{IE}. It is important to note that next-to-next-neighbor couplings will be introduced in the next order of the expansion, along with additional longer-range couplings as the expansion continues [35]. As previously mentioned, the cross section between the single edge and the entangling sphere reduces to a single point. Thus, any possible correlations that contribute to entanglement, that is between I and E, must pass through this point, specifically through the coupling between ϕ_n and ϕ_{n+1}. Since $\Omega_{IE\,n,1}$ is the sole term in Ω_{IE} at this order, because only next-neighbor couplings are taken into account, the total contribution to the entanglement arises exclusively from the correlation between ϕ_n and ϕ_{n+1}. Therefore, solving the eigenvalue problem for $\gamma^{-1}\beta$ up to the first order $\mathcal{O}(M^{-1})$ [35] yields a single non-vanishing eigenvalue $\lambda_{n+1} = 1/8M^4$. As anticipated, the eigenvalue λ_{n+1}, and consequently ξ_{n+1} in Eq. (4.20), is independent of n, such that the entanglement entropy is expected to be independent of the number of traced out lattice points and consequently of R. Inserting λ_{n+1} into Eq. (4.20) results in the entanglement entropy at the first order $\mathcal{O}(M^{-1})$ given by $S^{(1)} = (1 + 4\ln(2M))/16M^4$. If we expand further in the inverse mass expansion, we obtain [35], up to the third order,

$$S^{(3)} \approx S^{(1)} + \frac{1 + 328\ln(2M)}{512M^8} + \frac{-599 + 5880\ln(2M)}{3072M^{12}}\,, \tag{4.22}$$

with $M = \sqrt{2 + \mu^2 a^2}$.

As in the numerical investigation, for large masses the entanglement entropy remains constant with respect to R. In particular, for $\mu a = 1$ Eq. (4.22) agrees quantitatively with the numerical value to 97%. Consequently, for this value of the mass, we can assume that the entanglement across the surface of the entangling sphere is exclusively due to up to three next-neighbor couplings, as indicated by the third order of the inverse mass expansion. In other words, the correlations relevant for entanglement at $\mu a = 1$ involve the lattice points ϕ_{n+3} and ϕ_{n-2} at most.

Analytical Entanglement Entropy

For $\mu a \ll 1$, an analytical expression for the total entanglement entropy has been found in [33] for infinite $(1+1)$-dimensional quantum systems of finite ξ: $S^{\text{plat}} = 1/6 \ln(\xi/a)$, which also agrees with the constant numerical result for the entanglement entropy of Fig. 4.6 for $\mu a = 10^{-1}$. In fact, for finite correlation lengths within the range $a \ll 1/\mu \ll \min(l, L-l)$, finite-size effects are significant only near the endpoints of the edge. When R is sufficiently far from these endpoints, the setup becomes equivalent to that considered in [33] for an infinitely long edge.

Furthermore, for the same condition $\mu a \ll 1$ with finite ξ but for $(1+1)$-dimensional quantum systems of finite size L, an analytical expression for the entanglement entropy of a subsystem of length $L/2$, is asserted to be [33]

$$S^{\text{fin}}(L,\xi) = \frac{1}{6}\left[\ln\left(\frac{L}{2a}\right) + S^{\text{fs}}\left(\frac{L}{2\xi}\right)\right]\,, \tag{4.23}$$

where $S^{\text{fs}}(L/(2\xi))$ accounts for finite size effects. For lengths L much greater than ξ, $S^{\text{fs}}(L/(2\xi)) \approx -\ln(L/(2\xi))$ such that, at $L/2$, $S^{\text{fin}}(L,\xi)$ reduces again to the constant plateau value

$$S^{\text{plat}}(L,\xi) = \frac{1}{6}\ln\left(\frac{\xi}{a}\right)\,, \tag{4.24}$$

confirming once again the numerical result in Fig. 4.6 for $\mu a = 10^{-1}$ at $R = R_{L/2}$. However, as previously explained, for correlation lengths comparable to L, the boundaries influence the value of the entanglement entropy even at $L/2$ and the general expression S^{fin} for the entanglement entropy aligns perfectly with the behavior observed numerically in [38]. Finally, for finite systems where $\xi \to \infty$, for which $L \ll 1/\mu$, our numerical implementation agrees with the analytical result found in [33].

In conclusion, when $1/\mu \ll a$ the assumptions of the perturbative expansion are satisfied and the entanglement entropy $S^{(3)}$ is determined by Eq. (4.22). In the range $a \ll 1/\mu \ll L$ Eq. (4.24) provides the correct value S^{plat} for the entanglement entropy. When $1/\mu \geq L$ or for larger values, we transition into a new regime described by the general analytical expression S^{fin} at least for the entanglement entropy evaluated at the midpoint of the edge. The numerical implementation covers all mass ranges. To summarize the ranges of validity for the various methods, we plotted in Fig. 4.7 the entanglement entropy as a

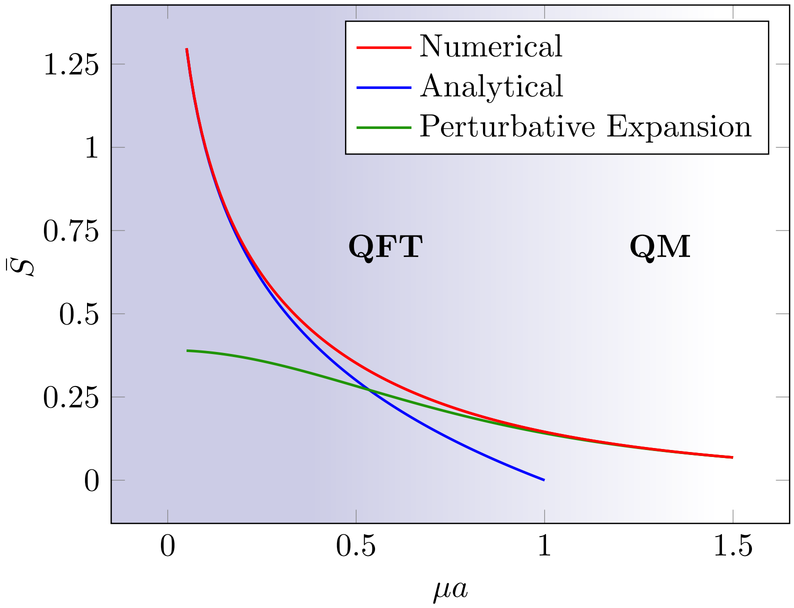

Figure 4.7: Entanglement entropy of degrees of freedom spatially confined to a single edge that intersects the entangling surface at its midpoint, as a function of μa. The length L of the edge allows for $N = 500$ lattice points with equidistant lattice spacing a. This guarantees $\mu a \gg 0.004$ in the displayed domain $\mu a \in (0.05, 1.5)$ so that finite-size effects do not affect the entanglement entropy. The red curve shows the numerical value obtained with the code [38], while the blue and green curves, respectively, show S^{plat} and $S^{(3)}$ given in the main text. The background shading indicates the domain of validity of quantum field theory as an effective theory for the one-dimensional lattice.

function of μa for the single edge of Fig. 4.4, which intersects the entangling surface at its midpoint. The finite resolution structure is reflected, on the edge, in a one-dimensional lattice of constant spacing a and $N = 500$ lattice points, such that $L = (N+1)a$. This specific choice implies a lower bound $\mu a \gg 0.004$, such that size effects are negligible at the edge midpoint. The red curve represents the numerical value of the entanglement entropy, the blue curve shows the analytical result [33] S^{plat} evaluated at the edge midpoint, as given in Eq. (4.24) and, finally, the green curve shows $S^{(3)}$ as given in Eq. (4.22). As can be seen from the picture, the function S^{plat} is a good approximation for values of μa up to 0.2. For values $\mu a > 0.9$ the perturbative result $S^{(3)}$ is in good agreement with the numerical result. However, in the intermediate range, specifically for $0.2 < \mu a < 0.9$, no analytical approximation is available, to the best of our knowledge.

Experimental Entanglement Entropy

Strikingly, the entanglement entropy for a single-edge graph has received even experimental verification [39]. In fact, in this very recent experiment, an ultracold atom simulator of a $(1+1)$-dimensional scalar quantum field theory was employed to measure entanglement properties of the ground state at $T \approx 48\,\text{nK}$. The effective free field was shown to satisfy a massive Klein-Gordon equation with $\mu \approx 5 \cdot 10^4\,\text{m}^{-1}$, resulting in a correlation length $\xi \approx 20\,\mu\text{m}$. In this experiment, the finite resolution structure is determined by the resolution of the imaging system, which enforces a short-distance cutoff $a \approx 7\,\mu\text{m}$. Additionally, the one-dimensional field support extended over $L \approx 49\,\mu\text{m}$.

After dividing the field configuration in two subsystems, the mutual information is experimentally observed to follow a plateau value. At zero temperature and for pure states of the total field configuration, the mutual information equals twice the entanglement entropy of either of the subsystems. Therefore, this leads to the first experimental verification of the constant plateau value of the entanglement entropy for free scalar $(1+1)$-dimensional field theories. Notably, despite the presence of a very low temperature, the experimental entanglement entropy agrees with numerical results for the same μa value. In addition, the field mass satisfies the hierarchy of scales $a < 1/\mu < L$, allowing the plateau value to be described by the analytical expression $S^{\text{plat}}(L, \xi) = \frac{1}{6} \ln\left(\frac{\xi}{a}\right)$, which also accurately approximates the experimental result.

Periodic boundary conditions: the loop graph

Consider again the arbitrary network depicted in Fig. 4.3. So far, we have fully analyzed how the entanglement properties of the quantum field on the single edge are affected by the entangling sphere. We learned that in Minkowski spacetime, a vertex connecting only two edges can be removed without affecting the system, and that the angles at which the edges intersect the entangling sphere, as well as their relative orientations, are irrelevant. Therefore, the subgraph of Fig. 4.3 formed by connecting two edges at a vertex is equivalent to the case of a single edge analyzed above, although with a larger value of L, and thus encodes the same entanglement properties.

In the following, we focus on the elementary subgraph consisting of four edges e_i of length L_{e_i} connected together to form a loop, as highlighted in blue in Fig. 4.8. In this subsection, similar to the single-edge case, we first consider the loop as disconnected from the network, treating the four vertices of the loop in Fig. 4.8 as each connecting only two edges. As previously mentioned, once we understand how entanglement properties behave in the presence of a non-removable node – connecting more than two edges – we can then analyze the loop with all its actual connections in the network. Since each of the four vertices of the loop is thought to connect only two edges, they can all be removed in Minkowski spacetime.

Thus, in Minkowski, such a loop configuration can be described by a field spatially confined on a single edge of length $\sum_{i=1}^{4} L_{e_i}$, with periodic boundary conditions at its endpoints, that is, its endpoints are topologically identified. Exactly as we did for the single edge with Dirichlet boundary conditions, we equip the edge with a finite resolution structure, that is, the field spatially confined to the edge is discretized on a one-dimensional lattice $\{\phi_1, \ldots, \phi_N\}$ of constant spacing a. The position of the lattice point is labeled by $\xi_i = ia$. The discretized Hamiltonian reads as in Eq. (4.10). However, the periodic boundary conditions now translate to $\phi_0 = \phi_N$ and $\phi_{N+1} = \phi_1$, which effectively means that the lattice points ϕ_1 and ϕ_N interact as nearest neighbors. Accordingly, we consider K, Eq. (4.12), with an additional coupling:

$$K_{ij} = M^2 \delta_{ij} - \delta_{i,j+1} - \delta_{i+1,j} - \delta_{i,1}\delta_{N,j} - \delta_{i,N}\delta_{1,j} \,.$$

Using this new form of the matrix K, we can compute Eq. (4.20) as before and examine the entanglement properties along the loop arising from the intersection with the entangling sphere. In particular, the entangling surface intersects the loop at two points, shown as

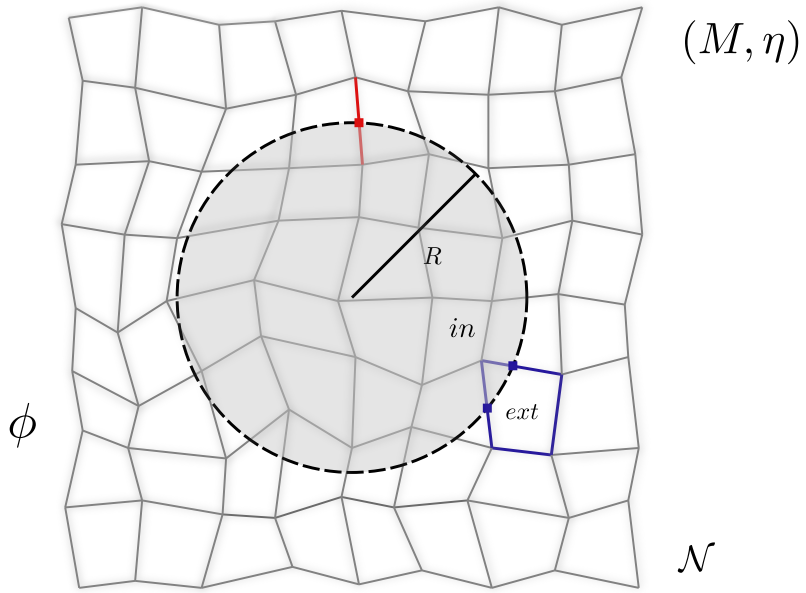

Figure 4.8: Spatial two-dimensional section of Fig. 4.2 for a quantum field ϕ (depicted in gray shades) spatially confined to the arbitrary three-dimensional network $\mathcal{N}$ embedded in Minkowski spacetime (M,η). The entangling sphere of radius R (disk in the 2D visualization) divides the network into an interior and an exterior sector. On the loop subgraph highlighted in blue, the entangling surface reduces to two entangling *points*, depicted with blue squares. Accordingly, the loop is divided into an interior and an exterior sector. Due to quantum field correlations across the entangling points, the exterior and interior sectors of the loop may be entangled, with the entanglement entropy quantifying the degree of entanglement.

small blue squares in Fig. 4.8, dividing the loop into an interior sector I and an exterior sector E that may be entangled.

The corresponding numerical entanglement entropy is shown in Fig. 4.6, in terms of the radius of the entangling sphere R, for two different values of μa. For numerical details we refer the reader to the code written for this analysis and published in [38]. For both cases $\mu a = 1$ and $\mu a = 10^{-1}$, the value of the entanglement entropy for fluctuations spatially confined to a loop crossing the entangling sphere at two different locations is twice the value computed for the single edge, i.e. $\bar{S}_{loop} = 2\bar{S}_{edge}$. For $\mu a = 10^{-1}$, this leads to $\bar{S}_{loop} = 2\bar{S}_{edge} = 2$.

This result is supported by the analytical computation of the entanglement entropy.

In fact, in the perturbative approach (Sec. 4.2.1), the matrix Ω for the loop configuration differs from Eq. (4.21) only in its submatrix Ω_{IE}, which is now given by

$$\Omega_{IE\,ij} = -\frac{\delta_{i,n}\delta_{j,1}}{2M} - \frac{\delta_{i,1}\delta_{j,N-n}}{2M}\,, \tag{4.25}$$

at first order in $1/M$. Moreover, recall that Ω_{IE} is a $n\times(N-n)$ matrix. We observe that Ω_{IE} now contains two non-vanishing elements, both corresponding to next-neighbor couplings. In fact, at this order in the inverse mass expansion, only next-neighbor couplings are relevant. This means that along the loop, any correlation between the interior and exterior can arise solely from correlations between lattice points that are adjacent to each other on opposite sides of the entangling sphere. The new term in Ω_{IE} suggests that the additional connection in K established a new communication channel along the loop, linking the interior and exterior of the entangling sphere. As a result, there are now two next-neighbor correlations contributing to entanglement, facilitated by the two intersections with the entangling sphere, represented as small blue squares in Fig. 4.8. Compared to Ω_{IE} as given in Eq. (4.21), the additional coupling introduces a new non-vanishing eigenvalue $\lambda_N = 1/8M^4$. This eigenvalue contributes an extra term independent of n to S in Eq. (4.20), effectively adding the same value as that introduced by λ_{n+1}. As a result, we obtain $S_{loop} = 2S_{edge}$, as in the numerical derivation.

This result can be understood also in terms of correlation lengths. Consider the entangling sphere radius R to be as in Fig. 4.8 such that two edges e_1, e_2 of the loop are intersected. Let $l_{1,2}$ be the size of the traced out subsystems along the first and second edge respectively, such that the total size of the traced out sector I of the loop is $l_1 + l_2$. If $1/\mu \ll \min(l_1, l_2, L_{e_1} - l_1, L_{e_2} - l_2)$, quantum field fluctuations residing in the exterior (interior) of each edge are solely entangled with those residing in the interior (exterior) of the same edge. In other words, for correlation lengths that meet the above condition, the loop configuration is effectively reduced to two decoupled single edges each piercing the entangling sphere at distinct locations. In this case, according to Sec. 4.2.1, the entanglement entropy on each edge can be expressed as $S^{\text{plat}}_{e_1}(\xi) = 1/6\ln(\xi/a)$ and $S^{\text{plat}}_{e_2}(\xi) = 1/6\ln(\xi/a)$ since $1/\mu \ll \min(l_1, L_{e_1} - l_1)$ and $1/\mu \ll \min(l_2, L_{e_2} - l_2)$ on each edge, respectively. Therefore, the total entanglement entropy for a field spatially confined to the loop results in $S_{\text{loop}}(R) = 1/3\ln(\xi/a) = 2S^{\text{plat}}$. As a consequence, it appears that for a quantum field mass μ such that $1/\mu \ll \min(l_i, L_{e_i} - l_i)$ on each intersected edge e_i, the entanglement entropy is fully determined by the number of communication channels established across the entangling sphere.

This result can be generalized to any configuration of $\mathcal{A}$ single edges intersecting the entangling sphere, provided that $1/\mu \ll \min(l_i, L_{e_i} - l_i)$ for each edge e_i, with $i \in \{1, \ldots, \mathcal{A}\}$. As indicated by the analysis above, even if the edges are connected through vertices, if the field confined to them has a mass satisfying the above condition for each edge, the total entanglement entropy for this configuration is given by

$$S(R) = \mathcal{A}\, S^{\text{plat}} = \frac{\mathcal{A}}{6} \ln\left(\frac{\xi}{a}\right) . \tag{4.26}$$

Therefore, within this range of masses, the total entanglement entropy can be determined by solely knowing the entanglement entropy for a field confined to a single edge. Note that this is in agreement with the proposal suggested in [33] based on the cluster decomposition principle of QFT.

Lastly, in the case of very long correlation lengths, i.e. $1/\mu \gg L_{e_i}$ on each edge of the loop, our numerical computation aligns with the analytical results for a single edge with periodic boundary conditions as investigated in [33, 40].

Having thoroughly examined the behavior of the entanglement entropy in elementary single-edge graph configurations intersected by the entangling sphere – gaining new insights while also reconciling established findings in the literature – we are now ready to embark on a completely new investigation into the entanglement properties of fields spatially confined to subgraphs where single edges connect at non-removable nodes, such as a star graph with three edges, as introduced in Sec. 3.2.2.

4.2.2 Entanglement Entropy on Three-Edge Star Graphs

With the above analysis of entanglement properties for quantum fields spatially confined to single-edge graphs, arising from the presence of an entangling sphere, we are now one step closer to investigating the same entanglement properties in the configuration shown in Fig. 4.2. It is evident that the entire network consists of single-edge graphs connected into nodes. After a comprehensive analysis of the entanglement entropy along these edges, we now only need to focus on what occurs at the nodes, where three or more edges meet. Once we achieve this, the entanglement entropy of quantum fields confined to the history of the arbitrary network considered above will be determined, and its possible agreement with $(1+3)$-dimensional results [9, 10] will be verified.

The most fundamental subgraph configuration of the network containing a single non-removable node consists of three edges connected at a vertex, forming a star graph $\mathcal{G}_3$

as depicted in Fig. 4.3. In the following, we aim to compute the entanglement entropy for a quantum field spatially confined to this subgraph. For simplicity, as in the previous section, we first consider the three-edge star graph to be completely disconnected from the rest of the network, such that for each edge, we impose Dirichlet boundary conditions at the endpoints that are not common to all three edges.

Following the construction of Sec. 3.2.2, we introduce a quantum field theory on the three-edge star graph. To this end, in each edge history H_{e_i}, we introduce a coordinate system $x_i = \{\xi_i^a\} = (T, \xi_i)$ and an action functional $\mathcal{A}_{e_i}[\phi_i]$ for a field ϕ_i. For the sake of notation, we let $i \in \{1, 2, 3\}$ in the following discussion. At the node worldline, we require continuity of the total field configuration on $\mathcal{G}_3$ by introducing Lagrange multiplier fields λ^{12}, λ^{23} so that the total action functional $\mathcal{A}_{\mathcal{G}_3}$ reads (Eq. (3.27))

$$\mathcal{A}_{\mathcal{G}_3}[\phi_1, \phi_2, \phi_3, \lambda^{12}, \lambda^{23}] = \mathcal{A}_{e_1}[\phi_1] + \mathcal{A}_{e_2}[\phi_2] + \mathcal{A}_{e_3}[\phi_3] + \mathcal{J}[\phi_1, \phi_2, \phi_3, \lambda^{12}, \lambda^{23}] \,, \tag{4.27}$$

where, as introduced in Sec. 3.2.2, $\mathcal{J}$ is a functional designed to ensure continuity for the total field configuration at the node worldline.

Within our analysis of the entanglement entropy, it is natural to focus on Lagrangian densities for free massive real scalar fields. Accordingly, on each two-dimensional edge's history H_{e_i}, we consider $\mathcal{L}_{e_i} = \frac{1}{2}\left(\eta^{ab}\partial_a\phi_i\,\partial_b\phi_i - \mu^2\phi_i^2\right)$, where μ is the mass of the field and η the two-dimensional Minkowski metric. As derived in Sec. 3.2.2, when the subgraph $\mathcal{G}_3$ is embedded in the Minkowski spacetime, along with the equations of motion $-\partial_T^2\phi_i + \partial_{\xi_i}^2\phi_i + \mu^2\phi_i = 0$ for each ϕ_i on H_{e_i}, the following Kirchhoff-Neumann conditions on $\mathcal{G}_3$ hold at the node worldline $v(T)$ (Eq. (3.50))

$$\begin{cases} \lim\limits_{\epsilon\to 0} \phi_1 \Big|_{v(T)-\epsilon}^{1\to v} \overset{!}{=} \phi_2 \Big|_{v(T)} \overset{!}{=} \lim\limits_{\epsilon\to 0} \phi_3 \Big|_{v(T)-\epsilon}^{3\to v} \,, \\ \lim\limits_{\epsilon\to 0} \partial_{\xi_1}\phi_1 \Big|_{v(T)-\epsilon}^{1\to v} + \partial_{\xi_2}\phi_2 \Big|_{v(T)} + \lim\limits_{\epsilon\to 0} \partial_{\xi_3}\phi_3 \Big|_{v(T)-\epsilon}^{3\to v} \overset{!}{=} 0 \,, \end{cases} \tag{4.28}$$

where ϵ is a constant, infinitesimal distance from $v(T)$ and we assume that the vertex worldline belongs to the domain of ϕ_2. For additional details regarding this construction, we refer the reader to Sec. 3.2.2. We recall that Dirichlet boundary conditions hold at the free endpoints of the three edges. For a visualization of the continuity condition, the first equation of Eq. (4.28), we refer to Fig. 3.9.

The matrices A and B (Eq. (3.51)) associated with the above Kirchhoff-Neumann conditions read,

$$A = \begin{pmatrix} 1 & -1 & 0 \\ 0 & 1 & -1 \\ 0 & 0 & 0 \end{pmatrix}, \quad B = \begin{pmatrix} 0 & 0 & 0 \\ 0 & 0 & 0 \\ 1 & 1 & 1 \end{pmatrix}. \tag{4.29}$$

Since the 3×6 composite matrix (A, B) has rank 3 and $AB^\dagger$ is self-adjoint for this form of A and B, the Laplace operator – defined as $\partial^2_{\xi_i}\phi_i$ on each e_i – is also self-adjoint on $\mathcal{G}_3$ [16, 19]. Thus, on each edge history H_{e_i}, we can use its eigenfunctions to construct quantum field and conjugate momentum operators.

To this aim, from each Lagrangian density $\mathcal{L}_{e_i}$, we introduce the corresponding conjugate field momentum $\pi_i(T, \xi_i) = \frac{\partial \mathcal{L}_{e_i}}{\partial(\partial_T \phi_i)}$. The quantum field ϕ_i and the conjugate momentum operator π_i then satisfy the canonical equal-time commutation relations on each edge history H_{e_i},

$$\begin{aligned} &[\phi_i(T, \xi_i), \pi_i(T, \xi_i')] = i\delta(\xi_i - \xi_i'), \\ &[\phi_i(T, \xi_i), \phi_i(T, \xi_i')] = [\pi_i(T, \xi_i), \pi_i(T, \xi_i')] = 0. \end{aligned} \tag{4.30}$$

with $i \in \{1, 2, 3\}$.

By performing a Legendre transformation, we derive the associated Hamiltonian density $\mathcal{H}_{e_i}(T, \xi_i, \phi_i, \pi_i)$ from each Lagrangian density $\mathcal{L}_{e_i}$ defined on the history of each edge of $\mathcal{G}_3$. Each Hamiltonian density is given by $\mathcal{H}_{e_i} = \frac{1}{2}\left[\pi_i^2(T, \xi_i) + (\partial_{\xi_i}\phi_i(T, \xi_i))^2 + \mu^2\phi_i^2(T, \xi_i)\right]$.

As explained in Sec. 4.2.1, in order to compute the entanglement entropy for a field spatially confined to $\mathcal{G}_3$, it is convenient to adopt the Schrödinger representation of quantum field theory. For the construction of the quantum field theory on the star graph in the Heisenberg representation, we refer the reader to [20, 21]. Within the Schrödinger picture, we can promote the Hamiltonian on each edge history to the following Hamiltonian functional differential operator

$$H_i = \int \mathcal{H}_{e_i}\, d\xi_i = \frac{1}{2}\int \left[\pi_i^2(\xi_i) + (\partial_{\xi_i}\phi_i(\xi_i))^2 + \mu^2\phi_i^2(\xi_i)\right] d\xi_i, \tag{4.31}$$

where the functional differential representation of the conjugate momentum field π_i is $\pi_i(\xi_i) = -i\frac{\delta}{\delta\phi_i(\xi_i)}$. Note that both ϕ_i, π_i and consequently the Hamiltonian operator H_i, are time-independent. Furthermore, the form of the Kirchhoff-Neumann conditions in Eq. (4.28) ensures that the scattering matrix associated with the node of $\mathcal{G}_3$ is unitary [16, 19].

Consider a basis of eigenstates $\{|\phi_i\rangle\}$ of ϕ_i. By introducing the wave functional $\Psi_i[\phi_i] = \langle\psi_i|\phi_i\rangle$, which represents the coordinate representation of the time-dependent state $|\psi_i\rangle$ in terms of $\{|\phi_i\rangle\}$, we can write, on each edge history, a Schrödinger-like equation for the quantum field theory in functional differential form

$$i\frac{\partial}{\partial T}\Psi_i[\phi_i] = H_i\Psi_i[\phi_i]\,. \tag{4.32}$$

The above equation fully characterizes the time evolution of the wave functional $\Psi_i[\phi_i]$. On each edge history H_{e_i}, the normalized ground state wave functional for a free real scalar field operator ϕ_i can be found to be [36],

$$\begin{aligned}\Psi_{0\,i}[\phi_i] &= \langle\phi_i|0\rangle = \left(\det\left(\tfrac{\Omega_i}{\pi}\right)\right)^{1/4}\exp\left(-\tfrac{1}{2}\int d\xi_i\int d\xi_i'\phi_i(\xi_i)\,\Omega_i(\xi_i,\xi_i')\,\phi_i(\xi_i')\right) = \\ &= \left(\det\left(\tfrac{\Omega_i}{\pi}\right)\right)^{1/4}\exp\left(-\tfrac{1}{2}\phi_i\cdot\Omega_i\cdot\phi_i\right)\,,\end{aligned} \tag{4.33}$$

where Ω_i is given as $\Omega_i(\xi_i,\xi_i') = \int\frac{dk}{2\pi}\,\omega_k\,e^{ik(\xi_i-\xi_i')}$. In what follows, we assume that each field ϕ_i is in its ground state on the corresponding edge history H_{e_i}, and we consider the total ground state wave functional on the history of $\mathcal{G}_3$ as $\mathbf{\Psi}_{0\,\mathcal{G}_3} = (\Psi_{0\,1},\Psi_{0\,2},\Psi_{0\,3})$.

Now that we have defined a quantum field configuration spatially confined to the elementary subgraph $\mathcal{G}_3$, we perform instantaneous measurements to study entanglement properties arising from an entangling sphere intersecting the subgraph.

Consider the three-edge star graph highlighted in green in Fig. 4.9. On a spacelike hypersurface Σ_T, the entangling sphere divides the quantum field configuration on $\mathcal{G}_3$ in an interior sector I and an exterior one E. The cross section between the star graph and the entangling sphere, at the radius shown in the figure, consists of two entangling *points*, depicted as green squares in the figure. The entangling points trace out an interval along each intersected edge, effectively reducing the entanglement analysis on $\mathcal{G}_3$ to the same framework used for single-edge graphs. However, one endpoint of each edge is connected to the other two edges via a (non-removable) node. We now aim to explore how the presence of this node influences the entanglement entropy for the quantum field configuration spatially confined to $\mathcal{G}_3$.

According to our discussion of previous sections, we equip the star graph with a finite resolution structure, obtaining a regularized entanglement entropy $S_{\mathcal{G}_3}$ for the quantum field spatially confined to the subgraph. On each edge e_i, the quantum field is spatially restricted to a one-dimensional lattice of N_{e_i} sites, with constant spacing $a \in \mathbb{R}^+$. Note that

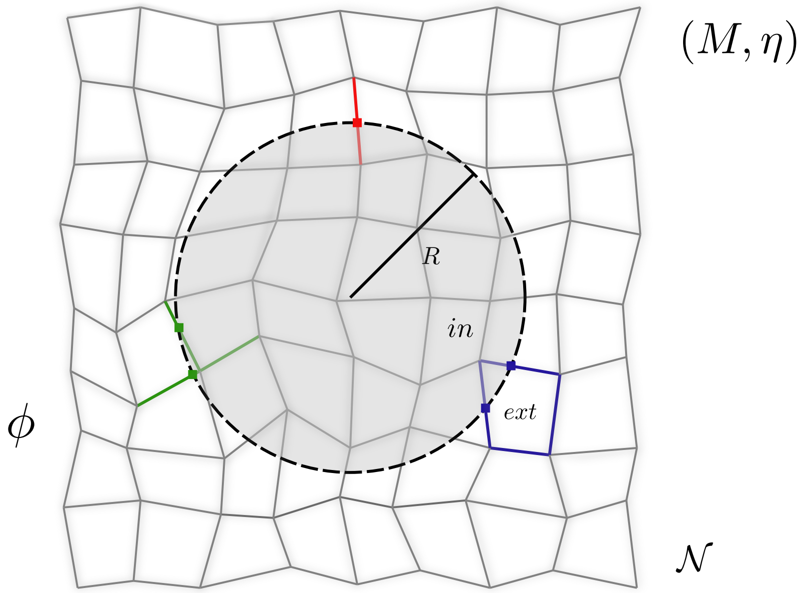

Figure 4.9: Spatial two-dimensional section of Fig. 4.2 for a quantum field ϕ (depicted in gray shades) spatially confined to the arbitrary three-dimensional network $\mathcal{N}$ embedded in Minkowski spacetime (M, η). The entangling sphere of radius R (disk in the 2D visualization) divides the network into an interior and an exterior sector.
On the three-edge star graph highlighted in green, the entangling surface reduces to two entangling *points*, depicted with small green squares. Accordingly, the star graph is divided into an interior and an exterior sector. Due to quantum field correlations across the entangling points, the exterior and interior sectors of $\mathcal{G}_3$ may be entangled, with the entanglement entropy quantifying the degree of entanglement.

since a represents the extrinsic distance scale determined by the experimental apparatus, it is assumed to be identical for each edge. For clarity, we introduce the notation (i, k) where i labels the edge, and k denotes the sites along the lattice; $i \in \{1, 2, 3\}$ and $k \in \{1, \dots, N_{e_i}\}$. Each lattice point has the position $\xi_{(i,k)} = ka$ along the edge e_i. Note that the edge endpoints are denoted by $\xi_{(i,0)}$ and $\xi_{(i,N_{e_i}+1)}$. Finally, the length of each edge is $L_{e_i} = (N_{e_i} + 1)a$.

According to the finite resolution structure, each Hamiltonian H_i given in Eq. (4.31) is reduced to

$$H_i = \frac{1}{2a}\left\{\sum_{k=1}^{N_{e_i}}\left[\pi^2_{(i,\,k)} - \phi_{(i,\,k)}\left(\phi_{(i,\,k+1)} - 2\,\phi_{(i,\,k)} + \phi_{(i,\,k-1)}\right) + \mu^2 a^2\,\phi^2_{(i,\,k)}\right]\right\}\,, \tag{4.34}$$

where we integrated by parts Eq. (4.31) and we discretized according to Eq. (4.9). Note that μa is dimensionless and $\pi_{(i,\,k)}$ and $\phi_{(i,\,k)}$ satisfy $[\phi_{(i,\,k)}, \frac{\pi_{(i,\,k')}}{a}] = i\frac{\delta_{kk'}}{a}$. Furthermore, by integrating by parts, we obtain boundary terms for each H_i, which satisfy the boundary conditions imposed through the variational principle and result, in our case, in a total vanishing contribution. The discretized version of Dirichlet boundary conditions at one endpoint of each edge leads to $\phi_{(1,\,N_{e_1}+1)} = \phi_{(2,\,N_{e_2}+1)} = \phi_{(3,\,N_{e_3}+1)} = 0$. The Kirchhoff-Neumann conditions at the node v are discretized in the following way [41]. Consider Eq. (4.28) and the associated form of the matrices A and B as in Eq. (4.29). As discussed in Sec. 3.2.2, the Kirchhoff-Neumann conditions can be expressed in the general form:

$$A\,\Phi(T,v) + B\,\Phi'(T,v) = 0\,, \tag{4.35}$$

at the node worldline. In our case, it reads

$$\begin{pmatrix}1 & -1 & 0\\ 0 & 1 & -1\\ 0 & 0 & 0\end{pmatrix}\begin{pmatrix}\phi_1\,|_v\\ \phi_2\,|_v\\ \phi_3\,|_v\end{pmatrix} + \begin{pmatrix}0 & 0 & 0\\ 0 & 0 & 0\\ 1 & 1 & 1\end{pmatrix}\begin{pmatrix}\partial_{\xi_1}\phi_1\,|_v\\ \partial_{\xi_2}\phi_2\,|_v\\ \partial_{\xi_3}\phi_3\,|_v\end{pmatrix} = 0\,. \tag{4.36}$$

Recall that while $\phi_i\,|_v$ denotes the value of the field ϕ_i at the vertex v of $\mathcal{G}_3$ for each time T, we introduced the field theory on the star graph such that the vertex worldline belongs only to the domain of ϕ_2. Since the node is located at $\xi_{(i,\,0)}$ for each edge e_i, $\phi_2\,|_v$ translates to $\phi_{(2,\,0)}$ in the discretization scheme. However, based on our construction, $\phi_1\,|_v = \lim_{\epsilon\to 0}\,\phi_1\,|^{1\to v}_{v(T)-\epsilon}$ and $\phi_3\,|_v = \lim_{\epsilon\to 0}\,\phi_3\,|^{3\to v}_{v(T)-\epsilon}$. Due to the resolution structure, the field at locations between $\xi_{(i,\,0)}$ and $\xi_{(i,\,1)}$ cannot be resolved and an infinitesimal distance ϵ away from the vertex is still associated with the node. Therefore, given the minimal distance scale a, within the finite resolution structure we can claim that also $\lim_{\epsilon\to 0}\,\phi_1\,|^{1\to v}_{v(T)-\epsilon}$ and $\lim_{\epsilon\to 0}\,\phi_3\,|^{3\to v}_{v(T)-\epsilon}$ reduce to $\phi_{(1,\,0)}$ and $\phi_{(3,\,0)}$, respectively. On the other hand, following the discretization rule given in Eq. (4.9), $\partial_{\xi_i}\phi_i$ corresponds to $\left(\phi_{(i,\,k+1)} - \phi_{(i,\,k)}\right)/a$. In the light of the previous discussion, when evaluated at the vertex worldline, $\partial_{\xi_i}\phi_i\,|_v$ becomes $\left(\phi_{(i,\,1)} - \phi_{(i,\,0)}\right)/a$ for all values of i.

Therefore, the discretized version of the Kirchhoff-Neumann conditions in Eq. (4.36), can be expressed as

$$\begin{pmatrix}1 & -1 & 0\\ 0 & 1 & -1\\ 0 & 0 & 0\end{pmatrix}\begin{pmatrix}\phi_{(1,0)}\\ \phi_{(2,0)}\\ \phi_{(3,0)}\end{pmatrix}+\frac{1}{a}\begin{pmatrix}0 & 0 & 0\\ 0 & 0 & 0\\ 1 & 1 & 1\end{pmatrix}\begin{pmatrix}\phi_{(1,1)}-\phi_{(1,0)}\\ \phi_{(2,1)}-\phi_{(2,0)}\\ \phi_{(3,1)}-\phi_{(3,0)}\end{pmatrix}=0\,. \tag{4.37}$$

In particular, solving this equation for $\phi_{(1,0)}$, $\phi_{(2,0)}$ and $\phi_{(3,0)}$, the Kirchhoff-Neumann conditions provide

$$\phi_{(i,0)}=\frac{1}{3}\sum_{j=1}^{3}\phi_{(j,1)}\,. \tag{4.38}$$

Note that, unlike the single-edge case where Dirichlet boundary conditions were imposed at each edge endpoint, $\phi_{(i,0)}$ is now non-vanishing. Specifically, each boundary value $\phi_{(i,0)}$ is expressed in terms of internal sites, which are also associated with other edges. This suggests that the three lattices are indeed connected, further highlighting the junction-like nature of the Kirchhoff-Neumann conditions.

Finally, along the lines of Sec. 4.2.1, due to the finite resolution structure the function $\Omega_i(\xi_i,\xi_i')$ in Eq. (4.33), reduces to a matrix $\Omega_i=\sqrt{K}_i$, defined such that if there is a orthogonal matrix U with $K_i=U^T K_{i\,D}U$, where $K_{i\,D}$ is diagonal, then $\Omega_i=U^T\sqrt{K}_{i\,D}U$. Recall that the label i refers to the considered edge e_i on which K_i or Ω_i are defined and it is not to be considered as an index. As a result, the ground state wave functional $\Psi_{0\,i}[\phi_i]$ of Eq. (4.33) reduces to the wavefunction

$$\Psi_{0\,i}(\boldsymbol{\phi}_i)=a^{N_{e_i}/2}\,\pi^{-N_{e_i}/4}\left(\det\left(\Omega_i\right)\right)^{1/4}\exp\left(-\tfrac{1}{2}\boldsymbol{\phi}_i\cdot\left(\Omega_i\boldsymbol{\phi}_i\right)\right), \tag{4.39}$$

where $\boldsymbol{\phi}_i:=(\phi_{(i,1)},\ldots,\phi_{(i,k)},\ldots,\phi_{(i,N_{e_i})})$ and $a^{N_{e_i}/2}\left(\det\left(\Omega_i\right)\right)^{1/4}$ is a dimensionless quantity. Consequently, $\boldsymbol{\Psi}_{0\,\mathcal{G}_3}=(\Psi_{0\,1},\Psi_{0\,2},\Psi_{0\,3})$ also reduces to the total wave function on the history of $\mathcal{G}_3$.

With all this in mind, we can express the total Hamiltonian operator $H_{\mathcal{G}_3}$ on $\mathcal{G}_3$, acting on $\mathbf{\Psi}_{0\,\mathcal{G}_3} = (\Psi_{0\,1}, \Psi_{0\,2}, \Psi_{0\,3})$ as a $(N_{e_1}+N_{e_2}+N_{e_3}) \times (N_{e_1}+N_{e_2}+N_{e_3})$ matrix of the form

$$H_{\mathcal{G}_3} = \begin{pmatrix} \boxed{H_1} & \dots & 0 \\ \vdots & \boxed{H_2} & \vdots \\ 0 & \dots & \boxed{H_3} \end{pmatrix} + \mathcal{C}\,, \tag{4.40}$$

where $\mathcal{C}$ is a matrix that accounts for possible couplings between lattice sites on different edges. Note that each Hamiltonian operator H_i acts on the corresponding ground state wave function $\Psi_{0\,i}(\boldsymbol{\phi}_i)$.

Considering the form of each discretized Hamiltonian H_i as given in Eq. (4.34), together with the boundary conditions specified above, we can find the matrix $K_{\mathcal{G}_3}$ associated with the above matrix $H_{\mathcal{G}_3}$. Note that $K_{\mathcal{G}_3}$ is also a $(N_{e_1}+N_{e_2}+N_{e_3}) \times (N_{e_1}+N_{e_2}+N_{e_3})$ matrix and encodes all the couplings between the $N_{e_1}+N_{e_2}+N_{e_3}$ lattice sites located on $\mathcal{G}_3$.

The above condition $\phi_{(i,0)} = \frac{1}{3}\left[\phi_{(1,1)} + \phi_{(2,1)} + \phi_{(3,1)}\right]$ for all i, produces a non-vanishing term of the form $-\phi_{(i,1)}\phi_{(i,0)} = -\frac{1}{3}\phi_{(i,1)}\left(\phi_{(1,1)} + \phi_{(2,1)} + \phi_{(3,1)}\right)$ in $H_{\mathcal{G}_3}$, specifically in $\mathcal{C}$. In particular, this term couples the first lattice point of the edge e_i with the first lattice sites of the other two edges as next-neighbors. For instance, in the case of $i=1$ this provides the terms $-\frac{1}{3}\phi_{(1,1)}\,\phi_{(2,1)}$ and $-\frac{1}{3}\phi_{(1,1)}\,\phi_{(3,1)}$. As a consequence, new coupling terms in $K_{\mathcal{G}_3}$, between the first lattice points located on each edge, are introduced, effectively junctioning the three lattices together. It is important to note that the coupling strength of $-\frac{1}{3}$ is equally distributed among the three sites $\phi_{(i,1)}$ and is weaker than the couplings between consecutive sites along the same edge, $-\phi_{(i,k)}\,\phi_{(i,k+1)}$. For a clearer understanding of how the discretized Kirchhoff-Neumann conditions give rise to an effective node between the first sites of the three lattices, we refer to Fig. 4.10.

Numerical Entanglement Entropy

Incorporating all the boundary conditions, we obtain the final form of the matrix $K_{\mathcal{G}_3}$ related to the subgraph $\mathcal{G}_3$ of Fig. 4.9. Therefore, following the same steps as in Sec. 4.2.1, we can introduce the matrix $\Omega_{\mathcal{G}_3}$ to compute the entanglement entropy as in Eq. (4.4), for vacuum fluctuations spatially confined to $\mathcal{G}_3$ and reduced to a system of $N_{e_1}+N_{e_2}+N_{e_3}$

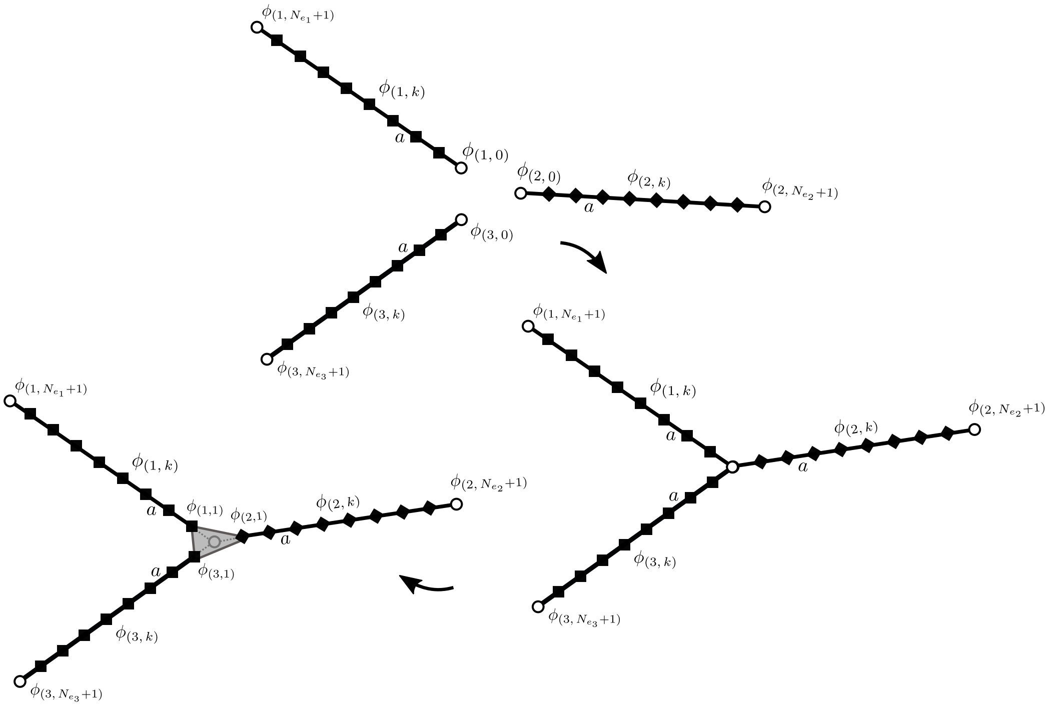

Figure 4.10: Visualization of the discretized Kirchhoff-Neumann conditions at the node of a three-edge star graph. The extrinsic distance scale a imposes a finite resolution structure on the three edges e_1, e_2 and e_3 restricting the fields ϕ_1, ϕ_2 and ϕ_3 to spatial one-dimensional lattices of N_{e_i} sites with constant spacing a. The white circles represent the boundary sites of the lattices, denoted by $\phi_{(i,0)}$ and $\phi_{(i,N_{e_i}+1)}$ for all i. Couplings between lattice sites on the same edge e_i are depicted as black lines and are of the form $-\phi_{(i,k)}\phi_{(i,k+1)}$. Note that for clarity, the figure only depicts the three lattices themselves and omits the underlying edges, which are of course connected at the node, forming the star graph structure. Dirichlet boundary conditions are applied at the free endpoints, so that $\phi_{(i,N_{e_i}+1)} = 0$ for all i. Reading the figure clockwise, the first condition in Eq. (4.28) enforces that, at the vertex, all boundary sites must agree, resulting in $\phi_{(1,0)} = \phi_{(2,0)} = \phi_{(3,0)}$. Consequently, the lattices are connected through each $-\phi_{(i,1)}\phi_{(i,0)}$ term. Together with the second condition in Eq. (4.28) then this dictates that, since $\phi_{(i,0)} = \frac{1}{3}\left[\phi_{(1,1)} + \phi_{(2,1)} + \phi_{(3,1)}\right]$, each $\phi_{(i,1)}$ is coupled to $\phi_{(j,1)}$ for all i, j, (dark gray lines in the picture) as next-neighbors, with the coupling strength equally distributed as $-1/3$. This results in the emergence of an effective node between the first sites of the lattices.

lattice points.

To this end, we developed and implemented the code published in [38], assuming, for simplicity, the same number of lattice sites N on each edge. The entanglement entropy in terms of the radius of the entangling sphere is reported in Fig. 4.11, for different values of μa. To facilitate reading the plot, we refer to Fig. 4.9.

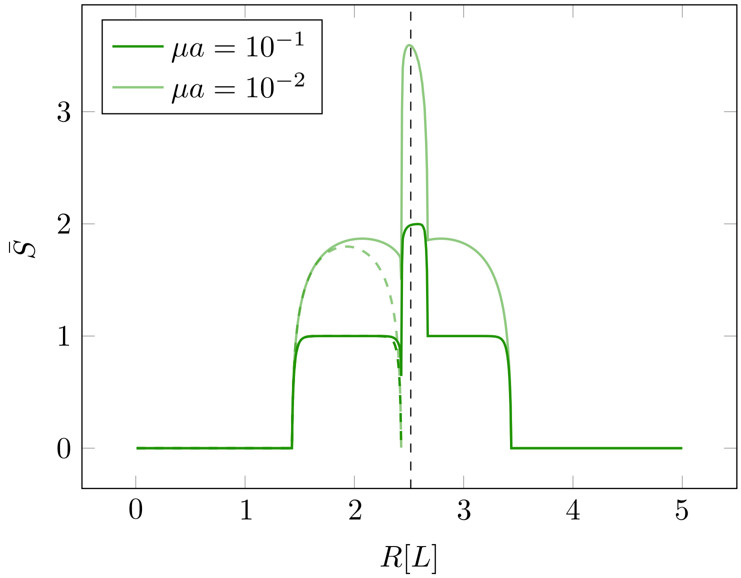

Figure 4.11: Entanglement entropy for vacuum fluctuations spatially confined to the elementary subgraph $\mathcal{G}_3$ of a network $\mathcal{N}$ as shown in Fig. 4.9, in terms of the radius of the entangling sphere. In particular, the entanglement entropy is given for the three-edge star graph equipped with a finite resolution structure consisting of $N = 300$ lattice sites on each edge, for two different choices of μa. The radius of the entangling sphere is expressed in multiples of the length L of the single edge. The value explicitly chosen in Fig. 4.9, $R = 2.5L$, is marked by a vertical dashed line. For comparison, the entanglement entropy of vacuum fluctuations spatially confined to a single edge with Dirichlet boundary conditions at both endpoints is depicted by dashed green lines, also for $N = 300$ lattice sites and the same two values of μa.

As a starting point, consider the radius R of the entangling sphere to have values smaller than $R = 1.4L$. In this configuration, the entangling sphere does not cross $\mathcal{G}_3$ and no lattice sites are traced out, resulting in a vanishing entanglement entropy, as confirmed by Fig. 4.11. As the radius of the entangling sphere grows, it begins to intersect the first edge of $\mathcal{G}_3$, gradually tracing out more sites along this edge. Since, for these values of R, the cross section between $\mathcal{G}_3$ and the entangling sphere is only a point, there is only one communication channel between the interior and the exterior of the entangling surface, along $\mathcal{G}_3$. As the radius continues to grow and approaches $R = 2.4L$, the vertex of the subgraph is reached. Increasing the radius further, part of the second and third edge is traced out, while the first edge is completely traced out and fully enclosed within the interior of the entangling sphere. In particular, Fig. 4.9 illustrates the configuration at $R = 2.5L$. As a result, for values of R in the range $2.4L < R < 2.7L$, two communication channels are established between the interior and exterior of the entangling sphere. Finally, for $R \geq 2.7L$ the second edge is also entirely within the entangling sphere (Fig. 4.9), leaving only the third edge partially traced out. This configuration is fully symmetric to the initial one, where only the first edge crossed the entangling sphere, and the other two edges resided completely in its exterior.

As a first observation, we notice that for lower values of μa, the entanglement entropy increases, as discussed and explained in Sec. 4.2.1. Specifically, for $\mu a = 10^{-1}$, we find that for $R < 2.4L$ and $R \geq 2.7L$ the entanglement entropy matches that of vacuum fluctuations with the same mass spatially confined to a single edge with Dirichlet boundary conditions: $\bar{S} = \bar{S}_{edge} = 1$. In fact, in these two ranges of radii, only a single communication channel exists between the interior and exterior of the entangling sphere. Since $\mu a = 10^{-1}$ satisfies $a \ll 1/\mu \ll L$ on each edge, it ensures that, sufficiently far from the edge endpoints, the entanglement entropy is described by Eq. (4.26) with $\mathcal{A} = 1$, just as it would be in the case of a single-edge graph. Since Dirichlet boundary conditions are imposed at the free endpoints of each edge in $\mathcal{G}_3$, the two configurations become indistinguishable for values of R sufficiently far from the node of $\mathcal{G}_3$. For comparison, the entanglement entropies of vacuum fluctuations spatially confined to a single edge of the same length L, with Dirichlet boundary conditions at both endpoints, are shown as green dashed lines for $R < 2.4L$, again considering $N = 300$ sites and the two values of μa.

Similarly, for $2.4L < R < 2.7L$, the entangling sphere intersects $\mathcal{G}_3$ at two points, and for $\mu a = 10^{-1}$ we obtain $\bar{S} = 2\bar{S}_{edge} = 2$, sufficiently away from the node of $\mathcal{G}_3$ and the free endpoint of the second edge, consistent with our previous discussion.

For $R = 2.4L$, the entangling sphere reaches the vertex of the graph. Due to the implementation of Kirchhoff-Neumann conditions at the node of $\mathcal{G}_3$, the field content at the vertex is represented by the final configuration in the bottom left of Fig. 4.10, that is, the first three lattice sites of each edge are coupled together. As the entangling sphere reaches the vertex, it resolves this structure, which in turn affects the entanglement entropy. Therefore, the specific configuration of the Kirchhoff-Neumann conditions at the node plays a fundamental role in the analysis. Fig. 4.11 captures its influence on the entanglement entropy. As discussed earlier, the three sites at the vertex, responsible for connecting the three lattices, are coupled through weaker interactions. Specifically, the coupling terms $-\frac{1}{3}\phi_{(i,1)}\phi_{(j,1)}$ set interactions three times weaker as the usual $-\phi_{(i,k)}\phi_{(i,k+1)}$ interactions. Consequently, when the radius of the entangling sphere approaches the node and the lattice points contributing to entanglement – those within a distance $\xi = 1/\mu$ from the intersection point – include some located beyond the vertex on a different edge, the total contribution to the entanglement entropy becomes smaller than it would be if they were all along the same edge. In fact, any possible correlations that contribute to entanglement must pass through the vertex, and thus through the weaker couplings $-\frac{1}{3}\phi_{(i,1)}\phi_{(j,1)}$. As a result, the entanglement entropy is decreased compared to its value for radii sufficiently smaller than $R = 2.4L$, as shown in the plot Fig. 4.11. Note that the minimum entanglement entropy is reached when the entangling surface lies between a pair of lattice points $\phi_{(i,1)}$, $\phi_{(j,1)}$. In fact, although two communication channels are now established in the system, their weaker direct correlations contributes the most to the entanglement.

In particular, note that if the Kirchhoff-Neumann conditions were not implemented and Dirichlet boundary conditions were instead imposed at $R = 2.4L$, the lattice site $\phi_{(i,1)}$ on the first edge e_i would not be coupled to the ones of other edges. As a result, no correlations would occur through these couplings to other edges, and as the intersection point on the edge approaches its endpoint, fewer lattice sites would contribute to the entanglement compared to the case where a node replaces the endpoint. In fact, as shown in Fig. 4.11, as the radius approaches $R = 2.4L$, the entanglement entropy for vacuum fluctuation spatially confined to $\mathcal{G}_3$ is larger than that for vacuum fluctuations confined to the single-edge configuration with Dirichlet boundary conditions at both endpoints, depicted by the dashed green lines. For lower masses, e.g. $\mu a = 10^{-2}$, the effect becomes even more pronounced. In fact, due to the longer correlation length $\xi = 1/\mu$, more lattice sites on $\mathcal{G}_3$ contribute to entanglement, resulting in a much larger deviation in the entanglement entropy compared to that of the same vacuum fluctuations on a single edge with Dirichlet boundary conditions. In particular, the entanglement entropy in Fig. 4.11 does not vanish at $R = 2.4L$, unlike in the single-edge case with Dirichlet boundary conditions. This highlights the fact that, under the Kirchhoff-Neumann conditions, the vertex functions as a junction rather than a boundary, allowing the system to extend to the other two edges.

Furthermore, an interesting effect arises when the free endpoints of two edges of $\mathcal{G}_3$ are connected to form a loop. Since the subgraph is embedded in Minkowski spacetime, the configuration is equivalent to the one depicted in green in Fig. 4.12. To investigate the entanglement entropy for such a graph configuration, we developed the code available in [38]. The entanglement entropy in terms of the radius of the entangling sphere is shown in Fig. 4.13, for $\mu a = 10^{-1}$. As a result, we find that for R close to the vertex, the entanglement entropy for vacuum fluctuations on this configuration is significantly increased – surpassing even the plateau value S^{plat} – compared to the entanglement entropy relative to $\mathcal{G}_3$, provided the size of the loop is sufficiently small. To understand this result,

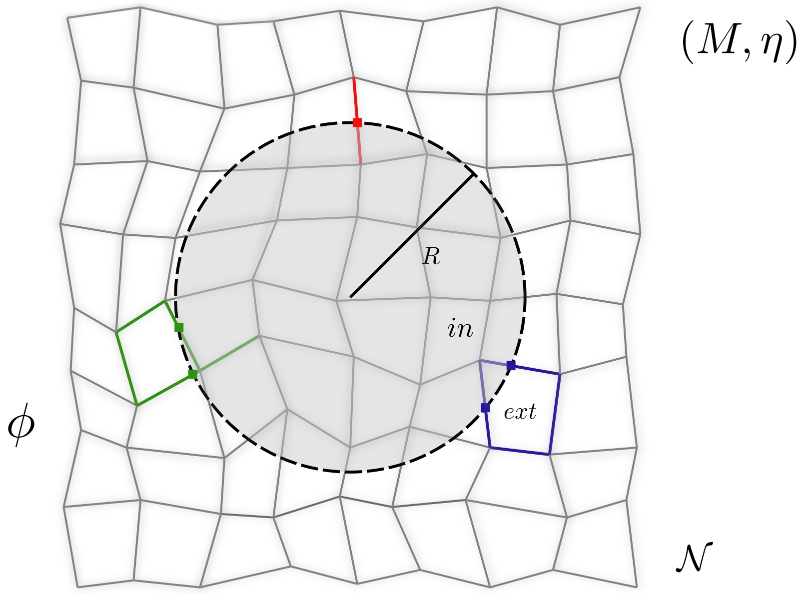

Figure 4.12: Spatial two-dimensional section of Fig. 4.2 for a quantum field ϕ (depicted in gray shades) spatially confined to the arbitrary three-dimensional network $\mathcal{N}$ embedded in Minkowski spacetime (M, η). The entangling sphere of radius R (disk in the 2D visualization) divides the network into an interior and an exterior sector. The subgraph highlighted in green is equivalent to the configuration of the three-edge star graph of Fig. 4.9, with two edges' free endpoints connected together.

recall that, for $R < 2.4L$ the entangling sphere intersects only the first edge in Fig. 4.12, while the loop resides entirely in its exterior. As R approaches the node at $R = 2.4L$, the presence of the loop introduces additional correlations between lattice sites inside and outside the entangling surface along the subgraph, compared to the configuration of $\mathcal{G}_3$. In fact, if the loop length is comparable to or smaller than the correlation length $\xi = 1/\mu$ for a given mass, a lattice site inside the entangling sphere on the first edge of Fig. 4.12 can be correlated with a site on the loop outside the entangling sphere both directly and through an extended correlation that travels around the entire loop, eventually reaching the same site on the loop again.

If the loop size exceeds the typical correlation length, such that ξ is not even sufficient to span half of the loop, the loop is effectively "cut" with respect to the quantum information measure we use, and the network configuration becomes effectively equivalent to $\mathcal{G}_3$. This

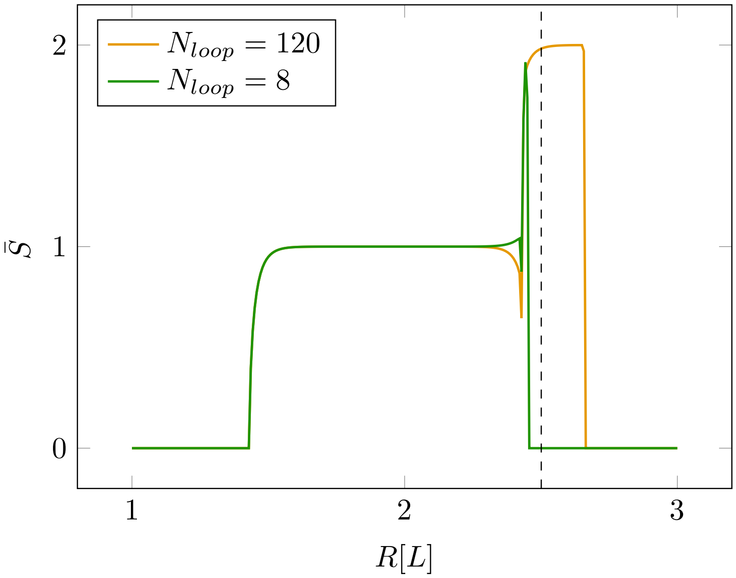

Figure 4.13: Entanglement entropy for vacuum fluctuations spatially confined to the elementary subgraph of a network $\mathcal{N}$, highlighted in green in Fig. 4.12, in terms of the radius of the entangling sphere. The subgraph is equipped with a finite resolution structure consisting of $N = 140$ lattice sites along the edge with a free endpoint, with the entanglement entropy shown for two different choices of the number of lattice sites along the loop: $N_{loop} = 120$ (orange) and $N_{loop} = 8$ (green). The radius of the entangling sphere explicitly chosen in Fig. 4.12, $R = 2.5L$, is marked by a vertical dashed line.

demonstrates that near the vertex, although the entanglement entropy decreases due to the Kirchhoff-Neumann conditions, the influence of the loop is still strong enough to counteract this effect and significantly increase the entanglement.

In conclusion, we have learned that the entanglement entropy for vacuum fluctuations spatially confined to the most elementary subgraph of $\mathcal{N}$ containing a node, is determined by the interplay of all these effects. When considering the radius of the entangling sphere crossing one of the three edges, for example, $R < 2.4L$, and approaching the node, we first observe deviations from the entanglement properties of the same vacuum fluctuations on a single edge with Dirichlet boundary conditions at both endpoints. The presence of a node at one of the edge endpoints, along with the implementation of Kirchhoff-Neumann conditions, introduces a range of new effects.

As a general rule, we can conclude that three key factors appear to influence the entanglement in the system, that is, the amount and strength of quantum correlations between the interior and exterior of the entangling surface. First, entanglement can be increased by increasing the number of lattice points correlated across the entangling sphere for the same vacuum fluctuation mass. This is facilitated by the presence of a node, which allows new correlations between lattice points within the traced-out interval on one edge and sites on different edges. The more edges connected to the node, the more new lattice sites can be correlated, resulting in an overall increase in entanglement. Second, the correlations across the node are weaker than those between sites on the same lattice due to the Kirchhoff-Neumann conditions at the vertex worldline, as illustrated in Fig. 4.10. Thus, although the node introduces additional correlations into the system, these correlations are weaker, leading to a decrease in entanglement compared to the case where the same amount of lattice sites would be coupled with the usual strength along a single, longer lattice. Third, the configuration of edges beyond the vertex also influences the entanglement entropy; for instance, for the same number of lattice sites, loop configurations joining the node introduce additional correlations between the interior and exterior of the entangling surface.

As a result, even though for $R < 2.4L$ only one communication channel across the entangling sphere is established, sufficiently close to the node the entanglement entropy of the entire subgraph is governed by its topology, rather than solely by the number of intersections with the entangling sphere. For the first time, the quantum information measure we use proves to be sensitive to the local structure of the network, probing the freedom to explore different spatial directions enabled by the non-removable node and consequently resolving the spatial extension of the network in the ambient space.

In this sense, for vacuum fluctuations with masses such that $\xi > L_{e_i}$ on the partially traced-out edge e_i, or for values within the range $a \ll 1/\mu \ll L_{e_i}$ but with the entangling surface sufficiently close to the node, the simple three-edge star graph $\mathcal{G}_3$ becomes the first graph configuration where a $(1+1)$-dimensional quantum field theory description proves insufficient, highlighting the relevance of a broader theoretical framework, such as our quantum network model.

With these findings for the entanglement entropy of quantum fields spatially confined to the most elementary subgraph of $\mathcal{N}$ containing a non-removable node, we are ready to investigate arbitrary, more complex networks, constructed by connecting multiple star graphs together.

4.3 Entanglement on Network Histories in Minkowski

Before constructing and detailing the procedure required to compute the entanglement entropy for general, arbitrary networks, we can use the results and intuition developed from the analysis of entanglement entropy on elementary graphs, to infer its qualitative behavior on more complex networks.

In fact, consider an arbitrary quantum network $\mathcal{N}$ such as the one depicted in Fig. 4.2, along with its two-dimensional spatial section shown in Fig. 4.14. Consider the crossing points of $\mathcal{N}$ with the entangling sphere, depicted as small green squares in the spatial two-dimensional section. From each crossing point, the correlation length defines paths starting at the crossing point and extending to a length of ξ along the network. The collection of

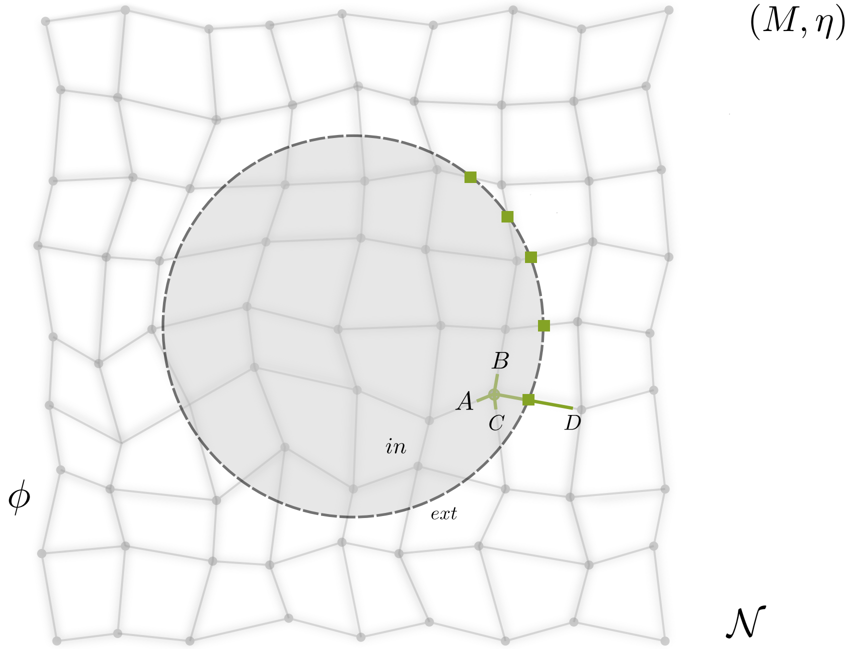

Figure 4.14: Spatial two-dimensional section of Fig. 4.2 for a quantum field ϕ (depicted in gray shades) spatially confined to the arbitrary three-dimensional network $\mathcal{N}$ embedded in Minkowski spacetime (M, η). An entangling sphere (disk in the 2D visualization) divides the network into an interior and an exterior sector. The crossing points are depicted as small green squares. Highlighted in green an example of a sub-region of $\mathcal{N}$ defined such that the locations A, B, C and D on the network are all at a distance ξ along $\mathcal{N}$ from the considered crossing point. In the particular case shown in the picture, the resulting sub-region forms a four-edge star graph. It is important to note that the edges of the sub-region do not necessarily correspond to entire edges of $\mathcal{N}$.

all these paths defines a finite local *sub-region* of the network, including the considered crossing point itself. Whenever a path extends through a node of $\mathcal{N}$, the node is part of the sub-region as well, however, note that these sub-regions do not necessary correspond to subgraphs of $\mathcal{N}$ as defined in Sec. 3.2, since they may contain sub-intervals of the edges of $\mathcal{N}$. As an example, a two-dimensional sub-region is highlighted in green in Fig. 4.14.

Recall that, by definition, each sub-region represents the support of those vacuum fluctuations that are entangled across the entangling sphere, thereby localizing, near each crossing point, the correlations contributing to the entanglement entropy. If the correlation length ξ is such that, locally, each sub-region is disconnected from the others then, based on the effects studied in the previous sections, we can conclude that the entanglement entropy of the quantum field spatially confined to the network $\mathcal{N}$ is given by the sum of contributions S_n from each sub-region n,

$$S_{\mathcal{N}} = \sum_{n}^{N_s} S_n \,, \tag{4.41}$$

where N_s is the number of sub-regions of the network under consideration. In particular, if all the sub-regions are equivalent relative to the quantum information measure we use, then the total entanglement entropy is given by $S_{\mathcal{N}} = N_s\, S_n$. Note that this naturally includes the specific case where $\xi \ll \min\{l_i, L_{e_i} - l_i\}$ on each intersected edge e_i of $\mathcal{N}$, causing Eq. (4.41) to reduce to Eq. (4.26). In fact, this formula generalizes to arbitrary networks the idea of Sec. 4.2.1, up to identifying each sub-region with an edge of $\mathcal{N}$, or part of it.

If, on the other hand, the mass of the quantum field is sufficiently small, or equivalently ξ is sufficiently large, the sub-regions associated with the crossing points begin to overlap, becoming entangled and creating a crossover between them. In this case, the entanglement entropy is no longer a simple sum – or multiple – of the entropies relative to each sub-region. Instead, due to correlations between sub-regions, the entanglement increases throughout the system, resulting in a larger overall value of the entanglement entropy,

$$S_{\mathcal{N}} > \sum_{n}^{N_s} S_n \,. \tag{4.42}$$

To summarize, three different regimes of entanglement arise on the network, depending on the relation between the correlation length ξ and each L_{e_i}. When the correlation length on e_i of $\mathcal{N}$ is such that $\xi \ll \min\{l_i, L_{e_i} - l_i\}$, the entanglement entropy does not capture any underlying graph structure and remains independent of the network's topology. In this case, the network configuration traced out by the entangling sphere behaves, relative to entanglement, as a collection of disconnected edges. As a result, entanglement between vacuum fluctuations confined to the network history can be treated on each edge using standard $(1+1)$-dimensional QFT methods, with the entanglement entropy described by a specific case of Eq. (4.41), behaving as an extensive quantity. As an intermediate step, if the correlation length exceeds the size L_{e_i} of e_i, (i.e. $1/\mu \sim L_{e_i}$ or larger), but a new set of effectively disconnected sub-regions can still be identified, then the entanglement entropy remains an extensive quantity on larger scales and is given by Eq. (4.41). However, if the correlation length causes the sub-regions to overlap, thus becoming entangled, then a complex interplay of effects – similar to those discussed in Sec. 4.2.2 – arises on the network, significantly impacting the entanglement entropy. It is exactly in this regime that we leave the usual $(1+1)$-dimensional QFT treatment in favor of a full quantum network description.

4.3.1 Area Scaling of Entanglement Entropy on Networks Histories

After developing a solid intuition about the entanglement properties on arbitrary networks and constructing the theoretical framework to study them in detail, we are now prepared to complete our investigation by examining the key pilot phenomenon introduced at the start of this chapter: the area scaling of entanglement entropy for free quantum fields in their ground states in Minkowski spacetime.

As discussed in the beginning of the chapter, this investigation seeks to address the core question of whether quantum networks can serve as effective diagnostic tools for probing physical phenomena embedded in spacetime, using only fields confined to the networks and their histories. Through this pioneering study, we aim to determine whether the entanglement entropy for vacuum fluctuations spatially confined to a network, for example the one depicted in Fig. 4.2, follows the same area-scaling behavior as that of vacuum fluctuations in full Minkowski spacetime.

The first step to this end is to select the specific network structure we wish to implement in our investigation. As discussed in Sec. 3.2.3, a general, arbitrary network $\mathcal{N}$ can be thought as constructed by several star graphs connected together, each with an arbitrary number of legs. However, the way we select, position, and arrange these star graphs is crucial, as different configurations result in different network structures.

To probe physical phenomena embedded in spacetime using only fields confined to network histories, the network must be shaped in a way that allows these fields to approximate quantum fields in the full embedding spacetime as closely as possible. For instance, as previously mentioned, photons in a single optical fiber can certainly provide valuable insights into photon propagation in one dimension and related (1+1)-dimensional experiments, but they cannot capture higher-dimensional phenomena, such as the relationship between the incident and transmitted angles at an interface, as encoded in the Snell's law. Generally, the more complex the network design, the more details and subtleties it can capture about higher-dimensional phenomena.

To further specify the structure and complexity of a network, it can be helpful to introduce the concept of local vertex density. Consider an arbitrary network $\mathcal{N}$ embedded in a globally hyperbolic background (M, g), as shown in Fig. 4.15. By specifying a value for

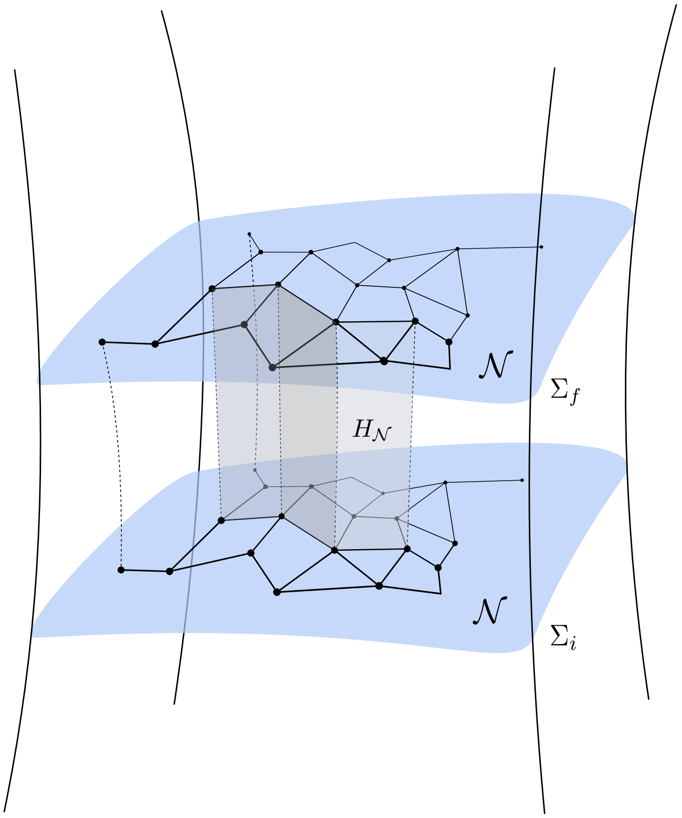

Figure 4.15: Arbitrary network $\mathcal{N}$ embedded in a globally hyperbolic spacetime (M, g). If τ is a time parameter, the history of the network can be visualized as the network worldsheet. For the sake of clarity, only a part of the network history $H_{\mathcal{N}}$ is shown in the picture. Note that each Σ_τ is a three-dimensional spacelike hypersurface.

the (time) parameter τ, the network lies on the three-dimensional spacelike hypersurface Σ_τ. We define the local *vertex density* d_v of the network as the number of vertices per unit hypersurface volume. In other words, it is a measure for the local filling of the hypersurface Σ_τ by the network. Ideally, the more the hypersurface is locally covered by network nodes, the more accurately quantum fields on the network history approximate their counterparts embedded in the full spacetime. However, this could lead to networks that are so complex that they become impractical, with an almost diverging vertex density. In such cases, the advantages of using network histories to explore natural phenomena, as an alternative to $(1+3)$-dimensional field theories, would be lost.

To fully capture the properties of phenomena in the full embedding spacetime, but with a finite vertex density, we consider quantum fields confined to the network history, with the mass chosen such that the network satisfies $d_{v\mathcal{N}} \gg 1/\xi^3$, where $\xi = 1/\mu$ is the correlation length. In fact, in this limit, the quantum field spatially confined to the network does not resolve its coarse-grained structure and can effectively approximate a full-dimensional field theory. This gives us the freedom to opt for a much simpler structure, while employing fields with a sufficiently large correlation length, still allowing us to approximate their full-dimensional counterparts. As a result, quantum networks prove to be a versatile tool, allowing us to strike a balance between capturing as much detail as possible about a phenomenon while maintaining the simplicity of the network design. Nevertheless, it is important to note that in some cases the network can be designed to capture only specific aspects or a particular level of detail about a phenomenon, for which a simple structure, like a basic star graph, may be sufficient.

Furthermore, note that although for $d_{v\mathcal{N}} \gg 1/\xi^3$ the field does not resolve the coarse-grained structure of the network and effectively populates the full embedding spacetime, the large-scale structure of the network must still ensure that the effective field theory satisfies the same symmetries as those of fields in the full spacetime. For example, inhomogeneities in the network design on scales larger than the correlation length will be resolved by the field, potentially resulting in an effective field theory that does not preserve the same spatial symmetries as fields in the full embedding spacetime. It follows that generally, the more we know about a phenomenon, the more constrained and specific the network structure becomes, as it aims to reflect the same quantum field theory as in the full spacetime. However, when quantum networks are implemented to explore an unknown phenomenon, we aim to use networks that are as arbitrary as possible.

Building on the previous discussion, in our investigation of the entanglement entropy for fields confined to network histories, we can implement any three-dimensional network with a finite vertex density $d_{v\mathcal{N}}$, as long as the field mass satisfies $d_{v\mathcal{N}} \gg 1/\xi^3$, since the field spatially confined to the network will not resolve its coarse-grained structure. Moreover, since vacuum fluctuations in Minkowski spacetime exhibit Poincaré invariance, we need to constrain the network to have a homogeneous vertex density. The simplest three-dimensional network that meets these constraints is a regular grid, with all edges having the same length L. In fact, in this case, the vertex density is given by $d_{v\mathcal{N}} = 1/L^3$ and is homogeneous throughout the network. Consequently, our setup of Fig. 4.2 simplifies to the configuration shown in Fig. 4.16. In what follows, we aim to compute the resulting entanglement entropy for a free, real scalar quantum field of mass μ, spatially confined to the three-dimensional grid.

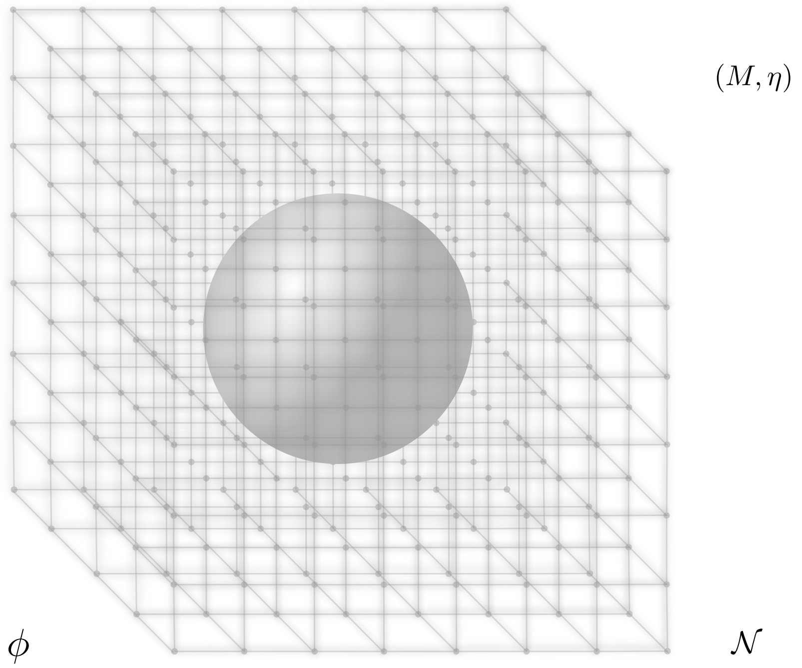

Figure 4.16: Three-dimensional visualization of a quantum field ϕ (depicted in gray shades) spatially confined to a network $\mathcal{N}$, designed as a regular grid of finite size, embedded in Minkowski spacetime (M, η). An arbitrary sphere divides the network setup into an interior and an exterior sector. If the interior of the sphere is inaccessible, an external observer loses information about the internal quantum field degrees of freedom. Due to quantum field correlations across the sphere's surface, the exterior and interior sectors of the network may be entangled, with the entanglement entropy quantifying the degree of entanglement.

Emerging spacetime properties of entanglement

The three-dimensional network $\mathcal{N}$ of Fig. 4.16 is a network $\mathcal{N} = (\mathcal{V}, \mathcal{E}, \iota)$ constructed entirely by connecting star graphs together. Specifically, the eight corners of the network consist of three-edge star graphs $\mathcal{G}_3$, while the central core of $\mathcal{N}$ is formed by six-edge star graphs $\mathcal{G}_6$. The six external surfaces of the network are made up of five-edge star graphs $\mathcal{G}_5$, with four-edge star graphs $\mathcal{G}_4$ forming the borders between adjacent surfaces. In particular, the star graphs are connected by pairing free endpoints together with Neumann conditions, reflected, in Minkowski spacetime, by removable nodes. As a result, every edge is connected to two nodes, leaving no free endpoints.

Following the notation of Sec. 3.2.3, we let $V := \sharp\mathcal{V}$ denote the cardinality of $\mathcal{V}$, i.e. the number of vertices of $\mathcal{N}$ and $N := \sharp\mathcal{E}$ the number of its edges. Furthermore, let a be an index that runs over the set of edges $\mathcal{E}$ and b an index that labels each node in $\mathcal{V}$, with $a \in \{1, \ldots, N\}$ and $b \in \{1, \ldots, V\}$. By construction, we assume that all edges of the network have the same length L. Furthermore, each vertex of the network is labeled as v_b, and N_b denotes the number of edges incident to each v_b. For details on the construction of the network history and the introduction of a field configuration on it, we refer to Sec. 3.2.3.

At each node v_b of the network, a continuity condition is enforced for the fields on the histories of the edges incident to the node through the introduction of Lagrange multiplier fields. This accounts for an additional functional $\mathcal{J}$ in the total action functional $\mathcal{A}_{\mathcal{N}}$ defined on the entire network history. Along the lines of Sec. 3.2.3, applying the variational principle to $\mathcal{A}_{\mathcal{N}}$ yields equations of motion of the form $(\Box_{\eta_a} + \mu^2)\,\phi_a = 0$ on each edge history H_{e_a}, along with the Kirchhoff-Neumann junction conditions at each node v_b. The Kirchhoff-Neumann conditions are given in their general form for real scalar fields in Eq. (3.81). In Minkowski spacetime, given a coordinate system $x_a = \{\xi_a^c\} = (T, \xi_a)$ on each edge history H_{e_a}, they take the form

$$\begin{cases} \phi_1\Big|_{v_b(T)} \overset{!}{=} \phi_2\Big|_{v_b(T)} \overset{!}{=} \ldots \overset{!}{=} \phi_b\Big|_{v_b(T)} \overset{!}{=} \ldots \overset{!}{=} \phi_{N_b}\Big|_{v_b(T)} \,, \\ \displaystyle\sum_{a=1}^{N_b} \partial_{\xi_a}\phi_a\Bigg|_{v_b(T)} \overset{!}{=} 0\,, \end{cases} \tag{4.43}$$

for each vertex worldline $v_b(T)$ of the network.[1] Depending on the position of the considered

---

[1] Please recall that although we label the field ϕ_b with the same index of the vertex v_b, when labeling the field, b only aims to single out the field ϕ_a with the vertex in its domain, and as such, is a special value of a, running over the N_b edges connected to the node.

node v_b in $\mathcal{N}$, that is, whether it belongs locally to $\mathcal{G}_3$, $\mathcal{G}_4$, $\mathcal{G}_5$ or $\mathcal{G}_6$, the matrices A and B (Eq. (3.51)) associated with the above Kirchhoff-Neumann conditions read,

$$
\begin{aligned}
A_{\mathcal{G}_3} &= \begin{pmatrix} 1 & -1 & 0 \\ 0 & 1 & -1 \\ 0 & 0 & 0 \end{pmatrix}, \quad B_{\mathcal{G}_3} = \begin{pmatrix} 0 & 0 & 0 \\ 0 & 0 & 0 \\ 1 & 1 & 1 \end{pmatrix}, \\
A_{\mathcal{G}_4} &= \begin{pmatrix} 1 & -1 & 0 & 0 \\ 0 & 1 & -1 & 0 \\ 0 & 0 & 1 & -1 \\ 0 & 0 & 0 & 0 \end{pmatrix}, \quad B_{\mathcal{G}_4} = \begin{pmatrix} 0 & 0 & 0 & 0 \\ 0 & 0 & 0 & 0 \\ 0 & 0 & 0 & 0 \\ 1 & 1 & 1 & 1 \end{pmatrix}, \\
A_{\mathcal{G}_5} &= \begin{pmatrix} 1 & -1 & 0 & 0 & 0 \\ 0 & 1 & -1 & 0 & 0 \\ 0 & 0 & 1 & -1 & 0 \\ 0 & 0 & 0 & 1 & -1 \\ 0 & 0 & 0 & 0 & 0 \end{pmatrix}, \quad B_{\mathcal{G}_5} = \begin{pmatrix} 0 & 0 & 0 & 0 & 0 \\ 0 & 0 & 0 & 0 & 0 \\ 0 & 0 & 0 & 0 & 0 \\ 0 & 0 & 0 & 0 & 0 \\ 1 & 1 & 1 & 1 & 1 \end{pmatrix}, \\
A_{\mathcal{G}_6} &= \begin{pmatrix} 1 & -1 & 0 & 0 & 0 & 0 \\ 0 & 1 & -1 & 0 & 0 & 0 \\ 0 & 0 & 1 & -1 & 0 & 0 \\ 0 & 0 & 0 & 1 & -1 & 0 \\ 0 & 0 & 0 & 0 & 1 & -1 \\ 0 & 0 & 0 & 0 & 0 & 0 \end{pmatrix}, \quad B_{\mathcal{G}_6} = \begin{pmatrix} 0 & 0 & 0 & 0 & 0 & 0 \\ 0 & 0 & 0 & 0 & 0 & 0 \\ 0 & 0 & 0 & 0 & 0 & 0 \\ 0 & 0 & 0 & 0 & 0 & 0 \\ 0 & 0 & 0 & 0 & 0 & 0 \\ 1 & 1 & 1 & 1 & 1 & 1 \end{pmatrix},
\end{aligned}
\tag{4.44}
$$

where each pair of A and B matrices are $N_b \times N_b$ matrices.

Since for each node v_b we can show that, for the corresponding form of A and B, the $N_b \times 2N_b$ composite matrix (A, B) has rank N_b and $AB^\dagger$ is self-adjoint, the Laplace operator defined as $\partial^2_{\xi_a}\phi_a$ on each edge e_a, is also self-adjoint on e_a, regardless of the specific structure of the nodes at the edge endpoints, and consequently is self-adjoint on $\mathcal{N}$ [16,19]. Therefore, on each edge history H_{e_a} we can employ its eigenfunctions to construct the quantum field and the conjugate momentum operators.

In fact, by defining $\pi_a(T, \xi_a) = \frac{\partial \mathcal{L}_{e_a}}{\partial(\partial_T \phi_a)}$ for each Lagrangian density $\mathcal{L}_{e_a}$ on H_{e_a}, the quantum field ϕ_a and the conjugate field operator π_a satisfy the canonical equal-time commutation relations on each edge history H_{e_a},

$$\begin{aligned}
&[\phi_a(T,\xi_a),\pi_a(T,\xi'_a)] = i\delta(\xi_a-\xi'_a)\,,\\
&[\phi_a(T,\xi_a),\phi_a(T,\xi'_a)] = [\pi_a(T,\xi_a),\pi_a(T,\xi'_a)] = 0\,.
\end{aligned} \tag{4.45}$$

Through a Legendre transformation, we derive the associated Hamiltonian density $\mathcal{H}_{e_a}(T,\xi_a,\phi_a,\pi_a)$ from each Lagrangian density $\mathcal{L}_{e_a}$ on the history of each edge of $\mathcal{N}$. Each Hamiltonian density is given by $\mathcal{H}_{e_a} = \frac{1}{2}\left[\pi_a^2(T,\xi_a) + (\partial_{\xi_a}\phi_a(T,\xi_a))^2 + \mu^2\phi_a^2(T,\xi_a)\right]$. As a result, we constructed a network $\mathcal{N} = (\mathcal{V},\mathcal{E},\iota)$ where each edge history supports a quantum field theory, and the junction conditions between them are ruled by Kirchhoff-Neumann conditions at each vertex worldline.

We have seen (Sections 4.2.1, 4.2.2) that for the specific task of computing the entanglement entropy, it is convenient to formulate the quantum field theory in the Schrödinger picture. Building on its introduction for $\mathcal{G}_3$ in Sec. 4.2.2, we now extend this formulation to the network case. For each edge history, we can promote the Hamiltonian function to the functional differential operator $H_a = \int \mathcal{H}_{e_a}\,d\xi_a = \frac{1}{2}\int\left[\pi_a^2(\xi_a) + (\partial_{\xi_a}\phi_a(\xi_a))^2 + \mu^2\phi_a^2(\xi_a)\right]\,d\xi_a$ where the conjugate momentum field π_a reads, in its functional differential representation $\pi_a(\xi_a) = -i\frac{\delta}{\delta\phi_a(\xi_a)}$. Note that, according to the Schrödinger representation of QFT, ϕ_a, π_a and consequently H_a are now time-independent operators.

In particular, we can write the ground state wave functional on the history of the network $\mathcal{N}$ as

$$\mathbf{\Psi}_{0\mathcal{N}} = (\Psi_{0\,1},\Psi_{0\,2},\ldots\Psi_{0\,N})\;, \tag{4.46}$$

where each $\Psi_{0\,a} = \Psi_{0\,a}[\phi_a]$, with $a\in\{1,\ldots,N\}$, is the ground state wave functional (Eq. (4.33)) introduced for the quantum field ϕ_a confined to the history of the edge e_a of the network and satisfying $i\frac{\partial}{\partial T}\Psi_{0\,a}[\phi_a] = H_a\Psi_{0\,a}[\phi_a]$.

Consider Fig. 4.16. The quantum field configuration on the network, continuous through the nodes as enforced by the continuity conditions in Eq. (4.43), is partly traced out by an entangling sphere. We perform an instantaneous measurement of the entanglement entropy to quantify the degree of entanglement between the exterior and interior sectors of the network.

The extrinsic distance scale a, introduced as a consequence of the finite resolution of experimental devices, leads to a discretization of the quantum field ϕ_a on each edge on a one-dimensional lattice with $N_{e_a} = N_e$ sites, each separated by constant spacing a. The length of the edges is $L = (N_e+1)a$. Note that in the current analysis, each edge supports the same number of lattice sites denoted by N_e.

According to the discretization scheme Eq. (4.9), each Hamiltonian operator H_a reads, in its discretized form

$$H_a = \frac{1}{2a}\left\{\sum_{k=1}^{N_e}\left[\pi^2_{(a,\,k)} - \phi_{(a,\,k)}\left(\phi_{(a,\,k+1)} - 2\,\phi_{(a,\,k)} + \phi_{(a,\,k-1)}\right) + \mu^2 a^2\,\phi^2_{(a,\,k)}\right]\right\}\,, \tag{4.47}$$

where $\phi_{(a,\,k)}$ and $\pi_{(a,\,k)}$ satisfy $[\phi_{(a,\,k)}, \frac{\pi_{(a,\,k')}}{a}] = i\frac{\delta_{kk'}}{a}$ and are dimensionless.

Since both endpoints of each edge are connected to a node, both $\phi_{(a,\,0)}$ and $\phi_{(a,\,N_e+1)}$ independently satisfy a discretized version of the Kirchhoff-Neumann conditions given in Eq. (4.43). We refer to v_b and v_b' as the nodes related to $\phi_{(a,\,0)}$ and $\phi_{(a,\,N_e+1)}$ respectively.

In the case where the node is connected to three edges ($\mathcal{G}_3$), the discretized version of the Kirchhoff-Neumann conditions, as given in Eq. (4.37), results in the relation $\phi_{(a,\,0)} = \frac{1}{3}\sum_{a'=1}^{3}\phi_{(a',\,1)}$ at v_b, for all times. Note that, symmetrically, $\phi_{(a,\,N_e+1)} = \frac{1}{3}\sum_{a'=1}^{3}\phi_{(a',\,N_e)}$ at v_b'.[2] In a similar fashion to Sec. 4.2.2, for a node connected to four edges ($\mathcal{G}_4$), we can derive the following discretized form of the junction conditions at v_b, for all times

$$\begin{pmatrix} 1 & -1 & 0 & 0 \\ 0 & 1 & -1 & 0 \\ 0 & 0 & 1 & -1 \\ 0 & 0 & 0 & 0 \end{pmatrix}\begin{pmatrix} \phi_{(1,\,0)} \\ \phi_{(2,\,0)} \\ \phi_{(3,\,0)} \\ \phi_{(4,\,0)} \end{pmatrix} + \frac{1}{a}\begin{pmatrix} 0 & 0 & 0 & 0 \\ 0 & 0 & 0 & 0 \\ 0 & 0 & 0 & 0 \\ 1 & 1 & 1 & 1 \end{pmatrix}\begin{pmatrix} \phi_{(1,\,1)} - \phi_{(1,\,0)} \\ \phi_{(2,\,1)} - \phi_{(2,\,0)} \\ \phi_{(3,\,1)} - \phi_{(3,\,0)} \\ \phi_{(4,\,1)} - \phi_{(4,\,0)} \end{pmatrix} = 0\,. \tag{4.48}$$

Solving for $\phi_{(a,\,0)}$, yields $\phi_{(a,\,0)} = \frac{1}{4}\sum_{a'=1}^{4}\phi_{(a',\,1)}$. More generally, we can show that for N_b edges joining a node v_b, the discretized version of the Kirchhoff-Neumann conditions yields

$$\phi_{(a,\,0)} = \frac{1}{N_b}\sum_{a'=1}^{N_b}\phi_{(a',\,1)}\,, \tag{4.49}$$

for all times, or, symmetrically, $\phi_{(a,\,N_e+1)} = \frac{1}{N_b'}\sum_{a'=1}^{N_b'}\phi_{(a',\,N_e)}$ at v_b'. Therefore, depending on the displacement of each edge in the three-dimensional grid of Fig. 4.16, $\phi_{(a,\,0)}$ and $\phi_{(a,\,N_e+1)}$ satisfy $\phi_{(a,\,0)} = \frac{1}{N_b}\sum_{a'=1}^{N_b}\phi_{(a',\,1)}$ and $\phi_{(a,\,N_e+1)} = \frac{1}{N_b'}\sum_{a'=1}^{N_b'}\phi_{(a',\,N_e)}$ at the node worldlines $v_b(T)$ and $v_b'(T)$ respectively. Recall that for the network under consideration $N_b, N_b' \in \{3,4,5,6\}$.

Finally, on the history of each edge, according to the final resolution structure, the

---

[2] For notational simplicity, when focusing on $\phi_{(a,\,0)}$, we have considered boundary sites on other edges $e_{a'}$ as $\phi_{(a',\,0)}$. However, for geometrical reasons, they could just as well be $\phi_{(a',\,N_e)}$ sites.

ground state wave functional reduces (See Sec. 4.2.2 for details) to the following ground state wave function

$$\Psi_{0\,a}(\boldsymbol{\phi}_a) = a^{N_e/2}\,\pi^{-N_e/4}\,(\det(\Omega_a))^{1/4}\exp\left(-\tfrac{1}{2}\boldsymbol{\phi}_a\cdot(\Omega_a\boldsymbol{\phi}_a)\right), \tag{4.50}$$

where $\boldsymbol{\phi}_a := (\phi_{(a,\,1)},\ldots,\phi_{(a,\,k)},\ldots,\phi_{(a,\,N_e)})$, Ω_a is a $N_e \times N_e$ matrix and $a^{N_e/2}\,(\det(\Omega_a))^{1/4}$ is a dimensionless quantity.

As a result, the ground state wave functional reduces to the total ground state wave function on the network

$$\boldsymbol{\Psi}_{0\mathcal{N}}(\boldsymbol{\phi}_1,\ldots,\boldsymbol{\phi}_N) = (\Psi_{0\,1}(\boldsymbol{\phi}_1),\,\ldots\,,\Psi_{0\,N}(\boldsymbol{\phi}_N))\;. \tag{4.51}$$

Accordingly, the total Hamiltonian $H_{\mathcal{N}}$ on the network $\mathcal{N}$, acting on the above wave function $\boldsymbol{\Psi}_{0\mathcal{N}} = (\Psi_{0\,1},\ldots,\Psi_{0\,N})$, can be expressed as a $(NN_e)\times(NN_e)$ matrix of the form

$$H_{\mathcal{N}} = \begin{pmatrix} \boxed{H_1} & & & 0 \\ & \boxed{H_2} & & \\ & & \ddots & \\ 0 & & & \boxed{H_N} \end{pmatrix} + \mathcal{C}\,, \tag{4.52}$$

where, again, $\mathcal{C}$ is a matrix that accounts for possible couplings between lattice sites on different edges, while each Hamiltonian operator H_a acts on the corresponding ground state wave function $\Psi_{0\,a}(\boldsymbol{\phi}_a)$. Finally, we can find the $NN_e \times NN_e$ matrix $K_{\mathcal{N}}$ associated with the above Hamiltonian $H_{\mathcal{N}}$. Note that $K_{\mathcal{N}}$ encodes all the couplings between the NN_e lattice sites located on $\mathcal{N}$.

In particular, when substituted in Eq. (4.47), the boundary value $\phi_{(a,\,0)}$ (or, symmetrically, $\phi_{(a,\,N_e+1)}$), expressed as in Eq. (4.49), generates a non-vanishing term of the form $-\frac{1}{N_b}\phi_{(a,\,1)}\left(\phi_{(1,\,1)}+\phi_{(2,\,1)}+\cdots+\phi_{(N_b,\,1)}\right)$ in the matrix $\mathcal{C}$ in $H_{\mathcal{N}}$, coupling the first lattice site $\phi_{(a,\,1)}$ on the edge e_a with the first lattice sites on the other $N_b - 1$ edges, as next-neighbors (or, in terms of $\phi_{(a,\,N_e+1)}$, the last lattice site $\phi_{(a,\,N_e)}$ on e_a with the last lattice points on the other $N_b' - 1$ edges).

As a result, new coupling terms are introduced in $K_{\mathcal{N}}$, connecting lattice points located on different edges and effectively joining N_b lattices at each node v_b of the network. Again, it is important to note that the coupling strength, $-\frac{1}{N_b}$, is equally distributed among the sites $\phi_{(a,\,1)}$ (or $\phi_{(a,\,N_e)}$) and is weaker than the couplings between consecutive sites along the same edge, given by $-\phi_{(a,\,k)}\,\phi_{(a,\,k+1)}$ with strength -1.

As mentioned above, in our specific case of the three-dimensional network $\mathcal{N}$ of Fig. 4.16, $N_b \in \{3, 4, 5, 6\}$. Similar to Fig. 4.10, which illustrates the case for $N_b = 3$, we refer to Fig. 4.17 for a visualization of how the Kirchhoff-Neumann conditions give rise to effective nodes connecting four, five, and six edges, respectively. The resulting $\mathcal{G}_3$ graphs form corners of the grid, $\mathcal{G}_5$ graphs form the structure of its external surfaces, while $\mathcal{G}_4$ graphs the borders between them. Finally, $\mathcal{G}_6$ graphs make up the bulk structure of the network $\mathcal{N}$.

With the specific form of $K_{\mathcal{N}}$ resulting from the couplings dictated by the network design, we ultimately obtain the matrix $\Omega_{\mathcal{N}} = \sqrt{K_{\mathcal{N}}}$. Consequently, we can follow the steps outlined in Sec. 4.2.1 to compute the entanglement entropy as expressed in Eq. 4.4, for vacuum fluctuations confined to $\mathcal{N}$ as in Fig. 4.16 and reduced to a system of NN_e lattice points, in the presence of an entangling sphere. To this aim, we developed and implemented the code published in [38].

A few words deserve to be dedicated to the exact configuration of the setup. In the (1 + 3)-dimensional case, the setup consists of quantum fields embedded in Minkowski spacetime, where a spherical region is traced out and made inaccessible, as shown in Fig. 4.1. For free real scalar quantum fields, the resulting entanglement entropy follows an area scaling, as demonstrated in [10]. The larger the area of the entangling sphere, the greater the entanglement entropy of the system, with the entropy depending solely on the surface area of the sphere and being insensitive to its volume.

In our network experiment, the setup is depicted in Fig. 4.16. Here, the entangling sphere defines a region of the network that supports field degrees of freedom which are traced out and made inaccessible to an external observer. However, there is a notable difference compared to the setup for fields in full Minkowski spacetime. When comparing the entanglement entropies for the same surface area, a discrepancy arises. The part of the network traced out by the entangling sphere occupies a spacetime volume that only approximates the sphere's interior, due to the structure of the regular Cartesian grid. Although for $d_{v\mathcal{N}} \gg 1/\xi^3$, the approximation improves significantly, the area of the traced-out region, which approximates the surface area of the entangling sphere, will

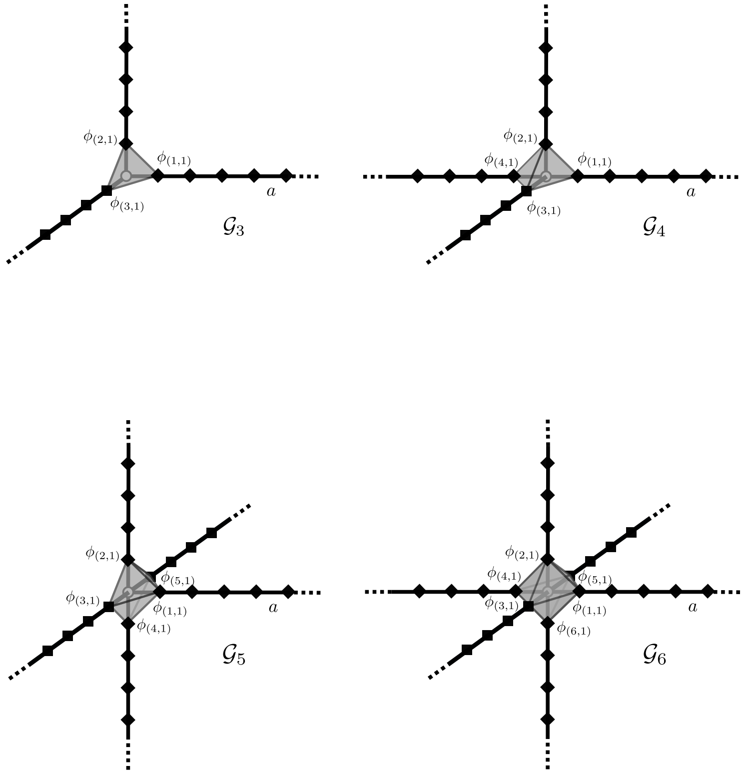

Figure 4.17: Visualization of the discretized Kirchhoff-Neumann conditions at the node of a three-edge star graph $\mathcal{G}_3$, a four-edge star graph $\mathcal{G}_4$, a five-edge star graph $\mathcal{G}_5$ and a six-edge star graph $\mathcal{G}_6$, respectively. The extrinsic distance scale a imposes a finite resolution structure on the edges reducing the fields ϕ_a, for $a \in \{1, \ldots, N_b\}$ to spatial one-dimensional lattices of N_e sites with constant spacing a. The white circles represent the boundary sites of the lattices, $\phi_{(a,\,0)}$ or $\phi_{(a,\,N_e+1)}$ for all a. For clarity and without loss of generality, we focus on $\phi_{(a,\,0)}$ in this figure. Couplings between lattice sites on the same edge are depicted as black lines and are of the form $-\phi_{(a,\,k)}\phi_{(a,\,k+1)}$. The first condition in Eq. (4.43) enforces that, at the vertex, all boundary sites must agree, resulting in $\phi_{(1,\,0)} = \cdots = \phi_{(N_b,\,0)}$. Consequently, the lattices are connected through each $-\phi_{(a,\,1)}\phi_{(a,\,0)}$ term. Together with the second condition in Eq. (4.43) then this dictates that, since $\phi_{(a,\,0)} = \frac{1}{N_b}\sum_{a'=1}^{N_b} \phi_{(a',\,1)}$, each $\phi_{(a,\,1)}$ is coupled to $\phi_{(a',\,1)}$ for all a, a', (dark gray lines in the picture) as next-neighbors with the coupling strength equally distributed as $-1/N_b$. This results in the emergence of effective nodes between the first sites of the lattices.

always overestimate it by a factor of $4/\pi$. This intrinsic geometrical discrepancy arises from approximating a spherical region using a regular Cartesian grid, which cannot perfectly capture the sphere's curvature, regardless how large the vertex density is.

Consequently, unlike in the full spacetime case, the surface of the entangling sphere and that of the traced-out region do not necessarily coincide when using quantum networks. As a result, for the same radius of the entangling sphere, the actual surface of the traced-out region may be inequivalent between the two setups, making direct comparison challenging. In light of this discrepancy, and to facilitate a meaningful comparison with the (1+3)-dimensional result, we multiply all numerical entanglement entropies by a factor of $\pi/4$. This ensures that, in the limit $d_{v\mathcal{N}} \gg 1/\xi^3$, the entanglement entropy values are appropriately adjusted and ready for direct comparison.

Note that two distance scales now play a role in determining the entanglement entropy. The extrinsic distance scale a introduces a minimal distance resolved by measurement devices, such that, in our construction, the minimum length for each edge is $L = (N_e+1)a = 2a$, which corresponds to only one lattice point $N_e = 1$ per edge. For the lattice sites to spatially approximate a quantum field on the network, we require $\xi = 1/\mu \gg a$. On the other hand, for the regular grid under consideration, the edge length L sets a lower bound for the correlation length ξ such that the field spatially confined to $\mathcal{N}$ does not resolve the coarse-grained structure of the network. In fact, for the chosen regular grid with $d_{v\mathcal{N}} = 1/L^3$, if $\xi = 1/\mu \gg L$ we have $d_{v\mathcal{N}} = 1/L^3 \gg 1/\xi^3$. By combining these two conditions, we find that $\xi = 1/\mu \gg L$ automatically satisfies $\xi \gg a$, indicating that for values of the correlation length such that $d_{v\mathcal{N}} = 1/L^3 \gg 1/\xi^3$, vacuum fluctuations confined to the regular grid are not only effectively described by the lattice points of the finite resolution structure, but can also be considered as effectively populating the full embedding spacetime.

To compute the entanglement entropy, we take as a first concrete example the length L of each edge in the network to be $L = 7a$ and set $\mu a = 10^{-3}$ accordingly. In fact, the value $\mu a = 10^{-3}$ is sufficiently small to ensure that $d_{v\mathcal{N}} = 1/L^3 \gg 1/\xi^3$. As discussed, for such values of the mass not only can the lattice points effectively describe a quantum field, but this effective quantum field also does not resolve the coarse-grained structure of the network itself. The network vertex density may be large enough to approximate quantum fields in the full $(1+3)$-dimensional Minkowski spacetime. Consequently, an area scaling behavior, similar to that in full spacetime, could be expected. On the other hand, as suggested by the intuition developed in the previous subsection, if ξ is sufficiently large, correlations across the entangling sphere entangle the sub-regions associated with the crossing points. These correlations are no longer localized near the surface of the entangling sphere, but instead spread throughout the bulk of the network. As they reach deeper regions within the network inside the entangling sphere, an area scaling may no longer be feasible for such a system.

The numerical entanglement entropy in terms of the area A of the entangling sphere is shown in Fig. 4.18, for $\mu a = 10^{-3}$.

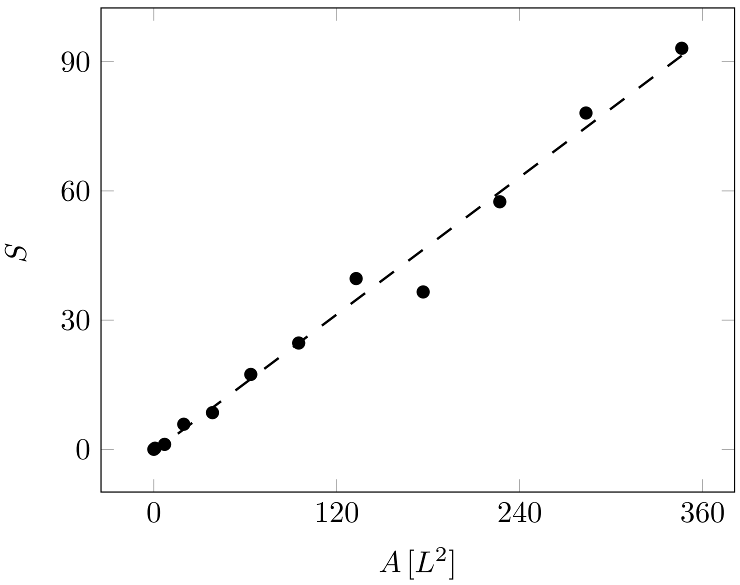

Figure 4.18: Entanglement entropy for vacuum fluctuations spatially confined to the three-dimensional network $\mathcal{N}$ shown in Fig. 4.16, in terms of the area of the entangling sphere for $\mu a = 10^{-3}$. A fitted curve is depicted with a dashed line. The grid consists of 10x10x10 edges and is equipped with a finite resolution structure of $N_e = 6$ lattice sites with spacing a on each edge, such that $L = 7a$. Note that the entanglement entropy has been multiplied by a factor of $\pi/4$.

Remarkably, the entanglement entropy still exhibits a linear dependence on the area of the entangling sphere.

This result is particularly striking, as the area scaling of the entanglement entropy is a phenomenon characteristic of entangled fields extending throughout full spacetime [9, 10]. Yet, we are probing the entanglement properties of fields confined to two-dimensional Lorentzian histories, with field configurations spatially confined to the edges of the network.

Specifically, in $(1+3)$ dimensions, fields that are not confined to a network history but extend freely into compact regions of spacetime carry angular momentum, which acts as an effective contribution to the field mass μ. The presence of angular momentum – and the summation over all its possible values – ensures that the total mass remains large, thereby shortening the correlation length and localizing the entanglement between the interior and exterior of the entangling sphere near its surface, even when the intrinsic mass μ of the field vanishes [10]. Consequently, an area law for the entanglement entropy of the ground state in $(1+3)$ dimensions is inevitable. However, quantum fields on two-dimensional network histories are spatially confined to one-dimensional edges and, therefore, do not carry angular momentum. In this case, the correlation length is solely determined by the field mass μ. When μ is small, correlations across the surface of the entangling sphere spread deep into its volume and throughout the network. For mass values such that $\xi = 1/\mu \gg L$, various local phenomena, such as those discussed in Sec. 4.2.2, arise. The interplay of these phenomena effectively makes the entanglement entropy sensitive only to the surface of the entangling sphere, rather than to its volume or to the finite size of the network, simulating the role of angular momentum as seen in the full $(1+3)$-dimensional theory. In particular, it is exactly in this mass regime that $d_{v\mathcal{N}} = 1/L^3 \gg 1/\xi^3$ and fields spatially confined to one-dimensional edges effectively emerge as fields in full Minkowski spacetime, no longer resolving the coarse-grained structure of the network. Although not carrying angular momentum by definition, these emerging fields nonetheless exhibit an area scaling of the entanglement entropy, characteristic of fields with angular momentum. This striking result suggests that Fig. 4.18 captures the emergence of an effective angular momentum on the quantum network, giving rise to the observed area scaling of the entanglement entropy.

It is important to note that, to obtain the same proportionality factor as in the $(1+3)$-dimensional result, we would need to continuously increase the density of the quantum network such that, ideally, the support of the field confined to the network approximates a portion of the embedding four-dimensional Minkowski spacetime to arbitrary accuracy. However, this limit cannot be achieved, as the minimal distance scale a, as previously discussed, imposes a minimal edge length L, which in turn sets an upper bound on the vertex density d_v. As a result, the proportionality factor Λ determining the slope of the curve in Fig. 4.18 will approach, but not exactly match, its three-dimensional counterpart. In general, we expect the proportionality factor to depend on the vertex density, specifically on L and a and on the mass of the field μ, $\Lambda = \Lambda(L, a, \mu)$.

The curve in Fig. 4.18 presents a dip for $A = 180L^2$. This is due to the specific local structure of the three-dimensional grid, as visualized in Fig. 4.17. When the radius of the entangling sphere resolves the nodes of the network, crossing the couplings between lattice sites involved in the effective node structure, the entanglement entropy decreases. As discussed, at the nodes of the network, the couplings between lattice sites have a strength of $1/N_b$. For example, when the surface of the entangling sphere crosses the node of a $\mathcal{G}_6$ graph located in the bulk of the network, next-neighboring sites on opposite sides of the sphere surface are coupled via an interaction that is 1/6 the strength of the coupling between sites on the same edge. Although the presence of the node increases the number of communication channels, the weaker next-neighbor couplings result in a decrease in the overall entanglement entropy compared to when the sphere surface crosses the edges of the network.

This effect arises in Fig. 4.18 specifically due to the curvature of the entangling sphere intersecting a regular Cartesian grid and is, therefore, inevitable. However, by using a cubical entangling surface instead of a spherical one, the nodes of the network can be bypassed, thereby avoiding this systematic effect. To this end, and to further investigate the area scaling for free quantum fields in the Minkowski ground state, we explore in the following subsection whether the entanglement entropy is sensitive to the shape of the entangling surface rather than solely to its area.

The area scaling observed in Fig. 4.18 demonstrates that quantum networks and their histories can effectively capture the behavior of higher-dimensional phenomena in the full embedding spacetime using lower-dimensional theories. The central question posed at the beginning of this chapter has been affirmatively answered: quantum networks are emerging as potent arenas, capable of investigating phenomena experiencing all spacetime dimensions through lower-dimensional probes.

Shape dependence

The linear dependence of the entanglement entropy on the surface area of the traced-out region should be preserved even when the shape of the entangling surface differs from the spherical one. As mentioned above, choosing to trace out a cubical region could further improve the linearity of the curve. Therefore, in what follows, we aim to investigate the entanglement entropy for vacuum fluctuations spatially confined to the same three-dimensional grid as in Fig. 4.16, but with an entangling surface of a different shape. Investigations employing a spatially deformed entangling sphere or entangling surfaces containing corners have been developed in the context of conformal field theories [42, 43]. In our analysis, we trace out a cubical region, as depicted in the following Fig. 4.19.

For the corresponding code developed for this analysis we refer the reader to [38]. To compute the entanglement entropy, we choose the value $L = 4a$ for the length of each edge of the network and, accordingly, $\mu a = 10^{-3}$. The entanglement entropy in terms of the surface area A of the cube, is shown in Fig. 4.20. As a first result, we observe that the entanglement entropy still exhibits a linear dependence on the area A of the entangling

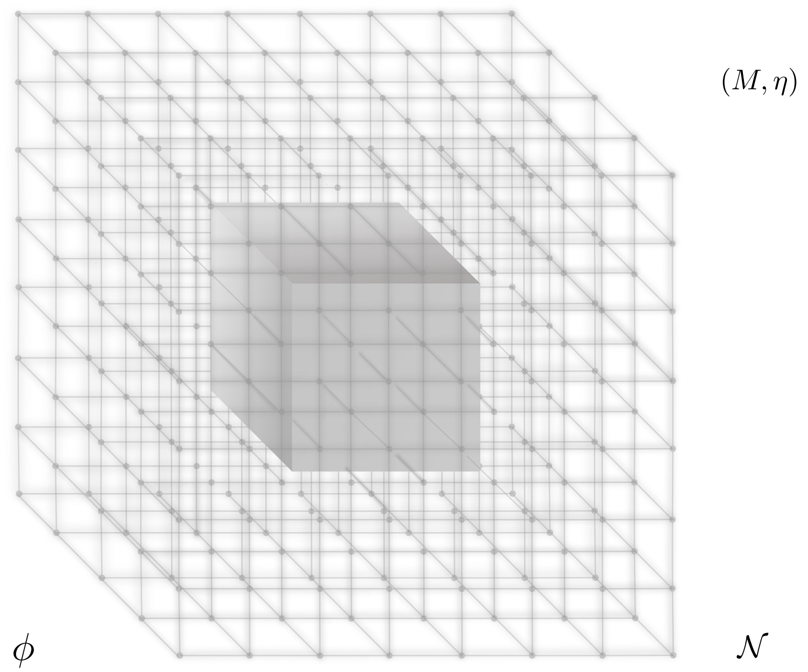

Figure 4.19: Spatial three-dimensional visualization of a quantum field ϕ (depicted in gray shades) spatially confined to a network $\mathcal{N}$, designed as a regular grid of finite size, embedded in Minkowski spacetime (M, η). An arbitrary cube divides the network setup into an interior and an exterior sector. If the interior of the cube is inaccessible, an external observer loses information about the internal quantum field degrees of freedom. Due to quantum field correlations across the cube's surface, the exterior and interior sectors of the network may be entangled, with the entanglement entropy quantifying the degree of entanglement.

surface, in this case, the surface of a cube. This result confirms that the entanglement entropy of vacuum fluctuations spatially confined to the network $\mathcal{N}$ embedded in Minkowski spacetime, depends linearly on the surface area of the traced-out region, regardless of its shape.

Furthermore, as expected, the dip observed in Fig. 4.18 for $A = 180L^2$ is no longer present. This is because, when tracing out a cubic region from a regular three-dimensional grid network, it is possible to select cube sizes that do not resolve the vertices of the network. As a result, the linear dependence on the area is achieved with greater accuracy. In particular, it is interesting to compare the entanglement entropy values for vacuum fluctuations spatially confined to $\mathcal{N}$ when tracing out spherical and cubic regions with the same surface area A. To this end, in Fig. 4.20 we depict the fitted curve for the entanglement entropy in the spherical case, shown as a red dashed line, for the same area

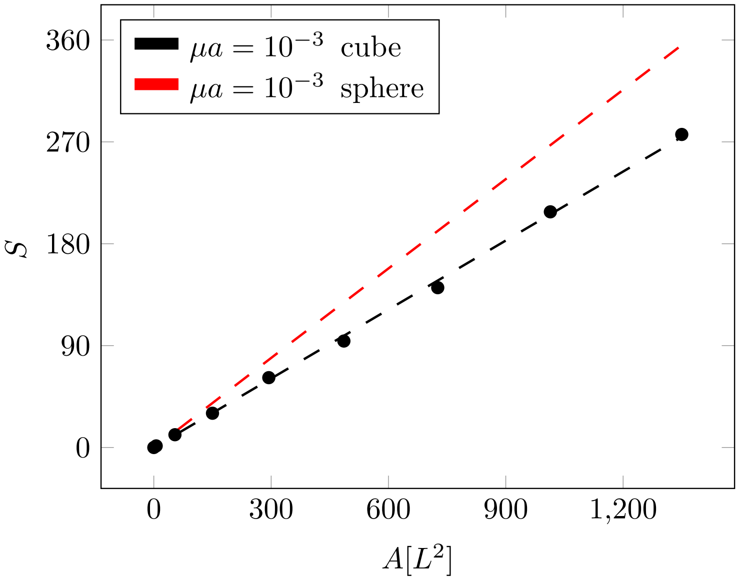

Figure 4.20: Entanglement entropy for vacuum fluctuations spatially confined to the three-dimensional network $\mathcal{N}$ shown in Fig. 4.19, in terms of the area of the entangling cube for $\mu a = 10^{-3}$. A fitted curve is depicted with a dashed line. The grid consists of 16x16x16 edges and is equipped with a finite resolution structure of $N_e = 3$ lattice sites with spacing a on each edge, such that $L = 4a$. For comparison, the fit of the entanglement entropy related to the case of an entangling sphere introduced in Fig. 4.18, is shown in red.

values. Surprisingly, the entanglement entropy differs between the two cases. Specifically, the entanglement is larger when a spherical region is traced out compared to a cubical one with the same surface area. Although an area scaling emerges in both cases, the quantum information measure distinguishes between the two shapes. While the cause of this discrepancy remains under investigation, we can state as a first result of our quantum network analysis that the entanglement entropy of vacuum fluctuations in the full Minkowski spacetime depends not only on the area of the traced-out region but also on its shape, with the shape information encoded in the proportionality factor.

The emergence of area scaling in Fig. 4.18 and the shape dependence in Fig. 4.20 for mass regimes $1/\mu = \xi \gg L$, demonstrate that quantum networks and their histories can effectively capture and reveal the behavior of higher-dimensional phenomena within the full embedding spacetime using lower-dimensional theories. The characteristic properties of these higher-dimensional phenomena emerge naturally on the network. In particular, Fig. 4.18 serves as a reference signature for applying this analysis in curved spacetimes. If, by placing the quantum network across a black hole horizon or in a curved background, we observe a discrepancy when tracing out a spherical region compared to the result in

Minkowski spacetime, it indicates that the fields confined to the network history have detected the curvature of the background, highlighting quantum networks as effective tools for probing the geometry of the embedding spacetime.

Extensive entanglement entropy on the network

So far we have proposed quantum networks as arenas where, in the limit $d_{v\mathcal{N}} \gg 1/\xi^3$, the $(1+1)$-dimensional field theories on each edge history of the network combine to give rise to an effective $(1+3)$-dimensional field theory emerging on $\mathcal{N}$, which can describe and reveal phenomena occurring in the full embedding spacetime.

As noted, in such a mass regime, the entanglement entropy is not an extensive quantity. Instead, it is qualitatively characterized by a larger value than the sum of the contributions from each sub-region, as expressed in Eq. (4.42).

In the following, we set aside the descriptive power of quantum networks for higher-dimensional physics to focus on the regime where the entanglement entropy becomes extensive. As discussed in previous subsections, this is only possible in a mass regime where each sub-region (defined as in Fig. 4.14) of the network is disconnected from the others, and its corresponding entanglement entropy simply adds up to the total entanglement entropy, as shown in Eq. (4.41). In this mass regime, quantum fields spatially confined to the network resolve its structure, and the resulting entanglement entropy depends on the local design of the network. There are cases where this regime becomes particularly important, for example, when the network is designed to capture only specific local aspects or a particular level of detail about a phenomenon, making the network's local structure crucial. In this subsection, we want to further explore this alternative use of network histories by considering the mass range $a \ll 1/\mu \ll \min(l, L-l)$ on each edge of the network shown in Fig. 4.16. For these mass values, the lattice points imposed by the finite resolution structure still effectively describe a quantum field theory on each edge, but the emerging quantum field theories are independent and locally influenced by the network structure, and do not manifest as a full-dimensional field theory throughout the network.

Consider the setups in Fig. 4.16 and Fig. 4.19 and denote by e_i each edge of $\mathcal{N}$ that is crossed by the entangling surface. For illustrative purposes, we highlight the edges e_i in Fig. 4.21, which depicts a two-dimensional spatial section of the considered setup. Quantum correlations across the entangling surface, and thus responsible for entanglement throughout the network, are all occurring through the crossing points on the edges e_i. If, on each of these edges, the field mass μ satisfies $1/\mu \ll \min(l_i, L-l_i)$, then, as discussed

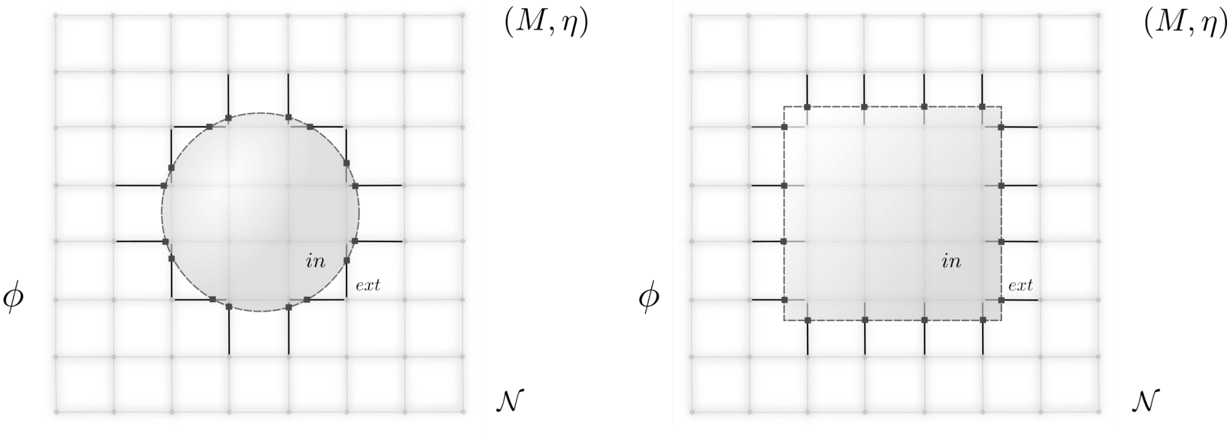

Figure 4.21: Spatial two-dimensional visualization of a quantum field ϕ (depicted in gray shades) spatially confined to a network $\mathcal{N}$, designed as a regular grid of finite size, embedded in Minkowski spacetime (M,η). An arbitrary sphere (left) and cube (right) divides the network setup into an interior and an exterior sector. Highlighted are the edges e_i of the network that are intersected by the entangling surface, along with their corresponding crossing points.

in Sec. 4.2.1, quantum correlations through the intersection between the edge e_i and the entangling surface, are fully localized on the respective edge e_i. In particular, they are supported only on sub-regions – defined by the correlation length $\xi = 1/\mu$ – which consist of intervals along the edges e_i, centered at the crossing points. No contributions to entanglement arise from vacuum fluctuations located in any other region of the network. As a consequence, relative to the quantum information measure we use, the network $\mathcal{N}$ is effectively equivalent to a collection of single edges piercing the entangling surface. As a result, the total entanglement entropy for vacuum fluctuations spatially confined to the network $\mathcal{N}$ is given, in this mass regime, as a sum of all contributions S_{e_i} coming from the sub-regions of the network localized on the edges e_i. According to Eq. (4.41), for a given size of the entangling surface, the total entanglement entropy reduces to

$$S_{\mathcal{N}} = \sum_{i=1}^{\mathcal{A}_{\mathcal{N}}} S_{e_i}\,, \tag{4.53}$$

where $\mathcal{A}_{\mathcal{N}}$ is the number of the crossing points with the entangling surface, determined by the specific structure of the network $\mathcal{N}$.

The entanglement entropy S_{e_i} associated with each edge partially traced out by the entangling surface has already been thoroughly analyzed in Sec. 4.2.1. Specifically, for

$1/\mu \ll \min(l_i, L - l_i)$ quantum fields on different edges contribute equally to the entanglement entropy, as for each edge only a single communication channel exists across the entangling sphere. Moreover, the value of S_{e_i} is independent of the angle at which each edge intersects the entangling surface, since quantum fields on the edge histories carry no information about the external embedding. Consequently, Eq. (4.53) simplifies to

$$S_{\mathcal{N}} = \mathcal{A}_{\mathcal{N}}\, S_{e_i}\,, \tag{4.54}$$

which aligns with the conjecture leading to Eq. (4.26). The exact value of S_{e_i} can be obtained numerically or analytically with $S_{e_i} = S^{\text{plat}} = \frac{1}{6}\ln\left(\frac{\xi}{a}\right)$. For simplicity, note that, in light of our discussion, the described setup is entirely equivalent to considering the edges as being crossed at arbitrary locations sufficiently far away from the endpoints. In the case of an entangling sphere, we align them along the radial direction and let them cross at $L/2$, as illustrated in Fig. 4.22.

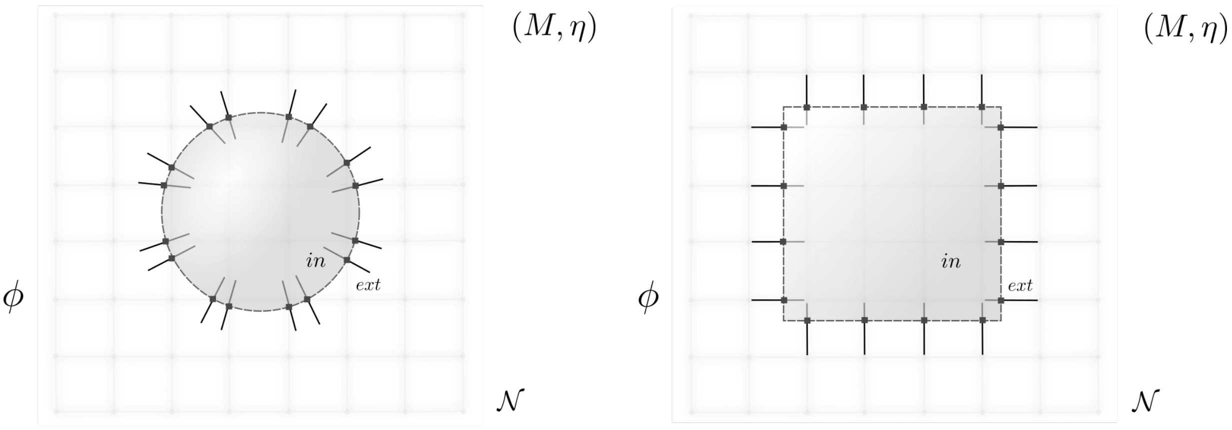

Figure 4.22: Equivalent configurations to the ones of Fig. 4.21 of a quantum field ϕ spatially confined to a network $\mathcal{N}$, designed as a regular grid of finite size, embedded in Minkowski spacetime (M, η). An arbitrary sphere (left) and cube (right) divide the network setup into an interior and an exterior sector. Highlighted are the edges e_i of the network that are intersected by the entangling surface, adjusted to be crossed precisely at $L/2$ in the case of an entangling sphere and aligned along the radial direction.

In order to compute exactly the entanglement entropy related to the three-dimensional grid when the field mass satisfies $1/\mu \ll \min(l_i, L - l_i)$ on each edge e_i, the remaining task is to determine the form of the factor $\mathcal{A}_{\mathcal{N}}$. In general, as the size of the entangling surface changes, the number of crossings with the network will vary. Therefore, $\mathcal{A}_{\mathcal{N}}$ depends not only on the local structure of the network but also on the radius R of the entangling sphere, i.e., $\mathcal{A}_\mathcal{N} = \mathcal{A}_\mathcal{N}(R)$, or the side length L_c of the entangling cube, $\mathcal{A}_\mathcal{N} = \mathcal{A}_\mathcal{N}(L_c)$. For a three-dimensional regular grid, the function $\mathcal{A}_\mathcal{N}$ can be estimated analytically. Recall that each edge of the regular grid has length L. In terms of the surface area of the traced out region defined by the grid, which approximates the interior of the entangling surface, the number of crossing points per unit area can be approximated by the constant value $1/L^2$ for $R, L_c \gg L$. By multiplying this density with the surface area of the traced out region, we obtain the total number $\mathcal{A}_\mathcal{N}$ of edges partially traced out, for any given value of R or L_c.

In the case of an entangling cube, the surface of the traced out region coincides with that of the cube. Consequently, this gives

$$\mathcal{A}_\mathcal{N}(L_c) = \frac{1}{L^2}\, 6\, L_c^2\, . \tag{4.55}$$

On the other hand, calculating the exact surface area of the traced out region becomes non-trivial in the case of an entangling sphere, as it requires detailed knowledge of the network's configuration near the sphere's surface for each value of R. For a regular grid with a high vertex density, this can be extremely challenging to compute. Nevertheless, as discussed previously, the total surface area of the traced out region is known to overestimate the surface area of the corresponding entangling sphere by a factor of $4/\pi$ for each R. Thus, we can rely on this relationship to calculate the surface area based on that of the sphere. Consequently, the function $\mathcal{A}_\mathcal{N}$ can be expressed analytically in terms of the radius R of the entangling sphere as

$$\mathcal{A}_\mathcal{N}(R) = \frac{1}{L^2}\,\frac{4}{\pi}\, 4\pi R^2\, . \tag{4.56}$$

Therefore, for each value of R or L_c and for a field mass in the range $1/\mu \ll \min(l_i, L-l_i)$ on each edge e_i, the network $\mathcal{N}$ is, in terms of entanglement, equivalent to a collection of $\mathcal{A}_\mathcal{N}(L_c) = 6\,\frac{L_c^2}{L^2}$ or $\mathcal{A}_\mathcal{N}(R) = 16\,\frac{R^2}{L^2}$ single edges crossing the entangling surface. The corresponding total entanglement entropy is given analytically by

$$S_\mathcal{N}(L_c) = \frac{1}{L^2}\, 6 L_c^2\, S_{e_i} = \frac{L_c^2}{L^2}\, \ln\left(\frac{\xi}{a}\right)\, , \tag{4.57}$$

for the case of an entangling cube, and

$$S_\mathcal{N}(R) = \frac{1}{L^2}\,\frac{4}{\pi}\, 4\pi R^2\, S_{e_i} = \frac{8}{3L^2}\, R^2 \ln\left(\frac{\xi}{a}\right)\, , \tag{4.58}$$

for an entangling sphere.

Since for a given mass μ the above expressions for the entanglement entropy are determined solely by the number of crossing points with the entangling surface – or equivalently, by the number of communication channels established between the interior and exterior sectors of the network – they naturally depend on the area of the traced out region.

To compare each analytical expression for the entanglement entropy with the corresponding numerical result for sufficiently large masses, we plot Eq. (4.57) and Eq. (4.58) as a function of the corresponding entangling surface's area, together with the numerical values for the same field mass, obtained by reapplying the code used previously [38]. The resulting entanglement entropies in terms of the surface area A of the entangling sphere or cube are shown in green in Fig. 4.23, for $\mu a = 1$ and using the respective parameters previously implemented for the three-dimensional grid in each case. Recall that since the numerical entanglement entropies for an entangling sphere were multiplied by a factor of $\pi/4$ to facilitate comparison with the (1+3)-dimensional result in full Minkowski spacetime, we apply the same adjustment to Eq. (4.58) when plotting it in terms of the entangling sphere's area.

From the plots, we observe that for both shapes of the entangling surface, the analytical entanglement entropy $S_{\mathcal{N}}$ agrees with the numerical results. This confirms the conjecture that for sufficiently large masses – ideally when $1/\mu \ll \min(l_i, L - l_i)$ on each crossed edge e_i of $\mathcal{N}$ – the entanglement entropy of vacuum fluctuations spatially confined to the entire network $\mathcal{N}$ is equivalent to that of vacuum fluctuations spatially confined solely to the local collection of single edges e_i of $\mathcal{N}$, as shown in Fig. 4.21. Consequently, the entanglement between the interior and exterior sectors of the network is confirmed to be localized near the entangling surface, with only short-range quantum correlations across the surface contributing significantly to the total entanglement entropy. An area scaling follows naturally.

Note that the specific geometry of the network $\mathcal{N}$ ensures that an entangling cube achieves a more accurate linear dependence on the area even for larger values of μa. This is a consequence of the cube's alignment with the underlying grid structure, which allows the nodes of the network to be avoided by the entangling surface, as previously discussed. Furthermore, for the same entangling surface area A, the entanglement entropies for both configurations agree, as the data points closely follow the same analytical curve. This demonstrates that, for large masses, the quantum information measure employed in our network experiment is insensitive to the shape of the entangling surface, unlike in the

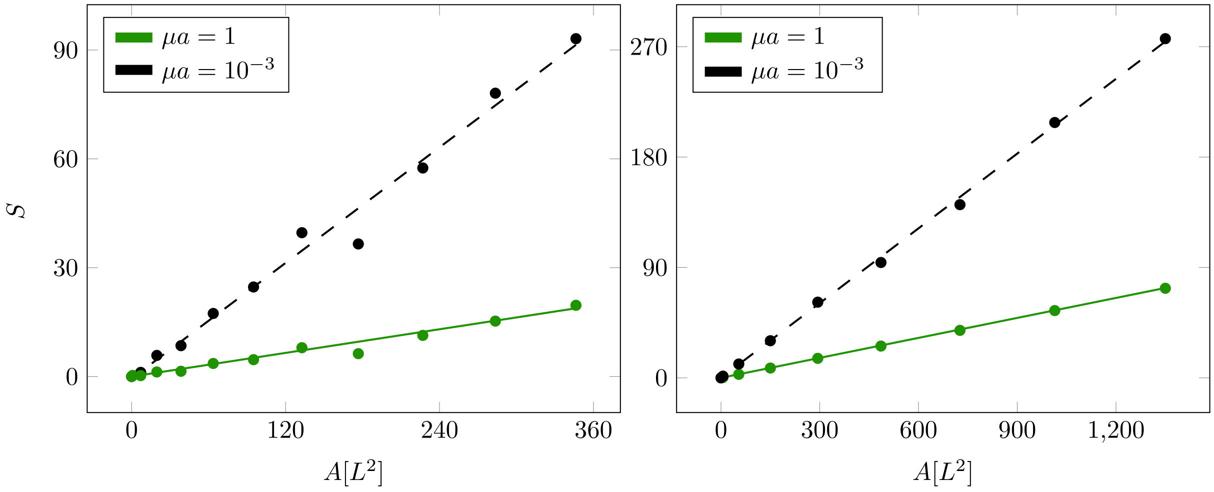

Figure 4.23: Entanglement entropy for vacuum fluctuations spatially confined to the three-dimensional network $\mathcal{N}$ shown in Fig. 4.16, in terms of the area A of the entangling sphere (left) and cube (right) for $\mu a = 1$. The analytical approximation $\frac{\pi}{4} S_{\mathcal{N}}(R) = S_{\mathcal{N}}(L_c) = \frac{1}{L^2} A\, S_{e_1}$ is shown with a solid line, while data points correspond to a numerical experiment for the same mass. The numerical results for $\mu a = 10^{-3}$ (Fig. 4.18 and Fig. 4.20) are reported again for comparison. For the left plot, the grid consists of 10x10x10 edges and is equipped with a finite resolution structure of $N_e = 6$ lattice sites with spacing a on each edge, such that $L = 7a$. In contrast, for the right plot, we choose a grid of 16x16x16 edges, equipped with $N_e = 3$ lattice sites with spacing a on each edge, such that $L = 4a$.

case where $\xi = 1/\mu \gg L$, where the entanglement entropy shows a shape dependence (Fig. 4.20).

Due to its simplicity, this analytical approach can serve as a substitute for numerical experiments when calculating the entanglement entropy of quantum fields confined to complex network configurations, provided the field masses satisfy certain constraints. This makes it particularly useful for more intricate scenarios, such as networks embedded in curved spacetimes, whenever $\mathcal{A}_{\mathcal{N}}$ is known or can be easily approximated, as demonstrated in the example above. Although within this mass range we lose the full predictive power of quantum networks for (1 + 3)-dimensional quantum field phenomena, this alternative, yet simpler analytical approach remains a powerful tool for probing and understanding phenomena on a local scale.

Chapter 5

Conclusion and Outlook

In this investigation, we developed and presented a novel framework for addressing natural phenomena in (curved) spacetimes, providing an alternative to conventional $(1+3)$-dimensional field theory methods, whenever these may prove insufficient. We relied on the key observation that lower-dimensional theories, particularly $(1+1)$-dimensional field theory, often offer significant simplifications in describing complex phenomena and, in some cases, provide exact solutions.

Rather than studying natural processes within a lower-dimensional framework, reducing the spacetime dimensions, we pursued an innovative approach by confining our probes, classical or quantum fields, to network-like structures as spatial supports. These physical structures, idealized as graphs or networks, are embedded within the surrounding $(1+3)$-dimensional background and exhibit their own dynamics, characterized by their histories. As such, they serve as theoretical devices that can be placed within the ambient space and employed as arenas where phenomena experiencing all spacetime dimensions can be investigated using lower-dimensional probes.

On the network history, by variational principles, we established a prescription to prevent degrees of freedom to leak into the surrounding space and set the conditions that control, at each node, the propagation of fields throughout the network. These conditions emerged as a generalization of Kirchhoff-Neumann conditions to arbitrary, curved spacetimes. Whenever these conditions ensure a self-adjoint Laplace operator, the fields on the network can be quantized.

The leitmotif of our analysis was to determine whether these (quantum) fields, confined to networks and their histories, can probe higher-dimensional phenomena and capture the same properties as fields within the full embedding spacetime.

To provide an answer, we have explored entanglement properties of vacuum fluctuations confined to networks histories embedded in the Minkowski spacetime. Strikingly, although the fields are spatially localized on the one-dimensional edges of the network, the entanglement entropy shows the same area scaling typical of fields in the full embedding $(1+3)$-dimensional spacetime, for any field mass μ. In particular, we observed that for sufficiently small masses, such that the correlation length $\xi = 1/\mu$ is larger than the length of the edges, fields populating the networks do not resolve their coarse-grained structure and they effectively describe a full-dimensional field theory. This is particularly remarkable since the area scaling in $(1+3)$ dimensions is rooted to the fact that fields in the full embedding spacetime carry angular momentum. Summing over all momenta for the field's ground state, results in a correlation length sufficiently short to localize entanglement across the entangling sphere close to its surface area, regardless of the field mass μ. In contrast, fields confined to network histories are restricted to a single spatial dimension along the edges and therefore lack any notion of angular momentum. Consequently, when the mass is sufficiently small, the correlation length increases unrestricted and entanglement across the entangling surface spreads throughout the network. The fact that, precisely within this range of masses, the fields on the network histories still give rise to an area law – rather than, for example, a volume scaling – is intriguing and suggests an effective emergence of angular momentum on the network.

Lastly, we investigated numerically the shape dependence of entanglement entropy by computing it for two different entangling surfaces: a sphere and a cube. We observed (Fig. 4.20) that for the same surface area, the entanglement on the network is equal for both shapes when the mass is sufficiently large. However, for sufficiently small masses, the entanglement entropy decreases when tracing out a cubical region. Since this mass regime is precisely where the network's coarse-grained structure is not resolved, with fields on the network effectively describing their counterparts in the full embedding spacetime, the shape dependence of entanglement entropy emerges as a property of fields in the $(1+3)$-dimensional Minkowski spacetime. Therefore, networks have not only proven capable of reproducing higher-dimensional phenomena with lower-dimensional field theories, but they have also delivered their first, new result, by capturing an insight on a still unknown phenomenon like the scaling of the entanglement entropy for vacuum fluctuations in the $(1+3)$-dimensional Minkowski spacetime, when tracing out a cubical region.

Throughout this work, we have found the theoretical devices we constructed to be highly versatile. Depending on the specific task, our approach allows for the design of networks that either yield exact analytical results on specific aspects of a phenomenon or, alternatively, serve as arenas where higher-dimensional phenomena emerge alongside an effective full-dimensional theory. In the latter case, as observed with the shape dependence of entanglement entropy, the network approach may provide numerical results rather than exact analytical solutions but can nonetheless offer pioneering insights into otherwise unknown phenomena. With further tuning of the network design based on these initial findings, a subsequent iteration could then yield targeted analytical results.

Although being forged as theoretical devices, networks also allow for experimental realization, and predictions from the network approach could be experimentally verified. For instance, as discussed with some authors of [39], there is potential to measure the entanglement entropy in experimental setups that resemble the graph configurations we considered, though technical limitations may constrain the complexity of networks that can be realized. In fact, more complex networks are already being manufactured, such as photon integrated circuits used in optical quantum computing applications [44], where, on a chip scale, squeezed states of light are fed into an optical network consisting of multiple optical paths and beam splitters. This setup could also serve as an excellent experimental model to study how, in the limit of large field correlation length, a one-dimensional photon propagator might effectively emerge within its three-dimensional counterpart.

Throughout this work, networks have been proposed as idealized representations of physical structures embedded within an ambient space. However, it is noteworthy that they could also be envisioned as fundamental structures of nature, not embedded but instead constituting the very fabric of the universe. From this perspective, the $(1+3)$-dimensional physics we observe might emerge as an effective theory on these four-dimensional networks, offering a revolutionary approach to our understanding of physics.

The area scaling of the numerical entanglement entropy found with networks, Fig. 4.18, also serves as a reference case for implementing the configuration depicted in Fig. 4.1 to investigate black hole scenarios. In fact, if we place the network partially across a Schwarzschild black hole horizon we can probe its processing of information as an emerging phenomenon on the network. In particular, if the area scaling of entanglement entropy deviates from the area law observed in Minkowski space, this discrepancy would indicate that the quantum information measure we use is sensitive to spacetime curvature. Building on this, it would be interesting to investigate the minimal network configuration capable of probing spacetime curvature. This feature would naturally lead to an implementation of networks to study horizon formation during a shell collapse. In fact, by positioning the network equipped with quantum fields across the surface of the collapsing shell at each instant of time, we could refer to the Schwarzschild result to investigate possible fingerprints of horizon formation left on the quantum information configuration on the network. Such a comparison could ultimately deliver a decisive verdict on black hole formation.

Bibliography

[1] R D Lehn, S S Chabysheva, and J R Hiller. Klein–gordon equation in curved spacetime. *European Journal of Physics*, 39(4):045405, May 2018.

[2] D.C. Mattis. The many-body problem: An encyclopedia of exactly solved models in one dimension. 1993.

[3] A.A. Belavin, A.M. Polyakov, and A.B. Zamolodchikov. Infinite conformal symmetry in two-dimensional quantum field theory. *Nuclear Physics B*, 241(2):333–380, 1984.

[4] Karl-Peter Marzlin and Michael P Kinach. Exactly solvable 2d model for photon propagation in curved space: loss of interference and bell inequality violation. *Classical and Quantum Gravity*, 39(6):065005, feb 2022.

[5] T. A. Harriott and J. G. Williams. Solution of the klein–gordon equation in a 2 + 1 curved space–time. *Modern Physics Letters A*, 16(18):1151–1156, 2001.

[6] Jacob D. Bekenstein. Black holes and entropy. *Phys. Rev. D*, 7:2333–2346, Apr 1973.

[7] Robert M. Wald. The thermodynamics of black holes. *Living Reviews in Relativity*, 4(1), July 2001.

[8] L. Susskind and J. Lindesay. *An introduction to black holes, information and the string theory revolution: The holographic universe*. 2005.

[9] Luca Bombelli, Rabinder K. Koul, Joohan Lee, and Rafael D. Sorkin. Quantum source of entropy for black holes. *Phys. Rev. D*, 34:373–383, Jul 1986.

[10] Mark Srednicki. Entropy and area. *Phys. Rev. Lett.*, 71:666–669, Aug 1993.

[11] Cecilia Giavoni, Stefan Hofmann, and Maximilian Koegler. Emerging entanglement on network histories. *Phys. Rev. D*, 109:085016, Apr 2024.

[12] Martin Schottenloher. *A mathematical introduction to conformal field theory*. Springer, 2nd ed. 2008. edition, 2008.

[13] Gregory Berkolaiko and Peter Kuchment. Introduction to quantum graphs. *Mathematical Surveys and Monographs*, 2012.

[14] Tsampikos Kottos and Uzy Smilansky. Quantum chaos on graphs. *Phys. Rev. Lett.*, 79:4794–4797, Dec 1997.

[15] Tsampikos Kottos and Uzy Smilansky. Chaotic scattering on graphs. *Phys. Rev. Lett.*, 85:968–971, Jul 2000.

[16] V Kostrykin and R Schrader. Kirchhoff's rule for quantum wires. *Journal of Physics A: Mathematical and General*, 32(4):595, jan 1999.

[17] Stephen A. Fulling. Local spectral density and vacuum energy near a quantum graph vertex. 2005.

[18] S. A. Fulling, L. Kaplan, and J. H. Wilson. Vacuum energy and repulsive casimir forces in quantum star graphs. *Phys. Rev. A*, 76:012118, Jul 2007.

[19] Robert Schrader. Finite propagation speed and causal free quantum fields on networks. *Journal of Physics A: Mathematical and Theoretical*, 42(49):495401, nov 2009.

[20] B. Bellazzini, M. Burrello, M. Mintchev, and P. Sorba. Quantum field theory on star graphs. 2008.

[21] B Bellazzini and M Mintchev. Quantum fields on star graphs. *Journal of Physics A: Mathematical and General*, 39(35):11101, 2006.

[22] Floyd R. M. Penrose, R. Extraction of rotational energy from a black hole. *Nature Physical Science*, 229:2058–1106, 1971.

[23] Demetrios Christodoulou and Remo Ruffini. Reversible transformations of a charged black hole. *Phys. Rev. D*, 4:3552–3555, Dec 1971.

[24] S. W. Hawking. Gravitational radiation from colliding black holes. *Phys. Rev. Lett.*, 26:1344–1346, May 1971.

[25] S. W. Hawking. Particle Creation by Black Holes. *Commun. Math. Phys.*, 43:199–220, 1975. [Erratum: Commun.Math.Phys. 46, 206 (1976)].

[26] Donald Marolf and Aron C. Wall. State-dependent divergences in the entanglement entropy. *Journal of High Energy Physics*, 2016(10), October 2016.

[27] Edward Witten. Aps medal for exceptional achievement in research: Invited article on entanglement properties of quantum field theory. *Rev. Mod. Phys.*, 90:045003, Oct 2018.

[28] H. Araki. Relative Entropy of States of Von Neumann Algebras. *Publ. Res. Inst. Math. Sci. Kyoto*, 1976:809–833, 1976.

[29] H. Casini and M. Huerta. A finite entanglement entropy and the c-theorem. *Physics Letters B*, 600(1–2):142–150, October 2004.

[30] H Casini. Mutual information challenges entropy bounds. *Classical and Quantum Gravity*, 24(5):1293, feb 2007.

[31] John L. Cardy and Ingo Peschel. Finite Size Dependence of the Free Energy in Two-dimensional Critical Systems. *Nucl. Phys. B*, 300:377–392, 1988.

[32] Christoph Holzhey, Finn Larsen, and Frank Wilczek. Geometric and renormalized entropy in conformal field theory. *Nuclear Physics B*, 424(3):443–467, August 1994.

[33] Pasquale Calabrese and John Cardy. Entanglement entropy and quantum field theory. *Journal of Statistical Mechanics: Theory and Experiment*, 2004(06):P06002, jun 2004.

[34] A. Riera and J. I. Latorre. Area law and vacuum reordering in harmonic networks. *Phys. Rev. A*, 74:052326, Nov 2006.

[35] Dimitrios Katsinis and Georgios Pastras. An Inverse Mass Expansion for Entanglement Entropy in Free Massive Scalar Field Theory. *Eur. Phys. J. C*, 78(4):282, 2018.

[36] Brian F. Hatfield. *Quantum field theory of point particles and strings.* Frontiers in physics ; v. 75. Addison-Wesley, Redwood City, Calif, 1992.

[37] Kerson Huang. *Scalar Fields.* John Wiley & Sons, Ltd, 1998.

[38] Cecilia Giavoni, Stefan Hofmann, and Maximilian Koegler. Emerging entanglement on network histories, https://doi.org/10.5281/zenodo.10437020, December 2023.

[39] Mohammadamin Tajik et al. Verification of the area law of mutual information in a quantum field simulator. *Nature Phys.*, 19(7):1022–1026, 2023.

[40] Yasaman K. Yazdi. Zero modes and entanglement entropy. *Journal of High Energy Physics*, 2017(4), 2017.

[41] Christophe Besse, Romain Duboscq, and Stefan Le Coz. Numerical Simulations on Nonlinear Quantum Graphs with the GraFiDi Library. *The SMAI Journal of computational mathematics*, 8:1–47, 2022.

[42] A B Kallin, E M Stoudenmire, P Fendley, R R P Singh, and R G Melko. Corner contribution to the entanglement entropy of ano(3) quantum critical point in 2 + 1 dimensions. *Journal of Statistical Mechanics: Theory and Experiment*, 2014(6):P06009, June 2014.

[43] Thomas Faulkner, Robert G. Leigh, and Onkar Parrikar. Shape dependence of entanglement entropy in conformal field theories. *Journal of High Energy Physics*, 2016(4):1–39, April 2016.

[44] Ulrik L Andersen. Photonic chip brings optical quantum computers a step closer. *Nature*, 591, 2021.

Danksagung - Acknowledgements

My first thank you goes to you, Stefan, for giving me the opportunity to embark on such a remarkable journey – one that has helped me grow both as a physicist and as a person, and for allowing me to work on such an inspiring project. You are an insightful, sensitive, and incredibly sharp mind, and I will never forget how, despite all the tough times, you managed to be there for me on the day I needed it most. I will always carry with me the wisdom of your words from that day, and I will never forget your genuine support. Next, I would like to thank Erik Curiel, an exceptional human being who introduced me to the international scientific community, guiding me through its pathways to all corners of the world. I am deeply grateful for the opportunities he provided and truly enjoyed our discussions. Furthermore, I would like to thank Dr. Michael Haack for serving as the second examiner of this thesis, as well as all the members of the defense committee.

My deepest thanks go to Marc and Maximilian – my fellow travelers, Maiskörner, and my best friends. Maximilian, you already know how grateful I am to have shared this journey with you. We went through so much together and found so much joy in research. Thank you for guiding me into this project and for always having an answer to my endless questions. None of this would have been possible without you. Thank you, Marc, for always being there for me and, more importantly, for always believing in me. I'm incredibly grateful for the DDM-PMS-CC1 trio, and I'm sure we will journey through much more together in this crazy world of physics. A big thank you to Florian for all our lunches and the fun times at university, and to Prof. Buchalla for welcoming me to their group lunches and insightful chats. Next, I would like to thank all my office mates and group members – among them Bruno, Katrin, Anamaria, Daniel, Ludwig and Jonas – for the enjoyable discussions and nice moments we shared.

Thanks to all my Munich friends – Nelvis, Kathi, Marivana, Pablo, Vroni, Sophie Marie, Gian, Vitto, Sara, Vale – all the Sant'Egidio friends, my football mentor Ire, e a tutti i miei amici a Monaco o sparsi per il mondo, che non vedono l'ora che io finisca questo dottorato

e incominci ad essere una persona seria con un lavoro serio. Un grazie di cuore a Maria, la donna più intelligente che conosco e che più ammiro, e a Sebastiano, per esserci sempre e per credere in me anche quando non lo faccio nemmeno io. Siete stati pilastri fondamentali di questi cinque anni. Un grazie speciale alle mie migliori amiche, alla mia famiglia, quella U. ma O., a quella allargata e ai davvero crazy Big Crazy.

Un grazie particolare va ai miei Nonni, specialmente Arrigo ed Edda. Anche se questi anni di dottorato mi hanno visto darvi un addio, rimanete le mie più grandi ispirazioni nella vita. Questa tesi è per voi.

Am End dank i dir, Jeff – mit dir is' Leb'n a riesngaudi Abenteuer. Infine, citando la mia ultima referenza di questo lavoro,

> Last but not least, I wanna thank me, I wanna thank me for believing in me, I wanna thank me for doing all this hard work. I wanna thank me for having no days off, I wanna thank me for, for never quitting. [...] I wanna thank me for just being me at all times.

Snoop Dogg